Non-local Impact ionisation coefficients in $Al_{0.8}Ga_{0.2}As$ and $Ga_{0.8}In_{0.2}N_{0.05}As_{0.94}Sb_{0.01}$ for GaAs-based APDs and SPADs

This thesis is presented for the degree of Doctor of Philosophy

Supervisor:
Dr. Andrew J. Marshall

Shadia Albeladi

February 2024

Declaration

I declare that the contents of this thesis are the result of my own independent investigation and work, and any material taken from any other published source has been stated. This work has not been submitted previously for any degree of qualification or to any other academic institution. This thesis is submitted in partial fulfilment of the requirements for the degree of Doctor of Philosophy.

Date **Signature**

9/2/2024

Conference presentations

S. Albeladi, A. P. Craig, J.P.R. David, A.R.J. Marshall" Non-local Impact Ionization Coefficients in Thin $Al_{0.8}Ga_{0.2}As$" UK Semiconductors, Sheffield university, UK (July 2023).

Acknowledgements

In the name of Allah, the most gracious and merciful, first and foremost, I am grateful to Almighty Allah for providing me with the strength, knowledge, ability, and opportunity to undertake and successfully complete this study. Secondly, I am grateful to King Abdulaziz University and the Saudi Arabic cultural bureau in the UK for giving me the opportunity to pursue my studies and for sponsoring me throughout these years.

I would also like to express my deepest appreciation to my supervisor, Dr. Andrew Marshall, for his patience, motivation, enthusiasm, and advice. Without his guidance and persistent help, this dissertation would not have been possible. My sincere thanks also go to Dr. Adam Craig for providing indispensable advice, information, and support on different aspects of my project. Much of my experimental and simulation work would not have been completed without his assistance. My thanks are extended to all the other members of the group who have supported me in one way or another.

I would also like to thank my family members and my friends for their support and encouragement through this long journey especially my sister Wadad and my cousin Aisha. I am extremely grateful to my parents for their love, prayers, and spiritual support. Special thanks to my husband and my kids.

Non-local Impact ionisation coefficients in $Al_{0.8}Ga_{0.2}As$ and $Ga_{0.8}In_{0.2}N_{0.05}As_{0.94}Sb_{0.01}$ for GaAs-based APDs and SPADs

Shadia Albeladi

February 2024

Abstract

This work attempts to develop AlGaAs/GaInNAsSb separate absorption and multiplication avalanche photodiodes (SAM APDs) and single photon avalanche diodes (SPAD). AlGaAs/GaInNAsSb is a promising structure, with significant potential benefits in detector and APD applications. The combination of the low-noise $Al_{0.8}Ga_{0.2}As$ avalanche multiplication layer with the high detection capability of the lattice-matched GaInNAsSb, would introduce a new choice of high-speed and cheap GaAs-based APD for 1.3 and 1.55 µm telecommunication applications. In this work, experimental measurements as well as a comparison to stochastic models were carried out to investigate the characterisation of different AlGaAs and GaInNAsSb materials and structures.

The use of GaInNAsSb, which is lattice-matched to GaAs, as an absorption layer in the SAM APD structure can exploit its narrow band gap energy to effectively detect wavelengths important to optical applications, such as 1.55 µm. When designing SAM APDs, it is crucial to consider if the absorber and avalanche materials have comparable electron-to-hole ionization coefficient ratios. Opposing coefficient ratios

of the absorber and multiplication layer would produce the worst case for APD noise and response time. An initial evaluation of the impact ionization coefficients and threshold energies of GaInNAsSb has been undertaken. Even though these coefficients have some degree of uncertainty, they can be used as a sufficient foundation for further research on this material. On the other hand, these coefficients can offer essential knowledge, such as the fact that beta is much greater than alpha, which would negatively affect noise in a poorly designed APD. In addition, the approximate fields where multiplication initiates and breaks down were identified. In the future, more work needs to be done to optimize these coefficients.

The large α/β ratio in bulk $Al_{0.8}Ga_{0.2}As$ structure offers low excess noise and low dark currents. Also, the wide indirect band gap of $Al_{0.8}Ga_{0.2}As$ enables fabrication of very thin multiplication widths without tunneling being a problem. Consequently, using $Al_{0.8}Ga_{0.2}As$ in a SAM structure can take advantage of the thin multiplication layer, exhibit desirable characteristics suited to high-speed, low-noise avalanche photodiodes, and maximise the reduction in excess noise due to the non-local ionisation effects. In order to characterize thin APDs, the non-local electron and hole ionization coefficients and threshold energies using the hard dead space model were extracted in this work and compared with those of other materials. It is demonstrated that, despite the fact that previously investigated thin GaAs APDs can achieve a similar significance of dead space with the associated minimisation of excess noise, it is difficult to exploit this advantage due to the significant tunnelling in GaAs. On the other hand, it is possible to produce a thin $Al_{0.8}Ga_{0.2}As$ APD with a dead space to ionisation path length ratio close to the fundamental limit, which leads to excellent low-noise multiplication without significant tunnelling. It is also found that in the case of the standard ideal *p-i-n* structure, these coefficients and threshold energies can effectively simulate multiplication in APDs as thin as 50 nm. This is substantially thinner than current state-of-the-art APDs.

The optimal charge sheet conditions for AlGaAs/GaInNAsSb SAM APDs can be determined by initially using GaAs as the absorber layer. Five samples were studied, and samples 3, 4, and 5 were found to be unsuitable for SAM APD applications as they failed to punch through. Sample 3 is suitable for SPAD applications operating at a higher voltage than the breakdown voltage. Sample 2 showed punch through into the absorber but kept the electric field below the required level for multiplication in the planned dilute nitride absorber layer. Therefore, the structure of sample 2 should be used as the nominal design for preparing to use a GaInNAsSb absorber layer. The AlGaAs/GaAs structure can be successfully simulated and redesigned based on correct coefficients to control the charge sheet conditions and achieve the desired punch-through voltage.

GaAs/AlGaAs SPADs with an extremely thin multiplication layer are found to exhibit a lower DCR than that in other common SPADs with relatively thicker multiplication layers, such as InGaAs/InP, InGaAs/InAlAs, and Ge/Si SPADs. On the other hand, these SPADs suffered from a higher afterpulsing probability than other SPADs. In the future, more work needs to be done to minimise the effect of afterpulsing, improving the SPAD's performance.

Despite the fact that this work provides the foundation for this structure's essential understanding, a lot of work must be done before it can be developed into products which improve on state-of-the-art APDs and SPADs. Using the extracted coefficients and threshold energies of AlGaAs and GaInNAsSb with a more sophisticated model such as a randomly generated ionization path length (RPL) can help to maximise the potential of the materials in new APDs and SPADs simulating important characteristics such as excess noise, impulse response, and breakdown probability. There is also scope for more open-ended simulation to explore the theoretical limits of APDs with multiplication widths which are substantially thinner than previously employed.

Contents

Chapter 1

1.1 Introduction

In general, photodetectors are electronic devices that receive a light signal as an input and produce an electrical signal that replicates the original signal. They play an essential role in almost every optoelectronic system and application. Photodetectors were first proposed in 1873 by W. Smith, who discovered photoconductivity in selenium [1]. However, Nobili and Macedonio Melloni in 1829 noted the sensitivity of the thermocouple to the passing heated body. This is now known as thermopile infrared detection.

Photodetectors can be classified based on the type of optical-to-electrical conversion effect, such as the photoelectric effect. Semiconductor based optoelectronic detectors take advantage of this effect when a material absorbs an incident photon along with its corresponding energy, releasing an electron-hole pair. This can be achieved only if the photon energy is equal to or greater than the bandgap. As a result, an electron from the valence band can be promoted to the conduction band. Photodetectors, which are based on semiconductors made from an alloy of group III and group V elements, are essential in many areas of our lives, such as healthcare, transportation, telecommunications, the internet, cybersecurity, quantum technologies, and retail.

Avalanche photodiodes (APDs) are an essential type of photodetector that provide high signal-to-noise ratios via internal gain due to impact ionisation. Impact ionization is a critical carrier generation process in semiconductors that influences the operation of several high-field electronic devices. An accurate knowledge of electron and hole impact ionization coefficients is important to simulate not only APDs but also electronic devices like transistors, especially as dimensions reduce and local electric fields increase. Recently, APDs have been used in various fields, such as commercial, military, optical fibre telecommunications, [2] imaging, [3], [4] and research applications. Due to the internal gain generated in APDs, a stage or two of subsequent noisy amplification can be avoided. As a result, APDs offer an advantage compared to *p-i-n* detectors, lowering overall system noise and increasing signal- to- noise ratio. However, APDs are slower compared to the *p-i-n* detector. This can negatively affect the performance of an optical communications system due to the reduction in the gain bandwidth product caused by the avalanching carriers' multiple sequential transits through the multiplication region.

Over recent decades, considerable effort has been made to improve the performance of APDs for optical fibre communication systems through optimization of material and device structure. In terms of structure, recent research has shown that using thin (<1 µm) APD multiplication regions helps to minimise excess noise due to the ionisation dead space, which reduces the fluctuation in the multiplication. In addition, using a thin multiplication layer can speed up the device due to the reduction in transit time and, hence, improves the gain bandwidth product. Today, for telecommunication systems operating at 1310–1550 nm, InP/$In_{0.53}Ga_{0.47}As$ SAM APDs are widely used. Mostly, the smallest InP multiplication layer thickness necessary to avoid excessive band-to-band tunnelling current determines the upper limit of these APDs' gain-bandwidth products (150 GHz) [5]. InAlAs (lattice matched to InP) with a slightly larger band gap (1.4 eV) compared to InP (1.35 eV) can achieve a thinner multiplication layer for a comparable level of tunnelling current. However, the gain-bandwidth products of AlInAs/InGaAs APD are still limited to ~180 GHz [6]. Si/InGaAs APDs can achieve gain band width product of 400 GHz [7].

Due to the wide indirect band gap of $Al_{0.8}Ga_{0.2}As$, an extremely thin multiplication layer has been reported with negligible tunnelling [8]. This is interesting because it should allow for the fabrication of fast devices with lower noise and a higher gain bandwidth than in Si, InP, and InAlAs APDs. In order to achieve that, Chapter 5 will investigate in detail the different characteristics of these devices.

Near-infrared wavelengths, particularly 1550 nm, are widely used in many applications, including fibre communication and light detection and ranging (LIDAR).

As 1550 nm infrared light has extremely small propagation losses in fibre, the signal can travel tens of kilometres without amplification, which is obviously desirable for fibre communication. For many LIDAR applications 1550 nm is also the optimal wavelength due to its relatively eye-safe nature. Compared to other options, these higher-power lasers provide users with superior fidelity, longer distances, and more accurate outcomes. LIDAR is a key component used in a wide range of applications, including autonomous vehicles, industrial robots, mapping and surveying and drones. It is used to precisely determine the distance between the sensor and the target object.

Dilute nitride alloys have shown promise for detection of near infrared wavelengths. This is because adding only a small amount of nitrogen results in a significant decrease in the energy band gap. For example, a band gap of ~0.8 eV was obtained for GaInNAsSb with just 5% nitrogen, whilst remaining lattice matched with GaAs. As a result, a dilute nitride layer can be used instead of InGaAs as an absorber layer due to its ability to detect near infrared wavelength up to 1550 nm [9]. Also, as dilute nitride is lattice matched with GaAs, it can be grown on an affordable GaAs substrate, which is available commercially in greater diameters compared to InP material. Since GaInNAsSb and AlGaAs are lattice-matched, the unique properties of these materials can be exploited in AlGaAs/ GaInNAsSb SAM APDs and SPADs. To prepare for that, in this thesis, particularly in Chapters 5, 6, and 7, the required foundational work is addressed.

Single photon detectors based on avalanche diode structures SPADs are electronic devices capable of detecting a single photon with sufficient detection efficiency. This allows them to be used in a wide range of applications. SPADs at near-infrared (NIR) wavelengths can be employed for LIDAR, atmospheric remote sensing, and some imaging systems, including autonomous vehicle trackers, allow detection down to the quantum limit. Due to the extremely low dark count rate (DCR) and afterpulsing probability of silicon-based SPADs, they are usually used for high-performance LiDAR. However, typically, they cannot operate at a wavelength over 905 nm. Despite the fact that InP/InGaAs SPADs provide an alternative platform to operate at longer wavelengths, their associated high DCR and afterpulsing significantly restrict their commercial applications. AlGaAs SPADs have been very rarely reported, but Chapter 7 reports some initial characterization of their properties.

1.2 Thesis Structure

The aim of this thesis is to lay the groundwork for future research to develop AlGaAs/GaInNAsSb SAM APDs and SPAD, enabling the most mature III-V substrate to reach the crucial telecommunications wavelength of 1550 nm. Chapter 2 covers the background information associated with the work presented in this thesis. This includes the essential parameters required to describe the photodiodes, such as the absorption coefficient, responsivity, quantum efficiency, and dark current mechanisms. It also introduces the background theory of APDs and SPADs. This is followed by a brief description of the dilute nitride material employed in this work. The literature review is discussed in Chapter 3. Chapter 4 illustrates the experimental techniques and characterisation setups used for APDs and SPADs studied in this thesis, including current-voltage, capacitance-voltage, photomultiplication, and DCR measurements. This chapter also provides the details of the modelling used to simulate multiplication and excess noise. The non-local electron and hole impact ionization coefficients and threshold energies of $Al_{0.8}Ga_{0.2}As$ are reported in Chapter 5. Avalanche multiplication characteristics of $Ga_{0.8}In_{0.2}N_{0.05}As_{0.94}Sb_{0.01}$ are investigated in Chapter 6. This chapter also reports the ionization coefficients and threshold energies of GaInNAsSb. In Chapter 7, a detailed investigation of $Al_{0.8}Ga_{0.2}As$ /GaAs SAMAPDs operated as SPADs is discussed. This includes device design, electrical characterisations, and photomultiplication measurements. This is followed by an analysis of the origin of the DCR and afterpulsing.

In the future, the demands for speed, high capacity of data, and security will be very essential for digital transformation. Also, photonics technologies will be crucial for the new field of telecommunication. The research in this thesis aims to contribute to these future advancements

1.3 References

[1] W. Smith, "Effect of Light on Selenium," *Nature,* vol. 7, p. 303, 1873.

[2] J. C. Campbell, "Advances in photodetectors," in *Optical Fiber Telecommunications VA*: Elsevier, 2008, pp. 221-268.

[3] N. Bertone and W. Clark, "Avalanche photodiode arrays provide versatility in ultrasensitive applications," *Laser Focus World,* vol. 43, no. 9, 2007.

[4] P. Mitra *et al.*, "Adaptive focal plane array (AFPA) technologies for integrated infrared microsystems," in *Intelligent Integrated Microsystems*, 2006, vol. 6232: SPIE, pp. 70-80.

[5] D. S. Ong, J. S. Ng, M. M. Hayat, P. Sun, and J. P. David, "Optimization of InP APDs for high-speed lightwave systems," *Journal of Lightwave Technology,* vol. 27, no. 15, pp. 3294-3302, 2009.

[6] A. Rouvie, D. Carpentier, J. Decobert, N. Lagay, F. Pommereau, and M. Achouche, "180-GHz gain-bandwidth product back-side-illuminated GaInAs–AlInAs APDs," *IEEE Photonics Technology Letters,* vol. 21, no. 11, pp. 712-714, 2009.

[7] W. Wu, A. R. Hawkins, and J. E. Bowers, "Design of InGaAs/Si avalanche photodetectors for 400-GHz gain-bandwidth product," in *Optoelectronic Integrated Circuits*, 1997, vol. 3006: SPIE, pp. 38-47.

[8] B. Ng *et al.*, "Avalanche multiplication characteristics of Al/sub 0.8/Ga/sub 0.2/As diodes," *IEEE transactions on electron devices,* vol. 48, no. 10, pp. 2198-2204, 2001.

[9] Y. Goh, S. Tan, S. Zhang, J. Ng, and J. David, "InGaAsN absorber for telecommunication wavelength APDs," in *2010 Photonics Global Conference*, 2010: IEEE, pp. 1-3.

Chapter 2

Background theory

2.1 Photodiodes parameters

2.1.1 Absorption coefficient

Free electrons in the valance band can be excited to the conduction band by absorption of a photon with higher energy than the band gap of the semiconductor. In a semiconductor material, the cut-off wavelength can be defined as the longest wavelength that can be detected, and it is given by:

$$\lambda = \frac{hc}{E_g(eV)} \qquad \textbf{2.1}$$

where λ is the photon's wavelength, h is Planck's constant, c is the speed of light, and $E_g(eV)$ is the bandgap of the semiconductor.

The absorption coefficient measures how far light can travel through a medium before it is absorbed, which has the dimension of inverse distance. If the absorption coefficient is high, the absorption occurs near the surface, while the light will penetrate further if the absorption coefficient is low.

Furthermore, it can be defined as the constant defining the rate of decrease in the intensity of light as it travels through the material. Absorption occurs with a profile given by Beer's Law [1] so the intensity of light, φ, can be expressed as:

$$\varphi(x) = \varphi_\circ(x)\exp(-\alpha_{abs}x) \qquad \textbf{2.2}$$

where $\varphi_\circ$ is the initial intensity of light at $x = 0$ and α_{abs} is the absorption coefficient.

In the absorption process, energy and momentum must be conserved during the transition of carriers between the valance band and the conduction band. Direct and indirect bandgap semiconductors clearly demonstrate energy conservation. The band gap is an important parameter for various semiconductor materials that indicates the minimum energy between the maximum of the valance band and the minimum of the conduction band.

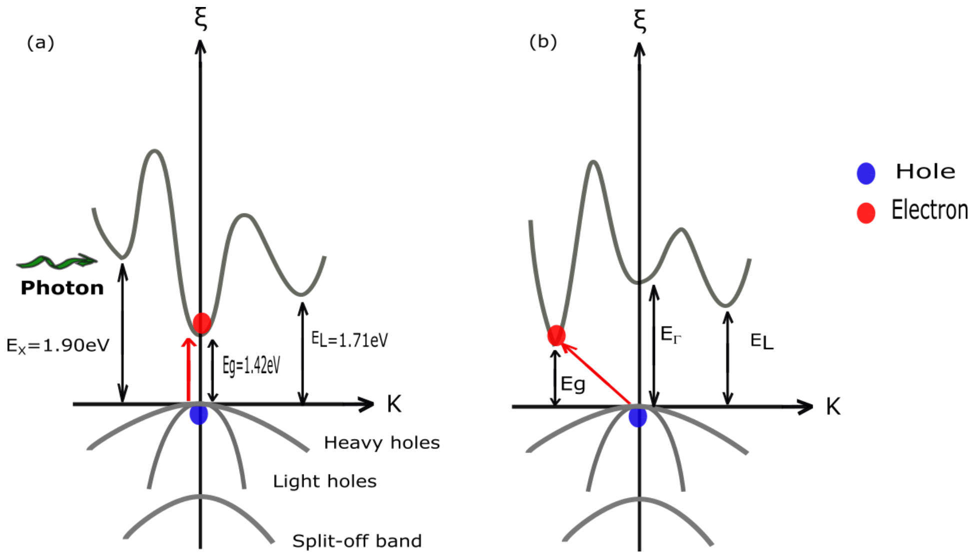

Figure 2.1: Examples of (a) the direct-gap band structure of GaAs, and (b) the indirect-gap band structure of Si. On both band structures, the absorption of a photon near the cut-off wavelength is shown (red arrow).

For photon energies close to the bandgap energy, indirect materials have a much lower absorption probability than direct materials. Figure 2.1 (a) shows the direct band gap in GaAs where the minimum of the conduction band is aligned in k space with the maximum of the valance band at Γ-point of the Brillouin zone. Consequently, an electron-hole pair can be easily generated by the absorption of a photon. Because the momentum is the same before and after the transition and it is conserved, the interaction with the phonon is not required to change the momentum. However, Figure 2.1(b) shows the case of photon absorption in Si. Si is an indirect semiconductor because the maximum in its valance band and the minimum in its conduction band (located at X point of the Brillouin zone) are at different wave vectors and hence different momentum. As a result, producing an electron-hole pair requires such an electron to interact not only with the photon to gain energy but also with a phonon in order to change the momentum.

When considering a wavelength close to the cut-off wavelength with photon energy close to the band gap energy, the absorption coefficient in a direct band gap is related to two parameters: the wavelength of the light, which represents the photon- absorbed energy $\hbar\omega$, and the absorption layer material, which represents the band gap energy, and it is given by [2]:

$$\begin{aligned} \alpha_{abs} &= (\hbar\omega - E_g)^{\frac{1}{2}}, \quad \hbar\omega \geq E_g \\ \alpha_{abs} &= 0 \qquad\qquad \hbar\omega < E_g \end{aligned} \tag*{2.3}$$

where $\hbar$ is the reduced Planck's constant and ω is the photon's angular frequency. However, in the indirect band gap, the previous expression must incorporate a term of $\pm\hbar\Omega$ which is the phonon absorption and emission as:

$$\begin{aligned} \alpha_{abs} &= (\hbar\omega - E_g \pm \hbar\Omega)^2 \;, \; \hbar\omega \geq E_g \\ \alpha_{abs} &= 0 \qquad\qquad \hbar\omega = E_g \end{aligned} \tag*{2.4}$$

where Ω is the phonon's frequency. The direct and indirect bandgap is determined by the horizontal intercepts of the α_{abs}^2 versus $\hbar\omega$ plot and $\alpha_{abs}^{\frac{1}{2}}$versus $\hbar\omega$, respectively as shown in Figure 2.2.

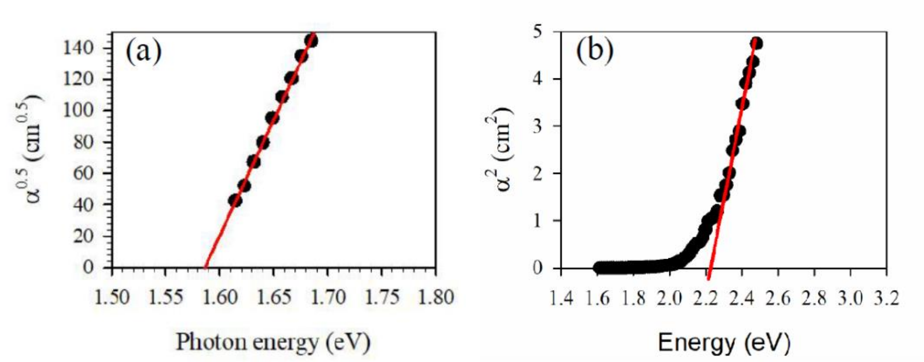

Figure 2.2: Extracting the direct (b) and indirect bandgap (a) for AlAsSb grown lattice matched to InP substrate. Adopted from [3].

2.1.2 Responsivity and quantum efficiency

Responsivity (R) and quantum efficiency (QE) are critical parameters in describing a photodetector's response to light. The responsivity is the fraction of the photocurrent generated in the detector to the power of the incident light, usually expressed in units of AW^{-1}, and it can be explained by the following equation:

$$R = \frac{I_{ph}}{P} \qquad \textbf{2.5}$$

where $\mathrm{I_{ph}}$ is the photocurrent, P is the optical power on the surface. In order to measure the power of a light source more conveniently, commercially available detectors usually use responsivity instead of quantum efficiency. The quantum efficiency QE refers to the ratio of photogenerated electrons collected by the electric field N_e to the number of incoming photons N_p which arrive at the detector's surface. The quantum efficiency (QE) is given by:

$$QE = \frac{N_e}{N_p} = \frac{I_p hc}{Pq\lambda} \qquad \textbf{2.6}$$

where λ is the wavelength of the source. From equations 2.5 and 2.6, quantum efficiency can be written in terms of Responsivity by:

$$QE = \frac{Rhc}{q\lambda} \qquad \textbf{2.7}$$

As hc equals 1240 eV nm, equation 2.7 can be rewritten as:

$$QE = 1240 \times \frac{R}{q\,\lambda(nm)} \qquad \textbf{2.8}$$

External quantum efficiency limitations

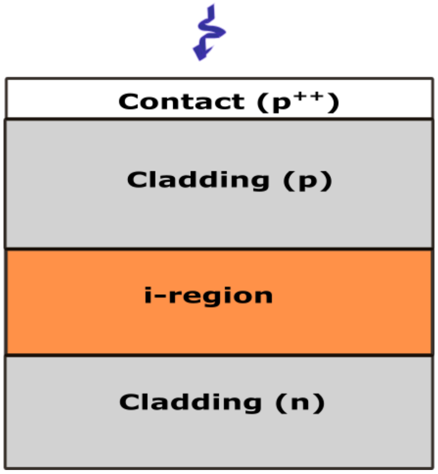

Figure 2.3: A schematic structure of typical *p*-*i*-*n* photodiode.

For typical photodiodes with top illumination, such as a *p*-*i*-*n* diode shown in Figure 2.3, there are some limitations to achieving unity quantum efficiency (QE) in real semiconductors. Quantum efficiency can be limited by the reflection of the incident photons on the surface of the photodiode, which is about 30% of the incident light (for most common semiconductors). The wavelength-dependent refractive index is ~3.4 for GaAs, while it is only 1 for air. The reflection is caused by the significant difference in refractive indices between the semiconductor and the air. The photodiode has a thin, highly doped top contact layer to reduce contact resistance. Furthermore, although this thin contact layer can absorb in the order of 10% of the incident light, the minority photogenerated carriers in this layer are unable to reach the junction and contribute to the photocurrent. This is due to the high majority carrier concentration in this layer, which results in a reduction in the minority carrier's lifetime. Because of the 30% surface reflection loss and the 10% non- photocurrent absorption in the contact layer, the quantum efficiency of many practical research photodiodes is expected to be 50–55%. The absorption in the contact layer can be avoided by etching it off from the optical window, which enhances the quantum efficiency and the device's performance. In order to remove the negative impact of reflection on quantum efficiency, an anti-reflection coating can be used. To achieve optimal performance, the refractive index of a single-layer AR coat (n_{AR}) should be:

$$n_{AR} = \sqrt{n_{SC}} \qquad \textbf{2.9}$$

where n_{SC} is the refractive index of semiconductors. The ideal single layer AR coating thickness (T_{AR}) can be calculated using the formula:

$$T_{AR} = \frac{\lambda_0}{4n_{AR}} \qquad \textbf{2.10}$$

where λ_0 is the wavelength of light in free space for which the AR coating is optimised. Once the light has passed through the air/semiconductor interface and the highly doped contact layer, it needs to be absorbed in the depletion or diffusion region to generate photocurrent. Both the absorption coefficient and absorption width have a significant impact on the quantum efficiency. Therefore, the maximum external quantum efficiency is given by:

$$QE_{max} = (1 - R_S)(1 - \exp(-\alpha_{abs}L)) \qquad \textbf{2.11}$$

where L is the thickness of the absorption width and R_S is the reflection coefficient at the surface of the semiconductor. When an anti-reflection coating is used, R_s equals 0 which means no light is lost due to reflection, resulting in a value known as the internal quantum efficiency. The internal quantum efficiency can be derived from the external quantum efficiency by dividing equation 2.11 by$(1 - R_S)$. [4]

According to equation 2.11, at constant L, a higher absorption coefficient results in a higher quantum efficiency. It is also shown that there is a proportional relationship between the absorption width and the maximum quantum efficiency. Absorption width can be defined as the length across which both absorption and depletion take place. Therefore, photons can be absorbed, and photocarriers can be created and accelerated in an electric field, resulting in photocurrent. In the simple case of a heterojunction diode, where absorption occurs only in the intrinsic layer the absorption width is equal to the intrinsic width. In addition, in the case of a homojunction diode with a constant α, the absorption width equals the total width of the depletion and diffusion lengths. Consequently, by increasing the depletion region or diffusion length, the absorption width will increase, allowing more photocurrent to be generated and thereby enhancing the quantum efficiency. The depletion width is restricted by the unintentional doping concentration of the intrinsic region. However, even if the carriers are generated outside the depletion region, it is possible for them to reach the space-charge region and contribute to the photocurrent by diffusion to the depleted region. The diffusion length of a carrier type in a material L_D is how far the excited carrier can travel before recombining. The diffusion length is related to the lifetime of the excited carrier τ by:

$$L_D = \sqrt{D\tau} \tag{2.12}$$

where D is the diffusion coefficient. The diffusion length is a function of the quality of the material, and it is one of the few parameters that characterize the purity of a material. Having a long diffusion length indicates a long lifetime. This means the carriers can travel long distances without any recombination due to material defects [5]. In addition, the diffusion length is strongly influenced by the doping concentration and temperature [6]. When absorption takes place in the p and n- cladding layers, the electron and hole minority carriers, respectively, diffuse to the space-charge region. The high doping concentration of these layers results in more recombination events, which in turn reduce the diffusion length. Diffusion length is related to mobility μ by:

$$L_D = \sqrt{\frac{k_B T \mu \tau}{q}} \tag{2.13}$$

where k_B, T , and q are Boltzmann's constant, temperature, and electron charge, respectively. At higher temperatures, carrier scattering rates increase which reduces μ. This in turn reduces diffusion length such that the temperature dependence of μ dominates the temperature dependence of the diffusion length. The diffusion length is also affected by band structure (either the semiconductor has a direct or indirect band gap). The lifetime of indirect band gap materials is typically longer than that of direct band gap semiconductors. For example, in AlGaAs, as the x fraction approaches

0.4, which is near the point at which AIGaAs becomes an indirect gap semiconductor, the lifetime and then the diffusion length is expected to be higher [7].

In another case of a homojunction diode with constant depletion and diffusion length, starting from the cut-off wavelength, the absorption becomes stronger as the wavelength decreases (α increases). Initially, this will lead to the absorption of an increased fraction of the incident photons and an increase in quantum efficiency. However, as the wavelength continues to reduce and alpha continues to increase, the absorption width will reduce and the number of photons absorbed in the deletion region or diffusion length will ultimately decrease, leading to a reduction in quantum efficiency. At extremely short wavelengths and high photon energies, absorption occurs close to the surface and far from the depletion region. Consequentially photogenerated carriers cannot be collected, photocurrent cannot be generated, and there is no quantum efficiency.

Furthermore, the structure may be more complicated, such as the separate absorption and multiplication SAM structure, where the absorption takes place on one side of the type of junction, to control the primary carrier type.

2.1.3 Dark current mechanisms

Dark current is defined as the currents that flow in a photodiode in the absence of light. In order to improve the signal-to-noise ratio and the photodiodes, the dark current must be minimized. As a result, a lot of efforts have been devoted to reducing the dark current, including material selection, heterostructure design, and passivation techniques. Several mechanisms can result in dark currents including diffusion I_{diff}, Shockley-Read-Hall (SRH) (generation and recombination ($I_{G\&R}$)), band to band tunnelling (I_{tunn}) and surface leakage (I_{surf}). The first three mechanisms are all bulk-limited, where the dark current is directly proportional to the device area. On the other hand, the last mechanism is surface dominated, which means that the magnitude of surface leakage current is proportional to the device perimeter.

Diffusion currents are caused by the injection of minority carriers into the junction from the extrinsic area of the device [8].

$$J_{diff} \propto n_i^2 \propto T^3 \exp\left(\frac{-E_g}{k_B T}\right) \qquad \textbf{2.14}$$

where E_g is the bandgap, and the factor of T^3 accounts for the density of states [9]. An Arrhenius plot of the dark current density of a photodiode on a logarithmic scale as a function of inverse temperature can be used to measure the activation energy from the gradient. When diffusion is the dominant leakage current mechanism, the activation energy is equal to the full bandgap.

In Shockley Read Hall (SRH) generated dark current, the defects and threading dislocations in the crystal lattice cause mid-gap trap states in the bandgap, which act as generation centres. The amount of energy needed to thermally excite an electron from the valance band to the conduction band is significantly decreased. This will allow for more transitions resulting in generation-recombination currents in the depletion region of *p-i-n* diodes [8]. So, the density of defects and the quality of the material influence the rate of thermal generation. Cooling the device can help to reduce the thermal generation current by reducing the thermal energy available to excite electrons into the conduction band. For SRH dark current, there is a direct relationship between the intrinsic carrier concentration and the dark current density as follows:[9]

$$J_{SRH} \propto n_i \propto T^{\frac{3}{2}} \exp\left(\frac{-E_g}{2k_B T}\right) \qquad \textbf{2.15}$$

In this case, according to an Arrhenius plot, the activation energy is approximately half the bandgap [9].

The band-to-band tunnelling and trap-assisted tunnelling currents can be significant sources of reverse-biased diode leakage current observed in III-V semiconductor materials. The magnitude of achievable electric field is often limited by tunnelling in these materials, which has significant consequences for photodetector design and performance, particularly for APDs. For example, devices fabricated with materials such as $Al_{0.8}$ $Ga_{0.2}$ As with a wide indirect band exhibit very low tunnelling current. This allows for the design of small devices with a high electric field. There is an essentially exponential relationship between the applied voltage and the tunnelling current. The generation-recombination or diffusion leakage current does not show this kind of behaviour. Band-to-band tunnelling current in reversed-biased, direct-gap semiconductors can be written as:

$$I = \frac{(2m^*)^{1/2} q^3 EVA}{4\pi^2 \hbar^2 E_g^{1/2}} \exp\left(-\frac{\theta m_0^{1/2} E_g^{3/2}}{q\hbar\xi}\right) \qquad \textbf{2.16}$$

where m^* is the effective mass of the tunnelling carrier, m_0 is the free electron mass, $\boldsymbol{\xi}$ is the electric field, V is the applied voltage across the junction, and A is the junction area. As shown in the equation, the tunnelling current increases with the electric fields and decreases with the band gap and the effective mass. The parameter θ is a dimensionless quantity expressed as:

$$\theta = \alpha \left(\frac{m^*}{m_0}\right)^{1/2} \qquad \textbf{2.17}$$

where α is a barrier shape characteristic. The exponential term in equation 2.16 represents the probability that a carrier in the valence band tunnels into the conduction band without thane aid of traps. Equation 2.16 can be applied if the total voltage, which includes both the applied voltage and the built-in voltage, exceeds $\frac{E_g}{q}$. At low electric fields or high temperatures, other sources of leakage may dominate, causing the leakage current to deviate from equation 2.16. During direct tunnelling, an electron moves from the valence band to the conduction band without absorbing or emitting a phonon. On the other hand, in the indirect tunnelling process, a tunnelling particle changes its momentum through the absorbing or emitting of a phonon. For this reason, direct tunnelling is more likely than indirect tunnelling. Trap-assisted tunnelling refers to tunnelling through traps located within the band gap. This mechanism is similar to the more fundamental band-to-band process, but it requires a lower electric field [10].

The source of surface leakage current is the termination of the regular crystal lattice, and hence the regular periodic potential that gives the band structure, at the device/air interface, which can result in a conducting surface layer around the perimeter of a mesa diode[11]. In some materials, this termination can lead to the bending of the bands and the accumulation of electrons, which makes the surface more conductive. In addition, due to this termination, dangling bonds can be created, and some of them can bond with atoms of other contaminated materials, such as oxygen, resulting in additional electronic states and hence surface leakage current.

According to the Arrhenius plots, surface leakage current has a small activation energy. This means it is less susceptible to temperature changes. Passivation using dielectric, such as $SU-8$, is a highly effective method of suppressing surface leakage current. In small devices with a high perimeter-to-area ratio, the surface leakage current is dominant. As a result, small devices can be used effectively to characterise the surface leakage current.

2.2 Avalanche photodiodes APDs

Photodiodes are one of the fundamental devices used to detect light, ranging from ultraviolet (UV) to infrared (IR). Under moderate reverse bias voltage, photodiodes employ the p-n junction and associated electric field to separate the photo-generated electron-hole pairs, which induces a current in an external circuit. An application with a low photon flux and a weak associated signal requires external amplification. This external amplification, however, introduces noise and limits the signal-to-noise ratio. The APD with its internal gain and high overall signal-to-noise ratio is an effective alternative to a *p-i-n* photodiode. APDs are also able to operate in Geiger mode, above their breakdown voltage, with a high ability to detect a weak optical signal as low as a single photon using impact ionization, which is the physical process that drives the internal gain in APDs. The gain, or multiplication at any given voltage $M(V)$, can be calculated by the ratio of the total photocurrent $I_{ph}(V)$ and the primary photocurrent I_{pr} which is the photocurrent without multiplication or the photocurrent at which $M(V)$ is unity.

$$M(V) = \frac{I_{ph}(V)}{I_{pr}} \qquad \textbf{2.18}$$

2.2.1 Impact ionization in semiconductors

Impact ionization is a scattering process where a new electron-hole pair can be generated at high electric fields in semiconductors. This phenomenon is the physical process that drives the internal multiplication/gain M in $APDs$. The energy of free carriers moving across high electric fields in a semiconductor can be identified by the sum of the kinetic energy gained from the high electric field and the loss due to phonon scattering. As a result of the high electric field in the depletion region of APDs, photogenerated carriers can gain sufficient energy to generate additional carriers. In this process, as shown in Figure 2.4, an energetic primary carrier (electron or hole) collides with an electron in the valence band and moves it to the conduction band, generating an electron-hole pair. In the same way, the initial carrier and the two new carriers can be accelerated by the electric field, and further electron and hole pairs can be generated, resulting in an internal gain. Under a high electric field, a sequence of impact ionisation events can occur, and the probability of each carrier ionising becomes, on average, 1, and the avalanche becomes self-sustaining, giving rise to avalanche breakdown. This is depicted schematically in Figure 2.4 for the multiplication process initiated by an electron in the high-field region of a *p*-*i*-*n* diode. Even though the electric field is uniform and the values of α and β remain unchanged, the distance travelled between ionisation events is not constant, demonstrating the random nature of impact ionisation and hence avalanche multiplication.

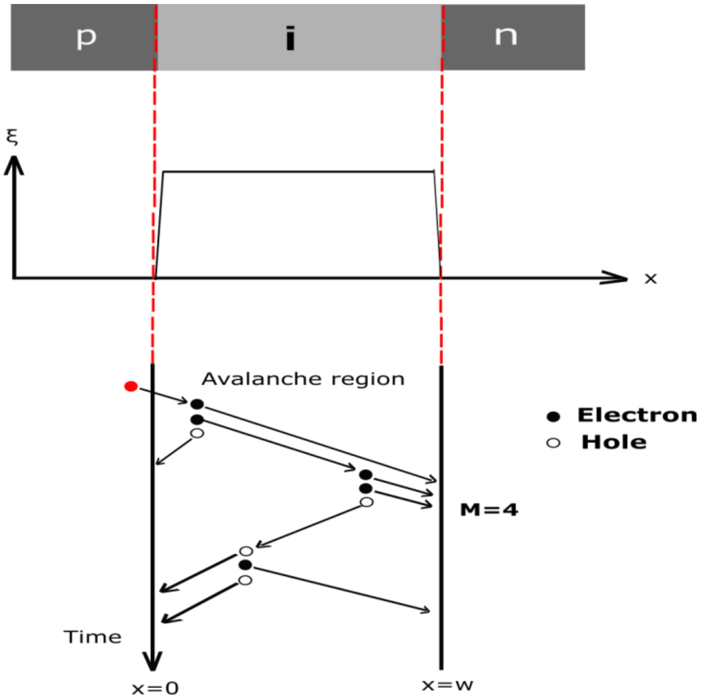

Figure 2.4: Schematic illustration of a possible electron-initiated multiplication process in the high- field region of a *p*-*i*-*n* diode.

A carrier traveling through an electric field ξ may obtain energy, E, which can be expressed as follows:

$$E = \xi q x \qquad \textbf{2.19}$$

where *x* is the travelling distance in the direction of the field. However, this equation doesn't consider the interactions between the carrier and its surrounding environment. The interactions with the crystal lattice or with other carriers might cause scattering of the carrier. An individual carrier's energies might increase or decrease due to any single scattering event. However, after initial heating due to movement in the electric field, the carriers attain equilibrium as a result of the competing effects of scattering and acceleration by the electric field. At equilibrium the rate of energy gained from the field is equal to the rate of energy lost due to the scattering. If the equilibrium energy is above the ionisation threshold, then ionisation is possible. When it occurs, ionisation is a major scattering event which takes the primary carrier back to a lower energy and out of equilibrium with the field.

The probability of a carrier ionizing depends on its energy where the carrier must have an energy greater than or equal to the threshold energy to ionize, for energies below this the probability of ionising is zero. In order to promote an electron from the valance band to the conduction band, the threshold energy must be greater than the bandgap energy as an absolute minimum. In practice, the threshold energy is strongly affected by the semiconductor material's band structure and the need to conserve energy and momentum. This means different band structures lead to correspondingly different E_{th}. Consequently, the material's band structure strongly determines the degree to which the threshold energy is greater than the bandgap energy.

The threshold energy for electrons was estimated by Anderson and Crowell [12] as

$$E_{th} = E_g\left(1 + \frac{m_e}{m_e + m_h}\right) \qquad \textbf{2.20}$$

where m_e and m_h are the electron and hole masses of the parabolic, spherical band. Wolff *et al.* [13] stated that E_{th} is equal to 1.5 E_g based on the assumption that the electron and hole effective masses are almost equal.

For a carrier to initiate ionisation, it must travel some distance in the high electric field to obtain the threshold energy. This distance is called dead space, and it is defined as the smallest distance that a carrier needs to travel to attain sufficient energy for impact ionisation. The ballistic model provides the first approximation of electron dead space d_e and hole dead space d_h as

$$d_e = \frac{E_{the}}{q\xi} \quad , d_h = \frac{E_{thh}}{q\xi} \qquad \textbf{2.21}$$

where E_{the} and E_{thh} is the electron and hole threshold energy respectively.

When a carrier gains the ionisation threshold energy, its ionisation probability becomes greater than zero, and it can be called "enabled". However, the carrier's ionisation probability depends on its energy, exhibiting an increase as the energy increases. As a result, the probability of impact ionisation for carriers increases in proportion to the strength of the electric field in which they move, which in turn increases the equilibrium energy distribution of those carriers. This probability is characterised by electric field-dependent impact ionisation coefficients (expressed by

α for electron and β for hole). $\alpha(\beta)$ can be defined as the average number of ionization events that an electron (or hole) experiences while moving a unit distance in the electric field. They are crucial parameters that describe the impact ionisation process, expressing the reciprocal of the average distance that a carrier moves between impact ionisation events. These two coefficients' values depend on the material band structure, electric field, and temperature. The ionisation coefficients can be affected by both the band gap and the scattering. At a given scattering rate, using a material with a smaller band gap provides higher ionisation probabilities and, hence, higher ionisation coefficients. In addition, at a given band gap, a material with stronger scattering exhibits lower ionisation probabilities and, thus, lower ionisation coefficients. Higher temperatures can minimise the probability of ionisation because of the significant carrier energy lost due to higher scattering. On the other hand, the ionisation probability can increase with temperature due to the reduction in the band gap, although this is usually a secondary effect.

A high electric field increases the carrier's energy, which in turn increases the possibility of ionisation. The electron and hole impact ionisation coefficients can be described by the following formula:

$$\alpha,\ \beta\ = A_{e,h}\ \exp\left(\frac{B_{e,h}}{\xi}\right)^{C_{e,h}} \qquad \textbf{2.22}$$

where$A_{e,h}$, $B_{e,h}$ and $C_{e,h}$ are parameters that are different depending on the material and the carrier's type. The ionization coefficient has a dimension of cm^{-1}.

2.2.2 Noise

It is important to notice that the gain in an APD comes at a price. Whereas the multiplication process amplifies the photogenerated signal, it also amplifies the dark currents, which leads to a further contribution of noise. In addition to the conventional electronic noise sources, there is another source of the excess noise resulting from the random nature of the impact ionization process characterised by the excess noise factor F which can hence limit an APD's maximum useful gain. The shot noise power of a primary or un-multiplied photocurrent $I_\circ$ is defined as:

$$I_n^2 = 2qI_\circ BW \qquad \textbf{2.23}$$

where BW is the bandwidth.

With the incorporation of the effect of multiplication, I_n^2 ,is rewritten as:

$$I_n^2 = 2qI_\circ M^2 FBW \qquad \textbf{2.24}$$

where F is the excess noise factor.

In $APDs$, the variance in multiplication values is as important as the average multiplication value. There are two factors that influence the variability of multiplication and the degree of determinism in the avalanche. The first consideration is the ionization coefficient ratio $k = \frac{\beta}{\alpha}$. The second consideration is the relative influence of dead space. In the early work of McIntyre [14], if the ionisation probability only depends on local electric field and α and β are constant, the excess noise factor F can be written as a function of M and the k_{eff} ratio as:

$$F = k_{eff}\, M + \left(1 - k_{eff}\right)\left(2 - \frac{1}{M}\right) \qquad \textbf{2.25}$$

where $k_{eff} = k$ for pure electron injection and $k_{eff} = \frac{1}{k}$ for pure hole injection.

It is clear that this is a reasonable approximation in a large number of cases to model avalanche multiplication and breakdown.

Two cases can be considered to demonstrate the effect of k on the variation of multiplication and, in turn, on the excess noise factor. The excess noise can be eliminated, and the avalanche breakdown can not be achieved in the first case where one of the ionization coefficients (α or β) is zero and initiating the avalanche process by a carrier type of the second ionization coefficient. On the other hand, in the second case, when both α and β are finite ($\alpha = \beta$) the excess noise can greatly increase, and the avalanche breakdown can take place. At a low electric field, there is typically a significant difference between α and β . When alpha (beta) is higher than beta (alpha) and the multiplication is initiated by electrons (holes), k_{eff} and hence the excess noise factor becomes a small value. On the other hand, at a high electric field,

α and β are typically found to converge, which leads k_{eff} to approaching unity and hence a high excess noise factor.

In the case of a thick avalanche width, where dead space is negligible, several useful design rules of APDs can be provided using this local noise model. The relationship between F and M for various values of k_{eff} was illustrated in Figure 2.5. This figure shows that if there is a wide difference between the ionization coefficients and the avalanche process has been initiated by carriers with the higher ionization coefficient, the low excess noise can be recorded. However, high excess noise can be achieved by the wrong carrier type.

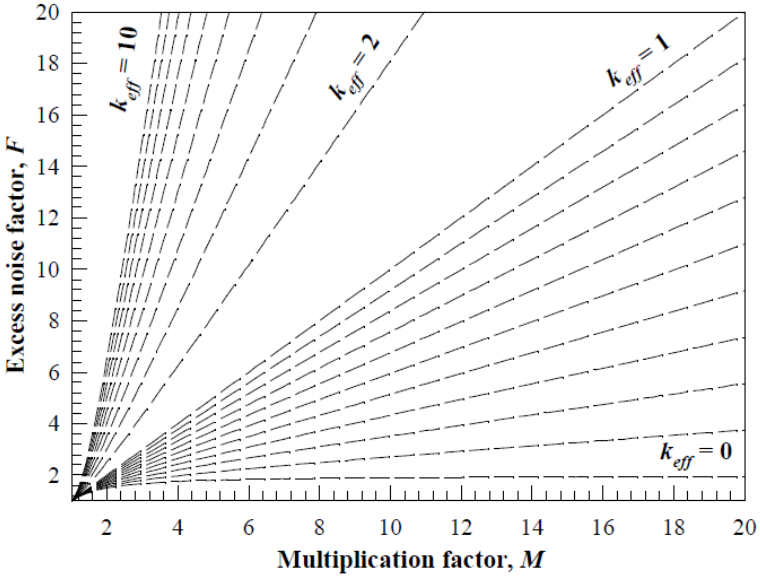

Figure 2.5: McIntyre's local noise predictions for k_{eff} = 0 to 1 in steps of 0.1 and k_{eff} = 2 to10 in steps of 1 where k_{eff}=k for the injection of electrons and k_{eff}=1/k for the injection of holes.

The excess noise factor is related to the stochastic gain (M_n) that is experienced by each injected primary carrier by:[15]

$$F = \frac{\frac{1}{z}\sum_{n=1}^{n=z} M_n^2}{\left(\frac{1}{z}\sum_{n=1}^{n=z} M_n\right)^2} \qquad \textbf{2.26}$$

where z represents the total number of injected carriers. This formulation for F considers all determinism enhancements, including those due to dead space.

McIntyre’s local noise theory offers the possibility of designing APDs with minimal excess noise. An effective method for decreasing background noise is to choose a material with a significant difference between α and β. Since a thick multiplication region with a low electric field is generally required to achieve low noise due to the significant difference between alpha and beta, the associated response time is long. To meet the high-speed requirements, however, a thinner multiplication layer with a high electric field must be used to obtain the same gain as a conventional APD with a thick multiplication layer. Based on the local model, thinner APDs with a high electric field and a low ionization coefficient ratio are predicted to have more measurable noise. However, in reality, the device's performance was found to be better than expected, with lower excess noise [16]. Thus, in the APDs with a thinner multiplication width, where the dead space is an important portion of the avalanche width, the McIntyre local model really fails in modelling the multiplication and noise in APDs. This is especially noticeable when calculating low level multiplication, typically less than 2. This is shown by the recent measurements on several III-V semiconductors [17, 18], [19], [20]. In this case, the increased significance of dead space will reduce the multiplication and noise achieved in practice below the expected values. There is no way for carriers to ionise in the dead space region. As a result, the probability density function (PDF) is more deterministic, which reduces the potential variance in multiplication that primary carriers can initiate and thus reduces the current noise. When a carrier must travel through multiple dead spaces to ionise multiple times, the probability of a carrier achieving a large number of ionisation events in any single transit is low, which reduces the probability of getting high multiplication of any carrier.

In order to model multiplication and the excess avalanche noise accurately and consider the effect of dead space in the excess noise model, several non-local models can be used. The most realistic way to simulate high-field carrier scattering is through Monte Carlo MC models; however, these models are computationally intensive and therefore not desirable for analysing experimental results. The recursive technique, which is another nonlocal model, was developed by Hayat *et al*. based on the probability distribution function (PDF) of the carrier's ionisation path length in the electric field [21]. It has been shown that this model can successfully simulate the multiplication and excess noise of APDs with multiplication widths as thin as 0.1 μ m [22]. Several researchers have utilised the recursive approach of Hayat *et al*. to correctly analyse the measured excess noise in thin structures [18] [23] [24]. Ong *et al*. developed the random path length model RPL, which calculates the probability of carrier ionization based on the random choice of ionization path lengths [15]. The displaced ionisation path length PDFs are used within a MC framework to estimate the multiplication and excess noise in APDs. The two models may be used to simulate experimental measurements and produce comparable predictions for gain and noise. The RPL model that was employed in this work is described in detail below.

2.2.3 Random path length model

Modelling is an effective tool for interpreting experimental results and optimising the device structure, which facilitates an understanding of impact ionisation, avalanche multiplication, and noise characteristics. Ong *et al*. presented the principles of the RPL model as described below[15]. The RPL technique is a simple Monte Carlo model that can be used to quantitatively investigate the ability of the hard-threshold dead space model to predict both multiplication characteristics and avalanche noise in small devices. It was found that there is excellent agreement, even for the smallest devices, between the mean multiplication obtained using this RPL and that resulting from an analytical-band structure Monte Carlo (AMC) model that considers soft-threshold effects. Since the AMC model takes into account the scattering events, it fits lower threshold energies than the RPL model, which uses a ballistic dead space. In the RPL model, the probability of an electron traveling a distance x in a uniform electric field ξ to be ionized, $P_e(x)$, is given by the formula:

$$P_e(x) = \begin{cases} 0, x \leq d_e^* \\ \alpha^* \exp[-\alpha^*(x - d_e^*)], \quad x > d_e^* \end{cases} \tag*{2.27}$$

where $\alpha^\star$ is the ionization probability per unit distance after the dead space and the hard-threshold dead space, $d_e^\star$ is given by:

$$d_e^* = \frac{E_{th}^*}{q\,\xi} \qquad 2.28$$

where q is the electron charge and $E_{th}^{\star}$ is the effective ionization threshold energy. $\alpha^{\star}$ can be determined from the local ionization coefficient α using the following equation:

$$\alpha = \frac{1}{d_e^{\star} + \frac{1}{\alpha^{\star}}} \qquad 2.29$$

The relationship between α and α* in terms of d_e^* can be expressed by Figure 2.6.

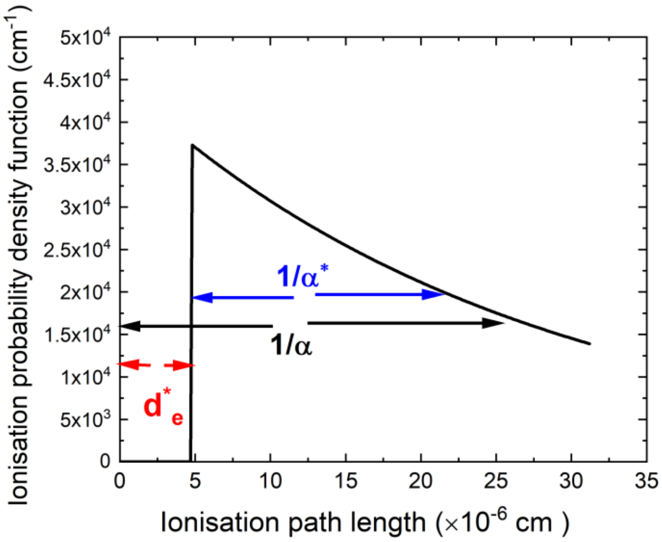

Figure 2.6: The ionisation probability density function as a function of the ionisation path length.

From equation 2.27, and when the carrier has not ionized, the probability $S_e(x)$, can be written as:

$$S_e(x) = \begin{cases} 1, x \le d_e^* \\ \alpha^* \exp[-\alpha^*(x - d_e^*)], \quad x > d_e^* \end{cases} \qquad 2.30$$

The random electron ionization path length of each individual carrier, l_e, can be calculated using the following formula:

$$l_e = d_e^\star - \frac{\ln(r)}{\alpha^\star} \qquad \textbf{2.31}$$

where r is random number between 0 and 1. The same argument can be applied for holes by substituting $P_h(x)$, $S_h(x)$,β , $\beta^\star$, $d_h^\star$,$and\ l_h$ for $P_e(x)$, $S_e(x)$,α , $\alpha^\star$, $d_e^\star$,$l_e and$ in equations 2.27-2.31

For each injected carrier and all secondary carriers generated by impact ionisation, the RPL model tracks their movement through the depletion region and provides a record of the position and number of impact ionisation events of all carriers until there are no carriers remaining in the avalanche region. Then, the value of the multiplication at the end of each trial M_n is calculated from the total number of ionisation events (number of events plus one). This process is carried out and averaged over $\sim 10^5$ trials to achieve an accurate and consistent simulation. The mean multiplication, M, and excess noise, F, can be determined from

$$M = \frac{1}{z}\sum_{n=1}^{n=z} M_n \qquad \textbf{2.32}$$

and

$$F = \frac{\frac{1}{z}\sum_{n=1}^{n=z} M_n^2}{\left(\frac{1}{z}\sum_{n=1}^{n=z} M_n\right)^2} \qquad \textbf{2.33}$$

where z is the total number of trials performed.

2.2.4 Separate absorption and multiplication avalanche photodiodes SAM APDs

Using SAM APDs with a separate wide bandgap avalanche layer and a low bandgap absorption layer is an effective way to achieve high multiplication with low band- to- band tunnelling in the multiplication layer and strong absorption in the absorption layer. As shown in Figure 2.7, the electric field in both the absorber layer and the multiplication layer are controlled by the width and the doping concentration of the charge sheet. The charge sheet doping density must be chosen carefully, not only to maintain an electric field in the multiplication layer high enough to achieve the required avalanche multiplication but also to have a sufficient electric field under a threshold electric field in the absorber layer to both direct photogenerated carriers towards the junction and suppress any tunnelling.

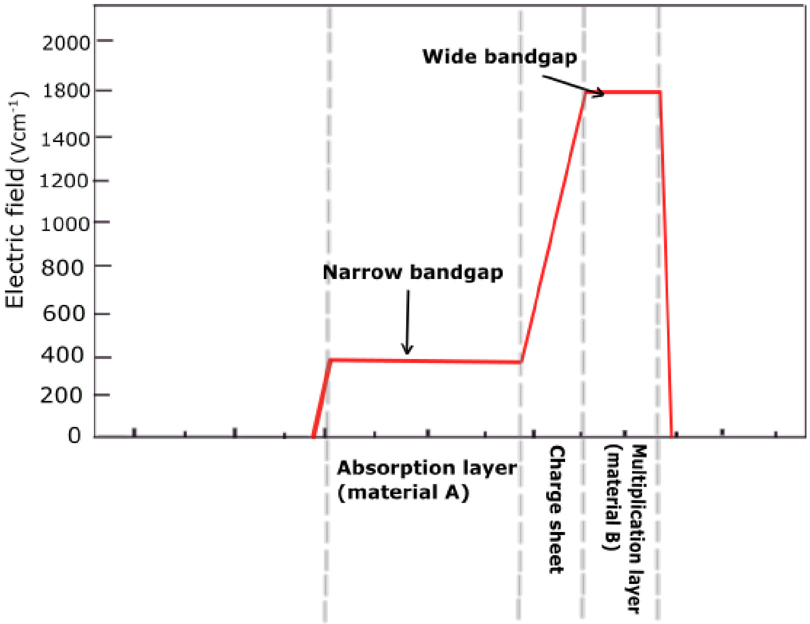

Figure 2.7: Schematic representation of the *SAM APD* structure, illustrating a low electric field in the absorption region with material *A* and a high electric field in the multiplication region with material *B*.

2.2.5 GaAs/ AlGaAs SAM APDs

One of the most important advantages of using III-V materials such as $Al_xGa_{1-x}As$ is the ability to customize the material characteristics, particularly the bandgap at the nanoscale, by varying the fraction x in the alloy. In addition, since $Al_xGa_{1-x}As$ with x =0.8 has a wide indirect band gap, it would be desirable to use it as a multiplication layer in a SAM structure to reduce tunnelling currents [25]. Consequently, a very thin multiplication layer can be considered without tunnelling. The large electron and hole mobilities of AlGaAs as well as using a thin multiplication layer can be combined, resulting in a short response time and a faster device. In addition, because of the large ionisation coefficient ratio in AlGaAs, the noise is small[16]. Also, the easy growth of AlGaAs results in a reduction of the defect-related dark current. In addition to the high speed and low noise performance of $Al_{0.8}Ga_{0.2}As$ APDs, they are also essentially lattice-matched with GaAs substrates, which are larger and less expensive than InP substrates [26]. Moreover, in terms of the absorption process, the direct band gap of GaAs compared to other materials with an indirect band gap increases the absorption coefficient, leading to a shorter absorption length and allowing the device to be thinner. Furthermore, GaAs with a high atomic number (Z_{Ga} = 31 and Z_{As} = 33) has higher absorption coefficient [27] and hence higher detection efficiency than Si (Z_{Si}= 14) sensor of the same thickness [26]. Consequently, a faster response time might be achieved by the combination of greater electron mobility and a smaller device with a shorter absorption length.

In the future, the GaAs material in the absorption layer of the SAM structure can be replaced with a dilute nitride, which has a narrower band gap. This allows for an extended cut-off wavelength.

2.3 Single Photon Avalanche photodiodes SPADs

2.3.1 Operation mode of APDs

This section will highlight several differences between APDs and SPADs. As shown in Figure 2.8, it is possible to use APDs as either linear APDs or Geiger mode SPADs depending on the voltage being applied. In linear mode, because the applied reverse bias voltage is less than the breakdown voltage (V_{bd}), the avalanche gain due to impact ionisation events is finite, typically not exceeding 1000 in practical devices. Consequently, this gain is unable to detect light at a single photon level. On the other hand, single photon sensitivity can be achieved with Geiger mode APDs (SPADs), which operate above (V_{bd}) and have a large gain (infinity). With such a high gain, a single primary carrier is capable of producing macroscopic self-sustaining avalanche currents, which can be detected by the readout circuit. However, this large avalanche current comes at a price, causing excessive heat that can destroy the diode. As a result, it is necessary to use a quenching circuit to lower the applied bias below V_{bd} and suppress the avalanche current. The most common quenching circuits are passive quenching circuits (PQC) [28] and Gated quenching circuit (as used in this work). Moreover, there are more advanced quenching circuits, such as active quenching circuit (AQC) and capacitive quenching circuit (CQC) [29] ,[30].

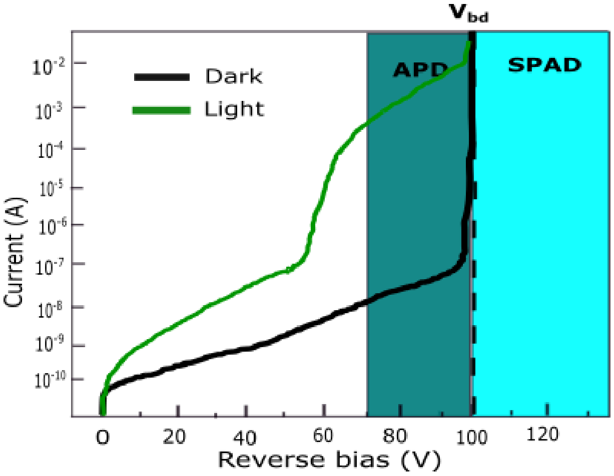

	APD	SPAD
Operation mode	Linear mode	Giger mode
Voltage	Lower than V_{bd}	higher than V_{bd}
Gain	Less than 1000	More than 10^6
Single photon sensitivity	No	Yes

Figure 2.8: Left: a typical I-V (in the dark or in the light) of an APD exhibiting the various operational modes. Right: a comparison between APD and SPAD adapted from [31].

2.3.2 Single Photon Detection Efficiency SPDE

Single photon detection efficiency is described as the fraction of the number of avalanche pulses triggered by photo-generated carriers and the number of incident photons (at the single photon level). As this work is based on the SAM APDs structure, SPDE can be expressed as the product of absorption efficiency, collection efficiency, and breakdown probability:

$$SPDE = P_{abs} \times (1 - P_{loss}) \times P_b \qquad \textbf{2.34}$$

where P_{loss} is the probability of losing the photo-generated carriers before reaching the multiplication region. Absorption efficiency P_{abs} can be defined as the probability that a photon is absorbed in the absorption layer. P_{abs} has an exponential expression as:

$$P_{abs} = 1 - \exp(-\alpha_{abs} \times w_{abs}) \qquad \textbf{2.35}$$

where w_{abs} is the absorption layer width. It is clear from the exponential expression that the remaining photon flux decreases with w_{abs} and $\alpha_{abs.}$ As a result, in order to achieve high P_{abs} and hence high SPDE, a thick absorption layer is required.

Collection efficiency refers to the ability of photo-generated carriers to reach the multiplication layer without any trapping or recombination. One of the disadvantages of the SAM structure is that the carriers can be trapped due to the heterojunction between the absorption and multiplication layers, thereby reducing the SPDE. To overcome this issue and minimize band discontinuity, a grading layer with an intermediate bandgap value can be used between the absorption and multiplication layers.

Breakdown probability describes the probability that a photo-generated carrier can trigger a sufficiently significant avalanche in the multiplication layer. P_b can be written as a function of the over-bias voltage ratio, which is given by $\frac{(V_b - V_{bd})}{V_{bd}}$. The P_b value usually rises from zero at V_{bd} and saturates at one when $V_b >> V_{bd}$. An example of P_b as a function of over-bias ratio is shown in Figure 2.9 for an $Al_{0.8}Ga_{0.2}As$ APD with a 100 nm thick multiplication layer.

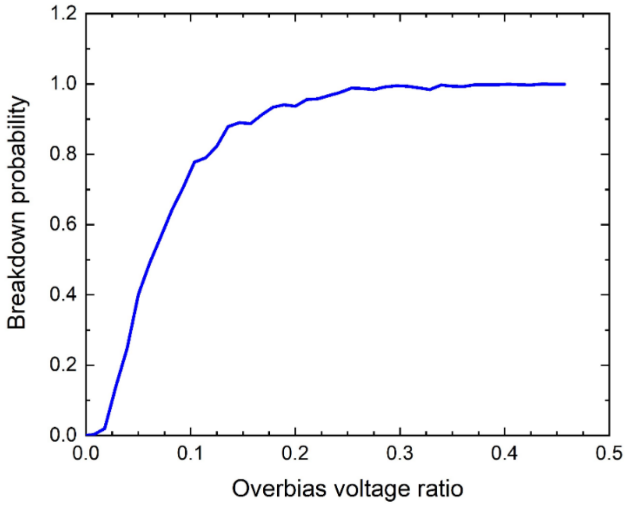

Figure 2.9: RPL simulated breakdown probability of an AlGaAs SPAD with 100 nm multiplication layer as a function of over-bias voltage ratio.

2.3.3 Dark Count Rate DCR

Dark counts represent the response of a photodetector under no light. DCR can be defined as the avalanche event's rate caused by carriers generated in the absence of illumination. In estimating the DCR, both primary and secondary pulses are considered [32]. There are two sources of the primary dark pulses, including thermal generation current (Shockley Read Hall SRH) and tunnelling current. Secondary dark pulses are formed because of afterpulsing, which will be explained in the next section [33], [34]. At constant over-bias voltage, the DCR increases exponentially with temperature. Increasing temperature can produce more thermal generation carriers especially in small band gap absorber layers, resulting in a higher DCR. To overcome such high DCR, the device should be cooled as much as possible. On the other hand, at a given temperature, DCR rises with over-bias voltage. When the over-bias voltage is increased, the electric field in the multiplication layer is high such that band-to-band or trap assisted BTB tunnelling can become significant, resulting in higher DCR. Furthermore, increasing the electric field in the small band gap absorber layer can also increase carrier generation, through tunnelling or SRH, which in turn increases DCR. In addition, as with SPDE, DCR also rises with over-bias voltage because of the increased breakdown probability. Therefore, there is always a trade-off between achieving high SPDE and low DCR. In order to optimise SPADs, it is important to improve SPDE and minimise DCR.

2.3.4 Afterpulsing

Afterpulsing is the source of secondary dark pulses [33] [34]. As avalanche current flows through the multiplication region, some carriers become trapped due to the defects. At a later time, these carriers are released, and can trigger an additional avalanche event, this process is known as afterpulsing. It is clear that the carrier generation (release) rate is proportional to the defect density. After the trapping of carriers, the time required for their release is described by an exponential time constant that varies based on the type of defect in the material and operating temperature. There are several ways to suppress afterpulsing. If a fast-quenching technique such as CQC and/or quenching with an extremely narrow gate is used, it is possible to reduce the carrier’s number that flow across the diode during the avalanche, resulting in a reduction in afterpulsing. Using low over-bias voltages can help reduce the total carriers and thus the after pulsing, but unfortunately, it will also reduce SPDE. Furthermore, introducing a hold-off time after an avalanche can also be used to reduce the afterpulsing effect. A long off time between avalanches allows the trapped carriers due to the current avalanche to release before the next avalanche without causing new avalanche pulses. Another way to suppress the afterpulsing effect is by using a high operating temperature. With increasing temperatures, less time is required for releasing carriers. Consequently, the trapped carrier can be released before the voltage is increased again, for the next avalanche. Increasing the temperature can reduce the afterpulsing, but at the price of a high DCR. So, it is important to work on achieving optimal temperature to reduce both afterpulsing and DCR. In the SAM structure, if the electric field in the absorber layer is sufficiently high, any type of released trapped carrier can trigger an avalanche, resulting in afterpulsing. On the other hand, if the electric field in the absorber layer is low, a released trapped carrier of the minority carrier type can move to the high electric field, causing an avalanche and hence afterpulsing. However, if the released trapped carrier is not of the minority carrier type, it will move away from the electric field and have no effect on afterpulsing.

2.3.5 Timing jitter

Timing jitter refers to the fluctuation in the time between a photon's arrival and the avalanche current caused by the incident photon reaching the detection threshold. This fluctuation is mostly caused by the variation in the build-up time of the avalanche current, due to the random nature of the avalanche process. Increasing over-bias voltage is an effective way to minimise the fluctuation of the built-up time. This can be attributed to the narrower spread of the ionisation path length probability density function (pdf), which has a significant impact on the degree of fluctuation in the avalanche process [35] [36]. As carriers can be absorbed in various positions in the absorption layer, they take various times to reach the multiplication layer. Differences in the arrival time of a carrier at the multiplication layer can also contribute to the timing jitter. If the carriers are generated in an undepleted portion of the absorption layer, there is a need for them to diffuse to reach the multiplication layer. So, there may be a significant amount of timing jitter due to the uncertainty of diffusion time.

2.4 Dilute nitride

Long-haul optical fibre communications typically take place within one of two windows defined by minima in dispersion and absorption in silica optical fibres, at 1310 and 1550 nm respectively. In order to design a photodiode for the latter wavelength, an absorbing semiconductor with a 0.8 eV band gap is required. $In_{0.53}Ga_{0.47}As$, hereafter referred to as InGaAs, offers several advantages that make it a suitable material for designing a lot of commercial detectors. The small band gap of 0.74 eV allows for effective detection at 1550 nm. Moreover, InGaAs growth is a fairly simple process, allowing for the creation of devices with a low dark current and a large depletion width (low unintentional doping concentration). Consequently, it is widely used for detecting near-infrared light up to 1700 nm in wavelength. As this alloy composition of InGaAs is lattice-matched to InP, it is possible for InGaAs bulk layers to be epitaxially grown on InP substrates without strain-related defects. On the other hand, compared to other materials such as GaAs, InP substrates are smaller and more expensive. Hence, moving to a GaAs-based photodetector might result in cheaper and more widely available communication receivers. Interestingly, the availability of an absorber lattice matched to GaAs might potentially benefit from the AlGaAs material system as a multiplication layer SAM APD. Compared to currently incumbent AlInAs layers, AlGaAs multiplication layers can operate with significantly thinner widths, resulting in extremely low noise and high bandwidth operation. In order to achieve the previous advantages, an absorber layer which is lattice-matched to GaAs and epitaxially grown without defects on GaAs substrates is required.

A detector with equivalent absorption properties to InGaAs can be produced with sufficient concentrations of nitrogen and indium. As the band gap strongly depends on the N concentration, N-containing alloys may be used in a wide range of extended- wavelength optoelectronic devices. Adding even a small amount of nitrogen to the crystalline structure of GaAs or InGaAs can significantly change the structural and optical characteristics of those materials, making the epitaxial technology of dilute nitrides a complex process.

InGaAsN is a novel semiconductor alloy system with the remarkable feature that adding only 2% nitrogen lowers the bandgap by more than 30% [37]. Incorporation of In and N into GaAs results in a strong redshift of the emission wavelength. It has been considered a promising material for laser devices that work at 1300 nm or 1500 nm. In addition, the opposite effects of In and N on the lattice constant make it possible to match the lattice of InGaAsN on GaAs. The addition of an N atom causes a large, local change in the crystal lattice potential. The anticrossing interaction between a narrow band of highly localised N states and the extended states of the semiconductor matrix results in a characteristic splitting of the conduction band into two different bands, E_+ and E_-. In this case, the band anti-crossing (BAC) model can be used to describe the band gap [38]. Dilute nitride has a new band gap defined by the energy level of E_-. These two levels of energy, caused by the impurity, can be written as:

$$E_{\pm} = \frac{1}{2}((E_N + E_M) \pm \sqrt{(E_N - E_M)^2 + 4V^2 y}\,, \qquad \textbf{2.36}$$

where E_N defines the nitrogen impurity level's energy with respect to the valence band, E_M represents the band gap of the nitrogen free alloy, V is the probability of the interaction between the bands and y is the nitrogen alloy composition. V and E_N are affected by the indium fraction of the alloy, as described by Vurgaftman *et al.* [39] for $Ga_{1-x}In_xNAs$

$$E_N(x) = 1.65(1-x) + 1.44x - 0.38x(1-x) \qquad \textbf{2.37}$$
$$V(x) = 2.7(1-x) + 2.0x - 3.5x(1-x)$$

The Antimony's effect on the band gap is described by Aho *et al.* [40]. Since it has been confirmed that Sb has no significant effect on the BAC parameters, it has been incorporated into E_M [41]. Figure 2.11 shows the range of band gaps that can be achieved by varying the concentrations of In and N. A nitrogen fraction of 6.4% and 20% In are needed to maintain lattice matched to GaAs and enable operation at 1550 nm. The thermal annealing of the dilute nitride alloy can improve its quality due to the reduction of the defect concentration [40].

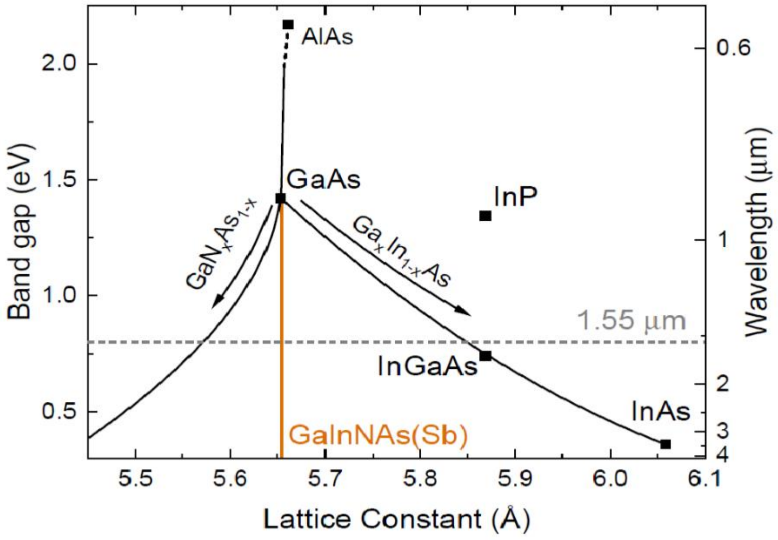

Figure 2.10: The incorporation of both In and N into GaAs decreases the band gap and can compensate for the strain caused by the complementary atom. The dashed line represents 0.8 eV, by using materials have a band gap lower than this energy, a 1550 nm wavelength can be detected. Adopted from [42].

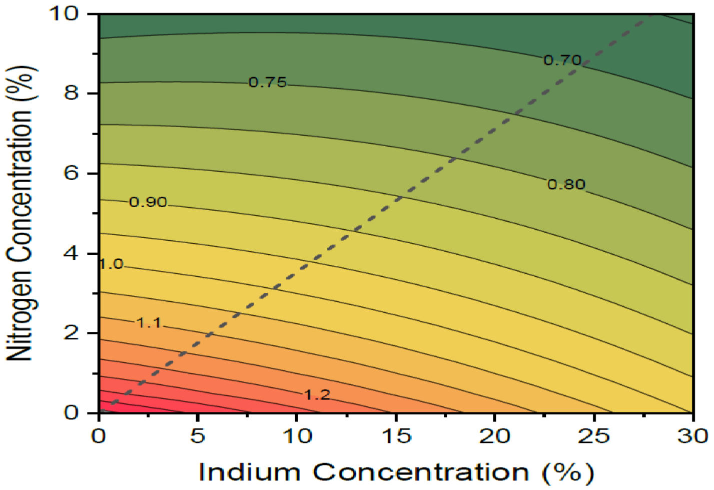

Figure 2.11: The band gaps values with variety fraction of In and N in GaInNAs. The dashed line represents the ratio necessary to maintain lattice matched to GaAs. Adopted from [42].

2.5 References

[1] M. D. McCluskey and E. E. Haller, *Dopants and defects in semiconductors*. CRC press, 2018.

[2] L. Hall, J. Bardeen, and F. Blatt, "Infrared absorption spectrum of germanium," *Physical Review,* vol. 95, no. 2, p. 559, 1954.

[3] X. Yi, "Impact ionization in AlAs0. 56Sb0. 44 photodiodes," University of Sheffield, 2020.

[4] M. Yernaux, C. Battochio, P. Verlinden, and F. Van De Wiele, "A one-dimensional model for the quantum efficiency of front-surface-field solar cells," *Solar cells,* vol. 13, no. 1, pp. 83-97, 1984.

[5] D. K. Schroder, "Carrier lifetimes in silicon," *IEEE transactions on Electron Devices,* vol. 44, no. 1, pp. 160-170, 1997.

[6] S. S. Li and W. R. Thurber, "The dopant density and temperature dependence of electron mobility and resistivity in n-type silicon," *Solid-State Electronics,* vol. 20, no. 7, pp. 609-616, 1977.

[7] H. Zarem *et al.*, "Effect of Al mole fraction on carrier diffusion lengths and lifetimes in Al x Ga1− x As," *Applied physics letters,* vol. 55, no. 25, pp. 2622-2624, 1989.

[8] P. Chakrabarti, A. Krier, and A. Morgan, "Analysis and Simulation of a Mid-Infrared P," *IEEE Transactions on Electron Devices,* vol. 50, no. 10, p. 2049, 2003.

[9] P. Klipstein *et al.*, "MWIR InAsSb XBn detectors for high operating temperatures," in *Infrared Technology and Applications XXXVI*, 2010, vol. 7660: SPIE, pp. 939-947.

[10] S. Forrest, M. DiDomenico Jr, R. Smith, and H. Stocker, "Evidence for tunneling in reverse-biased III-V photodetector diodes," *Applied Physics Letters,* vol. 36, no. 7, pp. 580-582, 1980.

[11] H. Kim *et al.*, "Performance improvement of InAs/GaSb strained layer superlattice detectors by reducing surface leakage currents with SU-8 passivation," *Applied Physics Letters,* vol. 96, no. 3, p. 033502, 2010.

[12] C. Anderson and C. Crowell, "Threshold energies for electron-hole pair production by impact ionization in semiconductors," *Physical Review B,* vol. 5, no. 6, p. 2267, 1972.

[13] P. Wolff, "Theory of electron multiplication in silicon and germanium," *Physical Review,* vol. 95, no. 6, p. 1415, 1954.

[14] R. McIntyre, "Multiplication noise in uniform avalanche diodes," *IEEE Transactions on Electron Devices,* no. 1, pp. 164-168, 1966.

[15] D. Ong, K. Li, G. Rees, J. David, and P. Robson, "A simple model to determine multiplication and noise in avalanche photodiodes," *Journal of applied physics,* vol. 83, no. 6, pp. 3426-3428, 1998.

[16] B. Ng, J. David, R. Tozer, M. Hopkinson, G. Hill, and G. Rees, "Excess noise characteristics of Al/sub 0.8/Ga/sub 0.2/As avalanche photodiodes," *IEEE Photonics Technology Letters,* vol. 14, no. 4, pp. 522-524, 2002.

[17] C. Hu, K. Anselm, B. Streetman, and J. Campbell, "Noise characteristics of thin multiplication region GaAs avalanche photodiodes," *Applied physics letters,* vol. 69, no. 24, pp. 3734-3736, 1996.

[18] K. Li *et al.*, "Avalanche multiplication noise characteristics in thin GaAs p/sup+/-in/sup+/diodes," *IEEE Transactions on Electron Devices,* vol. 45, no. 10, pp. 2102-2107, 1998.

[19] K. Li *et al.*, "Low avalanche noise characteristics in thin InP p/sup+/-in/sup+/diodes with electron initiated multiplication," *IEEE Photonics Technology Letters,* vol. 11, no. 3, pp. 364-366, 1999.

[20] K. Li *et al.*, "Low excess noise characteristics in thin avalanche region GaAs diodes," *Electronics Letters,* vol. 34, no. 1, pp. 125-126, 1998.

[21] M. M. Hayat, B. E. Saleh, and M. C. Teich, "Effect of dead space on gain and noise of double-carrier-multiplication avalanche photodiodes," *IEEE transactions on electron devices,* vol. 39, no. 3, pp. 546-552, 1992.

[22] M. A. Saleh *et al.*, "Breakdown voltage in thin III–V avalanche photodiodes," *Applied Physics Letters,* vol. 79, no. 24, pp. 4037-4039, 2001.

[23] C. Tan *et al.*, "Avalanche noise measurement in thin Si p+-in+ diodes," *Applied Physics Letters,* vol. 76, no. 26, pp. 3926-3928, 2000.

[24] K. F. Li *et al.*, "Avalanche noise characteristics of thin GaAs structures with distributed carrier generation [APDs]," *IEEE transactions on electron devices,* vol. 47, no. 5, pp. 910-914, 2000.

[25] B. Ng *et al.*, "Avalanche multiplication characteristics of Al/sub 0.8/Ga/sub 0.2/As diodes," *IEEE transactions on electron devices,* vol. 48, no. 10, pp. 2198-2204, 2001.

[26] G. Lioliou, X. Meng, J. Ng, and A. Barnett, "Characterization of gallium arsenide X-ray mesa pin photodiodes at room temperature," *Nuclear Instruments and Methods in Physics Research Section A: Accelerators, Spectrometers, Detectors and Associated Equipment,* vol. 813, pp. 1-9, 2016.

[27] J. H. Hubbell, "Photon mass attenuation and energy-absorption coefficients," *The International Journal of Applied Radiation and Isotopes,* vol. 33, no. 11, pp. 1269-1290, 1982.

[28] B. Korzh, N. Walenta, T. Lunghi, N. Gisin, and H. Zbinden, "Free-running InGaAs single photon detector with 1 dark count per second at 10% efficiency," *Applied Physics Letters,* vol. 104, no. 8, 2014.

[29] S. Cova, M. Ghioni, A. Lacaita, C. Samori, and F. Zappa, "Avalanche photodiodes and quenching circuits for single-photon detection," *Applied optics,* vol. 35, no. 12, pp. 1956-1976, 1996.

[30] S. Dimler, J. Ng, R. Tozer, G. Rees, and J. David, "Capacitive quenching measurement circuit for geiger-mode avalanche photodiodes," *IEEE Journal of Selected Topics in Quantum Electronics,* vol. 13, no. 4, pp. 919-925, 2007.

[31] X. Meng, "InGaAs/InAlAs single photon avalanche diodes at 1550 nm and X-ray detectors using III-V semiconductor materials," University of Sheffield, 2015.

[32] R. H. Haitz, "Mechanisms contributing to the noise pulse rate of avalanche diodes," *Journal of Applied Physics,* vol. 36, no. 10, pp. 3123-3131, 1965.

[33] S. Cova, A. Lacaita, and G. Ripamonti, "Trapping phenomena in avalanche photodiodes on nanosecond scale," *IEEE Electron device letters,* vol. 12, no. 12, pp. 685-687, 1991.

[34] A. Giudice, M. Ghioni, S. Cova, and F. Zappa, "A process and deep level evaluation tool: afterpulsing in avalanche junctions," in *ESSDERC'03. 33rd Conference on European Solid-State Device Research, 2003.*, 2003: IEEE, pp. 347-350.

[35] C. Tan, J. Ng, G. Rees, and J. David, "Statistics of avalanche current buildup time in single-photon avalanche diodes," *IEEE Journal of Selected Topics in Quantum Electronics,* vol. 13, no. 4, pp. 906-910, 2007.

[36] C. Niclass, A. Rochas, P.-A. Besse, and E. Charbon, "Design and characterization of a CMOS 3-D image sensor based on single photon avalanche diodes," *IEEE Journal of Solid-State Circuits,* vol. 40, no. 9, pp. 1847-1854, 2005.

[37] E. D. Jones *et al.*, "Optical properties of InGaAsN: a new 1-eV bandgap material system," in *Light-Emitting Diodes: Research, Manufacturing, and Applications III*, 1999, vol. 3621: SPIE, pp. 52-63.

[38] J. Ager III *et al.*, "Band Anticrossing in GaInNAs Alloys," *Physical Review Letters,* vol. 82, no. LBNL-42287, 1998.

[39] I. Vurgaftman and J. n. Meyer, "Band parameters for nitrogen-containing semiconductors," *Journal of Applied Physics,* vol. 94, no. 6, pp. 3675-3696, 2003.

[40] A. Aho *et al.*, "Determination of composition and energy gaps of GaInNAsSb layers grown by MBE," *Journal of Crystal Growth,* vol. 438, pp. 49-54, 2016.

[41] Y.-T. Lin, T.-C. Ma, T.-Y. Chen, and H.-H. Lin, "Energy gap reduction in dilute nitride GaAsSbN," *Applied Physics Letters,* vol. 93, no. 17, p. 171914, 2008.

[42] X. Collins, *Dilute Nitride GaInNAsSb for Next Generation Optical Communications*. Lancaster University (United Kingdom), 2021.

Chapter 3

Literature review

3.1 Impact ionization coefficients of $Al_xGa_{x-1}As$

To date a number of researchers have obtained data to determine both local and nonlocal electron and hole impact ionization coefficients for $Al_xGa_{1-x}As$ diodes, with different ranges of Al fraction and intrinsic width. The earlier measurements of Shabde *et al*. [1] assumed equal electron and hole ionization rates.

3.1.1 Local impact ionisation coefficients

Robbins *et al.* [2] reported experimentally the local electron and hole impact ionization coefficients for $Al_xGa_{1-x}As$ compositions $x \leq 0.4$ using the technique described by Stillman and Wolfe, [3] as shown in Table 3.1. The unit of B parameter was not clear in the papers, and it is checked and confirmed to be V cm^{-1}. It was found that as the Al fraction increases, both α and β, the electron ionization coefficient and hole ionization coefficient, respectively, decrease as shown in Figure 3.1. For comparison, the figure also illustrates the coefficients of GaAs with 0 Al composition [4]. As the figure shows, the α/β ratio remains relatively constant across the range of compositions and electric fields studied.

Material	**Electric field range ξ (kV cm^{-1})**	**Coefficient type**	**A (x10^{5} cm^{-1})**	**B (x10^{5} V cm^{-1})**	**C**
Al$_x$Ga$_{1-x}$As for x=0.1 [2]	300-400	α	1.81	6.31	2
		β	3.05	7.22	1.5
Al$_x$Ga$_{1-x}$As for x=0.2 [2]	300-400	α	10.9	13.7	1.3
		β	6.45	11.1	1.5
Al$_x$Ga$_{1-x}$As for x=0.3 [2]	300-400	α	2.21	7.64	2
		β	2.79	8.47	1.9
Al$_x$Ga$_{1-x}$As for x=0.4 [2]	300-400	α	174	33.9	1
		β	30.6	20.7	1.2
Al$_x$Ga$_{1-x}$As for x=0.15 [5]	327-461	α	1.97	7.38	1.79
		β	3.91	9.63	1.58
Al$_x$Ga$_{1-x}$As for x=0.30 [5]	310-460	α	5.16	10.7	1.49
		β	3.51	21	1.12
GaAs [7]	150-900	α	2.28	6.770	1.511
		β	2.24	7.148	1.554
Al$_{0.15}$Ga$_{0.85}$As [7]		α	2.17	7.740	1.533
		β	2.51	8.600	1.516
Al$_{0.30}$Ga$_{0.70}$As [7]		α	2.69	9.540	1.476
		β	3.20	10.62	1.430
Al$_{0.60}$Ga$_{0.40}$As [7]	330-1100	α	2.95	11.63	1.444
		β	3.11	12.15	1.433
Al$_{0.8}$Ga$_{0.2}$As [8]	328-519	α	1.40	8.05	2.03
		β	1.14	8.76	2.18

Table 3.1: The parameterized local electron and hole impact ionization coefficients for Al$_x$Ga$_{1-x}$As written as $\alpha(\beta) = A\ \exp\left[-\left(\frac{B}{\xi}\right)^{C}\right]$ in cm^{-1} where ξ is the electric field.

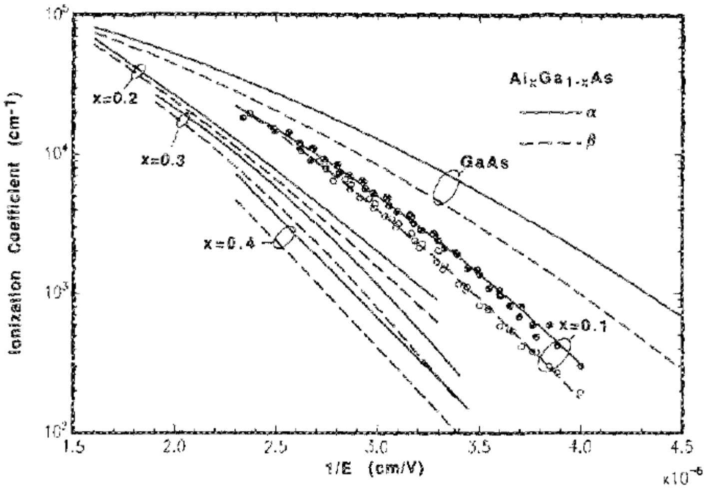

Figure 3.1: The fitted electron and hole impact ionization coefficients for $Al_xGa_{1-x}As$ over x = 0.1–0.4 [2]. For GaAs, the data from Bulman *et al.* are presented [4].

Another range of Al fractions of AlGaAs has been investigated by Plimmer *et al.* [5]. In two sets of $Al_xGa_{1-x}As$ (0.15, 0.30) *p-i-n* diodes with an intrinsic region width change from 1 down to 0.025 µm, the electron and hole photomultiplication characteristics, M_e and M_h, respectively, have been investigated using the technique described by Stillman and Wolff [3]. These multiplication measurements were used to determine the effective electron and hole ionization coefficients, α and β, respectively, based on the conventional "local" analysis illustrated by Grant [6] as shown in Table 3.1. In the thicker devices, there is a good agreement with data published previously in the literature. On the other hand, in thin structures, with $w \leq 0.1$ µm , the measured multiplication was reduced due to the effect of the dead space below their bulk values at lower bias voltage values. When the electric field is increased, α and β rapidly approach the values predicted for a local model, indicating that the dead space is being compensated for by velocity overshot effects. It was also confirmed that the breakdown voltage can be increased by increasing the alloy composition across all thicknesses.

For an extended range of $Al_xGa_{1-x}As$ (x = 0–0.60)[7] structures, the local ionization coefficients are extracted from photomultiplication data using the local analysis, as described by Stillman and Wolfe (1977) where the multiplication region thickness varies from 1 µm down to 0.05 µm. It was found that although dead space becomes a significant fraction of the device thickness when the thickness reduces, these coefficients implicitly consider, to some degree, the dead space effect. As a result, they can be utilised within the simple local ionization model to successfully simulate the avalanche processes in depletion region thickness down to 0.1 µm. This is because, once dead space becomes significant, only a small number of devices with similar geometries access the same high field. Hence, for devices that access this field, an 'effective' or averaged coefficient can be defined as shown in Table 3.1. These coefficients can give a reasonable estimate but do not properly address non-local behaviour. Consequently, for extremely thin devices with an intrinsic region as thin as 0.05 µm, the local model failed, as shown in Figure 3.2.

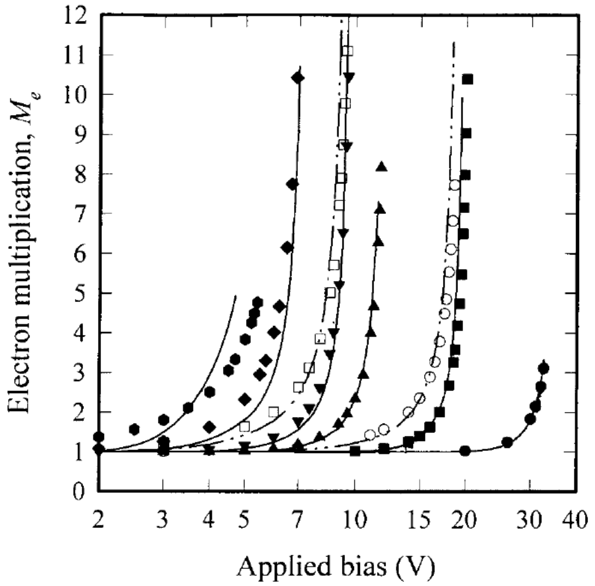

Figure 3.2: Pure electron multiplication M_e versus applied voltage in GaAs p^+-i-n^+s(——) with nominally intrinsic width equal to 1 µm (•), 0.5 µm (▪), 0.3 µm (▲), 0.2 µm (▼), 0.1 µm (◆) and 0.05 µm (hexagons) and M_e from p^+-n junctions (— · · —) with the n-side doped at 5 × 10^{16} cm^{-3} (○) and 2.2 × 10^{17} cm^{-3} (□). Measured (curves) and local model (symbols) [7].

Ng *et al.* [8] reported the local impact ionization coefficients in bulk AlGaAs of higher aluminium fraction alloys (x= 0.8) over the 328-519 kV/cm electric field range using the technique described by Stillman and Wolfe. Based on the experimental results, the parametrized expressions of the ionization coefficients were identified using least squares fit, and they are also illustrated in Table 3.1.

3.1.2 Non-local impact ionisation coefficients

The dead-space effect [9] was initially taken into consideration by Okuto and Crowell. They used a nonlocal coefficient instead of the conventional ionization coefficient. As well as the local coefficients, the nonlocal coefficient and threshold energies for the range of x = 0-0.6 have been determined by Plimmer *et al*. [10] based on the measured results, which cover the range of electric field from 250 kV/cm to 1200 kV/cm in each composition using a Monte-Carlo model as shown in Table 3.2 and plotted in Figure 3.3. The figure shows how the coefficients decrease with increasing x.

Material	**Electric field range ξ (kV cm^{-1})**	**Coefficient type**	**A (x10^{5} cm^{-1})**	**B (x10^{5} V cm^{-1})**	**C**	**E_{the} (eV)**	**E_{thh} (eV)**
GaAs [10]	<600	α	4.22	7.09	1.535	3.1	3.3
		β	5.89	8.89	1.402		
	>600	α	27.7	41.0	0.60		
		β	22.7	31.2	0.687		
$Al_xGa_{1-x}As$ for x=0.15 [10]	<600	α	33.6	23.5	1	3.2	3.4
		β	36.4	25.2	1		
	>600	α	12.6	18.0	1		
		β	14.3	20.0	1		
$Al_xGa_{1-x}As$ for x=0.30 [10]	<600	α	30.7	23.6	1	3.4	3.6
		β	34.3	25.3	1		
	>600	α	12.7	18.4	1		
		β	13.6	19.9	1		
$Al_xGa_{1-x}As$ for x=0.60 [10]	<600	α	34.7	28.2	1	3.4	3.6
		β	30.8	28.6	1		
	>600	α	13.9	22.7	1		
		β	14.8	23.8	1		
$Al_{0.8}Ga_{0.2}As$ [12]	328-1110	α	3.18	10.4	1.67	2.23	2.23
		β	3.55	11.2	1.85		
	1110-1540	α	38.4	102	0.55		
		β	38.4	102	0.55		

Table 3.2: The parameterized non-local electron and hole impact ionization coefficients for $Al_xGa_{1x}As$ expressed as $\alpha(\beta) = A\ \exp\left[-\left(\frac{B}{\xi}\right)^{C}\right]$ in cm^{-1} where ξ is the electric field. The threshold energy is also written for electron and hole in terms of E_{the} and E_{thh} respectively.

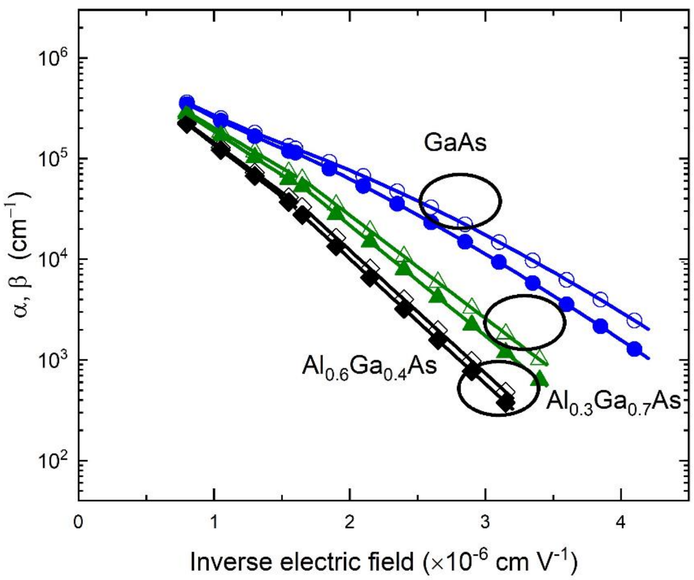

Figure 3.3: MC electron (open symbols) and hole (closed symbols) ionisation coefficients in GaAs (○, ●), $Al_{0.30}Ga_{0.7}0As$ (△, ▲), and $Al_{0.60}Ga_{0.40}As$ (◇, ◆). Solid lines indicate the parameterized coefficients written in Table 3.2 [10].

After determining the model parameters through experimental fitting, M_e and M_h were calculated for a range of ideal *p-i-n* diodes so that the effect of the alloy composition could be compared more accurately. The results for *p-i-n* diodes with a range of intrinsic widths of 1 µm, 0.1 µm, and 0.05 µm for Al fractions of 0, 0.30, and 0.60 are presented in Figure 3.4. It is obvious from the figure that both multiplication curves (M_e and M_h) shift to a higher electric field at each width as the Al composition increases. This is because both α and β decrease with increasing Al composition [11], as shown in Figure 3.5. As a result, there is a need to increase the electric field to compensate and achieve the breakdown. Figure 3.5 also shows how the α and β converge as the Al fraction approaches 0.6. As a result, in the composition range x = 0 to 0.6, at any given intrinsic width, the M_e/M_h ratio is closer to unity when the Al composition increases, as shown in Figure 3.4.

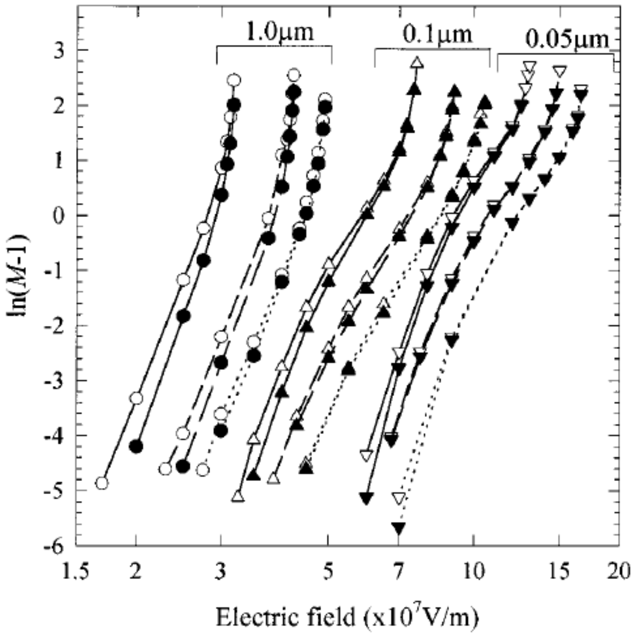

Figure 3.4: M_e (open symbols) and M_h (closed symbols) curves based on the MC model represented as ln(M-1) for ideal p^+-i-n^+ diodes of GaAs (—), $Al_{0.3}Ga_{0.70}As$ (——), and $Al_{0.60}Ga_{0.40}As$ (- - -) with intrinsic width equal to 1 μm (○, ●), 0.1 μm (△, ▲), and 0.05 μm (▽, ▼) [10].

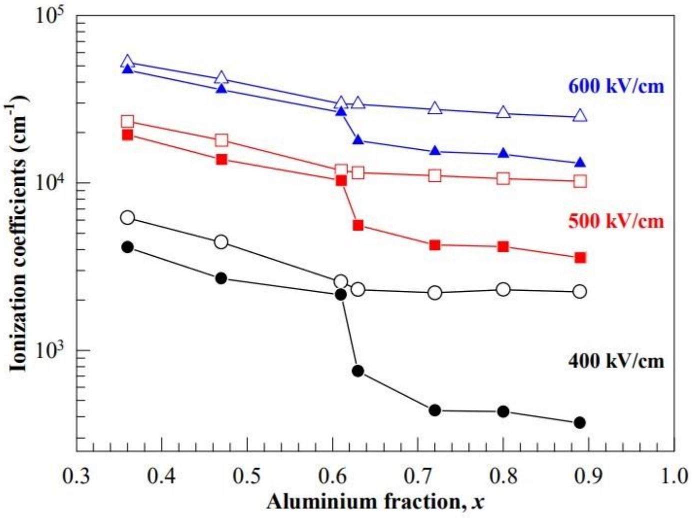

Figure 3.5: α and β as a function of a range of aluminium fraction x [11].

When the Al fraction is x<0.6 the nonlocal nature of ionization has been well investigated and the multiplication characteristics of thin devices can be simulated.

However, in this Al composition range the band gap is not wide enough to limit the tunnelling. Also, since the electron and hole ionization coefficients converge at the Al fraction of 0.6, this material is not a suitable multiplication medium for low noise avalanche photodiodes. On the other hand, at an Al fraction of 0.8, tunnelling is suppressed due to the wide indirect band gap, allowing the formation of extremely thin diodes, which take advantage of non-local effects such as reduced avalanche noise, increased speed and gain bandwidth product. Also, beta reduces significantly at this Al fraction, which increases the coefficient ratio to be greater than 10. Therefore, the excess noise can be significantly minimised in the case of electron injection. Consequently, there is a need to extract the non-local coefficient of $Al_{0.8}Ga_{0.2}As$ to exploit the advantages of its desirable properties and to investigate the multiplication in thin devices with low tunnelling and low excess noise.

In 2001, Ng *et al.* [12] extracted ionization coefficients for $\mathrm{Al_{0.8}Ga_{0.2}As}$ extending the electric field range of their previous results [8] to $328\ \mathrm{kV\ cm^{-1}} \leq \zeta \leq 1540\ \mathrm{kV\ cm^{-1}}$. These coefficients hereafter referred to Ng's coefficients. Ng *et al.* also extended their work by applying the simple correction of Okuto *et al* [9], which leads to a threshold energy. However, with only the first dead space considered, the energy fitted is not equivalent to that used by RPL or recurrence. Ng's coefficients [12] and electron and hole threshold energies are written in Table 3.2. As shown in Figure 3.6, by applying Ng's coefficients to the local model with the simple correction, the multiplication and breakdown can be accurately simulated.

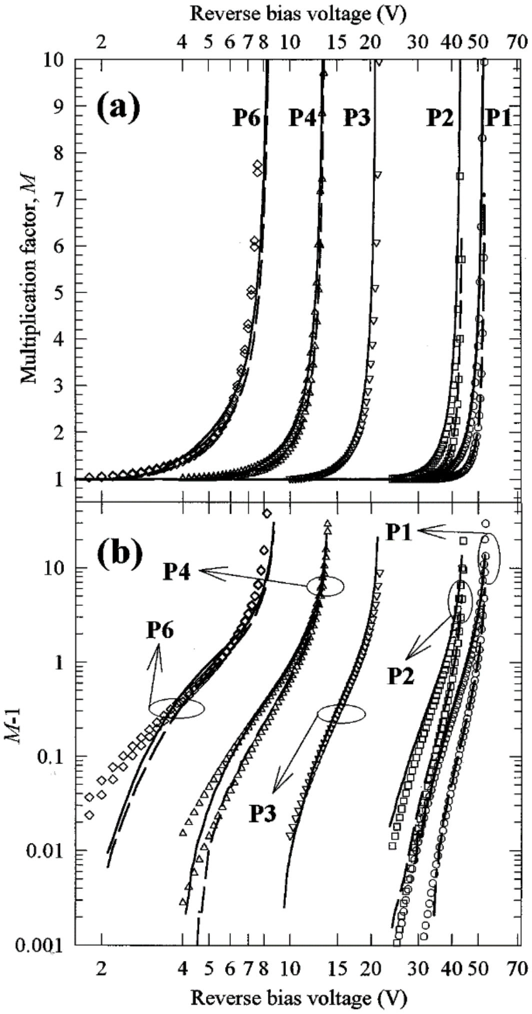

Figure 3.6: Solid lines indicate M_e and dashed lines indicate M_h from the *p-i-n* diodes investigated plotted on (Top) a linear scale and (bottom) as (M-1) on a logarithmic scale to show the low multiplication values. The symbols illustrate the calculated results using the local model and their simple dead space correction[12].

However, the effects of dead space on APDs can be investigated using a developed model, such as the hard threshold dead space model not only to simulate multiplication but many more important device characteristics, including excess noise, impulse response, and breakdown probability. This model can simulate the device's behaviour, with those modelling a hard-dead space-displaced PDF proving to balance speed with accuracy. The two most widely used hard-dead space models are RPL [13], [14] and recurrence [15], [16]. In Chapter 5, I report the nonlocal coefficients and threshold energies of $Al_{0.8}Ga_{0.2}As$ using a hard threshold dead space model.

3.2 AlGaAs/GaAs SAM Avalanche Photodiodes

The AlGaAs/GaAs SAM APD in terms of its structures and applications is discussed. Although complicated, a staircase structure is one of the most popular APD structures employing AlGaAs, and most of the reports considered here relate to it. On the other hand, some other structures without a staircase, which are close to the work in this thesis, have been mentioned too. Moreover, since x-ray detection is the most significant application currently targeted by researchers studying these devices, some of the applications mentioned in individual papers will be discussed [17] , [18], [19]. However, this is not the application targeted by the current work because dilute nitride allows absorption at important IR wavelengths, which GaAs does not.

3.2.1 SAM APD structure

Two types of APD structures—with staircases and without staircases—have been considered. Most of the III-V semiconductor materials exhibit similar magnitude electron and hole ionisation coefficients. Based on the shot noise theory of McIntyre [20], such behaviour results in worse noise characteristics than in silicon APDs. An attempt to address this problem was made by Capasso *et al.* in 1983 [21]. They proposed for the first time a structure called the “staircase diode” to artificially improve the α and β ratio. This used a SAM APD structure and the GaAs/AlGaAs material system, and hence is a comparison point for work in Chapter 7, studying GaAs/AlGaAs APDs.

A staircase structure is formed by thin layers of AlGaAs and GaAs that change periodically to produce a periodic modulation of the band gap. When the structure is reverse biased, the diode exhibits a conduction band like a staircase. In the first direction, electrons gain the energy of the conduction band offset when they move from the AlGaAs barrier into the GaAs well; in the other direction, holes lose the energy of the valence band offset. Ultimately, this causes a change in the energy distribution of the electrons in the GaAs well toward higher energies and a decrease in the energy distribution of holes. As a result, higher electron ionization rates and lower hole ionization rates were predicted. For this reason, one possible technique for creating low-noise APD in GaAs-based material systems is to use the staircase diode as an electron multiplication region. In this thesis, a higher Al fraction AlGaAs multiplication layer is used instead, but in other ways, the SAM APD structures are similar.

The staircase band structure described above illustrates the conduction and valance band edges when the carriers have low energy. However, when the APD is biased at high voltages necessary to achieve the gain, the carriers will have very high energy, and hence they might not be able to see the band edge steps and experience the same excess energy when they move from one material to another. As a result, the advantage of the staircase in reducing the excess noise based on the band edge might be less significant.

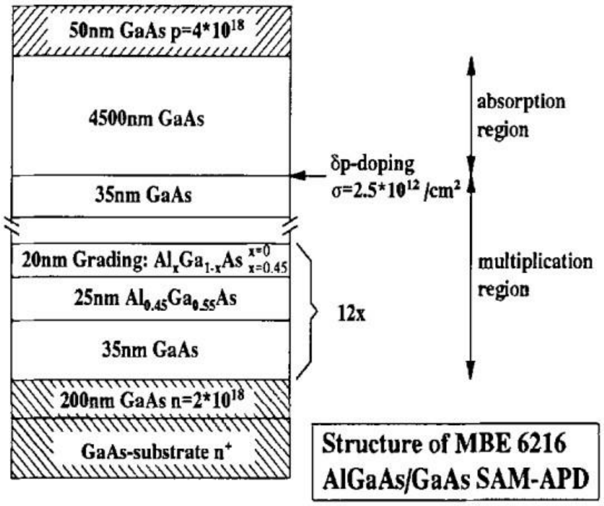

Figure 3.7: Schematic of the AlGaAs/GaAs APD with staircase multiplication region [17].

In 1994, Lauter *et al.* [17] developed an AlGaAs/GaAs SAM APD with separate absorption and staircase multiplication regions to use as an x-ray detector, the most common target application for AlGaAs/GaAs APDs reported in the literature. Molecular beam epitaxy (MBE) was used to grow the devices at a temperature of 600°C. The device structure is illustrated in Figure 3.7. A δ p-doped layer, which separates the multiplication region from the absorption region, was used to avoid the electric field reaching the absorption region (which has a lower band gap) by completely suppressing the penetration of the depletion region. The C-V measurement of the AlGaAs/GaAs SAM-APD is shown in Figure 3.8. The figure illustrates that this device is not entirely depleted, where the multiplication region is depleted while the absorption region remains undepleted. This device's behaviour provides the advantage of low dark currents. Dark current and photocurrent characteristics, which were carried out by focusing a white light on the top of the diode, were illustrated as a function of reverse bias in Figure 3.9. These measurements confirm that the devices experienced low dark current, which was always less than 100 pA at 90% of the breakdown voltage. They also confirm photocurrent was collected but do not give an indication of QE. In addition, a higher gain of ~20 was reported using this structure. The electron diffusion length is long enough [22], owing to the low doping density of p-GaAs 2×10^{14} cm^{-3}, which helps to collect a significant number of the generated electron-hole pairs in the depletion layer. Despite the fact that this device did not punch through, it provided high gain with low dark current and enough collection efficiency. To compare with the work in Chapter 7, this device has similar depletion behavior to samples 3 and 5, where the absorber layer has never been depleted. With the limitation of unknown QE in Lauter’s work, it appears that photocurrent was better collected from their undepleted absorber, likely due to the use of a lower Al fraction and a depleted linearly graded interface, compared to samples 3 and 5.

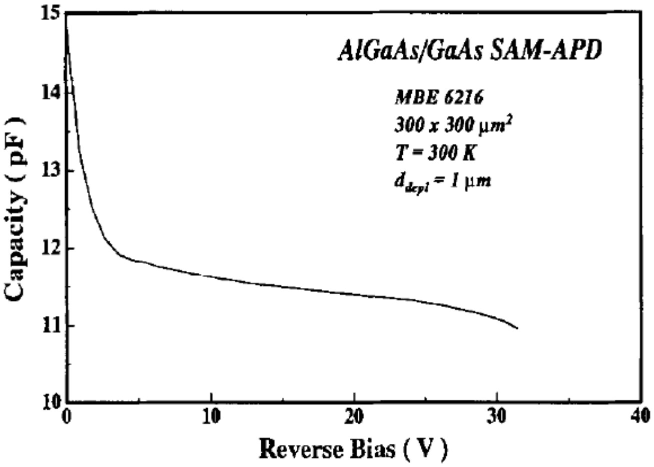

Figure 3.8: Room temperature C-V characteristic of the AlGaAs/GaAs SAM-APD [17].

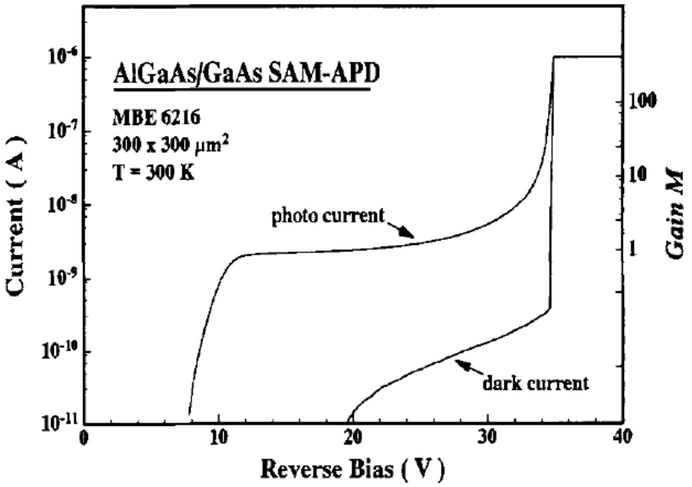

Figure 3.9: Photocurrent and dark current versus reverse bias voltage [17].

In 2017, Steinhartova *et al.* [23]used the same staircase structure as used in the previous paper to study the influence of the δ p-doping layer of carbon atoms on the behaviour of GaAs/AlGaAs SAM-APDs with separate absorption and multiplication regions grown also by molecular beam epitaxy MBE. The main structure of the device is shown in Figure 3.10.

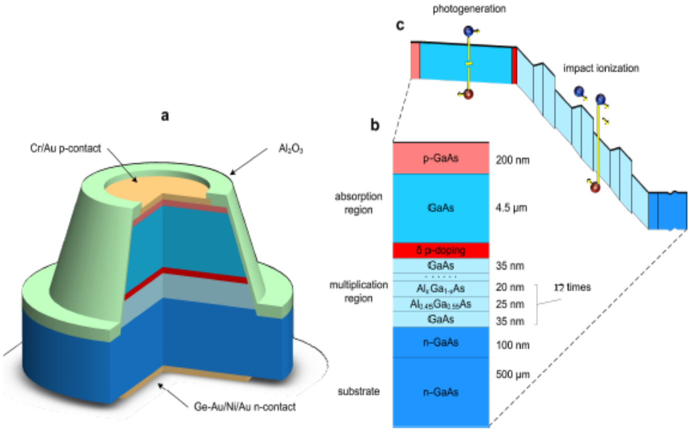

Figure 3.10: An illustrated sketch of the SAM-APD device structure (a), the layer sequence (b), and profiles of the band energy under an applied bias (c)[23].

Five samples with varying carbon areal densities were evaluated to explain the effect of the δ p-doped layer on the device's performance. The current-voltage characteristics (I-V) and capacitance-voltage characteristics (C-V) of the devices in the dark were investigated. The devices with the minimal leakage current can be selected using IV measurements, while the CV measurements illustrate information regarding the internal electric field and the potential distribution within the device.

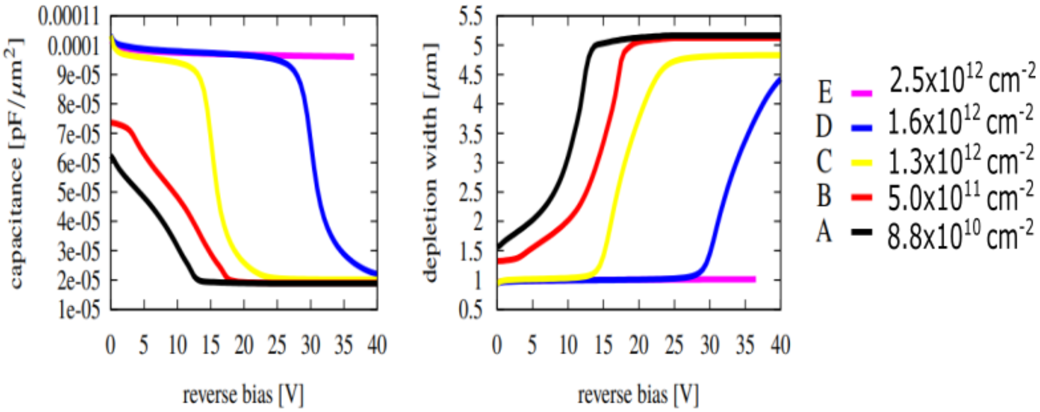

Figure 3.11: Capacitance (left) and associated depletion width (right) as a function of revers bias voltage for the different devices [23].

Figure 3.11 shows that the capacitance of all devices (except E) drops at certain voltage values as the absorber starts to deplete. When the δ p-layer doping density decreases, these voltage values decrease too, as expected. Sample E had the highest, and they deemed it the most suitable, doping density of the δ p-doping layer of about 2.5×10^{12} cm^{-2}, where the depletion width is equal to only the thickness of the multiplication layer. As a result, the depletion in the absorption layer was suppressed even up to the breakdown voltage. The author concluded that this doping was the minimum doping required to achieve electrostatic separation between the multiplication layer and absorber layer. In addition, the photoresponse of the devices was measured when all of the carriers were created throughout the first few hundred nm of the absorption region. Figure 3.12 shows the gain as a function of the reverse bias of devices B, C, and E using the BEAR beamline in the energy range 500–800 eV (left side) and green laser light ($\lambda = 532\,\text{nm}$) (right side). The low delta doping concentration devices have a much lower multiplication value at a given bias voltage, as should be expected given their increased depletion width and reduced electric field. However, the devices with sufficient doping density exhibit significant gain in this bias voltage range and clearly operate successfully as an APD.

It is not clear why the authors did not increase the voltage on samples B and C to achieve significant avalanche gain, but they had made the decision to design and operate the device for an undepleted absorber. Again, the devices have some similarities to samples 3 and 5 in this respect.

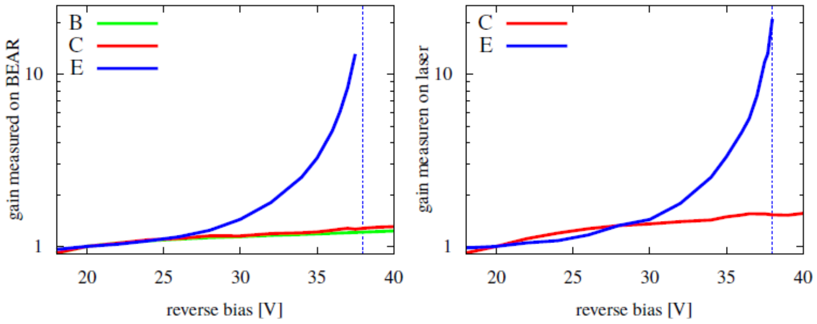

Figure 3.12: Gains of the tested devices with varying carbon atom concentrations in the δ p layer observed at the BEAR beamline with an average of seven different energies between 500–800 eV (left) and using the green laser (right). The dashed line indicates the breakdown voltage of device E (38 V) [23].

In 2019, Nichetti *et al.* [24] also investigated APDs based on GaAs/AlGaAs with separate absorption and staircase multiplication regions in terms of capacitance, light response (gain and noise), and time response, extending on earlier work. They used the same structure of device E in the previous paper. In addition, gain and noise measurements have been implemented on these devices by using photons in the range from visible light to hard x-rays. The noise factor (F) as a function of the gain has been illustrated in Figure 3.13. The area dependence of the extracted excess noise factor is a concern. The authors attribute this to "a larger influence of the substrate", which is assumed to refer to an increased fraction of hole injection. However, it is not clear why this would be more significant in larger devices.

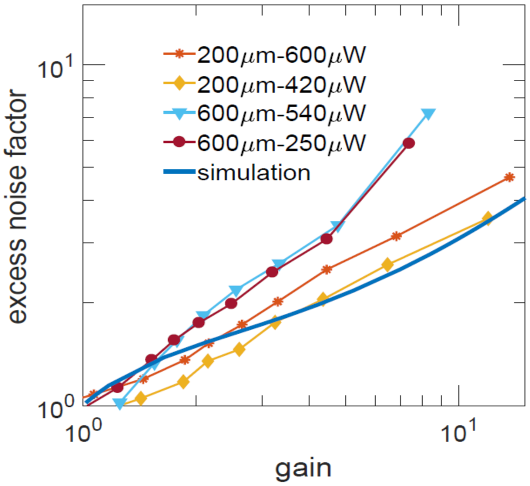

Figure 3.13: Excess noise factor versus the gain extracted from photomultiplication measurements performed on different device areas using different laser powers [24].

The excess noise reported in these devices can be compared with that reported for bulk (as opposed to staircase) AlGaAs diodes. Hing *et al*. [25] reported excess noise in a comparable $Al_{0.6}Ga_{0.4}As$ alloy with multiplication widths up to 850 nm (comparable to the 960 nm in the staircase design). The excess noise factors reported are similar, calling into question the advantage of the staircase design in terms of excess noise. In fact, $Al_{0.8}Ga_{0.2}As$ as reported by Ng *et al*. [26] and used in the APDs studied in Chapter 5, shows significantly lower excess noise as shown in Figure 3.14. Hence it is considered that using a high Al fraction alloy is a better route to low noise AlGaAs/GaAs SAM APDs.

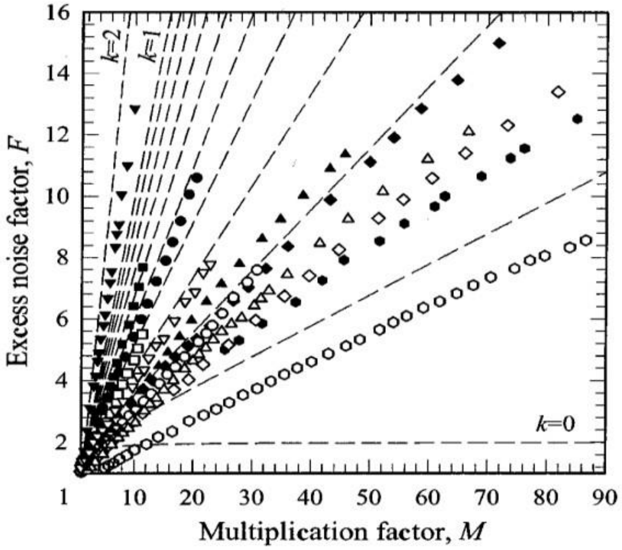

Figure 3.14: Excess noise factor as a function of multiplication factor measured in $Al_{0.8}Ga_{0.2}As$/GaAs APDs [26]. The comparable case with the work of Nichetti *et al.* [24] is the pure electron injection using 1.02 µm multiplication width (open circle).

In 2020, the same authors reported the characteristics of capacitance and light response of the same structure with a staircase in the form of either a δ p-doping sheet of C atoms with $p = 2.5 \times 10^{12}$ cm^{-2}(device A) (as the sample E characteristics in the previous article) or a 50 nm-thick GaAs C layer with $p = 6 \times 10^{12}$ cm^{-2} (device B) [18]. Looking very closely at the field at the edge of the absorber they found that it slightly penetrated into the absorber with the delta doped structure (A) but not at all with the 50 nm doped layer (B). Figure 3.15 shows the photocurrent associated with device A is notably higher than that of device B. This illustrates the significance of the small residual field reaching the absorption region of device A and depleting the interface with the absorber. Evidently this improved charge collection. In contrast, because of the absence of this field in the absorber layer and across the absorber interface in device B, the generated carriers were not collected as efficiently. Given this more detailed analysis, it is clear that device B in this work is even more comparable to samples 3 and 5 reported in Chapter 7. Differences in layer structures do remain, which further suppress carrier collection particularly in sample 5.

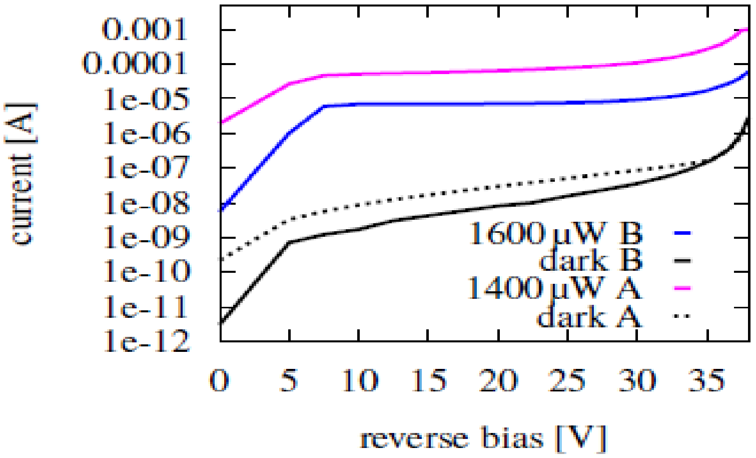

Figure 3.15: Current voltage characteristics IV of device A (magenta curve) and device B (blue curve). The laser power values used during the photocurrent measurements for A and B were 1400 µW and 1600 µW, respectively [18].

Unlike all previous researchers, in 2014, Gomes *et al*. did not use the staircase structure. They used the SAM structure as shown in Figure 3.16 [19]. This structure was similar to the structure used in Chapter 7 with the $Al_{0.8}Ga_{0.2}As$ multiplication region and the field-control layer, which has the same role as the charge sheet. However, the absorption layer was intrinsic rather than a low intentional doping layer in our structure. It is interesting to note that these devices show a dark current, approximately consistent with the dark current in our devices in Chapter 7, where the surface leakage mechanism also dominates. To evaluate the significance of dark current in these devices, the dark current density was calculated at 90 % of breakdown voltage and compared with other established SAM APDs materials. It is found that the dark current density in these APDs, with only 220 nm multiplication width, is <1 µA/cm^2 which is lower than that reported for 1200 - 1300 nm multiplication width InP/InGaAs SAM APDs (5 µA/cm^2)[27] and 400 nm multiplication width InAlAs/InGaAs SAM APD (~50 µA/cm^2) [28].

Note that it breaks down at a relatively low 22 V, for a SAM APD. However, as will be shown in Chapter 7, with a thinner multiplication region of ~50 nm, the breakdown voltage can be reduced further without increasing dark current. As shown in Figure 3.17, the CV measurements demonstrate that these devices punch in the normal way for a SAM APD. Their punch through voltage is similar to that observed in sample 2 (10 V). However, the larger difference between punch through voltage and breakdown voltage makes them more suitable for APDs and less suitable for SPAD applications compared to sample 2.

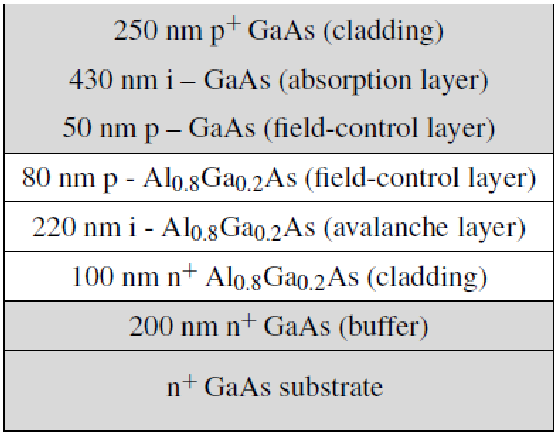

Figure 3.16: Structure details of the GaAs/$Al_{0.8}Ga_{0.2}As$ SAM APD wafer [19].

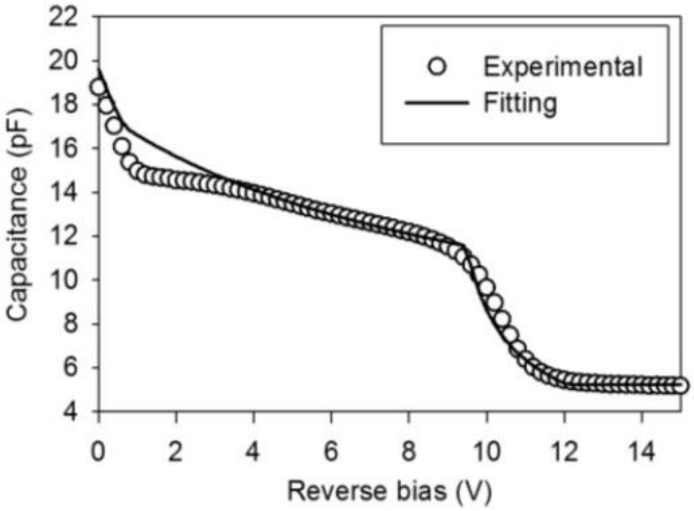

Figure 3.17: Measured (solid line) and modelled (symbols) CV characteristics of 200 µm diameter APD [19].

3.3 SAM Single Photon Avalanche Diodes (SAM SPADs)

SAM SPAD plays a critical role in applications such as satellite laser ranging [29], deep- space laser communication [30], quantum imaging [31], and quantum cryptography [32], [33]. The photon detection efficiency PDE and DCR are the main parameters used to evaluate the performance of SPADs. Very low DCR are currently required for the most demanding applications. There are a lot of studies that focus on improving the performance of SAM SPAD, especially a reduction in primary DCR and after-pulsing probability. There are many SPAD technologies based on different structure and different wavelength photon detection. This review focuses on III-V SAM SPADs for IR photon detection. InP/InGaAs SPADs dominate this space. The potential AlGaAs/GaInAsSbN APD targeted by this project is a possible long-term replacement for such SPADs.

In terms of the primary DCR, some authors investigated the effect of some factors on reducing the primary DCR, such as multiplication width, device area, absorption material quality, and temperature. They also tried to identify the source of the primary DCR, which includes field-assisted mechanisms of band-to-band tunnelling and tunnelling through defects, as well as the generation/recombination GR mechanism.

One of the factors that can play an important role in reducing the primary DCR of SPAD is the thickness of the multiplication region. This is investigated by Ramirez *et al.* on SAM SPADs with InP homojunction multiplication regions and InGaAs as absorber layer [34]. It was found that when the multiplication region thickness increases, the reduction in the number of dark carriers caused by field-assisted generation mechanisms opposes the increase in the number of GR dark carriers. Therefore, the authors concluded that there is an ideal value for the multiplication region width, achieving the lowest DCR of the SPAD. In the case of InP, they show that this optimum is quite thick, in the order of 1 μm.

Given that generation mechanisms depend on material characteristics, studies like this help understand trends but would need revisiting for different materials because the optimum structure will likely differ. In Chapter 7, since we use the $Al_{0.8}Ga_{0.2}As$

multiplication layer, which has a wide indirect band gap, the multiplication thickness can be reduced further down to 50 nm without significant tunnelling, illustrating the importance of the material chosen in the details of successful SPAD designs. Clearly, 50 nm InP multiplication widths could not be used, and the AlGaAs material has resulted in a lower DCR.

In order to identify the dominant primary DCR, Figure 3.18 demonstrates the calculated DCR as a function of the over-bias ratio using three different thicknesses of the multiplication region. Since DCR changes with the breakdown probability, ideally the x-axis of Figure 3.18 would show the breakdown probability. Figure 3.19 shows the width and normalised excess voltage dependence of the breakdown probability for comparison. This probability starts to saturate between 0.1 and 0.2, indicating this would be the likely operating range of a practical SPAD [35].

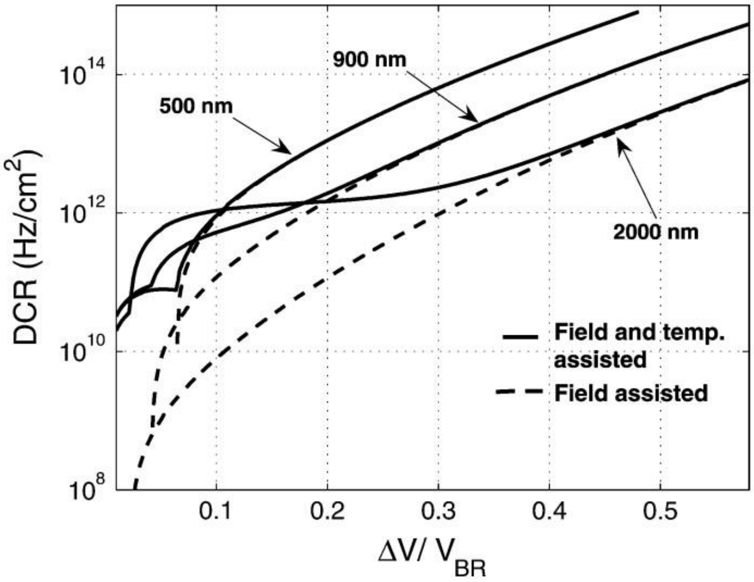

Figure 3.18: DCR as a function of over-bias ratio for multiplication region widths of 500 nm, 900 nm, and 2000 nm. Solid lines indicate the presence of both field-assisted and GR dark carriers, whereas dashed lines represent the absence of GR dark carriers [34].

In Figure 3.18, the solid lines represent the case where the model incorporates both field-assisted and temperature-assisted generation of dark carriers. In order to be clear, the case when only field-assisted generation happened is illustrated (dashed line). The figure illustrates that at higher normalized excess bias voltages, the tunnelling mechanism dominates the DCR curve for all the multiplication region thicknesses. It is also obvious that devices with thick multiplication > 800 nm have a more significant impact of temperature-assisted dark carrier generation on the DCR. However, in thin multiplication width devices, field-assisted mechanisms dominate the DCR curve over approximately the entire normalized excess voltage range. From this work, it is interesting to realise that for low operating temperatures, minimising the approximately temperature-independent tunnelling generation must be a primary goal because the GR contribution can be suppressed with reduced temperature. However, for high operating temperatures, the optimum thickness will be lower to reduce the volume of material in which GR is taking place.

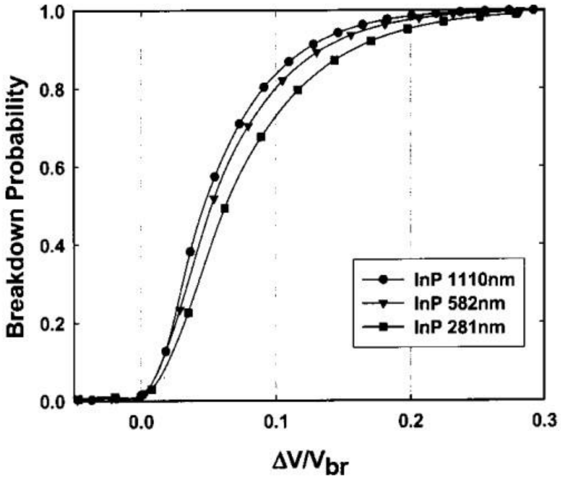

Figure 3.19: A comparison of the breakdown probability for InP devices with different multiplication widths and with pure hole injection [35].

Other factors that can affect the primary DCR are device area and absorption material quality. To illustrate the impact of these factors, the primary DCR in InGaAs/InP single–photon avalanche diodes has been characterized by Tosi *et al.* [36]. In order to avoid the afterpulsing, an effect which will be discussed later, long off-times are needed and the results in Figure 3.20 use off-times of T_{OFF} = 1 ms and T_{OFF} = 200 µs, comfortably long enough to ensure that only the primary DCR is being considered. The active area diameter of the old device is 40 µm while the new one has a 25 µm active area diameter. As shown in the figure, it is obvious that the new device with a smaller area, thicker multiplication width, and higher InGaAs absorption quality exhibits a lower primary DCR. The new device has advantages from both the smaller device area and improving the quality of the InGaAs absorption layer, which can decrease thermal generation. Moreover, as explained in the previous paper [34], using a wider InP multiplication layer reduces the tunnelling.

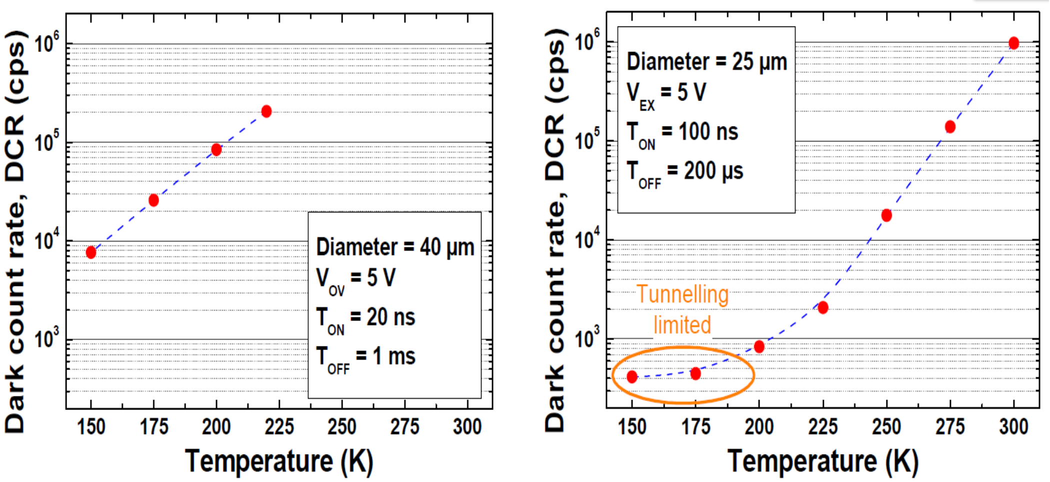

Figure 3.20: Temperature dependence of the primary DCR of an old (left) and a new (right) generation of $In_{0.53}Ga_{0.47}As$/InP SPAD [36].

The figure also identifies the source of the primary DCR by investigating the effect of temperature on primary DCR for a previous ("old") generation of Princeton Lightwave InGaAs/InP SPAD and a new generation device. For both devices, it is clear that primary DCR increases with temperature due to thermal generation. In the case of the old device, the DCR depends exponentially on temperature with a single slope, even at extremely low temperatures. On the other hand, the new SPAD exhibits a weak temperature dependence of the DCR at low temperatures (200 K – 150 K), and a strong dependence of the DCR between 300K and 225 K. Thus, the dominant contribution of DCR was thermal generation at high temperatures and tunnelling at low temperatures. Assuming the thermal generation rate is dominated by the InGaAs absorber, the new device is able to operate up to room temperature due to improvements in its material quality and the reduced device area, while the higher DCR in the old device limits the upper operation temperature. To exclude any area dependence, DCR per unit active area has been calculated for both old and new SPADs at 200 K. It was equal to 120 cps/μm^2 for the old SPAD and only 1.6 cps/μm^2 for the new one. Therefore, from the old to the new InGaAs/InP SPAD generations, there was an impressive enhancement of a factor of 75, although it is not clear that this is under exactly comparable detection efficiencies. This refined Princeton Lightwave device is a good reference for a well-developed III-V SPAD, for IR photon detection.

In Chapter 7, in order to exploit the previous advantage of using small devices to minimise the primary DCR, the DCR characteristics were investigated on thin 25- µm- diameter SPAD. Also, using a good-quality GaAs absorber layer should decrease the DCR associated with thermal generation and trap assistance tunnelling.

In terms of afterpulsing, there are several factors that can reduce its effect on SPAD performance. The afterpulsing probability can also be influenced and decreased by the same improvements implemented in the new devices described in the previous paper [36]. The dependence of DCR on the off-time intervals (T_{OFF}) for both the old and new SPAD generations has been investigated, as shown in Figure 3.21. Since the DCR in the new SPAD starts to increase at a shorter T_{OFF}, the afterpulsing has been reduced as well. Note that even the time constant is different in the new device, indicating that the improved material does not only reduce the magnitude of defects (primary and afterpulsing counts), but also the nature of the defects. The constant, primary only, DCR level is reached with only 10 µs off time in the new device, whereas closer to 100 µs is needed in the old device. Hence, it can be concluded that the old device had a significant number of deeper defects.

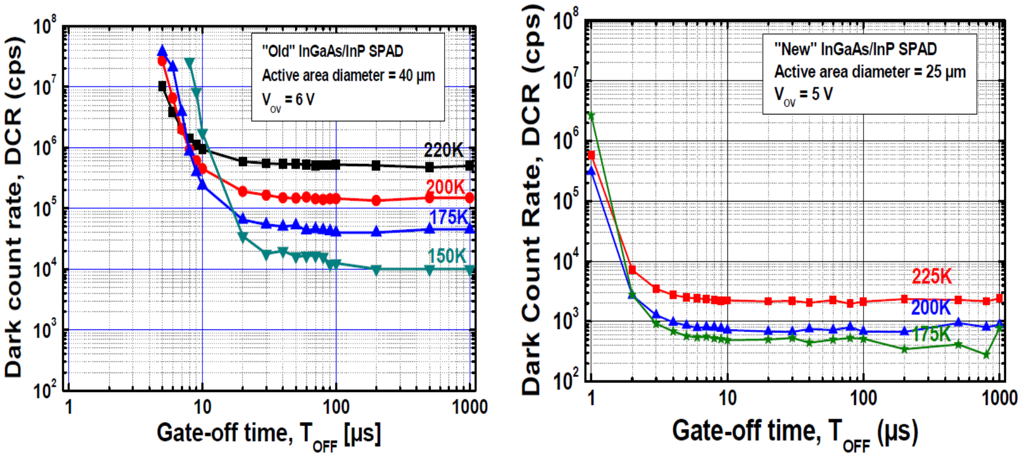

Figure 3.21: DCR as a function of the gate-off time of the old (left) and new (right) generations of InGaAs/InP SPAD devices at different temperatures in gate-on time equal to 20 ns [36].

Using a dead-time detector characterization setup, Comandar *et al*. provided a detailed investigation of the ideal operating parameters of the InGaAs/InP SPADs [37]. It was found that there were two parameters that can be optimized to reduce afterpulsing probability and hence improve SPAD performance, which include gate- on time and operation temperature. It is known that using a short gate-on time can decrease the number of carriers flowing in the device due to an avalanche, which decreases the number of trapped carriers and hence reduces afterpulsing. In order to find an optimal gate-on duration, the afterpulsing and dark count probability as a function of gate-on time at some selected SPDEs were investigated, as shown in Figure 3.22. It was found that a ~360 ps gate duration was the optimum value for their setup. It would be expected that the afterpulsing probability continues to decrease with shorter on times. However, in this work the gate durations are very short, and the authors have increased the bias voltage as the gate duration reduces, to maintain the same detection efficiency within the short gate. This has likely caused an increase in afterpulsing probability at the shortest gate durations.

In Chapter 7, one of the possible reasons for the high reported afterpulsing probability was using a long gate-on time (~50 μs). Therefore, using a shorter gate-on time would be expected to reduce the afterpulsing effect.

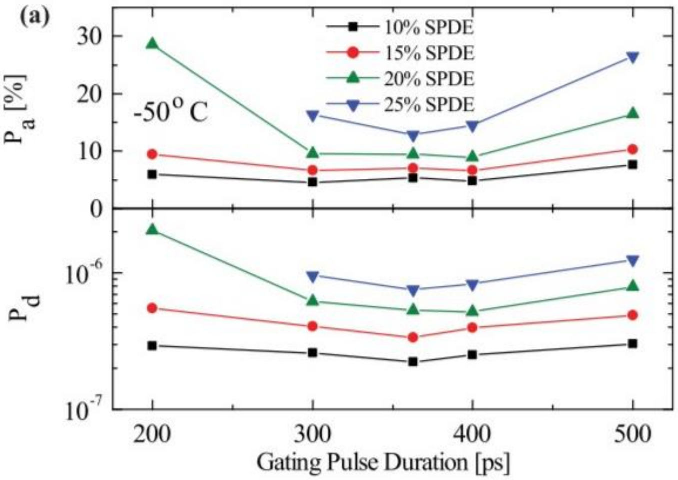

Figure 3.22: Afterpulsing probability (top) and dark count probability (bottom) versus the gating pulse duration at various SPDEs [37].

It was nicely demonstrated in the previous paper studying the devices from Princeton Lightwave that primary DCR increases with temperature [36]. In the paper of Comandar *et al*. [37], the effect of temperature on afterpulsing probability as well as DCR probability was investigated. Figure 3.23 shows the afterpulsing and dark count probabilities as a function of the SPDE for different operating temperatures from 50 °C to 20 °C (223 K- 293 K). As shown in the figure, despite the reduction of the afterpulsing probability with temperature, where the onset of the increase in the afterpulsing probability is shifted to higher efficiencies at higher temperatures, the DCR probability still exhibits an approximate doubling every 10 °C for temperatures above -30 °C. This indicates that the DCR is dominated by thermal generation in this specific range of temperatures. Interestingly the authors propose the reduction in afterpulsing at higher temperatures is not purely down to a shorter release time.

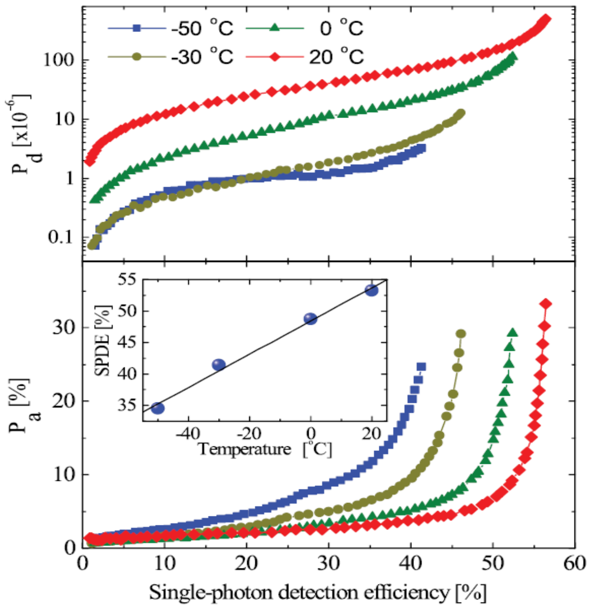

Figure 3.23: Dark count probability (top) and afterpulsing probability (bottom) versus the SPDE for a temperature range of -50 °C to 20 °C and at an amplitude of the applied gate of 18 V. Inset: The SPDE's temperature dependence with a 10% afterpulsing probability [37].

The dependence of DCR and afterpulsing on temperature was also studied at approximately the same temperature range for $In_{0.53}Ga_{0.47}As$–$In_{0.52}Al_{0.48}$ SPADs by Karve *et al.*[28] They found that in the temperature range below 130 K, DCR decreased as temperature increased because of the dominance of the afterpulsing probability, which decreased with increasing temperature, as shown in Figure 3.24. However, at higher temperatures, including the temperature range in the earlier paper, the contribution of thermal generation started to be dominant.

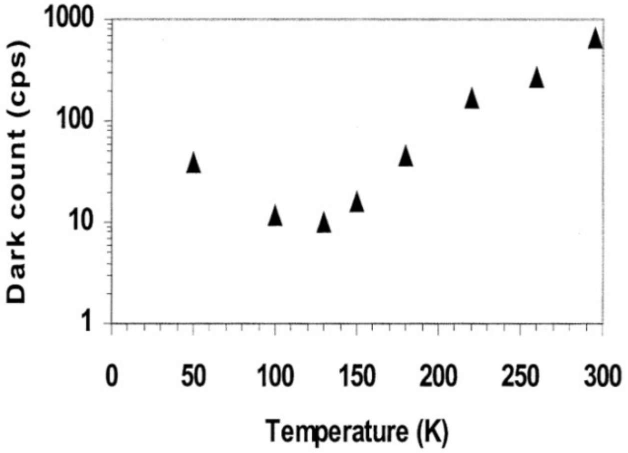

Figure 3.24: DCR versus temperature for $In_{0.52}Al_{0.48}As–In_{0.53}Ga_{0.47}As$ SAM APD [28].

In addition to the earlier simple SAM structure, there is a more complicated technique for the SAM structure which can reduce the DCR. In 2019, Farrell *et al.* suggested a novel SAM-APD platform for single photodetection consisting of vertical InGaAs–GaAs nanowire arrays [38]. As a result of this structure, the primary DCR as well as the afterpulsing probability were reduced. The small active area of the nanowire devices limited the number of thermal generation carriers and hence reduced the primary DCR. To confirm this observation, the DCR as a function of over- bias voltage at a range of temperature was measured as shown in Figure 3.25. The figure shows that the DCR in this temperature range is temperature-independent, confirming that trap-assisted tunnelling is the dominant source of dark current. Also, a very small afterpulsing probability and a DCR lower than 10 Hz were reported. The authors conclude that since the afterpulsing is negligible, the InGaAs-InP SPADs can be operated in free-running mode, avoiding the dead period that limits counting rates. Moreover, this technique can take advantage of the lower surface leakage current compared to the previous devices using etching.

Although the characteristics of the nanowire SPADs are exciting, substantial challenges remain before they can be considered ready for commercial application.

Control of nanowire growth is difficult, and efficient coupling of light into the small wire area will not be easy. It is also notable that the DCR presented is only for low temperatures, much less compatible with practical applications.

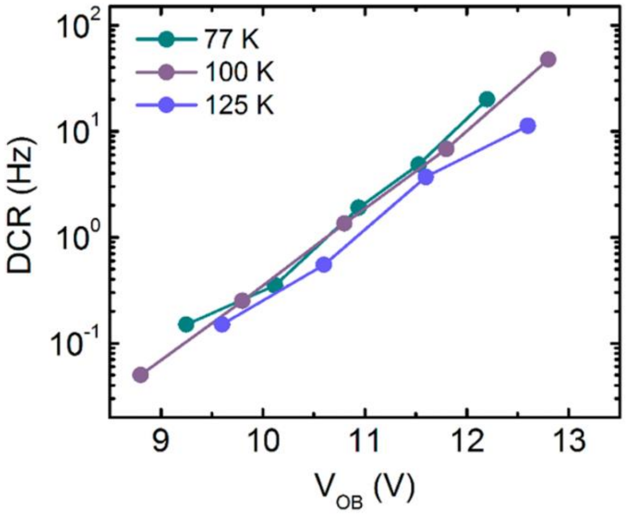

Figure 3.25: DCR versus over-bias voltage at a range of temperature (77 K-100 K-125 K) [38].

3.4 Dilute nitrides of InGaAs and related materials

The use of diluted nitride alloys with GaAs lattice matching was initially investigated in 1996, when Kondow *et al*. suggested GaInNAs for lasing at 1.3 μm and 1.55 μm telecommunication wavelengths [39]. In addition to the lasing, this material was also continued to be used in solar cells and photodetectors. There are different challenges associated with incorporating a diluted nitride alloy into each of these applications.

3.4.1 Unity gain detectors

Detectors that employ dilute nitrides on GaAs substrates were initially developed in 1999, shortly after Kondow's suggestion. Heroux *et al.* proposed an RCE GaInNAs photodetector that has the ability to detect a long wavelength up to 1.3 μm. With a 7 V bias voltage, a 72% quantum efficiency and a 0.9 mA cm^{-2} dark current density were obtained [40].

3.4.2 Dilute nitrides impact ionization coefficients

In order to minimise the APD's noise, the impact ionisation coefficients need to be significantly different. However, this condition is not achievable in the majority of the III-V materials used in optoelectronic devices, where α and β are nearly identical. In terms of dilute nitride, the early estimation of the impact ionisation coefficients was made by Adams *et al*. [41]using band anti-crossing model [42]. They suggested including highly mismatched atoms, such as nitrogen, in GaAs or GaInAs. This can split the conduction band into two different bands, as explained earlier, which reduces the band gap and is expected to increase the electron ionization rate α. On the other hand, α shows a reduction due to the increase in the effective mass, which results in more scattering and less acceleration. Moreover, defects such as N-N pairs can occur and increase the scattering. As the incorporation of nitrogen has no effect on the valence band, β remains unchanged, and α/β decreases to be much lower than unity. Consequently, GaAsN and GaInAsN APDs can achieve low noise in the case of hole-initiated multiplication.

However, this prediction contradicted what Kinsey *et al*. found [43]. They investigated the excess noise measurements on a GaNAs *p-i-n* APD including 0.75% nitrogen with electron injection into the high-field multiplication region. They confirmed that the excess noise in GaNAs is slightly lower than that reported for GaAs at comparable multiplication widths [11]. There are three possible interpretations for this behaviour. Firstly, by adding nitrogen, beta may decrease while alpha is constant. Secondly, an increase in dead space could reduce the noise, however as the multiplication width of 500 nm is quite large, this is highly unlikely. Thirdly, alpha and beta may both decrease, but alpha remains higher than beta. Thus, k=β /α is lower than in GaAs. I noticed that at the same multiplication width, the breakdown voltage for the GaNAs *p-i-n* diode takes place at a higher voltage (24 V) than in GaAs (20 V)[7]. This can be attributed to the scattering effect after N incorporation, which results in a reduction in the electron ionisation rate. As a result, the third reason is more likely to be behind this noise behaviour.

In 2010, Ng *et al*. [44], [45] investigated the electron and hole ionisation coefficient ratio for *p-i-n* and *n-i-p* $Ga_{0.90}In_{0.10}N_{0.038}As_{0.962}$ diodes. Compared to Kinsey's results, adding 10% of In and 3.8% of N allows for the detection of wavelengths up to 1.3 μm. $M_{e(h)}$(V) and M_{mix} (V) data for these samples were indistinguishable. This indicates that α and β are similar for a given electric field.

In 2013, Tan *et al*. [46] expanded the earlier investigations in Sheffield with more samples and excess noise measurements, ultimately somewhat confirmed Adams's prediction. They investigated the behaviour of impact ionization in dilute-nitride GaInNAs photodiodes with a variety of nitrogen concentrations below 4%. They found that, in addition to the significant reduction in alpha due to adding >2% of N in GaInNAs alloys, beta is also reduced, resulting in beta being higher than alpha. As a result, the ionization rate ratio k=β/α increased by a factor of 4. Given that GaAs is a material known to have a low background doping, it is reasonable to assume that the background doping in the ideal GaAs *p-i-n* diode [7]is the same or lower than in the GaInNAs *p-i-n* diode (sample E, ~1 x 10^{15} cm^{-3}) [46]. As a result, the breakdown voltage in the two cases can be compared to check for the reduction of alpha in the GaInNAs. Assuming approximately the same electric field profile, it is significant that the breakdown voltage in GaInNAs is 42 V, while it is lower than 40 V in the GaAs *p- i- n* diode. This emphasizes the reduction of alpha in GaInNAs material.

Despite using comparable samples with similar alloy compositions as in the previous paper, the coefficient ratio is different. According to our results presented in Chapter 6, unintentional doping UID of ~10^{16} cm^{-3} is enough to give a non-uniform electric field profile. Since the UID employed in these samples, which is ~10^{15} cm^{-3}, is 1 order less than in the previous paper with a non-uniform electric field profile, the simple comparison is less accurate.

The same earlier behaviour was noticed for GaInAsSbN in Chapter 6 where its electron and hole ionisation coefficients were extracted. Our results confirmed that beta is higher than alpha but with higher ionisation rate ratio k = β/α. In the future, noise measurements will be required to assess the effects of the coefficient's ratio on APD's noise operation.

3.4.3 GaInNAsSb SAM APD

Despite the fact that dilute nitride of GaInNAsSb has a photo response of ~1.5 µm, the performance of a photodiode can be negatively affected by using GaInNAsSb as a multiplication layer. This is attributed to the significant tunnelling current produced from the small band gap GaInNAsSb under the high electric field necessary for avalanche multiplication. On the other hand, since GaInNAsSb is lattice matched to both GaAs and $Al_{0.8}Ga_{0.2}As$, it can be used as an absorber in the SAM structure with the $AL_{0.8}Ga_{0.2}As$ multiplication layer and on the GaAs substrate. As a result, the desirable properties of AlGaAs as multiplication layer can be exploited. Using wide indirect band gap AlGaAs enables extremely thin multiplication layers with negligible tunnelling and very low noise operation. In 2008 David *et al*. proposed an GaInNAs/$Al_xGa_{1-x}As$ ($x > 0.7$) structure as the basis of inexpensive GaAs-based telecommunication APDs [11]. In Chapter 7, a 50 nm multiplication thickness was used, and the advantages of having such thin multiplication were exploited. Before incorporating GaInNAsSb as an absorber layer into a SAM structure, it is important to identify if the absorber is compatible with $Al_{0.8}Ga_{0.2}As$ in terms of the alpha-beta relationship and at what field impact ionisation in the absorber would start [47]. In Chapter 6, the electron and hole impact ionization coefficients of GaInNAsSb were extracted. Due to the complications associated with the growth of GaInNAsSb, $Al_{0.8}Ga_{0.2}As$/GaAs SAM APDs were initially investigated in Chapter 7 to determine the most suitable structure. These two chapters provide the foundations for future research to investigate GaInNAsSb/$Al_{0.8}GaAs_{0.2}$ SAM APDs and SPADs, realising the proposal of David *et al.*

3.5 References

[1] S. Shabde and C. Yeh, "Ionization Rates in (Al x Ga1− x) As," *Journal of Applied Physics,* vol. 41, no. 11, pp. 4743-4744, 1970.

[2] V. Robbins, S. Smith, and G. Stillman, "Impact ionization in Al x Ga1− x As for x= 0.1–0.4," *Applied physics letters,* vol. 52, no. 4, pp. 296-298, 1988.

[3] R. K. Willardson and A. C. Beer, *Semiconductors and semimetals*. Academic press, 1977.

[4] G. E. Bulman, V. M. Robbins, and G. E. Stillman, "The determination of impact ionization coefficients in (100) gallium arsenide using avalanche noise and photocurrent multiplication measurements," *IEEE transactions on electron devices,* vol. 32, no. 11, pp. 2454-2466, 1985.

[5] S. Plimmer *et al.*, "Impact ionization in thin Al x Ga 1− x As (x= 0.15 and 0.30) p-i-n diodes," *Journal of Applied Physics,* vol. 82, no. 3, pp. 1231-1235, 1997.

[6] W. Grant, "Solid State Electron," *Solid State Electron,* vol. 16, no. 10, pp. 1189-1203, 1973.

[7] S. Plimmer, J. David, G. Rees, and P. Robson, "Ionization coefficients in AlxGa1-xAs (x= 0-0.60)," *Semiconductor science and technology,* vol. 15, no. 7, p. 692, 2000.

[8] B. Ng, J. David, S. Plimmer, M. Hopkinson, R. Tozer, and G. Rees, "Impact ionization coefficients of Al 0.8 Ga 0.2 As," *Applied physics letters,* vol. 77, no. 26, pp. 4374-4376, 2000.

[9] Y. Okuto and C. Crowell, "Threshold energy effect on avalanche breakdown voltage in semiconductor junctions," *Solid-State Electronics,* vol. 18, no. 2, pp. 161-168, 1975.

[10] S. A. Plimmer, J. David, R. Grey, and G. Rees, "Avalanche multiplication in Al/sub x/Ga/sub 1-x/As (x= 0 to 0.60)," *IEEE Transactions on Electron Devices,* vol. 47, no. 5, pp. 1089-1097, 2000.

[11] J. David and C. Tan, "Material considerations for avalanche photodiodes," *IEEE Journal of selected topics in quantum electronics,* vol. 14, no. 4, pp. 998-1009, 2008.

[12] B. Ng *et al.*, "Avalanche multiplication characteristics of Al/sub 0.8/Ga/sub 0.2/As diodes," *IEEE transactions on electron devices,* vol. 48, no. 10, pp. 2198-2204, 2001.

[13] J. Ng *et al.*, "Effect of dead space on avalanche speed [APDs]," *IEEE Transactions on Electron Devices,* vol. 49, no. 4, pp. 544-549, 2002.

[14] D. Ong, K. Li, G. Rees, J. David, and P. Robson, "A simple model to determine multiplication and noise in avalanche photodiodes," *Journal of applied physics,* vol. 83, no. 6, pp. 3426-3428, 1998.

[15] A. Photodiodes, "Effect of Dead Space on Gain and Noise of Double—Carrier—Multiplication," *IEEE TRANSACTIONS ON ELECTRON DEVICES,* vol. 39, no. 3, 1992.

[16] K. M. Van Vliet, A. Friedmann, and L. M. Rucker, "Theory of carrier multiplication and noise in avalanche devices—Part II: Two-carrier processes," *IEEE Transactions on Electron Devices,* vol. 26, no. 5, pp. 752-764, 1979.

[17] J. Lauter, D. Protić, A. Förster, and H. Lüth, "AlGaAs/GaAs SAM-avalanche photodiode: An X-ray detector for low energy photons," *Nuclear Instruments and Methods in Physics Research Section A: Accelerators, Spectrometers, Detectors and Associated Equipment,* vol. 356, no. 2-3, pp. 324-329, 1995.

[18] C. Nichetti *et al.*, "Effects of p doping on GaAs/AlGaAs SAM-APDs for X-rays detection," *Journal of Instrumentation,* vol. 15, no. 02, p. C02013, 2020.

[19] R. Gomes, C. Tan, X. Meng, J. David, and J. Ng, "GaAs/Al0. 8Ga0. 2As avalanche photodiodes for soft X-ray spectroscopy," *Journal of Instrumentation,* vol. 9, no. 03, p. P03014, 2014.

[20] R. McIntyre, "Multiplication noise in uniform avalanche diodes," *IEEE Transactions on Electron Devices,* no. 1, pp. 164-168, 1966.

[21] F. Capasso, W.-T. Tsang, and G. F. Williams, "Staircase solid-state photomultipliers and avalanche photodiodes with enhanced ionization rates ratio," *IEEE Transactions on Electron Devices,* vol. 30, no. 4, pp. 381-390, 1983.

[22] M. Niemeyer *et al.*, "Minority carrier diffusion length, lifetime and mobility in p-type GaAs and GaInAs," *Journal of Applied Physics,* vol. 122, no. 11, 2017.

[23] T. Steinhartova *et al.*, "Influence of δ p-doping on the behaviour of GaAs/AlGaAs SAM-APDs for synchrotron radiation," *Journal of Instrumentation,* vol. 12, no. 11, p. C11017, 2017.

[24] C. Nichetti *et al.*, "Gain and noise in GaAs/AlGaAs avalanche photodiodes with thin multiplication regions," *Journal of Instrumentation,* vol. 14, no. 01, p. C01003, 2019.

[25] T. C. Hing, "Low multiplication noise thin Al0. 6Ga0. 4As avalanche photodiodes," *IEEE Trans. Electron Devices,* vol. 48, pp. 1310-1317, 2001.

[26] B. Ng, J. David, R. Tozer, M. Hopkinson, G. Hill, and G. Rees, "Excess noise characteristics of Al/sub 0.8/Ga/sub 0.2/As avalanche photodiodes," *IEEE Photonics Technology Letters,* vol. 14, no. 4, pp. 522-524, 2002.

[27] Y. Liu, S. R. Forrest, J. Hladky, M. Lange, G. H. Olsen, and D. Ackley, "A planar InP/InGaAs avalanche photodiode with floating guard ring and double diffused junction," *Journal of Lightwave Technology,* vol. 10, no. 2, pp. 182-193, 1992.

[28] G. Karve *et al.*, "Geiger mode operation of an In/sub 0.53/Ga/sub 0.47/As-In/sub 0.52/Al/sub 0.48/As avalanche photodiode," *IEEE journal of quantum electronics,* vol. 39, no. 10, pp. 1281-1286, 2003.

[29] C. P. Morath, K. Vaccaro, W. R. Clark, W. A. Teynor, M. A. Roland, and W. Bailey, "Performance characterization of an InGaAs/InP single photon avalanche diode," in *Infrared Spaceborne Remote Sensing XII*, 2004, vol. 5543: SPIE, pp. 100-111.

[30] A. Biswas and W. Farr, "Detectors for ground-based reception of laser communications from Mars," in *The 17th Annual Meeting of the IEEELasers and Electro-Optics Society, 2004. LEOS 2004.*, 2004, vol. 1: IEEE, pp. 74-75.

[31] M. B. Nasr, B. E. Saleh, A. V. Sergienko, and M. C. Teich, "Dispersion-cancelled and dispersion-sensitive quantum optical coherence tomography," *Optics express,* vol. 12, no. 7, pp. 1353-1362, 2004.

[32] H. Zbinden, H. Bechmann-Pasquinucci, N. Gisin, and G. Ribordy, "Quantum cryptography," *Applied Physics B: Lasers & Optics,* vol. 67, no. 6, 1998.

[33] J.-M. Merolla, Y. Mazurenko, J.-P. Goedgebuer, L. Duraffourg, H. Porte, and W. T. Rhodes, "Quantum cryptographic device using single-photon phase modulation," *Physical review A,* vol. 60, no. 3, p. 1899, 1999.

[34] D. A. Ramirez, M. M. Hayat, and M. A. Itzler, "Dependence of the performance of single photon avalanche diodes on the multiplication region width," *IEEE Journal of Quantum Electronics,* vol. 44, no. 12, pp. 1188-1195, 2008.

[35] S. Wang, F. Ma, X. Li, G. Karve, X. Zheng, and J. C. Campbell, "Analysis of breakdown probabilities in avalanche photodiodes using a history-dependent analytical model," *Applied Physics Letters,* vol. 82, no. 12, pp. 1971-1973, 2003.

[36] A. Tosi, A. Dalla Mora, F. Zappa, S. Cova, M. Itzler, and X. Jiang, "InGaAs/InP single-photon avalanche diodes show low dark counts and require moderate cooling," in *Quantum Sensing and Nanophotonic Devices VI*, 2009, vol. 7222: SPIE, pp. 426-434.

[37] L. C. Comandar *et al.*, "Gigahertz-gated InGaAs/InP single-photon detector with detection efficiency exceeding 55% at 1550 nm," *Journal of Applied Physics,* vol. 117, no. 8, 2015.

[38] A. C. Farrell *et al.*, "InGaAs–GaAs nanowire avalanche photodiodes toward single-photon detection in free-running mode," *Nano letters,* vol. 19, no. 1, pp. 582-590, 2018.

[39] M. Kondow, K. Uomi, A. Niwa, T. Kitatani, S. Watahiki, and Y. Yazawa, "GaInNAs: A novel material for long-wavelength-range laser diodes with excellent high-temperature performance," *Japanese journal of applied physics,* vol. 35, no. 2S, p. 1273, 1996.

[40] J. Heroux, X. Yang, and W. Wang, "GaInNAs resonant-cavity-enhanced photodetector operating at 1.3 µm," *Applied physics letters,* vol. 75, no. 18, pp. 2716-2718, 1999.

[41] A. Adams, "Band-structure engineering to control impact ionisation and related high-field processes," *Electronics Letters,* vol. 40, no. 17, pp. 1086-1088, 2004.

[42] W. Shan *et al.*, "Band anticrossing in GaInNAs alloys," *Physical Review Letters,* vol. 82, no. 6, p. 1221, 1999.

[43] G. Kinsey, D. Gotthold, A. Holmes Jr, B. Streetman, and J. Campbell, "GaNAs avalanche photodiode operating at 0.94 µm," *Applied Physics Letters,* vol. 76, no. 20, pp. 2824-2825, 2000.

[44] Y. Goh, S. Tan, S. Zhang, J. Ng, and J. David, "InGaAsN absorber for telecommunication wavelength APDs," in *2010 Photonics Global Conference*, 2010: IEEE, pp. 1-3.

[45] J. Ng *et al.*, "InGaAsN as absorber in APDs for 1.3 micron wavelength applications," in *2010 22nd International Conference on Indium Phosphide and Related Materials (IPRM)*, 2010: IEEE, pp. 1-4.

[46] S. Tan *et al.*, "Experimental evaluation of impact ionization in dilute nitride GaInNAs diodes," *Applied Physics Letters,* vol. 103, no. 10, 2013.

[47] J. Ng, C. Tan, and J. David, "Multiplication and excess noise of avalanche photodiodes with InGaAs absorption layer," *IEE Proceedings-Optoelectronics,* vol. 153, no. 4, pp. 191-194, 2006.

Chapter 4

Experimental techniques and modelling

4.1 Introduction

A variety of measurement techniques were used to characterise the devices employed in this study, allowing for accurate interpretation of the avalanche properties. Each measuring technique and its corresponding experimental setup are briefly described in this chapter.

4.2 Electrical Characterisation

4.2.1 Capacitance-voltage (C-V) measurements

C-V measurements were carried out using an Agilent e4980a Multi-Frequency LCR Meter with an AC test signal of 60 mV rms and a frequency of 1 MHz. C-V data were mainly utilized to evaluate the capacitance as a function of voltage, depletion width W, doping profile, and built-in potential V_{bi}. Diodes with different diameters were used to make sure that capacitance scaled with the device area.

When an external voltage is applied to a diode, the width of the depletion region that forms around the junction can increase or decrease. W can be characterised by measuring the junction capacitance C as a function of the total voltage across the junction V_t. The depletion width is calculated as:

$$W(V_t) = \frac{\mathcal{E}_0 \mathcal{E}_r A}{C(V_t)} \qquad \textbf{4.1}$$

where A is the area of the junction, $\mathcal{E}_0$ is the permittivity of a vacuum and $\mathcal{E}_r$ is the material dielectric constant. Using a model of a one-sided abrupt junction in which one side has much greater doping than the other, the doping concentration at the front of depletion is expressed by:

$$N(W) = \frac{2}{q\mathcal{E}_0\mathcal{E}_r A^2} \left(\frac{dV_t}{d[\frac{1}{C^2}]}\right) \qquad \textbf{4.2}$$

V_{bi} is the built-in voltage which can be identified by the plotting of $1/C^2$ as a function of the applied voltage V_{app}. The result will be a straight line for an abrupt single-sided junction with constant doping concentration.

When $1/C^2 = 0$, the built-in voltage can be calculated by:

$$V_{app} = V_{bi} - \frac{2k_BT}{q} \qquad \textbf{4.3}$$

In our case, we characterize *p-i-n* diodes instead of *p-n* diodes, and need to be aware that the depletion reaches into the claddings as the voltage increases. As a result, equation 4.3 can only be used to determine the built-in voltage by fitting the linear region where just the unintentionally doped "intrinsic" layer and one cladding are depleting. This is usually only the case at very low reverse voltages or even forward voltages. Furthermore, equation 4.2 is no longer valid to identify the doping levels and i-region width in the *p-i-n* structure and there is a need to fit a modelled C-V characteristic to the experimental C-V data. In order to achieve the best fit, a fitting algorithm was used with adjustable parameters for the doping concentration in the two cladding layers and the intrinsic layer, and the width of the intrinsic region. In the electrostatic model, it is assumed that the doping profiles are abrupt and the electric field gradient $\frac{dE}{dx}$, in a region with an ionized dopant density N can be calculated using Poisson's equation [1]:

$$\frac{dE}{dx} = \frac{qN}{\mathcal{E}_0\mathcal{E}_r} \qquad \textbf{4.4}$$

At a certain voltage V_t, the depletion width of the diode can be found by equating the area under the electric field to V_t. Then, the capacitance at a given reverse bias voltage, can be obtained using the following formula:

$$C(V_t) = \frac{\mathcal{E}_0\mathcal{E}_r A}{W(V_t)} \qquad \textbf{4.5}$$

The dielectric constant of $Al_xGa_{1-x}As$ is given by 13.18–13.12x [2], while for work on the dilute nitride the dielectric constant of GaAs was used, which is equal to 13.1.

4.2.2 Current-voltage (I-V) measurements

Current-voltage (I-V) measurements are the most basic characterization technique used to evaluate the performance of the photodiode. I-V measurements were taken using a Keithley 2400 source–measurement unit (SMU). Many details regarding an APD, its contacts, fabrication process, and its material can be derived from forward and reverse IV measurements. In order to minimize photocurrent during dark current measurements, the device was tested in a dark environment. The leakage currents and the breakdown voltages can be evaluated through the dark reverse I-V characteristics. The dark leakage currents can consist of bulk and/or surface leakage currents. Leakage mechanisms, including generation-recombination and tunnelling processes, are responsible for the bulk leakage current, which tends to scale with the area of the device. In contrast, surface leakage currents are caused by the existence of leakage paths in the mesa perimeter and, hence, scale with the device perimeter. Normalizing the dark current to the device area and perimeter provides the contributions of the bulk and surface leakage currents.

The ideal characteristics of the forward IV can be written as:[1]

$$I_F = I_0 \left[\exp\left(\frac{qV}{nk_BT}\right) - 1\right] \qquad \textbf{4.6}$$

where I_F is the current flowing in a diode or APD under forward bias, I_0 is the saturation current, V is the applied bias voltage, n is the ideality factor, k_B is the Boltzmann constant and T is the temperature. The value of the ideality factor n should range from 1 to 2, depending on whether diffusion current or defect related SRH recombination currents are more dominant, respectively.

At high forward (or reverse) current, there is a large current flowing through the device, which is enough to cause significant voltage drops across the contact resistance between the deposited metal contact and semiconductor. As a result, this series resistance R can affect both the forward and reverse IV and in turn the multiplication characteristic M(V), by supressing the actual voltage across the semiconductor junction itself. In order to correct the photomultiplication measurements for the series resistance effect, it is crucial to know the value of R. An example of how R is fitted for a GaInNAsSb *n-i-p* diode with 400 μm diameter is shown in Figures 4.1, 4.2.

The value of R can be determined from forward I-V characteristics as follows. First, equation 4.6 can be rewritten as:

$$\ln(\mathrm{I_F}) = \ln(\mathrm{I_0}) + \frac{\mathrm{qV}}{\mathrm{nk_BT}} \qquad \textbf{4.7}$$

As shown in Figure 4.1, by plotting $\ln(\mathrm{I_F})$ as a function of the forward voltage *V* and fitting linearly the linear part of the curve at low voltage, the values of *n* and *I₀* can be determined from the gradient $\frac{\mathrm{q}}{\mathrm{nk_BT}}$ and the intercept $\ln(\mathrm{I_0})$ of the graph respectively.

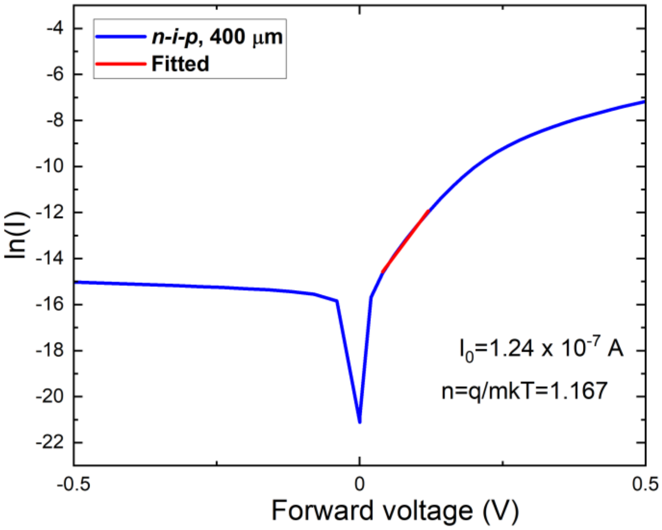

Figure 4.1: ln (I) as a function of forward voltage of a GaInNAsSb 400 μm diameter *n-i-p* diode.

Then, a series contact resistance R can be included in the forward equation 4.6 as:

$$\mathrm{I_F} = \mathrm{I_0}\left[\exp\left(\frac{\mathrm{q\{V\text{-}I_FR\}}}{\mathrm{nk_BT}}\right)\right] \qquad \textbf{4.8 (a)}$$

Since equation 4.8 (a) has I_F parameter in both sides, an equivalent equation (4.8 (b)) must be defined, which can be evaluated to test possible values of R. If the device has ohmic contacts, then a value of R can be found, where the calculated $I_{calc}(V)$ matches the measured $I_{meas}(V)$. However, if $I_{calc}(V)$ does not match $I_{meas}(V)$, including having a non-physical negative gradient, this shows that the resistance is not ohmic. This is checked by plotting both.

$$I_{calc} = I_0 \left[\exp\left(\frac{q\{V - I_{meas}R\}}{nk_BT} \right) \right] \qquad \textbf{4.8 (b)}$$

In this case of the GaInNAsSb *n-i-p* diode, it is impossible to find a value R, for which I_{calc} matches I_{meas}. An example case for R = 150 Ohms is shown in Figure 4.2. In order to match the magnitude of the measured current I_{meas}using equation 4.8 (b) at 0.5 V, a bigger series resistance is required. In comparison, a smaller series resistance is required at 1.5 V. Therefore, the calculated current I_{calc} is overestimated and underestimated at 0.5 V and 1.5 V, respectively.. This demonstrates that the contact resistance is nonohmic, and it decreases as the voltage increases.

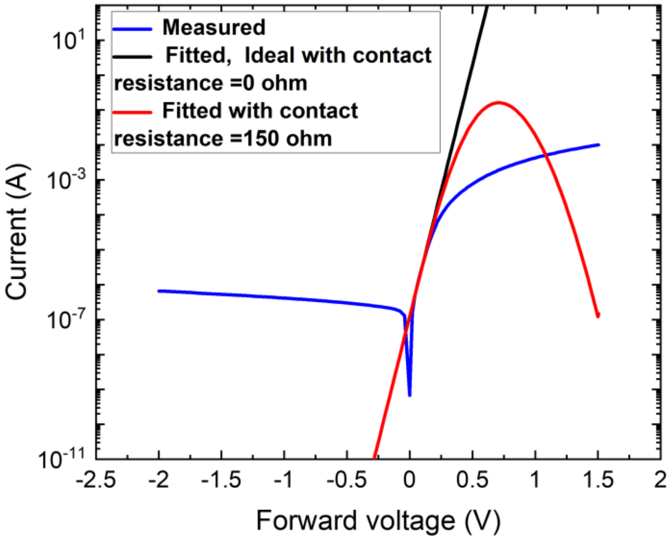

Figure 4.2: Measured and fitted forward I-V characteristics of a GaInNAsSb 400 µm diameter *n-i-p* diode.

In the case of ohmic contacts, one contact resistance value can be used to fit the forward I-V characteristic. Then, this resistance can be used to correct the applied reverse voltage using the following equation:

$$V_{corr} = V_{app} - I_{rever}R \qquad \textbf{4.9}$$

where V_{corr} is the corrected reverse voltage, V_{app} is the applied reverse voltage, and $I_{rever}$is the reverse current. On the other hand, in this case of the GaInNAsSb *n-i-p* diode with non-ohmic contact resistance, there is a need to find another way to correct the applied voltage. As shown in Figure 4.2, in the ideal case with zero contact resistance, equation 4.8 (a) can fit the *n-i-p* diode up to the current limit of ~50 µA. This indicates that the voltage dropped across the contact resistance when the current below 50 µA was negligible. Hence, there is no need to correct the reverse bias voltage at these current values in the reverse bias characteristics. However, at each forward current higher than 50 µA, the voltage dropped across the resistance is remarkable and can be identified by calculating the difference between the actual forward voltage and the ideal forward voltage. Then, in the reverse bias characteristics, at each current value, the voltage across the diode (corrected voltage) can be identified by taking out the voltage dropped across the resistance from the applied voltage. Considering example currents of 1 mA and 10 mA, the voltage dropped across the resistance represents only less than 1.5% and less than 5% of the applied voltage respectively. This illustrates that the effect of this resistance on the photomultiplication measurements is reasonably small, as explained later in Section 6.6.1. As a result, most working data is presented without taking voltage correction into account. However, all the multiplication data including in the fitting of the coefficients was corrected first.

4.2.3 Transmission line measurements (TLM)

TLM measurement is an effective method to check the ohmic contact for the upper and lower contact layers. To achieve this, the total resistance must be measured between a pair of contacts of width w. The distances between these contacts are shown in Figure 4.3 where $L_3 > L_2 > L_1$. The total resistance can be written as:

$$\mathrm{R_T} = 2\mathrm{R_m} + 2\mathrm{R_c} + \mathrm{R_{semi}} \qquad \mathbf{4.10}$$

where R_m is metal resistance, which can be ignored as it is a negligible value compared to both the contact resistance R_c, which is contact area dependent due to the interface between the metal and semiconductor, and semiconductor resistance R_{semi}. In addition, the semiconductor resistance can be written as $\mathrm{R_s}\frac{\mathrm{L}}{\mathrm{W}}$ where $\mathrm{R_s}$ is the semiconductor sheet resistance, L is the pad separation and W is the pad width. In the case of ohmic contact, as shown in Figure 4.4, the plotting of the total resistance R_T as a function of L results in a linear fit that can be used to identify R_c and R_s. The plot should intercept the y-axis at $2R_c$. Furthermore, from the fitted gradient m and the pad width W, R_s can be calculated via: $\mathrm{R_s} = \mathrm{mW}$

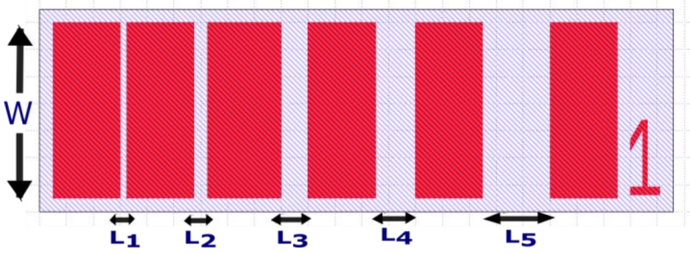

Figure 4.3: A schematic representation of the TLM pads (red), illustrates the increasing separation between adjacent pads.

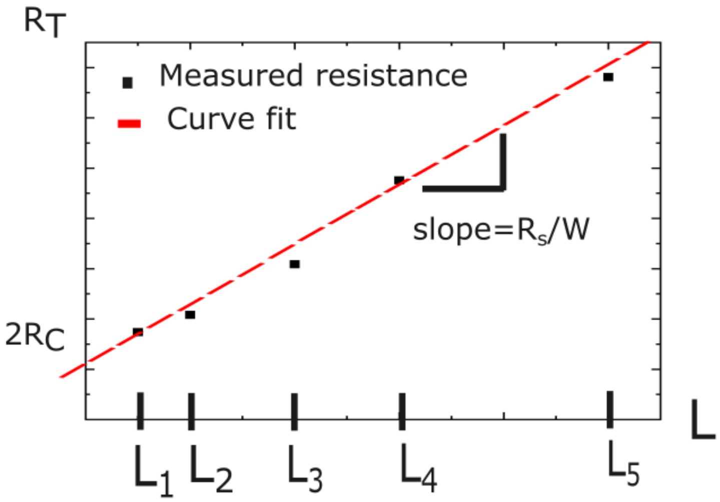

Figure 4.4: TLM measurements can be used to determine the contact resistance and sheet resistance.

4.3 Photomultiplication Measurements

A photomultiplication measurement is a fundamental method for characterising avalanche multiplication within an APD. In the case of a low leakage current, DC photocurrent measurements can be performed. On the other hand, when the leakage current is sufficiently high, such as in materials with a narrow band gap, photomultiplication measurement using phase-sensitive detection techniques are required to accurately distinguish AC photocurrent from DC leakage and minimize the noise associated with the dark current. The multiplication can be calculated by:

$$M(V_t) = \frac{I_{ph}(V_t)}{I_{pr}(V_t)} \qquad \mathbf{4.11}$$

where I_{ph} is the measured photocurrent and I_{pr} is the unmultiplied primary current.

Figures 4.5, 4.6 illustrate a schematic diagram of the experimental setup used for photomultiplication measurements under AC conditions. Light from a laser source was focused on the optical window of the diode using a fibre. A camera was also used to view the image of the device and laser point on a monitor. To guarantee a pure injection of carriers, the laser beam was focused just on the top mesa. The diode's reverse bias voltage was supplied by a Keithley 2400 source-measure unit.

To modulate the laser, two methods have been used, depending on the type of laser that we have. The fibre coupled 405 nm and 1550 nm lasers were modulated easily using the wave generator at 183 Hz as shown in Figure 4.5, while an optical chopper was used to modulate the free space 543 nm, 670 nm and 1310 nm lasers at the same frequency as illustrated in Figure 4.6, before they were also coupled into a fibre.

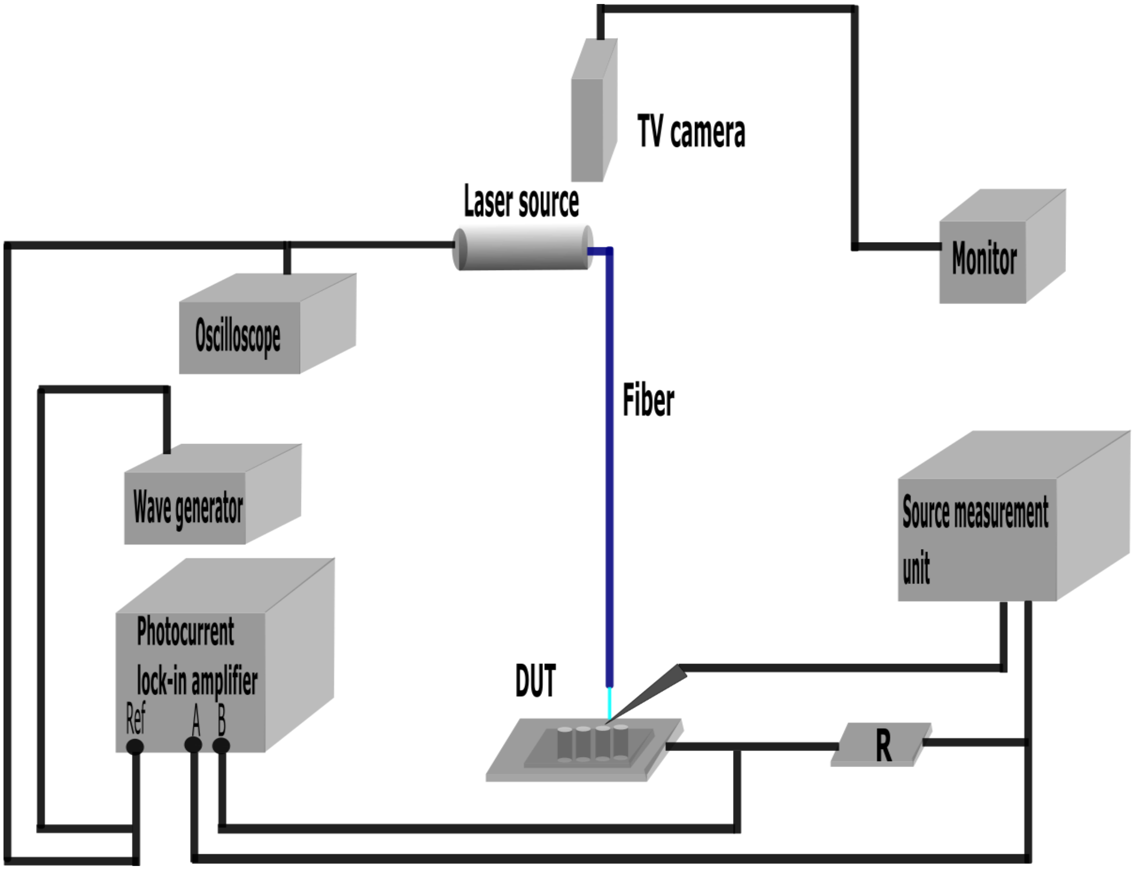

Figure 4.5: The phase-sensitive photomultiplication measurements set-up using fibre coupled laser modulated by the wave generator.

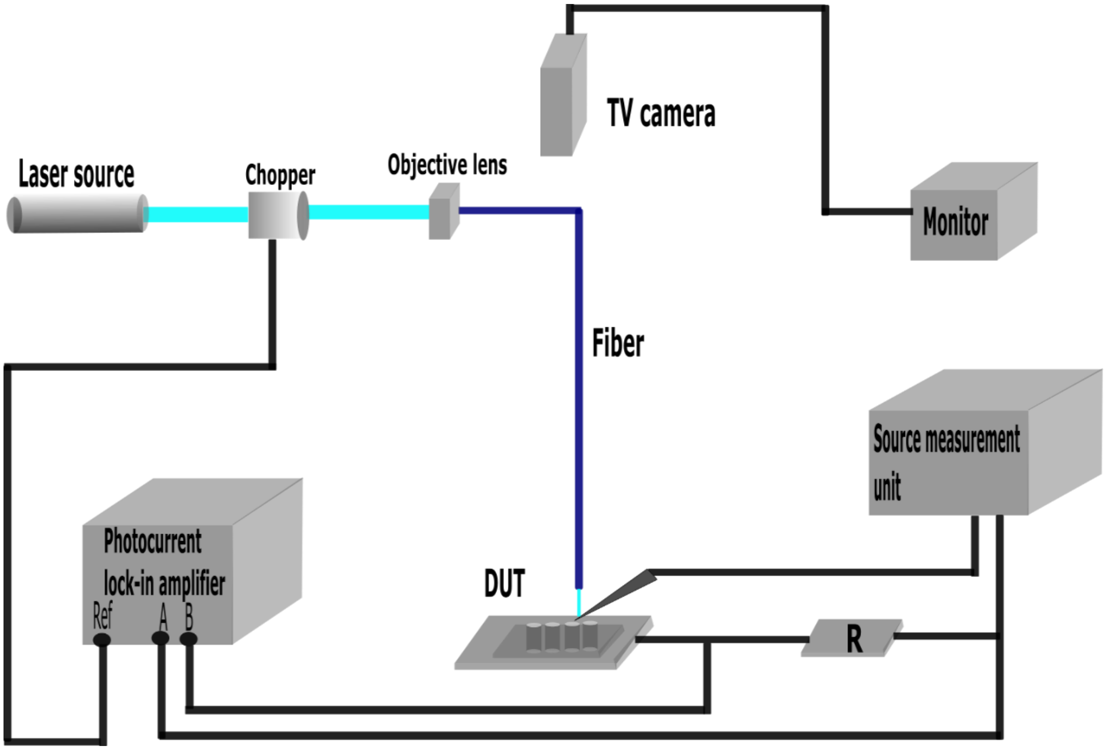

Figure 4.6: The phase-sensitive photomultiplication measurements set-up using free space laser modulated by chopping.

The reverse-biased diode illuminated by the modulated laser generated an AC photocurrent signal. Then the resulting signal was detected on a SR830 lock-in amplifier (LIA) via a resistor R.The frequency used to modulate the lasers was fed to the LIA as a reference frequency. The LIA is only capable of measuring signals at the reference frequency and attempts to ignore noise at other frequencies. Thus, photomultiplication measurement with an LIA are preferred for APDs with a large dark current.

For DC photocurrent measurements, the SMU can be used directly without the resistor and optical modulation, to measure both the dark current and the total current. The dark current I_{dark} was measured in the absence of laser light, whereas the total current $I_{total}$was acquired with laser illumination. By eliminating the dark current from the total current, the photocurrent I_{ph} can be obtained. The dark current measurement was always repeated before and after obtaining a photocurrent reading to make sure the diode hadn't been influenced by the ambient light. This is critical because the approach assumes dark current is essentially constant.

There are two possible reasons why the primary photocurrent, I_{pr}, can increase with bias voltage. With increases in bias voltage, the multiplication gain increases, which multiplies I_{pr}. This is the desirable increase exploited in APDs. As the bias voltage increases, the depletion region also extends, and more photo-generated carriers can be collected, increasing I_{pr}. I_{pr} can be then approximated as a function of voltage without any increase due to gain, by a linear function $I_{pr}=aV+b$. This equation can be used to fit how I_{pr}can change with V at low bias voltage values and then extrapolate the value of I_{pr} at different bias voltages [3]. Hence, the gain can be calculated using equation 4.11.

During multiplication measurements, it is desirable to get pure electron and hole multiplication. This can be achieved by controlling the injected photocurrent in the high-field region, where only one carrier type, either electrons or holes, is injected. Two different types of injection are shown in Figure 4.7: pure electron or hole injection and intended mixed injection using *p-i-n* or *n-i-p* diodes and the selection of a suitable laser wavelength.

Laser sources with two different wavelengths ($\lambda_1 < \lambda_2$) can be used to illuminate the top cladding layer of *p-i-n* or *n-i-p* diodes. Using λ_1 with high photon energy, all absorption takes place in the cladding layer, resulting in the injection of pure carriers (electrons or holes respectively) into the avalanche region, providing M_e on the *p-i-n* or M_h on the *n-i-p*. To check the purity of the injection, a slightly longer wavelength can be used. If the resulting multiplication is identical to the pure one, the purity can be confirmed. On the other hand, selected longer wavelengths (λ_2) can generate carriers within the structure, creating a mixed carrier injection multiplication characteristic (M_{mix}).

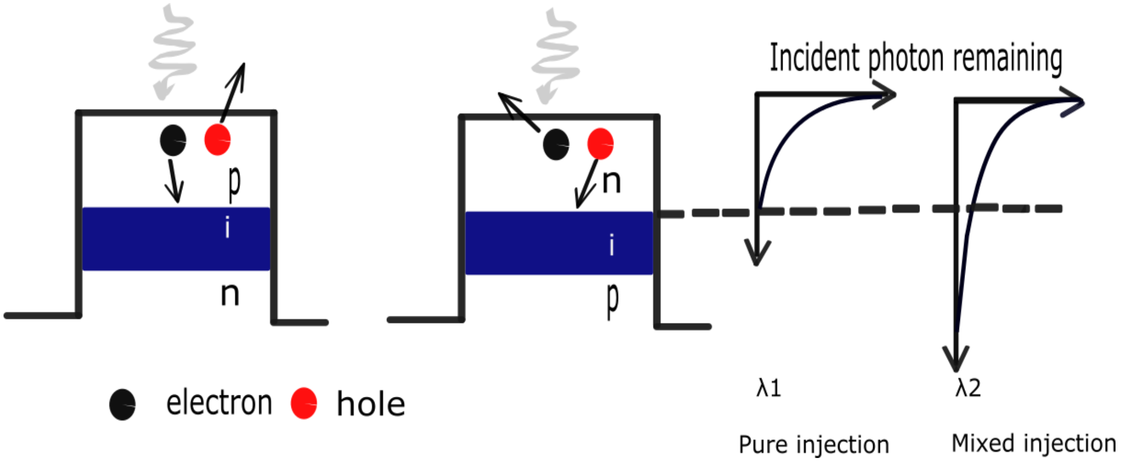

Figure 4.7: Schematic illustration of the mechanism used to control the photon-generated carrier type injected into the intrinsic region.

In reality, it is difficult to obtain pure carrier injection when measuring small devices or when using a relatively large laser spot. In this case, the shorter-wavelength light can accidentally hit the sidewall of the mesa and the area around its base, causing an unintended mixed injection. In order to test the purity of an injection, devices with different diameters can be used for measurement.

Another possible source of mixed injection is the absorption of re-emitted photons. When photo-generated carriers recombine radiatively, re-emission can occur in any direction at a wavelength equivalent to the bandgap energy. It is possible for this radiation to be re-absorbed anywhere through the structure, leading to a mixed injection into the high electric field. The risk of re-emission is inversely proportional to quantum efficiency [4].

4.4 Single Photon Avalanche photodiodes SPADs

In order to investigate the DCR and afterpulsing probability, a setup was used as shown in Figure 4.8, with the SPAD placed inside the Lakeshore probe station. To pulse-bias the SPAD over the breakdown voltage, a simple bias tee circuit was assembled to superimpose alternating voltage (V_{AC}) pulses on a DC bias (V_{DC}), which was set below the breakdown voltage. The DC bias was provided by a lead-acid battery and a variable linear regulator circuit to ensure a low-noise DC bias. The Agilent 8114A 100V/2A Programmable Pulse Generator can provide AC pulses with amplitudes up to 100 V and frequencies up to 15 MHz through a switch-selected capacitor (C_1) with a value ranging from 1nF to 10 µF. C_1 was used to block the flow of DC current from the DC supply to the AC generator, and also to couple-in the AC signal to point A and combine it with the DC voltage. (Note: If the DC is disregarded and just AC is used, charging and discharging the SPAD will take a longer time.) C_1 must be high enough to slow the discharge process through R_2 and maintain a nearly constant bias voltage at point A until the SPAD breaks down, hence providing precise values for the over-bias voltage. On the other hand, the capacitance needs to be as low as possible to limit the amount of energy that can be passed through the SPAD as current when it breaks down. Through the avalanche process, this current can heat the SPAD, and the carriers can fill the traps before releasing them later, resulting in an after- pulsing effect. C_1 also needs to be significantly higher in comparison to C_{SPAD} in order to avoid a decrease in voltage at C_1 during charging to the smaller C_{SPAD}. This will maintain a nearly constant bias voltage at point A until the SPAD breaks down.

The cathode of the SPAD (point A) was connected to the DC supply through a 10 kΩ resistor (R_2). For the same previous reason of having high C_1, R_2 must be sufficiently high to slow the discharge of C_1. However, R_2 and C_1 need to be low enough to minimise the time constant R_2C_1 required for recharging C_1 during the off time of the cycle. Then, the anode was connected to the ground through a switch-selected resistor (R_1) with a value ranging from 56 Ω to 68 k Ω. These resistance values were selected to allow for the time constant $C_{SPAD}R_1$, which defines the charge-up of the SPAD to vary from ~1 ns to ~1 µs. R_1 must be sufficiently high to achieve a measurable voltage at point B when the SPAD breaks down. Also, it needs to be high enough to limit the maximum current during avalanche breakdown and decrease the number of trapped carriers and, consequently, the after-pulsing effect. On the other hand, R_2 must be as low as possible to minimise the time constant $C_{SPAD}R_1$ and charge up the SPAD capacitance quickly, applying the over-bias, thereby making the charge up time minimal compared to the time to breakdown, even with high DCR.

The avalanche breakdowns were monitored by measuring the voltage at point B using a Teledyne LeCroy, WaveAce 1001 (40 MHz) (1 GS/s) oscilloscope. The oscilloscope connects to the PC to capture the voltage trace at point B from each breakdown. Repeated captures were made to give a desired number of N iterations of the test to be used to calculate the cumulative breakdown probability.

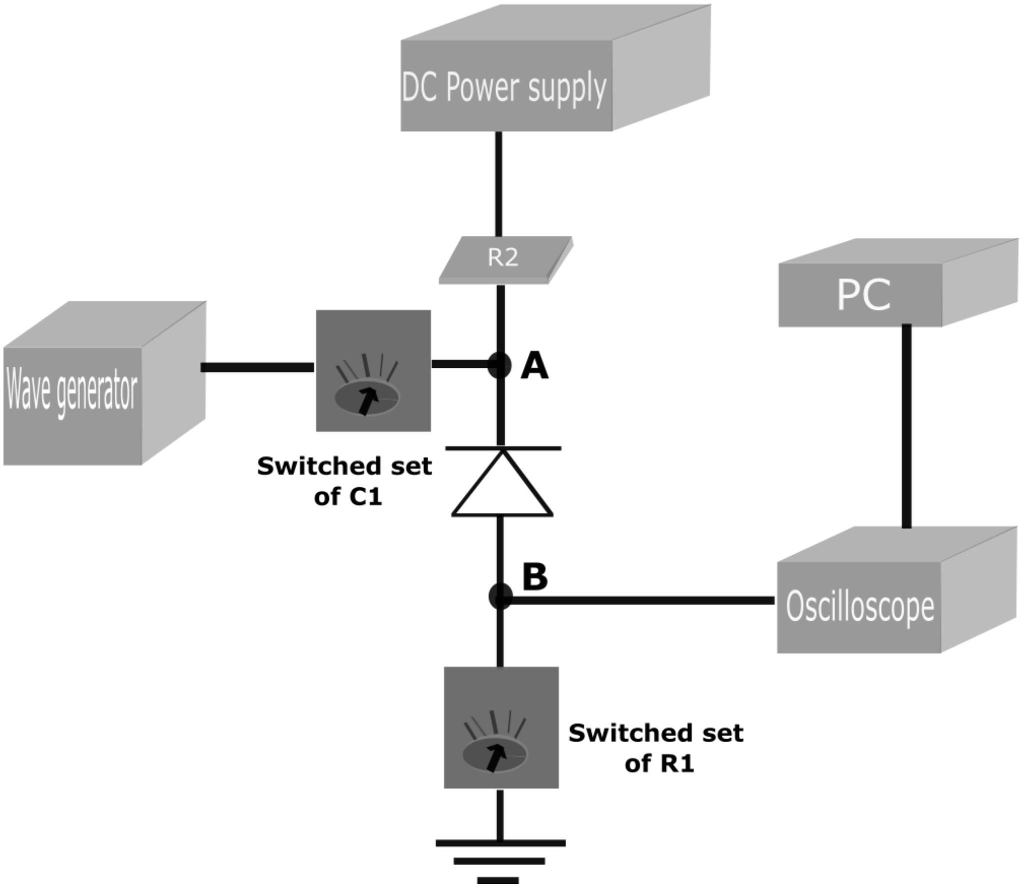

Figure 4.8: Experimental set-up for DCR and after pulsing probability measurements with gated quenching.

4.4.1 Dark count rate measurements

In order to determine the DCR, multiple iterations of breakdowns were captured as shown in Figure 4.9. Then, the code in the PC, which was written by Craig Adam, was used to record the time of breakdown at each iteration. Thereafter, it combines them together to build up a cumulative breakdown probability plot. This cumulative breakdown probability is fitted to find the time constant for the transition from 0 to 1 (not broken down to broken down). The inverse of this time constant is the DCR.

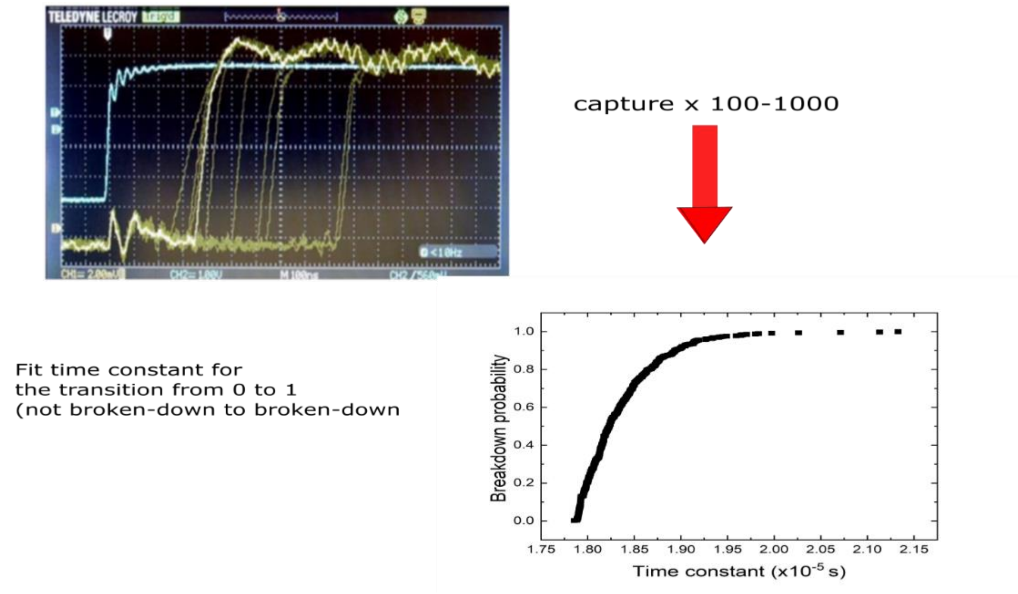

Figure 4.9: Schematic of DCR measurements. The oscilloscope screenshot shows the voltage at the pulse generator (blue) and the sensing voltage at point B (yellow) vs. time (top). After 100–1000 captures, the breakdown probability as a function of time was calculated to fit the time constant for the transition from 0 to 1 (bottom). This measurement is not for AlGaAs SPAD, but it is for a leakier AlGaAsSb SPAD.

4.4.2 Breakdown Iteration Test

To evaluate stability, the DCR was measured on a single diode many times, using the same number of iterations. These tests showed a variation in DCR values. This variation can be attributed to either the non-infinite iteration number, which provides a limited number of samples to represent the cumulative breakdown probability characteristic, or alternatively to other external uncontrolled factors such as device heating. In order to understand the effect of the number of iterations on the variation of the DCR values, the variation of DCR using different iteration values, starting from 10 to 600 iterations, was identified. As shown in Figure 4.10, the variation of DCR with 100 iterations is approximately ±15%, while it decreases to approximately ±10% with

300 iterations. With 600 iterations, there is still some small variation of approximately ±5%. However, the cumulative breakdown probability characteristic is clearly well approximated. In subsequent work, 300–600 iterations were used to achieve acceptable uncertainty due to the finite iteration number.

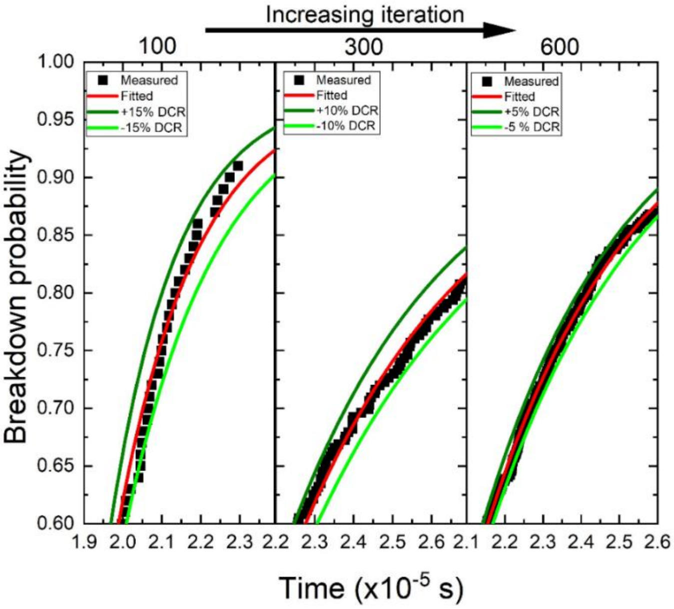

Figure 4.10: Measured and fitted breakdown probability as a function of time using a range of iteration values. Dark green represents the increase in DCR by the given percentage, while light green represents the decrease in DCR.

4.4.3 Duty cycle test

The duty cycle is defined as the gate-on time T_G over the pulse period T_P. To apply the planned and correct over-bias voltage for APDs, it is important that the equilibrium operation of the circuit achieves the expected voltage at point A when the AC voltage rises, equal to DC+AC, and maintains that voltage until the avalanche happens. In practice, the time to breakdown is in the order of microseconds, compared to an AC period in the order of milliseconds; hence, the AC+DC voltage is essentially constant while waiting for breakdown, unless the capacitor is particularly small. The discharging and subsequent recharging of the capacitor during the rest of the AC cycle were found to be the main reasons for achieving a lower AC+DC voltage at point A than expected. In the case when the off-time is significantly longer than the on-time, the capacitor will discharge negligibly during the on-time while there is sufficient time to recharge the capacitor during the off-time, and hence under equilibrium operation, the voltage at point A will have returned to essentially the full DC voltage by the next time the AC voltage rises, as shown in Figure 4.11 (top). On the other hand, if the off-time is much shorter than the on-time, the capacitor will discharge significantly while not having enough time to recharge, resulting in the voltage at point A not fully returning to the DC voltage by the time the AC voltage increases again, which results in a reduced maximum voltage achieved at point A, as shown in Figure 4.11 (bottom). In general, the off-time must be sufficient for the capacitor to recharge to essentially the DC voltage by the next time the AC voltage rises.

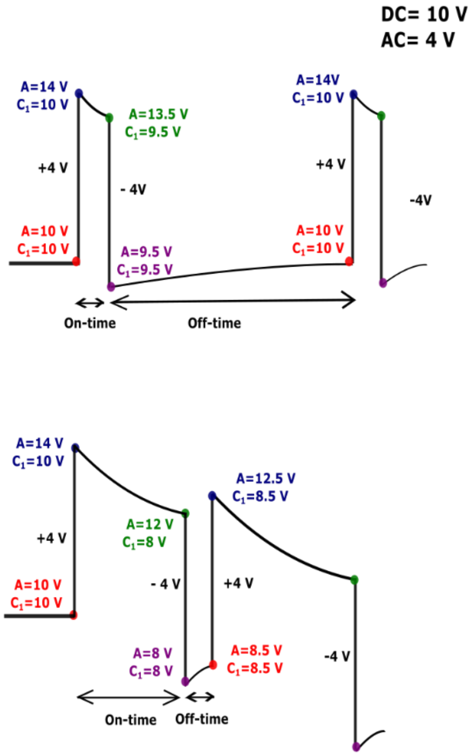

Figure 4.11: A schematic representation illustrates how the voltage values at C_1 and point A will initially change over time with operation of the circuit in two cases: Top: The off-time is significantly longer than the on-time (voltage at A at cycle start is ~V_{DC} at equilibrium). Bottom: The off-time is significantly shorter than the on-time (voltage at A at cycle start will be <V_{DC} at equilibrium).

There are two main factors that affect the equilibrium operation of the circuit and the voltage achieved during the over-bias part of the cycle, which are frequency and on- off keying duty cycle. The influence of these factors was investigated experimentally and mathematically. Both methods provide equivalent outcomes. This investigation informs suitable operating conditions in later SPAD characterisation.

At a constant frequency of 50 Hz, for example, keeping the duty cycle below 5% ensures that the peak voltage remains within only 1% off the expected AC+DC voltage. So, a duty cycle of less than 5% is considered acceptable for determining the over-bias voltage. As shown in Table 4.1, by increasing the duty cycle to more than 5%, the achieved voltage starts to decrease, reducing deterministic control of the over-bias voltage by setting the AC voltage.

Duty (%)	**Peak voltage (V) (calculated)**	**Peak voltage (V) (experimental)**
1%	13.982	14
5%	13.909	13.9
20%	13.631	13.6
50%	13.05	13.1
70%	12.6	12.7

Table 4.1: Calculated and experimental peak voltage values at point A over a variety of duty cycles and at a constant frequency of 50 Hz.

Since the capture rate of dark count measurements was low, it was possible to use a frequency down to 1 Hz. As shown in Table 4.2, at such a lower constant frequency, the voltage achieved at point A remained at the expected full value up to a duty cycle of 20%.

Duty (%)	**Peak voltage (V) (calculated)**
20 %	13.999
50 %	13.98
60 %	13.96
80 %	13.7

Table 4.2: Calculated peak voltage values at 1 Hz and a variety of duty cycles.

More importantly, it is critical to understand if the targeted overbias voltage will be achieved when the frequency used is changed during measurements, for example, when exploring after-pulsing. The impact of frequency on the voltage achieved at point A, at a 1% duty cycle, was investigated using a range of frequencies, as shown in Table 4.3. The voltage achieved at point A remains unchanged as the frequency increases in this range.

F (Hz)	Peak voltage (V) (calculated)	Peak voltage (V) (experimental)
1	13.9999	14
50	13.981	13.9
100	13.9809	13.9
150	13.9804	13.9
200	13.9806	13.9
1000	13.9804	13.9

Table 4.3: Calculated and experimental peak voltage values at 1% duty cycle and over a wide range of frequencies.

4.5 Modelling

Custom modelling software based on the solution of Poisson's equation in one dimension can be used to determine the device's depletion width. Even for more complex structures with an arbitrary number of layers, such as SAM APDs, this model can be successfully utilized to investigate the capacitance-voltage properties. In the simple consideration of a three-layer device such as a *p-i-n* diode, as shown in Figure 4.12, the electric fields at the layer boundaries, ζ_1 and ζ_2, can be determined as:

$$D_1 = qN_1X_1 \quad \textbf{4.12}$$

$$D_2 = D_1 + qN_2X_2 \quad \textbf{4.13}$$

$$D_2 = -qN_3X_3 \quad \textbf{4.14}$$

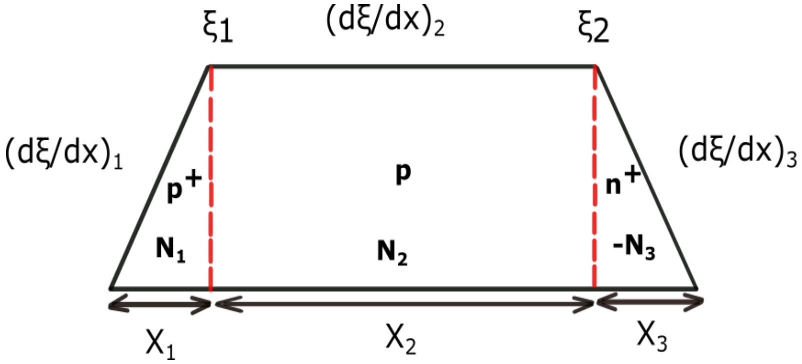

Figure 4.12: The electric field profile of a simple structure consisting of three layers with a width of X1, X2, X3, doping concentration of N1, N2, N3, and the electric field's boundary strengths of E1 and E2.

where q is the elementary charge, N_i and X_i are the doping concentrations, and the depletion width of each layer i. The doping densities, N_i, are negative for n-type layers. D_i is the electric displacement field, which can be expressed in terms of the electric field as:

$$\mathrm{D_i} = \varepsilon_o \varepsilon_r \zeta \qquad \textbf{4.15}$$

The following equation can be obtained by eliminating D1 in equations 4.12 to 4.14 by substitution:

$$\mathrm{X_3} = \frac{\text{-}\mathrm{qN_1X_1}\text{-}\mathrm{qN_2X_2}}{\mathrm{qN_3}} \qquad \textbf{4.16}$$

Moreover, the total voltage V_{tot}, which includes both the applied voltage and the internal voltage, can be related to the integral of the electric field by:

$$\mathrm{V_{tot}} = \frac{1}{2}\left(\frac{\mathrm{D_1X_1}}{\varepsilon_1} + \frac{\mathrm{D_2X_3}}{\varepsilon_3} + \frac{(\mathrm{D_1} + \mathrm{D_2})\mathrm{X_2}}{\varepsilon_2}\right) \qquad \textbf{4.17}$$

Then, substituting equations 4.12 to 4.14 and equation 4.16 into equation 4.17 yields the following quadratic equation for X_1:

$$\mathrm{X_1} = \frac{\text{-}\mathrm{b} + \sqrt{\mathrm{b^2}\text{-}4\mathrm{ac}}}{2\mathrm{a}} \qquad \textbf{4.18}$$

where the coefficients *a, b,* and *c* can be calculated using the following expressions:

$$a = N_1\left(\frac{1}{\varepsilon_1} - \frac{N_1}{N_3\varepsilon_3}\right)$$

$$b = 2N_1\left(\frac{X_2}{\varepsilon_2} - \frac{N_2X_2}{N_3\varepsilon_3}\right) \tag{4.19}$$

$$c = \frac{-(N_2X_2)^2}{N_3\varepsilon_3} + \frac{X_2^2N_2}{\varepsilon_2} - \frac{2V_{tot}}{q}$$

It is possible to apply this approach to more complicated structures consisting of an arbitrary number of layers where there is only one *pn* junction. Because of the complexity of the algebra involved, utilizing Maple software is strongly suggested. In this case, the quadratic coefficients can be rewritten as:

$$a = N_m\left(\frac{1}{\varepsilon_m} - \frac{N_m}{N_n\varepsilon_n}\right)$$

$$b = 2Nm\sum_{k=m+1}^{n-1}\left(\frac{X_k}{\varepsilon_k} - \frac{N_kX_k}{N_n\varepsilon_n}\right) \tag{4.20}$$

$$c = \frac{-\left(\sum_{k=m+1}^{n-1}(N_kX_k)\ \right)^2}{N_n\varepsilon_n} + \sum_{k=m+1}^{n-1}\left(\frac{X_k^2N_k}{\varepsilon_k}\right)$$

$$+ \sum_{k=m+1}^{n-2}\left(2N_kX_k\sum_{1=k+1}^{n-1}\left(\frac{X_1}{\varepsilon_1}\right)\right) - \frac{2V_{tot}}{q}$$

where the width obtained by solving equation 4.18 is the depletion width in the outermost m_{th} layer on the *p*-side of the junction. On the other hand, since the charges on each side of the junction must be balanced, the depletion width in the outermost (n_{th}) layer on the n-side of the junction is calculated by:

$$X_n = -\frac{\sum_{k=0}^{n-1} N_k\, X_k}{N_n} \tag{4.21}$$

In order to achieve the previous calculations, the program must first identify the position of m and n layers in the structure, as well as which layers are completely depleted. To achieve that, the code is running in a loop. Initially, X_m and X_n are calculated for the nearest layers to the electrostatic junction. If these values are more than the thicknesses of the layers under consideration, the depletion of the next layers will be considered. It is important to know the order in which the layers are depleted. The next depleted layer can be identified by calculating the charge density on both sides of the junction. Then the range can be expanded on the side with less charge density.

Thereafter, the device capacitance can be calculated from:

$$C = \varepsilon_0 \varepsilon_r \, A/d$$ **4.22**

where A is the device area and, d is the total depletion thickness. Then, the electric field profile is determined by integrating the charge density over the depleted region.

If the electric field profile and the parameterised ionisation coefficients for the material employed have been determined, the multiplication characteristics of any structure can be investigated. Initially, the electric field profile is divided into small elements, with the electric field assumed to be uniform within each element. In addition, the ionisation coefficients are calculated for each element. In order to model multiplication and excess noise behaviour more realistically under consideration of the dead space effect, a full field dependence RPL model was developed from the model of reference [5], which was described in Section 2.2.3. The electric field profile is initially divided into smaller elements with the assumption that each element experiences a uniform electric field [6]. In addition, the ionisation coefficients and then the enabled ionisation coefficients are calculated for each element. Thereafter, for each element, the dead spaces for both electrons and holes can be calculated by the integration of the electric field profile, according to:

$$\sum_{x}^{x_k} \zeta(x)\,.\,d(x) = E_{th(e)} \qquad \sum_{x}^{x_k} \zeta(x)\,.\,d(x) = E_{th(h)}$$ **4.23**

where ξ is the electric field, $E_{th(e)}$ and $E_{th(h)}$ are the electron and hole ionisation threshold energies, respectively. The element's position is denoted by x, and x_k is the location at which the dead space associated with that element ends.

In a *p-i-n* (*n-i-p*) diode, for the pure electron (hole)-initiated multiplication, the electrons (holes) are injected at the beginning of the depletion region at *j* = 0. On the other hand, the holes (electrons) are injected at the end of the depletion region at *j*=d to obtain pure hole-initiated multiplication.

In the case of mixed injection multiplication, the injected electron and hole pair positions are randomised over the normalised absorption profile. First, the E_{start}, which is the first element where the electric field is higher than zero, was determined. For each element, the cumulative absorption probability according to Beer's law has been calculated. The cumulative absorption probability of E_{start} includes both its own absorption probability and the absorption in the neutral regions outside the space charge region within the electron diffusion lengths (l_e). In the same way, the cumulative absorption probability of E_{end-1} includes its absorption probability as well as the absorption in the neutral regions outside the space charge region within the hole diffusion lengths l_h. Then, once the absorption profile is known, it is normalized to find multiplication for exactly one injected electron-hole pair (at a time for the desired total number of iterations). Initially, a random number between 0 and 1 is chosen. A loop over the elements is used to identify the injected electron and hole pair position. When the random number is smaller than the normalized cumulative absorption probability of a given element, this element is the injected electron and hole pair position.

For each generated carrier, the ionisation probability is evaluated in a loop as the carrier travels through the diode structure. Initially, a random number between 0 and 1 is chosen. For each element, the probability of an electron ionising can be obtained from $P_x = \alpha_x^*. w_x$ where α_x^* is the enabled ionisation coefficient and w_x is the width of element x. The cumulative probability of an ionized electron at a given position, j, denoted by Cj, is then calculated utilising additional summation as follows:

$$C_j = P_j \,.\, \sum_{x}^{j-1}(1\text{-}P_x) \qquad \textbf{4.24}$$

If C_j is larger than r for the first time, the ionization must have occurred at position j. The value of multiplication starts with 1, and then it increases by 1 for each ionisation event. The same process was employed for the holes. Then, a further loop with a number of iterations is used to calculate $\langle M \rangle$, $\langle M^2 \rangle$, $\langle M \rangle^2$ and excess noise F, as described in Section 2.2.3 [6]. Finally, a loop is used to determine the values of these parameters as a function of the applied bias voltage. RPL can be used to calculate multiplication and excess noise factor under the approximations of the local model, by setting the threshold energies to zero.

4.6 References

[1] S. M. Sze, Y. Li, and K. K. Ng, *Physics of semiconductor devices*. John wiley & sons, 2021.

[2] S. Adachi, "GaAs, AlAs, and Al x Ga1− x As: Material parameters for use in research and device applications," *Journal of Applied Physics,* vol. 58, no. 3, pp. R1-R29, 1985.

[3] M. Woods, W. Johnson, and M. Lampert, "Use of a Schottky barrier to measure impact ionization coefficients in semiconductors," *Solid-State Electronics,* vol. 16, no. 3, pp. 381-394, 1973.

[4] G. Bulman, L. Cook, and G. Stillman, "The effect of electroabsorption on the determination of ionization coefficients," *Applied Physics Letters,* vol. 39, no. 10, pp. 813-815, 1981.

[5] D. Ong, K. Li, G. Rees, J. David, and P. Robson, "A simple model to determine multiplication and noise in avalanche photodiodes," *Journal of applied physics,* vol. 83, no. 6, pp. 3426-3428, 1998.

[6] A. P. Craig, *Novel structures for lattice-mismatched Infrared photodetectors*. Lancaster University (United Kingdom), 2016.

Chapter 5

Non-local Impact Ionization Coefficients in $Al_{0.8}Ga_{0.2}As$

5.1 Introduction

APDs are electronic devices which have the advantage of high signal-to-noise ratios because of their internal gain resulting from impact ionization. Impact ionisation is a critical semiconductor process that controls the internal gain and avalanche breakdown of avalanche photodiodes. Consequently, accurate knowledge of the electron and hole impact ionisation coefficients α and β, respectively, is necessary for semiconductor material characterization. The criteria used to judge the performance of an optical device for use in optical fibre communications include signal-to-noise ratio, speed, operating voltage, and temperature sensitivity. There are some techniques that can be used to improve the device's performance, including reducing the avalanche region's length. This technique can lead to many benefits, such as reducing avalanche noise, shorter carrier transit times which speed up the device and hence maximise the gain band width product, improved temperature stability, and reduced breakdown voltage and hence reduced operation bias voltage. In the short devices operating at higher electric fields, the non-local effect can be exploited. The dead space represents an increasing fraction of the mean ionisation path length. As a result, the ionisation process becomes more deterministic, reducing the randomness in the gain of each carrier and hence and reducing excess noise [1]. Using a III-V material such as $Al_{0.8}Ga_{0.2}As$, APDs can take advantages of the unique properties of these material as described in section 2.2.5. Due to the wide indirect band gap of $Al_{0.8}Ga_{0.2}As$, an extremely thin multiplication layer can be used without significant tunnelling. As a result, the earlier advantages of using thin multiplication width to improve the APD's performance can be strongly exploited. In order to simulate and further investigate of the various characteristics of these thin $Al_{0.8}Ga_{0.2}As$ APDs, it is crucial to extract the non-local electron and hole ionisation coefficients and threshold energies using a suitable model.

The local model was the first successful model for an APD [2]. In this model, the impact ionization probabilities of a carrier were assumed to depend only on the local field strength and not on its past history as regards the position of the ionizing carrier and the electric field profile. It has been shown that the local model can adequately describe the impact ionization in thick multiplication regions. Based on this model, the local electron and hole impact ionization coefficients of a wide range of $Al_xGa_{1-x}As$ alloys (x=0-0.8) have been reported [3],[4], [5], [6]. On the other hand, in a thin device, where the non-local nature of the ionization process becomes significant, this model overestimates the multiplication and noise and underestimates the gain-bandwidth product. As a result, there was a need for an improved model that accounted for the path that a carrier travels before gaining sufficient energy to ionize, which is called "dead space". One of the theories that considers the nonlocal nature of the ionization process is the history-dependent theory [7]. This theory has been validated by Monte Carlo simulation, which is the most complete way of modelling history-dependent ionization coefficients. Monte Carlo models of semiconductor carrier transport automatically incorporate dead space effects and can provide realistic information on their consequences for temporal statistics [8], [9], [10].

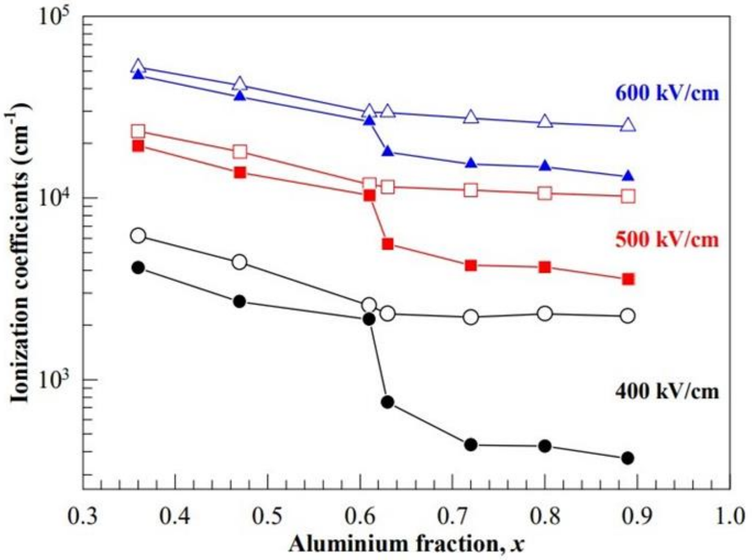

Figure 5.1: α (open symbols) and β (closed symbols) as a function of aluminium fraction for a range of electric fields [11].

Using the Monte Carlo model MC, the non-local electron and hole ionization coefficients and threshold energies for $Al_xGa_{1-x}As$, (x = 0-0.60) homojunction p^+-i-n^+ diodes with i-region thicknesses from 1000 nm to 25 nm have been extracted [12]. Consequently, it is possible to simulate multiplication and other APD properties within thin multiplication widths, accounting for the nonlocal nature of ionization within this range of Al composition. However, as shown in Figure 5.1, [11] when the Al fraction x<0.60, the electron-to-hole ionization coefficient ratio (α/β) is less than 2, which is not desirable. When x increases to just 0.62 a significant change is observed, α remains virtually constant while β suffers a sudden large drop. As a result, the α/β ratio becomes significantly greater than unity, more favourable for low noise APDs. The α/β ratio then continues to increase more slowly with Al fraction and was found to be greater than 10 for an 80% Al composition. This large α/β ratio, in combination with the previously mentioned large indirect bandgap suppressing tunnelling currents, mean that $Al_{0.8}Ga_{0.2}As$ offers highly desirable characteristics suited to high-speed, low-noise avalanche photodiodes, maximising the reduction in excess noise resulting from non-local ionisation effects. These advantages were evidenced experimentally by Ng *et al.* where the excess noise measurements for *p-i-n* and *n-i-p* $Al_{0.8}Ga_{0.2}As$ APDs with a wide range of multiplication widths (1200 nm- 20 nm) have been investigated [13]. The Low excess noise observed particularly in thin devices supports the large α/β ratio and shows the potential for exploiting thin AlGaAs multiplication regions in low noise APDs.

Consequently, this confirms the earlier mentioned need to get the non-local ionisation coefficient and threshold energies to simulate and properly develop thin $Al_{0.8}Ga_{0.2}As$ APDs and SPADs. Since MC modelling is time-consuming and very computationally intensive, an alternative and less computationally intensive model, such as the hard threshold dead space model can be used to investigate the effects of dead space on an APD. This model has been developed to simulate the impact ionisation process with sufficient physical accuracy, with those modelling a hard dead space displaced PDF proving to balance speed with accuracy. The two most widely used hard dead space models, RPL [14], [15], [16], [17] and recurrence [18], [19] , have been developed not only to simulate multiplication but many more important device characteristics, including excess noise, impulse response, and breakdown probability.

This chapter extracts the non-local ionisation coefficients using a variable field recurrence-based multiplication model [18] as well as an RPL model, via an evolutionary fitting algorithm.

5.2 Existing coefficients for $Al_{0.8}Ga_{0.2}As$

In 2001, Ng *et al*. [20] studied *p-i-n* and *n-i-p* diodes with a wide range of intrinsic widths, summarised in Table 5.1. Photomultiplication and capacitance-voltage data from this earlier study have been used in this new work. Ng *et al.* deduced ionisation coefficient in the electric field range 328 $kV\ cm^{-1} \leq \zeta \leq$ 1540 $kV\ cm^{-1}$and they applied a simple correction of Okuto *et al.* [21] that leads to a threshold energy. However, with only the first dead space considered, the energy fitted is not equivalent to that used by RPL or recurrence. As shown in Figure 5.2, based on the local model, Ng's coefficients with simple correction could successfully model the multiplication and breakdown in the thickest device (P1) without considering dead space. On the other hand, the multiplication values were slightly overestimated in the low-field range of the thinnest device (P5), where the dead space is significant.

Layer No.	**Doping type**	**Nominal i-region thickness (nm)**	**Fitted results**		
			Cladding doping p=n (×10^{18} cm^{-3})	**i-region doping (×10^{15}cm^{-3})**	**i-region thickness, w(nm)**
P1	*p-i-n*	1000	1.40	0.48	1024
P2	*p-i-n*	400	0.85	8.50	312
P3	*p-i-n*	100	0.625	1.00	100
P4	*p-i-n*	50	1.65	0.50	32
P5	*p-i-n*	25	1.64	6.00	15
N1	*n-i-p*	1000	1.64	0.51	1011
N2	*n-i-p*	100	1.60	9.50	88

Table 5.1: Measured and modelled parameters of the Al$_{0.8}$Ga$_{0.2}$As diodes [20].

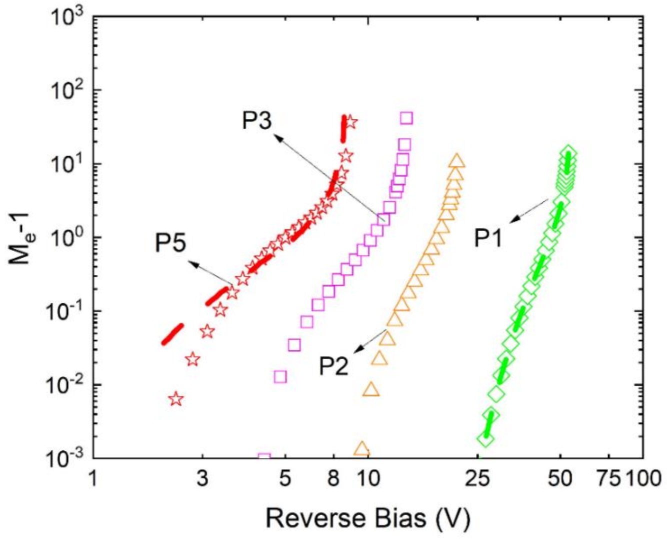

Figure 5.2: Electron-initiated multiplication as a function of the reverse bias voltage of the *p-i-n* diodes over a range of intrinsic width. Symbols represent experimental data, while dashed lines represent results calculated using the local model and a simple dead space correction [20].

In conclusion, these coefficients with the simple correction are able to successfully simulate the multiplication characteristics alone, for a wide range of intrinsic widths. However, as mentioned earlier, it is necessary to use more physically representative models such as RPL and recurrence models, not only to simulate multiplication but also several other crucial device properties such as impulse response, breakdown probability, and excess noise.

Given that Ng *et al.* proposed coefficients and threshold energies, these coefficients and threshold energies can be tested in a hard dead space model, such as the recurrence technique or RPL. An RPL model was used to simulate gain in the diode structures reported by Ng *et al.*, using their coefficients. As shown in Figure 5.3, in a device with the thickest multiplication regions (P1), where dead space is negligible, this approach is able to model the multiplication and breakdown accurately. However, as the multiplication region becomes thinner, the significance of dead space increases, and the simple correction no longer approximates the more physically representative hard dead space models. Consequently, if Ng's coefficients are applied in a hard threshold dead space model to simulate devices with thinner multiplication widths, the breakdown voltage becomes increasingly overestimated. Hence, it is necessary to determine revised nonlocal coefficients and threshold energies that are consistent with hard dead space models.

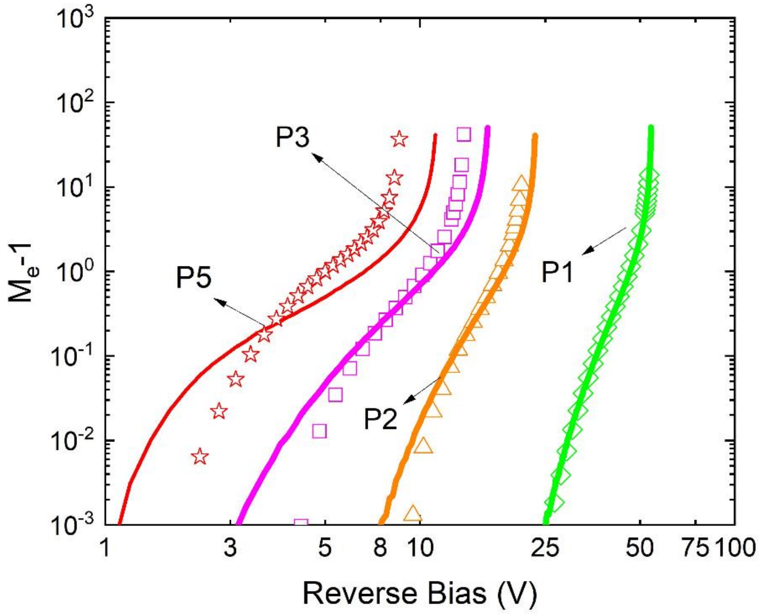

Figure 5.3: Electron-initiated multiplication as a function of the reverse bias voltage of the *p-i-n* diodes over a range of intrinsic width. Symbols represent experimental data, while solid lines represent results calculated using the RPL model with Ng's coefficients [20].

5.3 Experimental details

The details of growth, fabrication, and electro-optical characterization have been explained previously [20]. In summary, $Al_{0.8}Ga_{0.2}As$ *p-i-n* (*n-i-p*) diodes were grown by conventional solid-source molecular beam epitaxy on n+ (p+) GaAs substrates. The homojunction *p-i-n* and *n-i-p* devices have nominal intrinsic thicknesses of 1000, 400, 100, 50, and 25 nm, and 1000 and 100 nm, respectively. Circular mesa diodes were fabricated with diameters between 100 and 400 µm. Additionally, selected samples were back etched to allow optical access to both sides. Modelled fits to capacitance- voltage characteristics were used to determine the real structure of the diodes, which differed slightly from the nominal targets as shown in Table 5.1. Photomultiplication measurements were carried out using a 442 nm laser. Pure electron (hole)-initiated multiplication characteristics, M_e (M_h), were obtained using best-practise techniques, including the fitting of a primary photocurrent baseline, and they were extracted from the same diode using top and back-side illumination. This work was carried out previously by Ng *et al.* and his final data was used without reprocessing.

5.4 Ionisation coefficient fitting

For each of the diode structures, multiplication was calculated and compare with the experimental data to use in fitting the impact ionisation coefficients. Primarily, this was achieved using the RPL model, which was written and developed with genetic algorithm fitting procedure by Craig Adam and Collins Xiao. For a comparison, multiplication was also fitted independently by a researcher in the group using the recurrence technique with a hard threshold dead space, as described by Hayat *et. al*. [18]. As expected, given the equivalence of the models' approximations, the two methods give comparable coefficients.

5.4.1 Genetic algorithm fitting procedure

A modified chi-squared fitness function was defined, using logarithms of the simulated and measured M-1 data to ensure adequate weighting for points at the onset of gain and lower M-1. As shown in Figure 5.4, an evolutionary algorithm was utilised to simulate the electric field-dependent electron and hole impact ionization coefficients and threshold energies, through minimization of the fitness factor. To represent the thinnest devices as accurately as possible, a variable electric field profile has been considered rather than the simple, uniform electric field approximation made by Ng *et al.* This more accurately simulates the thin devices where a relatively significant thickness of the cladding layers has been depleted (given the <100 nm intrinsic widths), which makes the true electric field nonuniform [22].

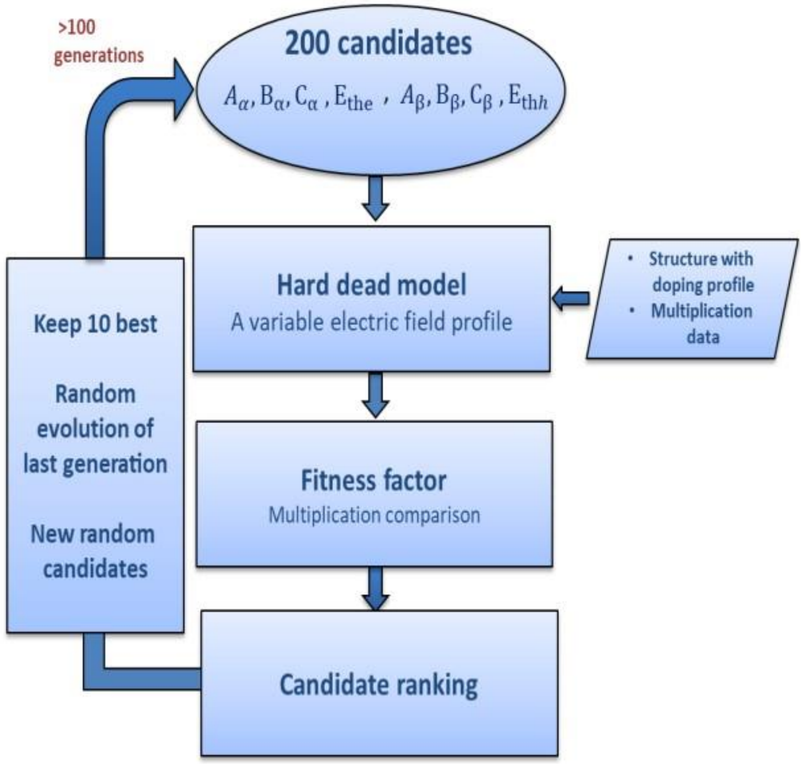

Figure 5.4: The genetic algorithm fitting process used to extract the non-local electron and hole coefficients and threshold energies of Al$_{0.8}$Ga$_{0.2}$As.

The input for fitting is the structure and the experimental multiplication data extracted by Ng *et al.* for each diode. Each candidate solution within the 200 populations is defined by A, B, and C, which give the parametrized ionization coefficients expressed by $\alpha(\beta) = A \exp\left[\left(\frac{B}{\zeta}\right)^{C}\right]$, and E_{th} for both electrons and holes. The fitting includes pure electron multiplications due to top illumination of 1000, 400, 100, 50, and 25 nm intrinsic width *p*-*i*-*n* diodes and due to back illumination of 1000 and 100 nm intrinsic width *n*-*i*-*p* diodes. Pure hole multiplication due to top illumination of 1000 and 100 nm intrinsic width *n*-*i*-*p* diodes and due to back illumination of 1000, 100, and 25 nm intrinsic width *p*-*i*-*n* diodes are also used. For each candidate solution, the parameters were used, for each device at each voltage value, to calculate the fitted multiplication M_{fit}. Then, the cumulative fitness factor was calculated from the difference between the fitted and experimental multiplication M_{exp} using a modified chi-squared fitness function χ^2as:

$$\chi^2 = \sum_{1}^{n}\sum_{V_{min}}^{V_{max}}\left(\log\left(M_{exp}(n,V)-1\right)-\log\left(M_{fit}(n,V)-1\right)\right)^2 \tag{5.1}$$

where n is the device number, V_{min} is the minimum voltage and V_{max} is the maximum voltage. Then, the populations were sorted starting with the candidate solution, which has the lowest fitting factor value. The best ten candidate solutions for the population were kept for the next generation, while some of the rests of the solutions were changed randomly to create evolved candidates and some of them were replaced with entirely new solutions. From rank 10-75, they were changed randomly within the range +/- 10%, around their values in the previous generation. From 75- 150, they were replaced with new solutions obtained by changing one of the five best solutions around their values, again by a randomly defined magnitude within the limited range of +/- 10%. From 150-200, they were replaced with new solutions obtained by changing the seed parameters randomly around their values within the range +/- 50 %. The seed parameters were those used to generate the initial population and were either taken from Ng's coefficients or an earlier fitting session. The fitting was repeated through multiple generations using newly evolved populations until the fitness factor stopped improving significantly.

As a test, I started the evolutionary fitting with constant α and β coefficients (equal to the coefficients reported by Ng *et al.*) and only allowed the electron and hole threshold energies to change. This fitting was attempted with all twelve multiplication data sets. It was found to be impossible to fit the multiplication of these devices without allowing the A, B, and C parameters in α and β to change. The fitness function did not improve through the 163 generations completed before the test was stopped. So, to achieve the fitting it is concluded that the A, B, and C parameters need to be changed in addition to the electron and hole threshold energies.

Where possible, it is desirable to have a single parameterisation of α and β that hold for the full electric field range under consideration. To test for the possibility of this, fitting was attempted using data from all twelve diodes, allowing the genetic algorithm to optimise only one set of α and β parameters. Despite the difference in fitting approach, compared to earlier work, a satisfactory fit could not be achieved as shown in Figure 5.5. Although it is worth noting that the approach does not yield an especially poor fit.

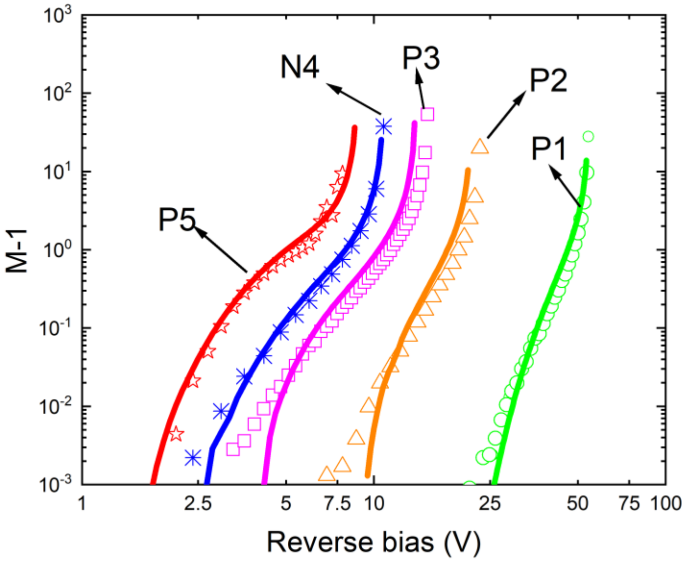

Figure 5.5: Electron and hole-initiated multiplication as a function of the reverse bias voltage of the *p-i-n* and *n-i-p* diodes over a range of intrinsic widths. The symbols represent the experimental data while the solid lines indicate results calculated using an RPL model where the fitting was attempted using data from all twelve diodes, allowing the genetic algorithm to optimise only one set of α and β parameters. Some datasets have been omitted for clarity [20].

To parameterize α and β across two ranges of the electric field, two fittings were carried out separately on thick diodes and thin diodes, representing low and high electric field ranges, respectively as shown in Figure 5.6. Populations were initiated with Ng's low and high field coefficients and evolved until the fitness factor stopped improving significantly. When using stochastic models, some fluctuation in the fitness factor is expected even when the best-fit parameters remain the same from generation to generation.

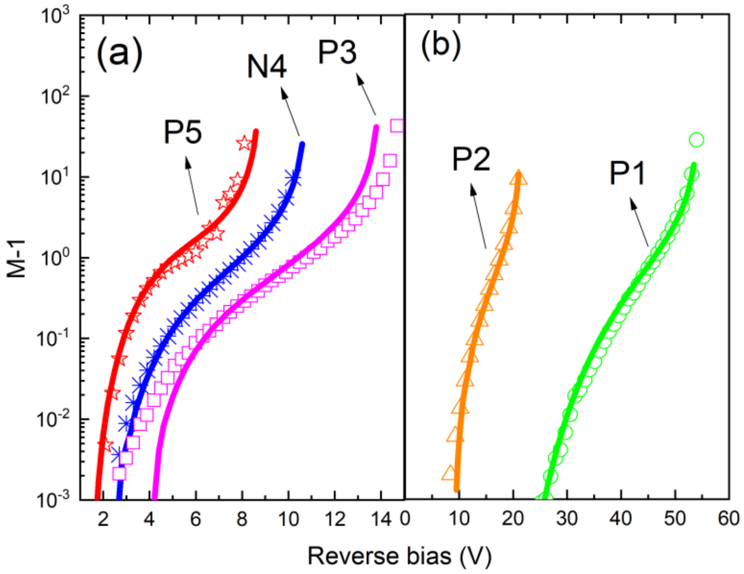

Figure 5.6: Electron and hole-initiated multiplication as a function of the reverse bias voltage of the *p-i-n* and *n-i-p* diodes over thin intrinsic widths (a) and thick intrinsic widths (b). The symbols represent the experimental data, while the solid lines indicate results calculated using the RPL model, where two fittings were carried out separately on thick diodes and thin diodes to parameterize α and β across two ranges of the electric field [20].

Unfortunately, independent low (<600 kV cm^{-1}) and high-field (>600 kV cm^{-1}) fittings yield coefficients that are non-continuous as shown in Figure 5.7.

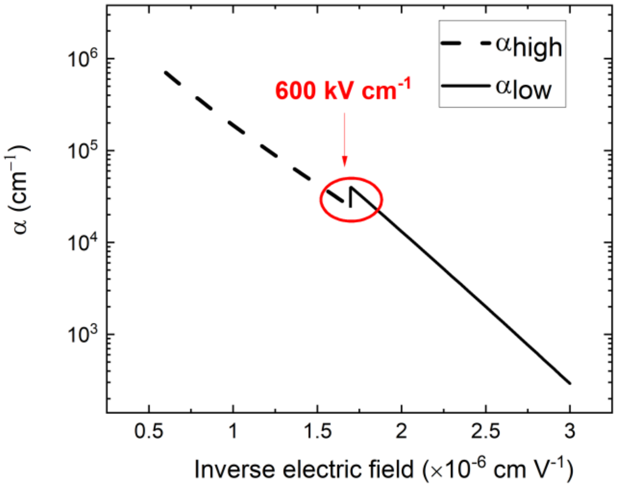

Figure 5.7: High and low electron impact ionisation coefficients (α) as a function of inverse electric field.

As result, these coefficients cannot simply be combined to cover the full electric field range as shown in Figure 5.8.

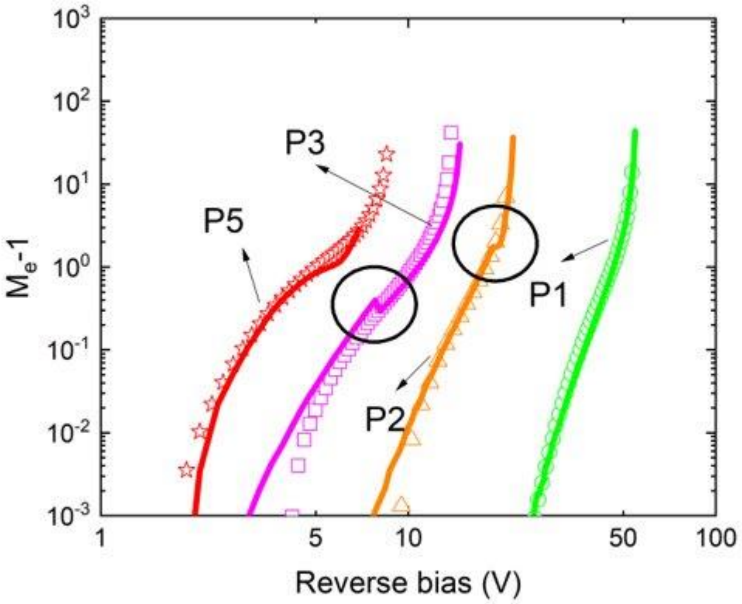

Figure 5.8: Electron-initiated multiplication as a function of the reverse bias voltage of the *p*-*i*-*n* diodes over a range of intrinsic widths. The symbols represent the experimental data, while the solid lines indicate results calculated using the RPL model. The discontinuity in the multiplication is attributed to the discontinuity in the coefficients resulting from the independent low- and high-field fitting. The same behaviour was observed in *n*-*i*-*p* diodes [20].

5.4.2 Fitting algorithm improvements

To obtain continuous coefficients, I did some changes to improve the fitting algorithm. A final fitting using data from all twelve diodes was performed, with candidate solutions extended to include two sets of electron and hole ionization parameters at low and high field range. Single threshold energies were maintained for electrons and holes, while the change-over electric field between the high and low ranges was included as an additional free parameter for both electrons ξ_{ch}(e) and holes ξ_{ch}(h). Hence, each candidate solution was defined by the parameters A_{low}, B_{low}, C_{low}, A_{high}, B_{high}, C_{high}, and E_{th} and the change over the field, for both electrons and holes. The candidate solutions were initiated with the output of prior high- and low-field fittings. The fitness function was modified to include a term χ' related to the continuity of α and β to avoid extracting discontinuous coefficients. This function was calculated from the difference of the log of α_{high} (β_{high}) and α_{low} (β_{low}) at a given change-over electric field for electron and hole as:

$$\chi' = abs[\log(\alpha_{\mathrm{low}}(\xi_{\mathrm{ch}}(\mathrm{e}))) - \log(\alpha_{\mathrm{high}}(\xi_{ch}(e)))] + abs[\log(\beta_{\mathrm{low}}(\xi_{\mathrm{ch}}(\mathrm{h}))) - \log(\beta_{\mathrm{high}}(\xi_{ch}(h)))] \tag{5.2}$$

Then, it was added to the cumulative fitness factor χ^2 calculated from the difference of the modelled and measured multiplication, described earlier. Since the magnitude of α and β is on the order of 10^4, the log was used to avoid this term dominating. Other refinements were made to the weightings within the fitness factor for some fitting sessions to ensure certain electric field ranges, for example, were given sufficient significance to drive the optimisation of the fit.

Since the low field range shows a more satisfactory fitting compared to the high field range, more improved fitting was achieved for the high field range by fixing the low field parameters and varying the high field ones. Figure 5.9 shows how these coefficients and threshold energies, as well as the change over the field for both electrons and holes, can adequately simulate the pure electron and hole multiplication for all diodes over the whole range of electric fields. For clarity and to avoid overlapping, some data sets have been omitted.

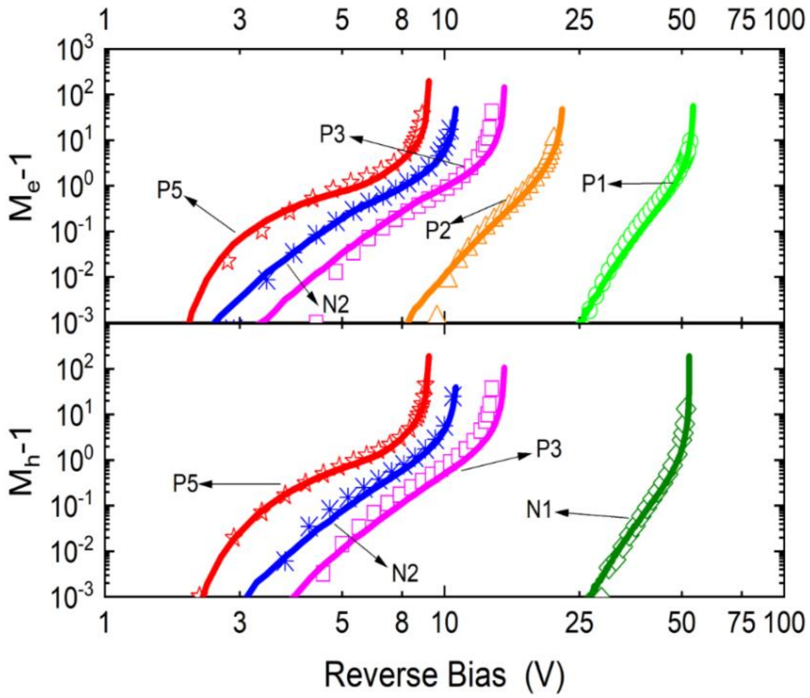

Figure 5.9: Pure electron multiplication M_e (top) and pure hole multiplication M_h (bottom) as a function of reverse bias voltage for *p-i-n* and *n-i-p* diodes over a range of intrinsic width. The symbols represent the experimental data while the solid lines indicate results calculated using an RPL model with the new non-local coefficients. M_e of top illumination of 50 nm *p-i-n* diode and back illumination of 1000 nm *n-i-p* diode as well as M_h of the back illumination of 1000 nm *p-i-n* diode have been omitted for clarity [20].

5.5 Result and discussion

Table 5.2 presents the fitted local (non-enabled) electron and hole impact ionisation coefficients together with the electron and hole threshold energies, $E_{th(e)}$ and $E_{th(h)}$. In combination these parameters allow simulation of the non-local impact ionisation in AlGaAs and hence are commonly referred to as the non-local ionisation coefficients. This convention is also followed in this thesis.

All parameters were fitted using a hard threshold dead space model, at high and low electric field ranges. The local coefficients α and β are fitted using the parameterized form (A, B, and C parameters) as a function of electric field, $\boldsymbol{\xi}$. Ng's coefficients were extracted based on considering the realistic electric field profile in all devices, particularly thin ones, using an improved technique by Grant [23]. In this work, the realistic electric field profile, which includes a peak electric field, was also taken into account using a variable electric field RPL model instead. The exponential field dependence of the coefficients ensures that the peak field has a significant contribution to the overall multiplication, even though it only occurs in part of the multiplication width. As a result, the peak field in the thinnest device at the maximum voltage value was considered as the highest limit in the electric field range for which the coefficients have been fitted, which is similar to what Ng *et al.* reported. On the other hand, the field obviously falls to zero in the real devices and the variable field RPL used, so in theory this work could quote coefficients to very low fields. This is dangerous since such low fields contribute very little to the multiplication so the fit can't be considered to force a reasonable value for α or β at low fields. In addition, since this work focuses on the high fields where the non-local nature is significant and the low fields can be covered adequately by the local model, it is safe to set the same low field limit value as reported by Ng *et al.*

Electron $\boldsymbol{\alpha}= \mathbf{A\,exp}\left[-\left(\frac{\mathbf{B}}{\xi}\right)^{\mathbf{C}}\right]$	**Hole** $\boldsymbol{\beta}= \mathbf{A\,exp}\left[-\left(\frac{\mathbf{B}}{\xi}\right)^{\mathbf{C}}\right]$
Low field $328\ \text{kV cm}^{-1} < \xi < 626\ \text{kV cm}^{-1}$ **A**= $1.12 \times 10^{7}\ \text{cm}^{-1}$ **B**= $3.23 \times 10^{3}\ \text{kV cm}^{-1}$ **C**= 1.039	Low field $328\ \text{kV cm}^{-1} < \xi < 676\ \text{kV cm}^{-1}$ **A**= $3.82 \times 10^{6}\ \text{cm}^{-1}$ **B**= $2.62 \times 10^{3}\ \text{kV cm}^{-1}$ **C**= 1.161
High field $626\ \text{kV cm}^{-1} < \xi < 1500\ \text{kV cm}^{-1}$ **A**= $6.41 \times 10^{6}\ \text{cm}^{-1}$ **B**= $6.46 \times 10^{3}\ \text{kV cm}^{-1}$ **C**= 0.685	High field $676\ \text{kV cm}^{-1} < \xi < 1500\ \text{kV cm}^{-1}$ **A**= $3.16 \times 10^{6}\ \text{cm}^{-1}$ **B**= $2.88 \times 10^{3}\ \text{kV cm}^{-1}$ **C**= 1.057
$\mathbf{E_{th(e)}} = 2.88\ ev$	$\mathbf{E_{th(h)}} = 2.94\ \text{eV}$

Table 5.2: The parametrized expressions for electron and hole impact ionisation coefficients, obtained using the hard threshold dead space model at low and high electric field ranges, as well as the electron and hole threshold energies.

The local α and β (non-enabled) extracted in this work are compared to Ng's coefficients, as a function of inverse electric field, in Figure 5.10. The figure illustrates how coefficients extracted using a non-local model (this work) and a local model [20] compare. It is clear that at low electric field range, α_{low} and β_{low} have a good agreement between the two models. On the other hand, at high field in thin devices where the effect of dead space is significant, α_{high} and β_{high} extracted with the hard dead space model are higher than those extracted with the local model. This behaviour is observed for other materials such as $Al_{0.6}Ga_{0.4}As$ as shown in Figure 5.11. The parameterized local α (non-enabled) extracted using the nonlocal model [12] is again higher than that extracted using the local one [5]. Note this work used a MC model, which accounts for dead space to a similar extent to the RPL model. It is common to report a local α and β, together with threshold energies for both electrons and holes, as an output when fitting with a non-local model.

As noted, before, in combination this output is often referred to overall as the non- local coefficients. Enabled coefficients $\alpha^*$and $\beta^*$are less often compared because they are calculated based on the specific ionization path length pdf assumed in the model (or models) for which they are reported. Hence, they are only comparable across models with the same founding assumptions. For example, RPL and recurrence can be compared because both the enabled coefficients are mathematically defined based on the ballistic hard dead space and displaced exponential pdf. Note, the enabled ionisation coefficients describe part of the non- local ionisation pdf and hence are not equivalent to the overall non-local ionisation coefficients.

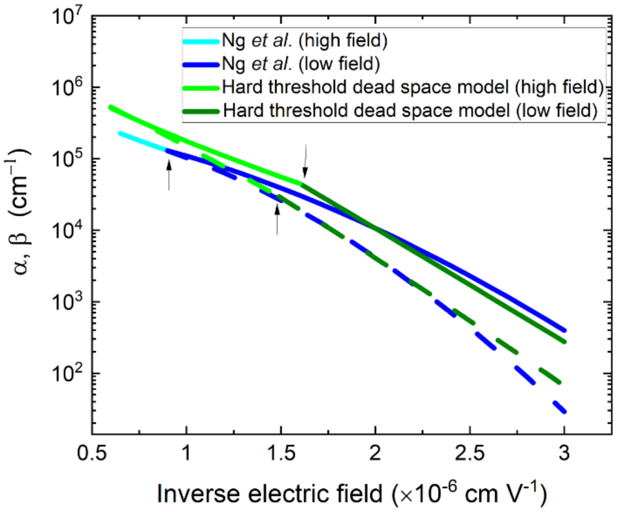

Figure 5.10: A comparison of the obtained local electron and hole impact ionization coefficients (non-enabled) for *p-i-n* diodes fitted using the hard threshold dead space model (green) with those reported from the local model of Ng *et. al*. (blue). The solid lines represent α, while the dashed lines represent β. The dark colour indicates the coefficients in the low electric field range, while the light colour indicates the coefficients in the high electric field range. The arrows show the break-electric field values [20].

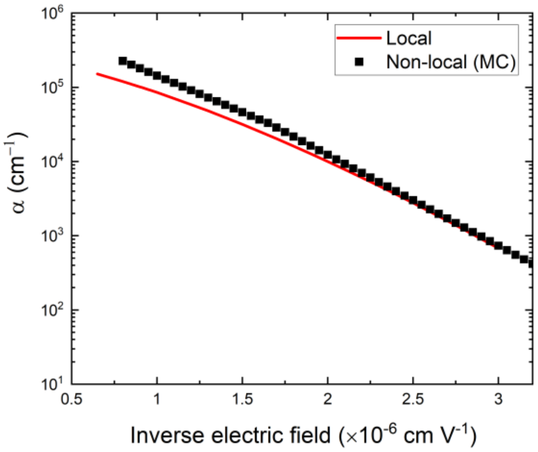

Figure 5.11: A comparison of the parameterised electron and hole impact ionization coefficients (non-enabled) for *Al0.6Ga0.4As* fitted using the Monte Carlo model (MC) [12] with those reported from the local model [5].

The local coefficients which Ng *et al.* determined and I then reported and compared with my new coefficients, were extracted from the multiplication characteristics at each voltage point, using the equations from the conventional local model [20]:

$$M_e(x,V) = \frac{1}{1 - \int_0^{w_T}\left[\alpha(x,V)\exp\left(-\int_0^{x}\left(\alpha(x,V) - \beta(x,V)\right)dx'\right)\right]dx} \tag{5.3}$$

$$M_h(x,V) = \frac{1}{1 - \int_0^{w_T}\left[\beta(x,V)\exp\left(\int_x^{w_T}\left(\alpha(x,V) - \beta(x,V)\right)dx'\right)\right]dx} \tag{5.4}$$

The resulting α and β are plotted against the inverse electric field as shown in Figure 5.12. As Ng *et al.* points out, extracting coefficients in this way relies on the assumption that it is possible to identify an extrapolated bulk value, with which the experimental coefficient data points will eventually converge. However, this convergence starts from significantly underestimated magnitudes, as much as 2 or 3 orders. Since the effect of dead space cannot be truly negligible, some underestimating of the coefficients is inevitable even when attempting to extrapolate, especially in the thinnest devices (at the highest electric fields). Since Ng's coefficients were initially extracted using the method outlined above, it is still expected that they will underestimate rather than overestimate the magnitude at the higher electric fields.

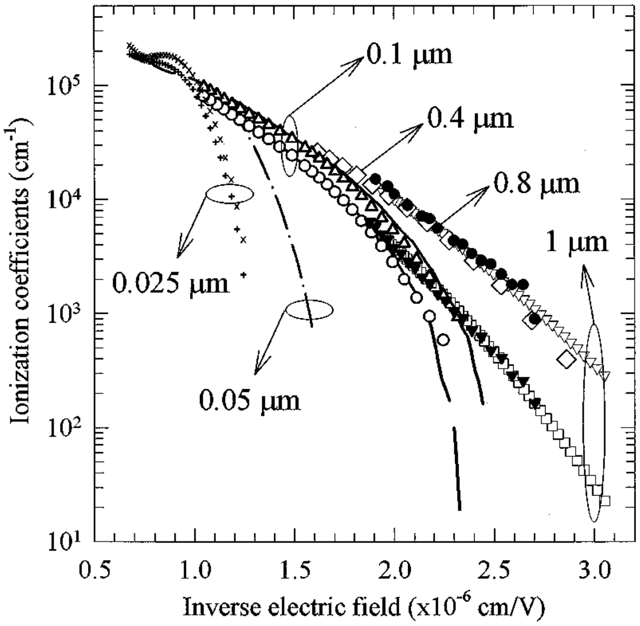

Figure 5.12: Ionisation coefficients extracted from M_e and/or M_h for diodes with a range of multiplication width. Adopted from [20], widths labelled correlate with the nominal intrinsic widths recorded in table 5.1 above [20].

To further investigate the significance of non-local effects, the ratio of the dead space to the electron ionisation path length ($d_e\alpha$) was calculated as a function of the inverse electric field, as shown in Figure 5.13. The maximum possible value for ratio is 1 when 1/α tends to equal the electron dead space, which means 1/α* tends to zero. This would be the limit case where the carriers ionised immediately after transiting the dead space. This limit case is obviously highly desirable since it represents full determinism, where the position of ionisation is no longer uncertain. The figure shows that at a low electric field, the ratio is small, and the dead space is negligible, but with increasing the electric field, the ratio increases, and the dead space becomes more significant, getting very close to the desirable limit case ($d_e\alpha = 1$), which will help achieve excellent low-noise multiplication. This confirms the significance of dead space at a high field observed in Figure 5.10.

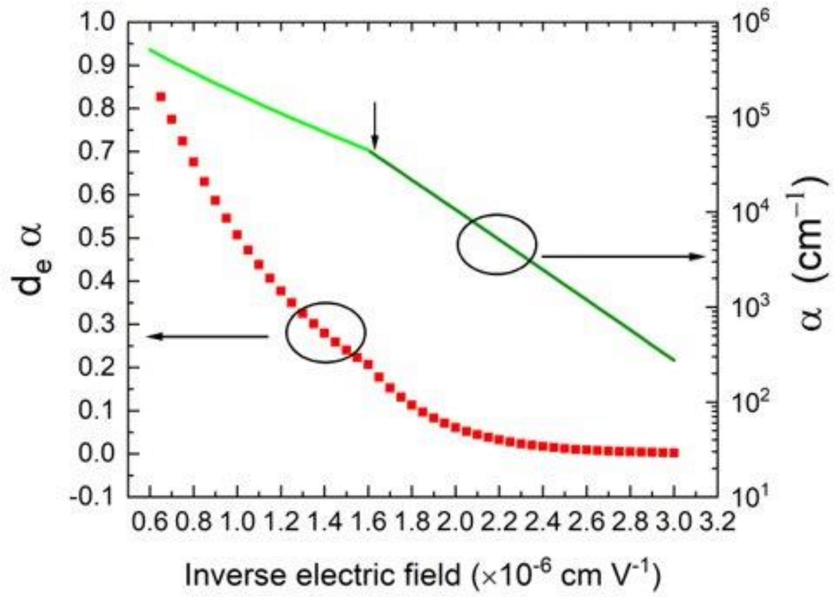

Figure 5.13: The ratio of dead space to the electron ionisation path length and the electron ionisation coefficient α as a function of the inverse electric field.

In order to illustrate the effect of the ratio on the excess noise within the RPL model, the excess noise factor as a function of multiplication for the 25 nm *p-i-n* diode from Ng *et al.* is shown in Figure 5.14. By ignoring the dead space effect, the RPL model can act as a local model, this condition was used to confirm the validity of the model. The excess noise factor was calculated at the two extreme cases of the local model when k equals 1 and 0, respectively. As shown in Figure 5.14, the simulated noise matches the respective McIntyre lines very well. Following this confirmation, the RPL model was used with the accurate new coefficients and threshold energies. As expected, the figure shows that the new coefficients can successfully simulate the experimental excess noise in the 25 nm *p-i-n* diode measured by Ng *et al.*

Starting with the new coefficients, the potential for affecting the noise can be explored. Firstly, by decreasing α and β, the electron and hole ionisation path lengths increase, and the dead space becomes less significant, and the avalanche of impact ionisation events become less deterministic. As a result, the excess noise increases toward the maximum limit noise in the local model at k = 1. Secondly, if α and β are increased, without changing the β/α ratio, the electron and hole ionisation path lengths decrease, and the dead space becomes more significant. Hence there is the potential for further reducing noise in thinner AlGaAs *p-i-n* diodes. $1/\alpha^*$ approaches zero when the coefficients are multiplied by a factor of 1.3 (shown in Figure 5.14), at which point the noise is reduced to be below F of 2 when the multiplication is up to ~15. Finally, to decrease noise even further, the β/α ratio would need to decrease. The figure also shows that when β equals 0, the diode can experience an excess noise factor < 2, which is the lowest limit in the local model. In fact, the excess noise factor becomes approximately equal to 1 in this hypothetical case, the ultimate theoretical limit, indicating almost perfect determinism.

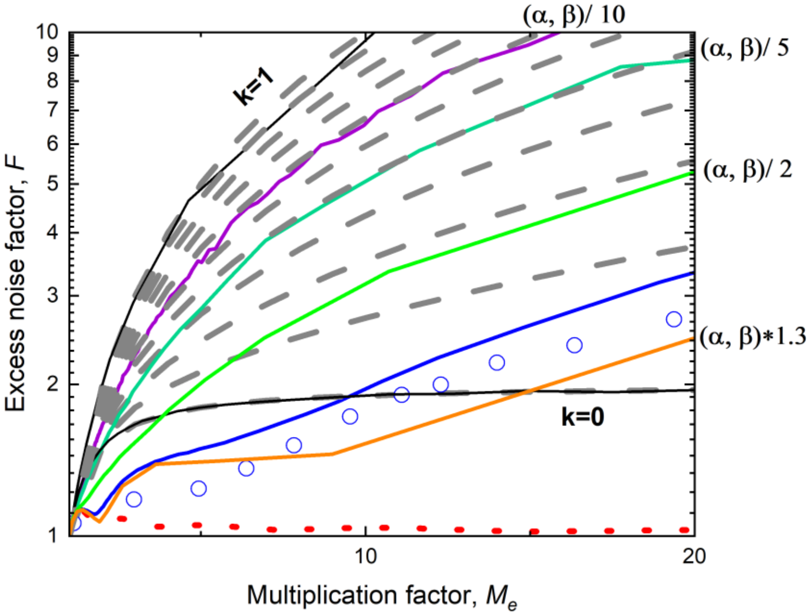

Figure 5.14: *F* versus *M_e* for the 25 nm $Al_{0.8}Ga_{0.2}As$ *p-i-n* diode (P5). Dashed lines are McIntyre's local predictions for k = 0 to 1 in steps of 0.1. The solid black lines represent the simulated noise for α = β and β = 0 validating the model. The open circles represent the experimental data, while the solid blue line represents the result calculated using the RPL model with the new coefficients and threshold energies. The other coloured solid lines show how the noise is affected by increasing or decreasing the magnitude of α and β. The red dots show the case where β alone is set to zero, further reducing noise towards the ideal limit.

In addition, the ionisation probability density function as a function of the ionisation path length at low (606 kV cm^{-1}) and high (1538 kV cm^{-1}) electric field values were calculated by:

$$P_e(x) = \begin{cases} 0, x \leq d_e^* \\ \alpha^* \exp[-\alpha^*(x - d_e^*)], \quad x > d_e^* \end{cases} \tag{5.5}$$

Figure 5.15 shows the dead space and the electron ionisation path length for both cases. With increasing the electric field, the dead space decreases linearly according to:

$$d_e = \frac{E_{the}}{\xi} \tag{5.6}$$

On the other hand, the ionisation path length decreases exponentially with the electric field. As a result, the significant of dead space at high electric field can explain how the extracted coefficients using the non-local model are higher than the extracted coefficients from the local model (Ng's coefficients).

In the case of a hole, since α and β converge at a high electric field, the same argument can be applied to the hole by substituting β, d_h, and $E_{th(h)}$. However, at low fields, due to the significant reduction in β compared to α, the ratio of the hole dead space to the hole ionisation path length is negligible.

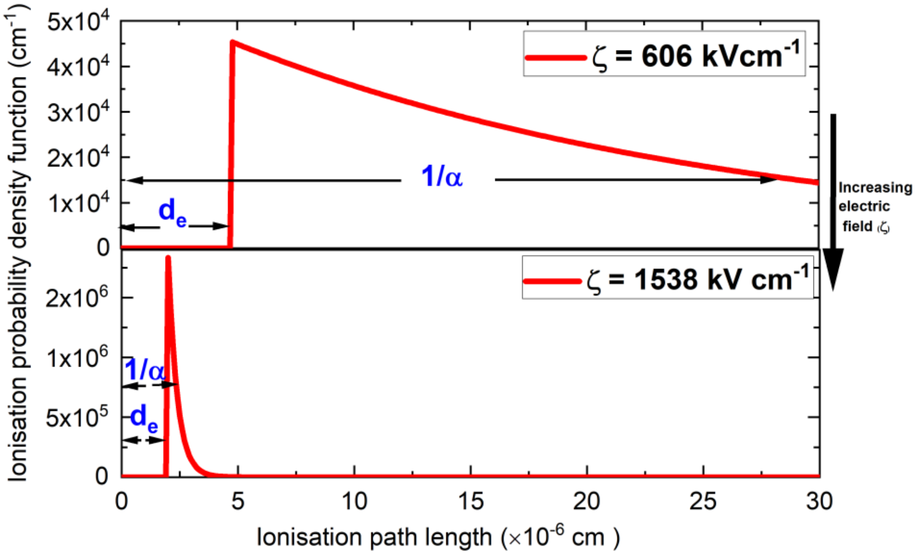

Figure 5.15: The ionisation probability density function as a function of the ionisation path length at 606 and 1538 kV cm^{-1}.

In order to further evaluate the new coefficients, Figure 5.16 shows a comparison with the extracted coefficients using the non-local model of $Al_xGa_{1-x}As$ with a range of different Al fractions (0%,30%, 60%)[12] . These coefficients were obtained based on MC model which is comparable to hard dead space models used in our work. It is obvious that with increasing the Al fraction, the electron and hole ionisation probability reduces. This is due to the increase of the band gap as the Al fraction increases [11]. The figure also confirmed the larger α/β ratio of $Al_{0.8}GaAs$ compared to $Al_{0.6}GaAs$, described earlier. As the figure shows, since the coefficients of all materials converge at a high field, the new coefficients were expected to converge too.

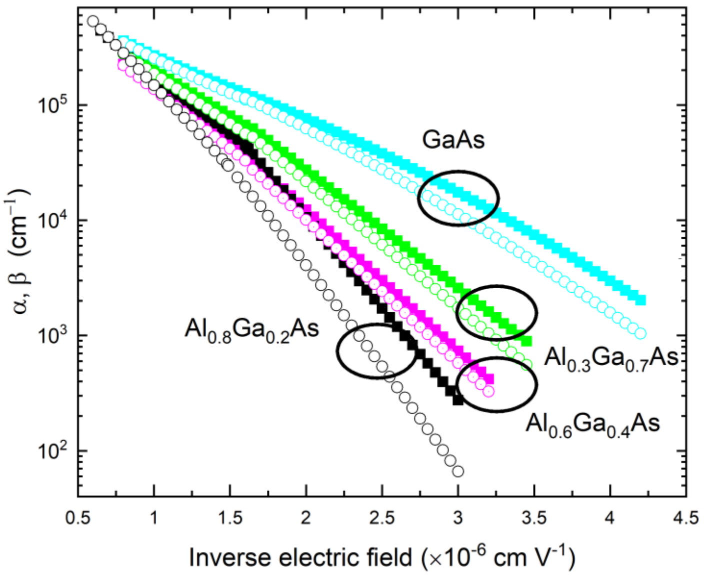

Figure 5.16: Electron and hole impact ionisation coefficients as a function of inverse electric field for $Al_xGa_{x-1}As$ with a range of Al fraction [12].

For further investigation, the ratio of the dead space to the electron ionisation path length for the same materials has been shown in Figure 5.17. As shown in Figure 5.1, from 0.3 to 0.6 the reduction in α is more significant than the negligible reduction from 0.6 to 0.8. As a result, from 0.3 to 0.6, the significance of dead space to the electron ionisation path length reduced significantly compared to the negligible reduction from 0.6 to 0.8. As the dead space for the different materials differs over an extremely small range where E_{the} changes in the range of 2.9–3.4, its effect on the ratio value can be negligible.

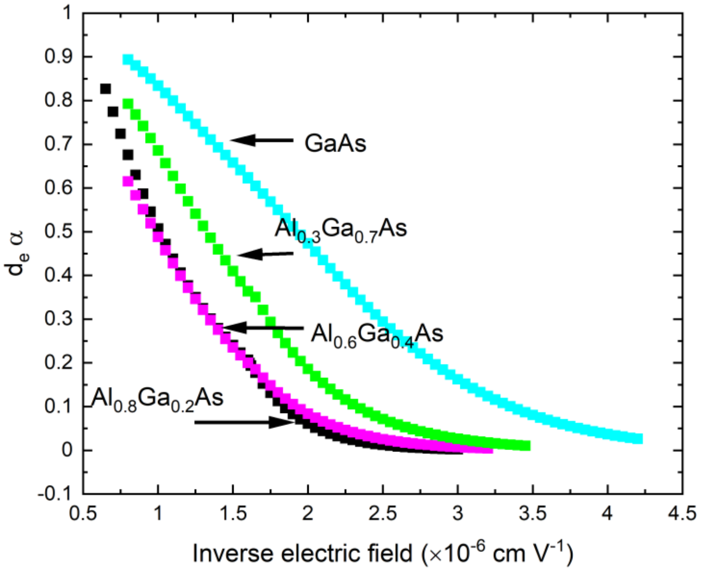

Figure 5.17: The ratio of the dead space to the electron ionisation path length as a function of inverse electric field for $Al_xGa_{x-1}As$ with a range of Al fraction.

5.6 Conclusion

In optical fibre communications and other optical applications, the APD's performance can be evaluated based on factors such as signal-to-noise ratio, speed, operating voltage rating, and temperature sensitivity. These factors can be improved by using a thin multiplication width. The wide indirect band gap of the $Al_{0.8}Ga_{0.2}As$ material allows for the fabrication of thin multiplication APDs with negligible tunnelling effects. As a result, by combining the large α/β ratio with the previously mentioned advantages of a thin multiplication layer, there is exciting potential to create high-speed and low-noise avalanche photodiodes with high gain bandwidth product, maximizing the desirable non-local ionisation effect. In this chapter, the local ionisation coefficient (non-enabled) and threshold energies of $Al_{0.8}Ga_{0.2}As$ were extracted using a hard dead space model for the first time. Both RPL and recurrence models have been used, and an equivalent result has been achieved. These coefficients enable accurate simulation of the multiplication and breakdown of $Al_{0.8}Ga_{0.2}As$ APDs, even those that are extremely thin with multiplication widths down to 25 nm with high electric field operation.

In the standard ideal case of the ideal *p-i-n* structure, with a need to have very high doping in the cladding layers (~10^{20} cm^{-3}), the new coefficient and threshold energies can accurately simulate a device with a multiplication width down to 50 nm. However, in practice, the highest possible doping of the cladding layers is lower, which allows to deplete a part of the cladding layers, increasing the depletion width and, hence reducing the non-uniform electric field. As a result, the reduction in multiplication due to decreasing the field can be compensated by the additional fraction of the depletion in the cladding layer, and so the breakdown can occur at a lower field than in the ideal case. As a result, these coefficients can simulate a realistic *p-i-n* diode with a multiplication width thinner than 50 nm. This can explain the validity of these coefficients to simulate the nominal 25 nm *p-i-n* diode from Ng *et al*. In Chapter 7, $Al_{0.8}Ga_{0.2}As$ SAM APD structures with 50 nm multiplication width will be investigated. Since the actual doping of the cladding layer is expected to be lower than in the ideal standard case, it is safe to use the new coefficients to simulate these devices.

In order to fit the electric field-dependent electron and hole impact ionization coefficients and threshold energies, an evolutionary algorithm was employed. The fitting was initiated with one set of parameters for electron and hole over the whole range of electric field for each candidate solution. Then, Independent low (<600 kV cm^{-1}) and high-field (>600 kV cm^{-1}) fittings were carried out on thick and thin sets of devices respectively results in noncontinuous coefficients. To improve the fitting and overcome the discontinuity, two sets of electron and hole ionization parameters at low and high field ranges were used as a candidate solution. In addition, the change-over electric field between the high and low ranges was included as an additional free parameter for both electrons and holes. Also, the fitness function was modified to include a term related to the continuity of α and β to avoid extracting discontinuous coefficients. Consequently, the fitting was improved, and the resultant coefficients and threshold energies successfully simulate the pure electron and hole multiplication for all diodes over the whole range of electric fields. Fitting the coefficients to the experimental data in this way included unprecedented degrees of freedom and hopefully represented the physical process in all important aspects. The degrees of freedom undoubtedly bring risk, with the fitted solution sure to be non- unique. However, many fitting sessions were run, including ones using the high- energy computing facility at Lancaster University, to rapidly progress through generations and include a large number of randomly generated/mutated candidates. This wide sampling of the candidate space gives good confidence that local minima have been avoided, combined with the use of two different models, overall, the presented coefficients are considered well optimised. It is hoped that future researchers will find the consideration of a representative non-uniform electric field profile and the inclusion of a fitted break electric field, to be an approach worth applying to future work extracting ionisation coefficients.

As explained earlier, the comparison emphasized that thin GaAs APD can achieve the highest ratio of dead space to the ionisation path length (α de). However, this advantage can not be exploited due to the significant tunnelling associated with this thin GaAs APD. On the other hand, a thin $Al_{0.8}GaAs$ APD can achieve a ratio close to the desirable limit, resulting in excellent low-noise multiplication with negligible tunnelling.

These coefficients help to prepare for characterising $Al_{0.8}Ga_{0.2}As$/GaInNAsSb APD and SPAD, which would have the ability to detect long wavelengths up to 1.5 μm. As a result, the desirable advantages of using such a long wavelength can be exploited in various applications, such as optical fibre communications and LIDAR. More investigation on the impact ionisation of GaInNAsSb and the optimal SAM APD structure will be discussed in detail in the next chapters.

5.7 Reference

[1] G. J. Rees and J. P. David, "Why small avalanche photodiodes are beautiful," in *Quantum Sensing: Evolution and Revolution from Past to Future*, 2003, vol. 4999: SPIE, pp. 349-362.

[2] R. McIntyre, "Multiplication noise in uniform avalanche diodes," *IEEE Transactions on Electron Devices,* no. 1, pp. 164-168, 1966.

[3] V. Robbins, S. Smith, and G. Stillman, "Impact ionization in Al x Ga1− x As for x= 0.1–0.4," *Applied physics letters,* vol. 52, no. 4, pp. 296-298, 1988.

[4] S. Plimmer *et al.*, "Impact ionization in thin Al x Ga 1− x As (x= 0.15 and 0.30) p-i-n diodes," *Journal of Applied Physics,* vol. 82, no. 3, pp. 1231-1235, 1997.

[5] S. Plimmer, J. David, G. Rees, and P. Robson, "Ionization coefficients in AlxGa1-xAs (x= 0-0.60)," *Semiconductor science and technology,* vol. 15, no. 7, p. 692, 2000.

[6] B. Ng, J. David, S. Plimmer, M. Hopkinson, R. Tozer, and G. Rees, "Impact ionization coefficients of Al 0.8 Ga 0.2 As," *Applied physics letters,* vol. 77, no. 26, pp. 4374-4376, 2000.

[7] R. McIntyre, "A new look at impact ionization-Part I: A theory of gain, noise, breakdown probability, and frequency response," *IEEE Transactions on Electron Devices,* vol. 46, no. 8, pp. 1623-1631, 1999.

[8] F. Ma *et al.*, "Monte Carlo simulation of low-noise avalanche photodiodes with heterojunctions," *Journal of applied physics,* vol. 92, no. 8, pp. 4791-4795, 2002.

[9] G. Dunn, G. Rees, J. David, S. Plimmer, and D. Herbert, "Monte Carlo simulation of impact ionization and current multiplication in short GaAs diodes," *Semiconductor science and technology,* vol. 12, no. 1, p. 111, 1997.

[10] D. Ong, K. Li, G. Rees, G. Dunn, J. David, and P. Robson, "A Monte Carlo investigation of multiplication noise in thin p/sup+/-in/sup+/GaAs avalanche photodiodes," *IEEE Transactions on Electron Devices,* vol. 45, no. 8, pp. 1804-1810, 1998.

[11] J. David and C. Tan, "Material considerations for avalanche photodiodes," *IEEE Journal of selected topics in quantum electronics,* vol. 14, no. 4, pp. 998-1009, 2008.

[12] S. A. Plimmer, J. David, R. Grey, and G. Rees, "Avalanche multiplication in Al/sub x/Ga/sub 1-x/As (x= 0 to 0.60)," *IEEE Transactions on Electron Devices,* vol. 47, no. 5, pp. 1089-1097, 2000.

[13] B. Ng, J. David, R. Tozer, M. Hopkinson, G. Hill, and G. Rees, "Excess noise characteristics of Al/sub 0.8/Ga/sub 0.2/As avalanche photodiodes," *IEEE Photonics Technology Letters,* vol. 14, no. 4, pp. 522-524, 2002.

[14] J. Ng *et al.*, "Effect of dead space on avalanche speed [APDs]," *IEEE Transactions on Electron Devices,* vol. 49, no. 4, pp. 544-549, 2002.

[15] D. Ong, K. Li, G. Rees, J. David, and P. Robson, "A simple model to determine multiplication and noise in avalanche photodiodes," *Journal of applied physics,* vol. 83, no. 6, pp. 3426-3428, 1998.

[16] M. Soroosh, M. K. Moravvej-Farshi, and K. Saghafi, "A simple empirical model for calculating gain and excess noise in GaAs/AlξGa1-ξAs APDs (0.3≤ ξ≤ 0.6)," *IEICE Electronics Express,* vol. 5, no. 20, pp. 853-859, 2008.

[17] A. Pilotto *et al.*, "An improved random path length algorithm for pin and staircase avalanche photodiodes," in *2018 International Conference on Simulation of Semiconductor Processes and Devices (SISPAD)*, 2018: IEEE, pp. 26-30.

[18] M. M. Hayat, B. E. Saleh, and M. C. Teich, "Effect of dead space on gain and noise of double-carrier-multiplication avalanche photodiodes," *IEEE transactions on electron devices,* vol. 39, no. 3, pp. 546-552, 1992.

[19] K. M. Van Vliet, A. Friedmann, and L. M. Rucker, "Theory of carrier multiplication and noise in avalanche devices—Part II: Two-carrier processes," *IEEE Transactions on Electron Devices,* vol. 26, no. 5, pp. 752-764, 1979.

[20] B. Ng *et al.*, "Avalanche multiplication characteristics of Al/sub 0.8/Ga/sub 0.2/As diodes," *IEEE transactions on electron devices,* vol. 48, no. 10, pp. 2198-2204, 2001.

[21] Y. Okuto and C. Crowell, "Threshold energy effect on avalanche breakdown voltage in semiconductor junctions," *Solid-State Electronics,* vol. 18, no. 2, pp. 161-168, 1975.

[22] M. Mitchell, *An introduction to genetic algorithms*. MIT press, 1998.

[23] W. Grant, "Electron and hole ionization rates in epitaxial silicon at high electric fields," *Solid-State Electronics,* vol. 16, no. 10, pp. 1189-1203, 1973.

Chapter 6

Avalanche multiplication characteristics of dilute nitride diodes

6.1 Introduction

The dilute nitride $Ga_{0.8}In_{0.2}N_{0.05}As_{0.94}Sb_{0.01}$, hereafter referred to as GaInNAsSb, is an interesting material system because a small incorporation of nitrogen N and Sb makes the energy band gap drop by a significant amount, whilst allowing the alloy to remain lattice matched to GaAs. In this chapter, the multiplication characteristics and the impact ionisation behaviour of dilute-nitride photodiodes have been investigated. From the photomultiplication measurements, the effective impact ionization coefficients in GaInNAsSb have been determined, the first time for the Sb containing penternary form of this alloy. Additional knowledge of the impact ionisation behaviour of dilute nitride might facilitate the evaluation of device performances such as breakdown voltage, avalanche multiplication, and excess avalanche noise. Hence this work provides a foundation from which AlGaAs/GaInNAsSb SAM APDs could be developed in the future.

The multiplication measurements were carried out on GaInNAsSb *p-i-n* and *n-i-p* diodes at room temperature, approximately 300K, referred to campaign one in [1]. The diodes were grown by IQE in the US, using molecular beam epitaxy (MBE), and the designed structures of the diodes are shown in Figure 6.1. The modelled band structure of a homojunction GaInNAsSb *p-i-n* diode at zero bias is shown in Figure 6.2.

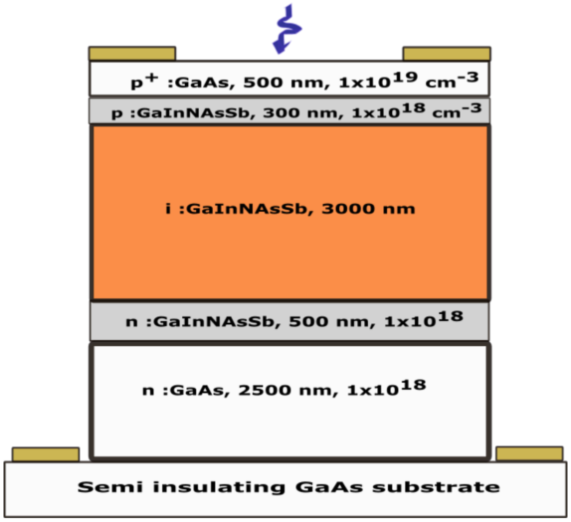

Figure 6.1: The designed structure of the GaInNAsSb *p*-*i*-*n* diode. The *n*-*i*-*p* diode was grown with the same doping concentration but with the opposite doping type.

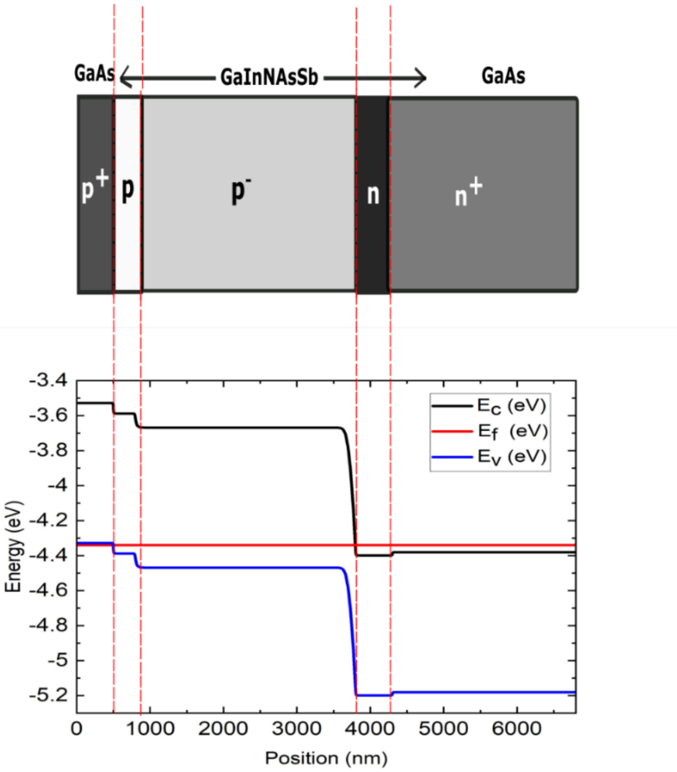

Figure 6.2: The energy band diagram of a homojunction *p*-*i*-*n* diode with zero bias voltage.

6.2 Electrical Characterizations

6.2.1 C-V measurements

CV measurements were carried out on *n-i-p* and *p-i-n* diodes for different device areas. The CV profile of the diodes was found to be proportional to the device area, indicating that they are well isolated. Then, the capacitance density has been fitted to identify the *p*, *n*, and *i*-region doping concentrations. Figure 6.3 shows the experimental and modelled capacitance densities as a function of the reverse bias voltage of different diameters *n-i-p* and *p-i-n* diodes. When operating at high voltages, leakage current increases, which causes errors in the capacitance inferred by the LCR meter based on its assumption of a two-component equivalent circuit. Hence fitting was limited to the data below ~-10 V. Table 6.2 summarises the fitted structures determined from the CV profiles.

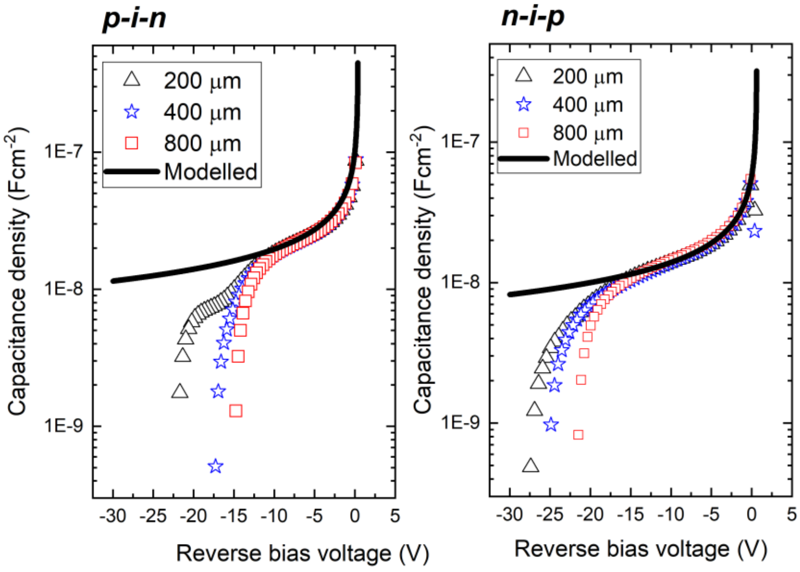

Figure 6.3: Measured (symbols) and modelled (solid line) CV characteristics of the GaInNAsSb *p-i-n* and *n-i-p* diodes.

Layer	**Material**	**Thickness (nm)**	**Doping Concentration (cm^{-3})**	
			p-i-n	***n-i-p***
5	GaAs	500	(p$^+$) 1×10^{19}	(n$^+$) 1×10^{19}
4	GaInNAsSb	300	(p) 1×10^{18}	(n) 0.2×10^{18}
3	GaInNAsSb	3000	(p$^-$) 4.4×10^{16}	(p$^-$) 2.5×10^{16}
2	GaInNAsSb	500	(n) 2×10^{18}	(p) 1×10^{18}
1	GaAs	2500	(n) 1×10^{18}	(p) 1×10^{18}
Semi Insulating GaAs substrate				

Table 6.1: The fitted structure of GaInNAsSb *p-i-n* and *n-i-p* diodes.

The capacitance-voltage characteristics for both *p-i-n* and *n-i-p* diodes were measured and then compared to that calculated using an electrostatic model, described in Section 4.5, and the designed structure given in Figure 6.1 The input devices were subsequently modified to match the experimentally measured CV, confirming a precise knowledge of the device structures as shown in Table 6.1. This fitting showed that the dilute nitride alloy has relatively high unintentional doping. This is normal in five-component materials such as GaInNAsSb due to the native growth defects. After the growth, both diodes were annealed by IQE at 785 °C. Trials made by IQE found this temperature showed the highest photoluminescence intensity. The annealed samples display a significant reduction in dark current compared to the unannealed ones, indicating significant success in improving the material by annealing, as shown in Figure 6.4 [1]. The dark current is an order of magnitude lower than that previously found in a similar band gap GaInNAsSb *p-i-n* [2]. The annealed band gap of the GaInNAsSb *p-i-n* and *n-i-p* diodes were found to be 0.796 eV and 0.807 eV respectively [1]. It is highly preferable to reach a band gap of 0.8 eV or a little less, to achieve a high absorption coefficient at 1550 nm.

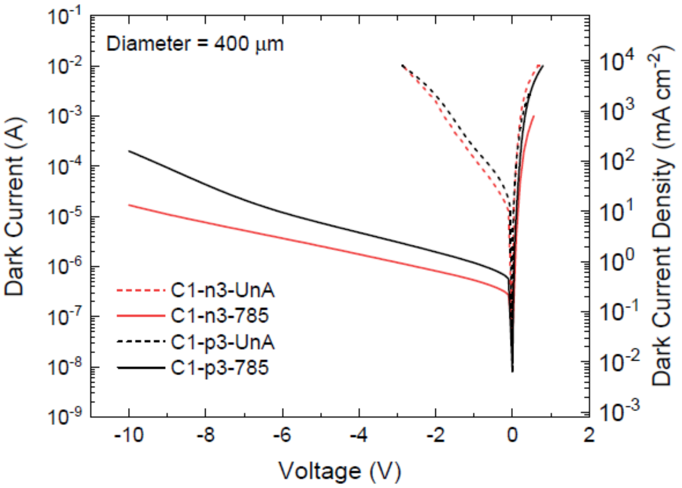

Figure 6.4: The current-voltage characteristics of GaInNAsSb *p-i-n* (C1-P3-785) and *n-i-p* (C1- n3- 785) diodes. The solid lines represent annealed devices and dashed lines represent unannealed devices. Adopted from [1].

Although annealing is used to reduce lattice defects, excessive annealing can ultimately lead to the formation of new defects and increases in unintentional doping and the dark current. Due to variations in the alloy's composition and growth conditions, the optimal annealing conditions cannot be applied similarly across the GaInNAsSb alloy range, instead they vary for specific band gaps and compositions [1].

Moreover, annealing can change the overall type of unintentional doping in the intrinsic region and hence the position of the electrostatic junction. To improve the quantum efficiency, it is preferable for the junction to be at the top of the diodes to collect more photogenerated carriers. However, controlling the anneal to select the background doping type without compromising leakage current or doping concentration is difficult. The electric field profiles for *p-i-n* and *n-i-p* diodes at different applied voltage values were calculated from the depletion width as described in Section 4.5 and shown in Figures 6.5 and 6.6, respectively.

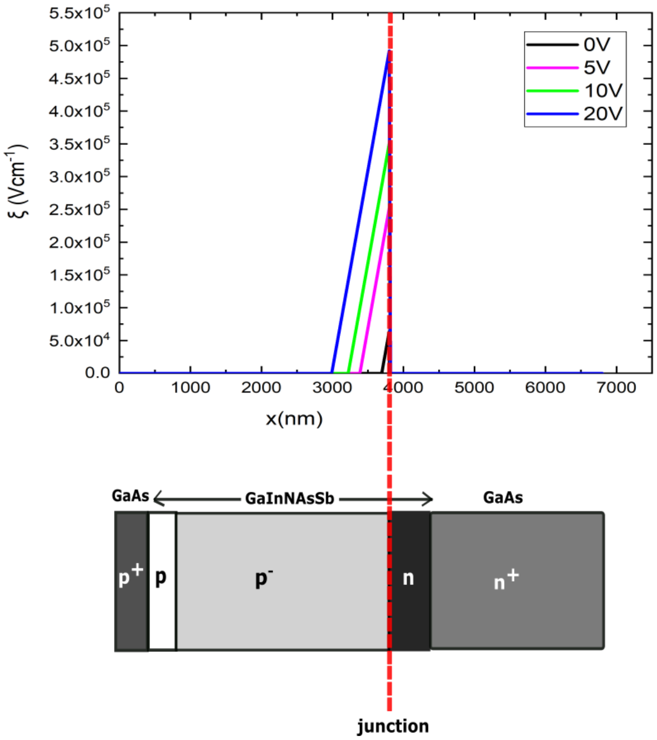

Figure 6.5: Calculated electric field profile in the GaInNAsSb *p-i-n* diode.

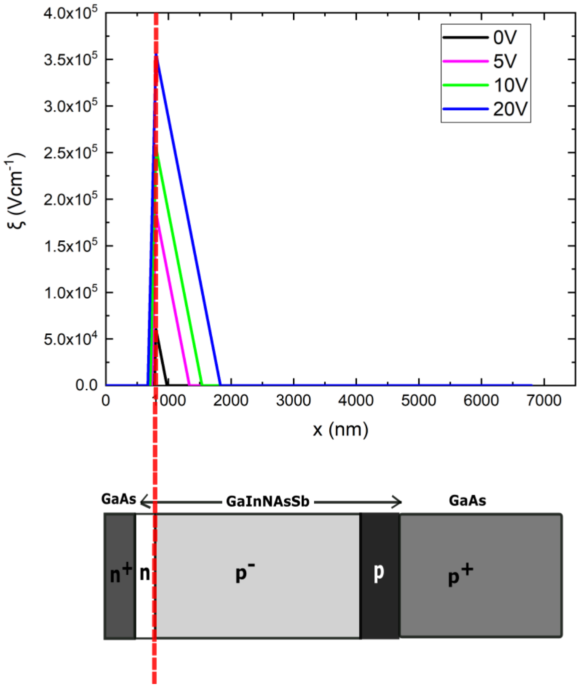

Figure 6.6: Calculated electric field profile in the GaInNAsSb *n-i-p* diode.

6.2.2 I-V Measurements

The measurements of the forward and reverse dark current-voltage (IV) characteristics were carried out using Keithley 2400 Source meter, which was connected to a desktop computer.

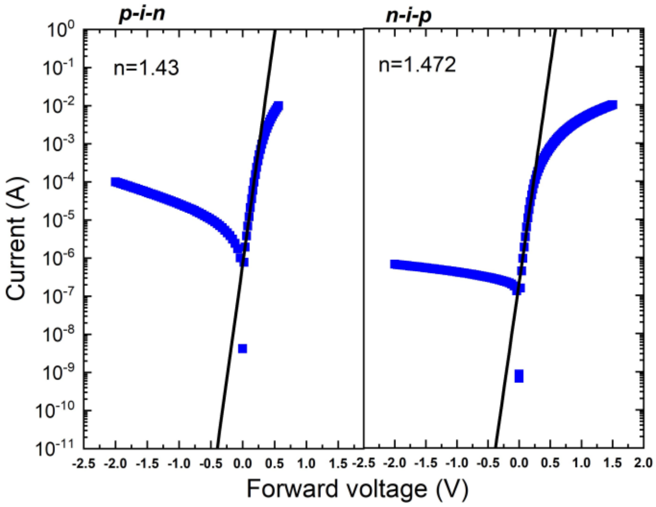

Figure 6.7: Forward IV characteristics of 400 µm diameter *p-i-n* and *n-i-p* diodes. The solid line represents the ideal case with a contact resistance equal to 0.

Although an APD typically functions under reverse bias conditions, the initial measurement conducted on a newly manufactured device involves a forward current- voltage (IV) measurement. This initial evaluation is performed to quickly evaluate the material properties and contact characteristics. Forward I-V measurements for 400 µm diameter *p-i-n* and *n-i-p* diodes have been investigated in order to evaluate the diodes, as shown in Figure 6.7. The solid line represents the ideal case with zero contact resistance. For both diodes, the ideality factors are closer to 1 than 2, indicate relatively low contribution from generation and recombination mechanisms and hence relatively good material quality. It also indicates that the doping in the diode's doped cladding layers is high enough, and the diffusion current is dominant.

The dark current density for both diodes is shown in Figure 6.8. It was demonstrated previously[1]that the dark current scaled with the area which indicates bulk- dominated currents rather than surface currents.

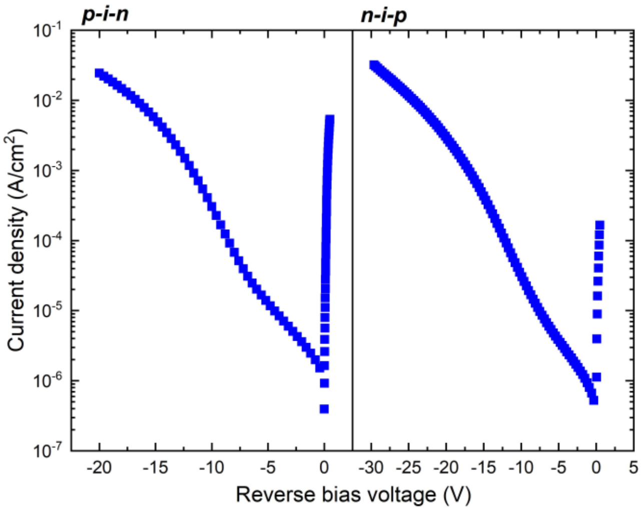

Figure 6.8: The dark current density characteristics of 100 μm diameter *p-i-n* and *n-i-p* diodes.

6.3 Factors affecting photomultiplication characteristics

In order to investigate the multiplication characteristics and understand the ionisation behaviour of this dilute nitride, homojunction *p-i-n*, and *n-i-p* diodes have been used. In this chapter, the impact ionisation of GaInNAsSb has been discussed theoretically and demonstrated experimentally. The impact ionisation on other compositions of dilute nitride has been discussed in the earlier literature review in Section 3.4.2. This specific work was started by Dr Collins as a small part of his research in the same group at Lancaster University [1]. He tried to obtain pure electron (hole) initiated multiplication characteristics M_e (M_h) for GaInNAsSb *p-i-n* (*n- i-p*) diodes by illuminating the top cladding layer with a 532.5 nm laser source. Thereafter, using the RPL model [3] and capacitance fitting, an evolutionary fitting algorithm was applied in an attempt to obtain the electron and hole impact ionization coefficients of GaInNAsSb. This method successfully fitted the impact ionization coefficients of $Al_{0.9}Ga_{0.1}As_{0.08}Sb_{0.92}$ for three different diodes [4]. However, the impact ionisation coefficients could not be determined successfully for GaInNAsSb using this method. The many potential reasons for this are discussed below.

6.3.1 Photon recycling

Photon recycling (re-emission) could be responsible for initiating some of the multiplication in both the *n*-*i*-*p* and *p*-*i*-*n*, structures, when absorption is confined to the layers above the depletion edge, leading to mixed injection multiplication rather than the intended pure initiated multiplication. Radiative recombination of photo- generated carriers can occur in the undepleted part of the upper cladding layers or unintentionally doped region, resulting in re-emission in any direction at a wavelength corresponding to the bandgap energy of these layers. This radiation can be re-absorbed in the rest of the structure, resulting in the creation of electron-hole pairs. If the re-absorption takes place in the depleted part of the structure (GaInNAsSb), electrons, and holes can be injected inside the depletion region in both diodes, resulting in mixed injection multiplication. Such re-absorption might increase below-band gap absorption or decrease above-band gap absorption with increasing reverse bias due to Franz-Keldysh electro-optical absorption, depending on the emitted photon's energy.[5] If the photons emit from the upper GaAs layer with energy significantly above-band gap absorption, the F-K effect is negligible. This is because the F-K effect is only significant around the band gap energy. On the other hand, if the re-emission takes place in the undepleted part of either the *p*-doped or unintentionally doped GaInNAsSb layers, the photon energy can be above or below band gap absorption, depending on the type of recombination transition. As a result, more investigation is needed to identify the dominant recombination transition. On the other hand, if the re-absorption occurs below the depletion region, electrons and holes in *n*-*i*-*p* and *p*-*i*-*n* diodes, respectively, can be injected into the depletion region. This is even more deleterious to the analysis, since it results in the opposite type of carrier being injected, compared to the original expectation.

The risk of re-emission in a *p*-*i*-*n* diode is higher than in a *n*-*i*-*p* diode. Since the intrinsic region is unintentionally doped *p*-type, the junction is located at the top of the *n*-*i*-*p* diode, whereas it is far from the surface in the *p*-*i*-*n* diode. As a result, in the *n*-*i*-*p* diode, the minority carriers only need to diffuse through, at most, 500 nm of GaAs and 300 nm of n-type GaInNAsSb in order to reach the electric field. On the other hand, in the *p-i-n* diode, the minority carriers must diffuse further through the majority of the 3000 nm intrinsic layer as well. Therefore, the vast majority of carriers are likely to recombine before reaching the electric field region, reducing the number of collected carriers and lowering the quantum efficiency. Compared to the *n-i-p* diode, the quantum efficiency of the *p-i-n* diode is indeed found to be lower, confirming that the risk of re-emission and re-absorption is higher. For example, by using a 405 nm laser source at 5 V, the quantum efficiency of the *n-i-p* diode is ~9.3%, while it is only ~0.7% for the *p-i-n* diode. Thus, almost pure hole-initiated multiplication can be expected for the *n-i-p* diode, whereas for the *p-i-n* diode, the multiplication initiated with a strongly absorbed visible wavelength is likely due to substantially mixed injection, rather than the desired pure-initiated electron multiplication.

Where re-absorption occurs, dealing with the mixed injection multiplication as a pure initiated multiplication provides an incorrect interpretation of the impact ionisation behaviour and hence inaccurate values for electron and hole impact ionisation coefficients when included in the fitting. In order to accurately determine the value of electron and hole impact ionisation coefficients using pure electron and hole-initiated multiplication, it is necessary to confirm the purity and eliminate this source of mixed injection. Other researchers have tackled this issue before. Bulman *et al.* [6] attempted to obtain pure carrier injection for the determination of electron and hole impact ionisation coefficients in InP. Because in InP the impact ionisation coefficient for holes is larger than for electrons, the pure initiated multiplication for holes was expected to be higher than for electrons. On the other hand, the risk of re-emission in the case of pure electron injection under back illumination was higher than in the case of the top pure hole injection. Based on their structure, the diffusing of the electrons and, hence, collecting them in the depletion region was difficult compared to the holes for two reasons. The width of the bottom p^+ cladding layer was thicker compared to the electron diffusion length of the material. In addition, the doping concentration of the p^+ bottom cladding layer was higher than in the top n^+ cladding layer, so the depletion is not wide enough for the electrons to be collected. Consequently, the measured electron pure-initiated multiplication was more mixed than the measured hole- initiated multiplication. Because of this, the predicted value of the electron ionisation coefficient would have been higher and the value of β/α ratio smaller. Therefore, the device structure was modified to minimise the effect of this contamination.

The ideal case for the best fitting of the alpha and beta can be achieved under two conditions, set out in 6.3.2 and 6.3.3 below.

6.3.2 Electric field profile

The first condition is that devices be grown with a small intrinsic layer with low doping concentration and, hence, a uniform electric field. In this case, at each voltage value, the electric field is uniform, and one value of alpha and one value of beta can be used to fit the corresponding multiplication. On the other hand, as GaInNAsSb is a five- component alloy, it is normal to have high unintentional doping concentration, as illustrated in detail by X. Collins [1]. As shown in Figures 6.5 and 6.6, due to the thick intrinsic layer of *p-i-n* and *n-i-p* diodes (3000 nm) having a relatively high doping concentration, the intrinsic region is not completely depleted, and the electric field profile in the devices is triangular with the maximum magnitude of the field at the junction and gradually decreasing into the depletion region. In the simulation, at each voltage, the electric field profile breaks down into many thin elements where the electric field is assumed to be uniform within each element. For each element, the candidate solution consisting of A, B, C, and E_{th} for both electrons and holes is used to calculate alpha and beta. So, each element has its own electric field and ionisation coefficients, and rather than calculating the multiplication related to a single value of alpha and beta, the calculated gain is a result of all different values of alpha and beta at the different fields. As a result, at each voltage value, it is difficult to fit the experimental multiplication using a single candidate solution. Consequently, a more advanced model with a more open-fitting algorithm is required.

Although not entirely new, it is rare to fit the measured multiplication and excess noise characteristics using the non-uniform electric field profile. Ng *et al.* attempted to use the nonuniform electric field profile to fit the measured multiplication and excess noise characteristics of 4H-SiC APDs in order to extract the (enabled) ionisation coefficients and the ionisation threshold energies [7]. In addition, X. Collins reported the impact ionisation coefficients of the quaternary alloy $Al_{0.9}Ga_{0.1}As_{0.08}Sb_{0.92}$ lattice matched to GaSb substrates using a variable electric field profile [4].

6.3.3 Back illumination

The second ideal condition is fitting using M_e and M_h from the same diode which can be achieved by back illumination. As illustrated in Figure 6.9, when alpha is greater than beta, in the *p-i-n* diode, the pure electron (hole)-initiated multiplication M_e (M_h) using short wavelength under topside (back) illumination is the greatest (smallest) multiplication that can be achieved, whereas the mixed injection multiplication using longer wavelength occurs between them. On the other hand, when beta is higher than alpha, the converse situation is accurate. Bulman tried to get a pure hole and electron- initiated multiplication from the same diode under the top and back illumination respectively [6]. There are a lot of advantages to using the back illumination technique in practical detection applications, hence the fabrication technology required can be well developed in some material systems. With a back- illumination scheme used by Li *et al.* [8] , the devices can readily be arrayed and flip-chip bonded to a silicon-based readout integrated circuit [9]. An improved back illumination technique is described by M. Grzesik *et. al* [10]. The authors entirely removed the GaSb substrate and bonded just the device's epilayers to a transparent substrate. This architecture allowed both pure electron and hole injection to be measured on the same diode, illuminating from the top side and from the bottom through the transparent substrate.

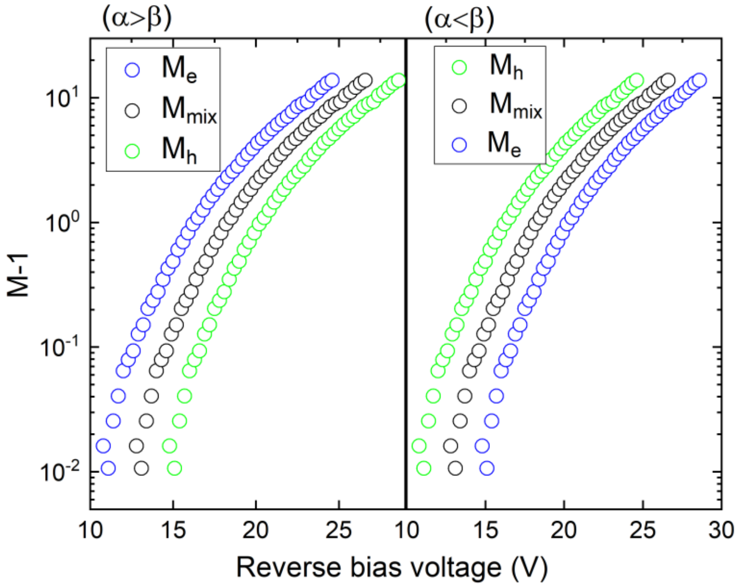

Figure 6.9: Multiplication characteristics modelled by RPL, under electron and hole-pure injection and mixed injection obtained from the same diode (*p-i-n* diode) when alpha is higher than beta and when the beta is higher than alpha.

In order to get M_e and M_h by illuminating the back of *n-i-p* and *p-i-n* diodes respectively in this work, we would need first to etch off the 800 μm of the semi-insulating substrate. Since the substrate width is >99% of the whole sample width, it is impossible to control the etching without using an etching stop. As currently grown the epi-structures do not have etch stops between the diode layers and the substrate, therefore, M_e and M_h cannot be extracted from the same diode using the current samples. In the future, this etching could be achievable if a thin AlGaAs layer is grown in the middle of the first GaAs layer. Using an acid that can etch the GaAs but not the AlGaAs, this layer may act as a stop etch point to control the etching process, thus making it possible to achieve the desired pure initiated multiplication under back illumination. An example of using an etching stop point has been done by Bulman *et al*. for an InP *n-i-p* diode. To minimise the risk of re-emission when targeting pure electron injection under back illumination, the width of the *p* cladding layer must be reduced to a thickness equal to several diffusion lengths. Since the electron diffusion length in InP is short, often less than 1 μm for these doping levels, it is difficult to control the etching without using an etch stop layer. A thin InGaAsP layer (0.7 µm) with a band gap equal to 1.08 eV was included in the structure to serve as an etch stop layer [6].

6.4 Previous comparison of ionisation coefficient magnitudes

Due to the non-uniformity of the electric field, the impossibility of obtaining M_e and M_h from the same diode, and the low probability of achieving pure electron-initiated multiplication in the *p-i-n* diode, it is necessary to find an effective way to enhance the fitting. To study the top-pure injection in the two diodes, a variety of laser sources of different wavelengths were utilized. Also, measurements with different device areas have been investigated as described below. Since the *p-i-n* and *n-i-p* diodes have different electric field profiles with different junction positions and doping concentrations, M_e(V)and M_h(V) cannot be simply compared to determine the relative magnitude of alpha and beta in the dilute nitride. As alpha and beta are functions of the electric field, for comparison, M_e and M_h can be plotted versus the electric field. On the other hand, the electric field profile is nonuniform at each voltage value. As a result, X. Collins tried to plot multiplication as a function of the peak electric field, which is expected to be dominant due to the ionisation coefficients being exponentially dependent on the field, to improve the comparison. This is still a significant simplification resulting in a poor comparison, as shown in Figure 6.10. The figure showed a concerning crossing when plotted as a function of the peak electric field and left many unanswered questions.

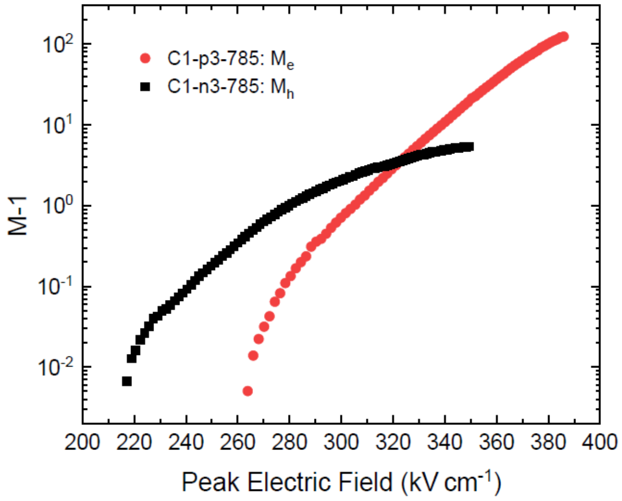

Figure 6.10: The multiplication characteristics for the homojunction *p-i-n* (C1-p3-785) and *n-i-p* (C1- n3-785) diodes as a function of the peak electric field as calculated by Dr Collins [1].

6.5 Mixed carrier injection

Since the carrier injection profile is wavelength-dependent, the magnitude of the multiplication also depends on the wavelength value. Short wavelengths are significantly absorbed on the surface, leading to pure injection into the depletion region, but long wavelengths are absorbed weakly and penetrate deeply into the structure, leading to mixed injection. Therefore, multiplication initiated by both pure and mixed injection can be characterised on the same diode, with the right choice of wavelength. Hence, the avalanche multiplication and the excess noise over a range of wavelengths can be investigated and used to confirm the purity and to interpret the relationship between alpha and beta as well. For example, in the case of *n-i-p* diode where beta is higher than alpha, and a range of wavelengths are used $\lambda_1 < \lambda_2 < \lambda_3$. In the beginning, ($\lambda_2$) can be used to obtain the proposed pure hole-initiated multiplication. By using a shorter wavelength (λ_1), there are three possibilities. The purity of the injection can be confirmed if the resultant multiplication using (λ_1) is identical to the multiplication using (λ_2). On the other hand, if the resultant multiplication using (λ_1) is higher than using (λ_2), (λ_2) is not short enough and it is necessary to use a wavelength shorter than λ_2 to get the pure hole injection. In addition, if the resultant multiplication using (λ_1) is lower than using (λ_2), the multiplication is mixed due to re-emission and re-absorption. Furthermore, by using (λ_3), the measured multiplication, which is then mixed multiplication, is expected to decrease while the excess noise is expected to increase. On the other hand, the trends and characteristics are inversed in the case of a *p-i-n* diode.

Pure initiated multiplication as well as mixed injection multiplication can be used to deduce the electron and hole impact ionization coefficients. This method has been utilized previously for thick APDs with a uniform electric field in 4H-SiC [11] and for thin APDs with non-uniform electric fields [7]. The avalanche multiplication and excess noise characteristics of 4H-SiC APDs as *p-i-n* structures with thin multiplication regions were investigated using a range of wavelengths from 230 nm to 365 nm. Pure electron-initiated multiplication was obtained with a laser source of 230 nm, and as the wavelength was increased, the multiplication became more mixed. The excitation wavelength was found to increase measured multiplication values while decreasing excess noise. Therefore, the carrier injection profile was used to fit the measured multiplication and excess noise characteristics of the structures so that the (enabled) ionization coefficients and the ionization threshold energies could be extracted. These measurements provide unambiguous evidence that $\beta > \alpha$, and the $\frac{\beta}{\alpha}$ ratios continue to be significantly greater than 1 even in these relatively thin 4H-SiC avalanche regions [7]. In addition, Ng *et al.* used the mixed carrier avalanche photomultiplication measurements on a series of *p-i-n* diode layers to deduce the electron and hole ionization coefficients in $In_{0.53}Ga_{0.47}As$ [12]. Furthermore, obtaining mixed injection multiplication for the two diodes as well as the pure injection multiplication enables us to incorporate additional data in the fitting, which can enhance the fitting.

6.6 Photomultiplication measurements

Photomultiplication measurements on GaInNAsSb diodes were carried out by focusing light from a laser source to a small spot on the top cladding of the diodes to inject carriers into the high-field regions. Since the leakage current is significant in both diodes as shown in Figure 6.8 and the signal is compromised by the associated noise, phase-sensitive detection has been used. In order to obtain pure electron (hole) initiated multiplication characteristics, M_e (M_h), for the *p*-*i*-*n* (*n*-*i*-*p*) homojunction diodes respectively, 405 nm light from a fibre-coupled diode laser has been used to illuminate the p^+(n^+) top cladding layer as shown in Figures 6.23 (a) (Figure 6.13 (a)). Since approximately 99.9% of the light is absorbed in the (500 nm) thick GaAs, this method worked well with the *n*-*i*-*p* diode to get an accurate M_h, but it fails to obtain an accurate M_e in the *p*-*i*-*n* diode, as described before. As a result, another technique with another laser wavelength was used and described later to get pure electron- initiated multiplication in the *p*-*i*-*n* diode. At low bias voltage, the increase of the primary photocurrent with voltage prior to the onset of photomultiplication was modelled using Wood's equation [13] which accounts for the movement of the depletion edge. Then, this current was extrapolated linearly to correct for the increase in the primary photocurrent with voltage after the onset of multiplication. Therefore, the experimental photocurrent was divided by the fitted primary photocurrent, to give experimental multiplication values.

6.6.1 Pure hole-initiated multiplication on *n-i-p*

M_h for the *n*-*i*-*p* diode has been investigated using a 405 nm laser source over different device area as shown in Figure 6.11. The good agreement between the multiplication characteristics for different device areas indicates that illumination is well-focused exclusively on the top of the mesa, that mixed carrier injection from the sides of the diode was avoided, and that multiplication is not affected by differing magnitudes of dark current. In some cases, when the dark current limits the multiplication, it is preferable to consider the smallest device with the lowest dark current so that higher multiplication values can be measured. When sufficient current flows through the diode, a non-negligible voltage drop occurs across the contact resistance R, depending on the contact resistance value. Therefore, the multiplication characteristics can be affected by this series resistance, resulting in an overestimation of the voltage across the depletion region when measuring the highest multiplication values. To carry out the photomultiplication measurements while accounting for the series resistance effect, it is essential to identify the value of R and then correct the applied voltage when processing the data. This is described in detail in section 4.2.2 for an example of GaInNAsSb *n*-*i*-*p* diode with a 400 μm diameter. Figure 6.12 shows the multiplication characteristics of the 400 μm diameter *n*-*i*-*p* diode with and without correcting for the series resistance effect. As shown in the figure, the difference between them is small. As a result, most working data is reported without considering the voltage correction. On the other hand, as the fitting is sensitive, all the multiplication data used for fitting was corrected first.

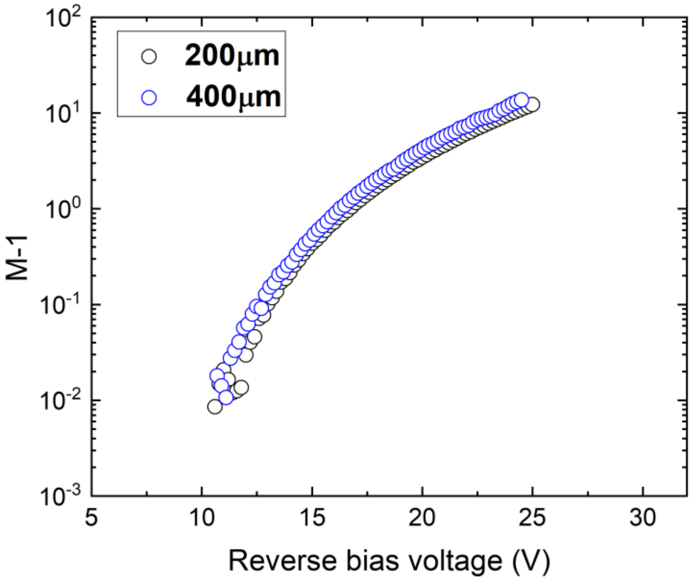

Figure 6.11: The multiplication characteristics of 400 μm and 200 μm diameter *n*-*i*-*p* diodes illuminated with a 405 nm laser source.

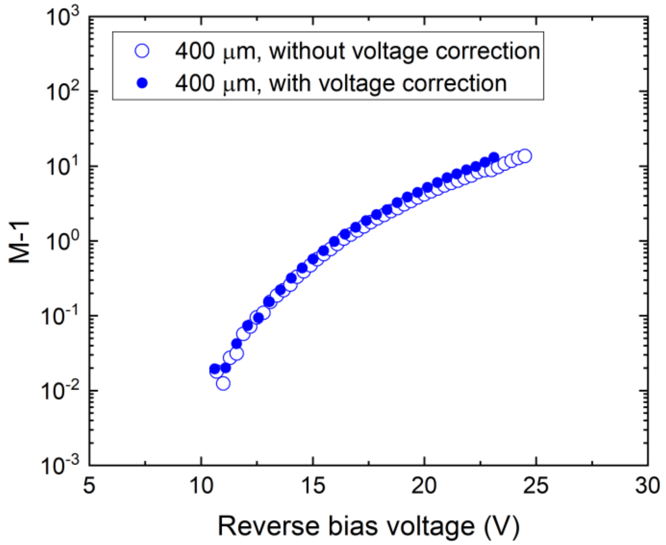

Figure 6.12: The multiplication characteristics of a 400 μm diameter *n-i-p* diode illuminated with a 405 nm laser source with and without correcting for the voltage dropped across the diode's series resistance.

In order to improve understanding of the ionization behaviour and confirm the purity, different laser wavelengths have been used for a 400 μm diameter *n-i-p* diode, as shown in Figure 6.13 (a). As we move from the blue laser (405 nm) with the highest photon energy to the red laser (670 nm) with the lowest photon energy, passing the green laser (543 nm), the light is absorbed deeper into the structure, leading to the generation of photocarriers in the depletion region, resulting in more mixed injection. Figure 6.14 shows the resultant multiplication as a function of reverse bias voltage due to the illumination by the three different wavelengths. Compared to the essentially pure hole-initiated multiplication using the blue laser, the mixed injection multiplications, using the green and red laser with progressively more electron contribution, are lower. This indicates, as described in the ideal case above, that β must be higher than α. In addition, the small difference between the multiplication measured with the blue laser and green laser can approximately confirm the purity. However, it is noted that the measured multiplication using the red laser is significantly lower than expected.

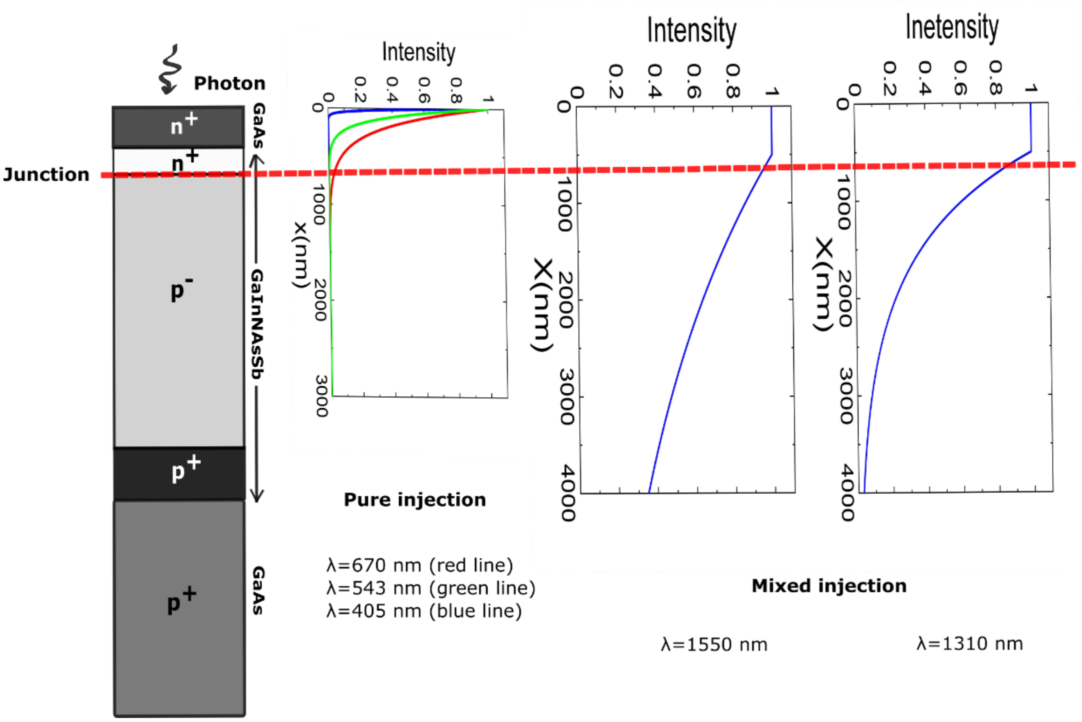

Figure 6.13: A schematic representation of how the pure electron injection and the mixed injection can be obtained in the *n-i-p* diode. (a) The intensity of light as a function of the position using red, green and blue laser source. (b) and (c) The two mixed injection cases using 1550 nm and 1310 nm laser source respectively.

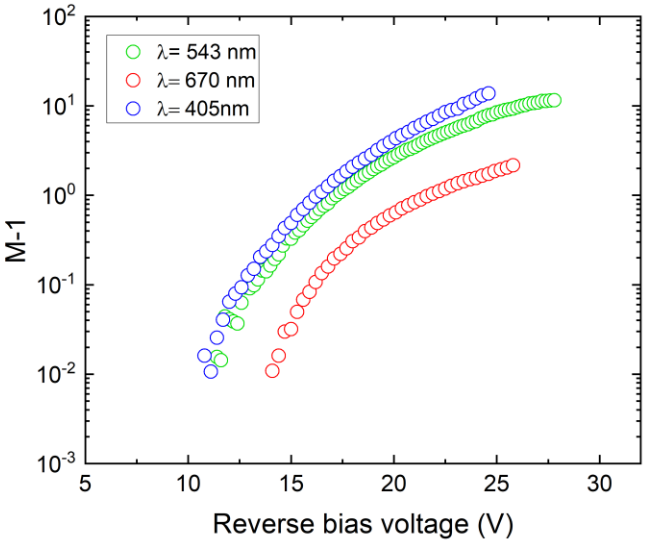

Figure 6.14: The multiplication characteristics of a 400 μm diameter *n-i-p* diode illuminated with 405 nm (blue), 670 nm (red), and 543 nm (green) laser source.

6.6.2 Mix injection multiplication on *n-i-p* diode

A 1550 nm fibre coupled diode laser was also used to investigate the multiplication characteristics, M_{mix}, of the *n-i-p* and *p-i-n* diodes under mixed carrier injection conditions as shown in Figures 6.13 (b) and 6.23 (b) respectively. Since the optical absorption coefficient of dilute nitride at 1550 nm wavelength is only ~3000 cm^{-1}, [1] the light is absorbed weakly, and photocarriers are generated almost uniformly throughout the high-field region.

In pure injection, where the absorption takes place outside the depletion region, as the voltage increases, the depletion increases too, and more photogenerated carriers can be collected. As a result, the baseline approximation method described by Wood can be used. On the other hand, for mixed injection multiplication, this approximation is no longer valid to quantify the primary photocurrent correctly. In mixed injection multiplication, the absorption takes place in and out of the depletion region so, it is difficult to identify how the primary photocurrent changes with voltage. So, a specific way to get the primary photocurrent is required. For example, Bulman *et al*. found it difficult to fit the primary photocurrent due to the pure electron injection under back illumination in an InP *n-i-p* diode. This was due to the considered structure, which increases the risk of re-emission and makes the primary photocurrent increase exponentially at lower voltages and linearly over high voltages. As a result, to identify the primary photocurrent, the absorption coefficient $\alpha(hv, E)$ resulting from a constant electric field E for a photon energy hv and a band gap E_g was initially calculated. Then, this coefficient was used to calculate the current density $J_g(hv, V)$ by integrating the field dependent generation across the depletion region [6]. In addition, Marshall *et al*. used a different process to calculate the primary photocurrent. It was calculated by dividing the experimental photocurrent by the modelled multiplication. This was then fitted to an exponential function [14].

At the wavelength of 1550 nm, the first GaAs layer is transparent to the light, and the absorption started at the dilute nitride n or p cladding layers for *n-i-p* and *p-i-n* diodes, respectively. At each voltage value, the magnitude of primary photocurrent expected can be determined by the difference between the light intensity at the beginning and end of the depletion region. The intensity of light φ can be calculated as:

$$\varphi(x) = \varphi_{\circ}(x)\exp(-\alpha_{abs}x) \qquad \textbf{6.1}$$

where $\varphi_{\circ}$ is the initial intensity of light, x is the travelling distance, and α_{abs} is the absorption coefficient of the semiconductor material. Then, since the primary photocurrent increases with the laser power, it needs to be scaled depending on the laser power to fit the lock-in voltage. Starting with a 400 µm diameter *n-i-p* diode, Figure 6.15 shows that the primary photocurrent cannot be fitted correctly without considering electron and hole diffusion lengths L_e and L_h in addition to the depletion width w. Initially, by considering L_h and ignoring L_e, the fitting is significantly improved. This improvement was attributed to the stronger absorption of light within the hole diffusion length at the start of the depletion caused by the exponential decay of the light intensity. By considering the suitable L_e (500 nm) and L_h (222 nm), the primary photocurrent fitted well, as shown in Figure 6.15. Then, the primary photocurrent was used to calculate and investigate the mixed injection multiplication in different area devices, as shown in Figure 6.16. In order to compare and understand the ionization behaviour of the dilute nitride, the almost pure hole-initiated multiplication M_h and the mixed injection multiplication M_{mix} of a 400 µm diameter *n- i-p* diode were plotted together in Figure 6.17.

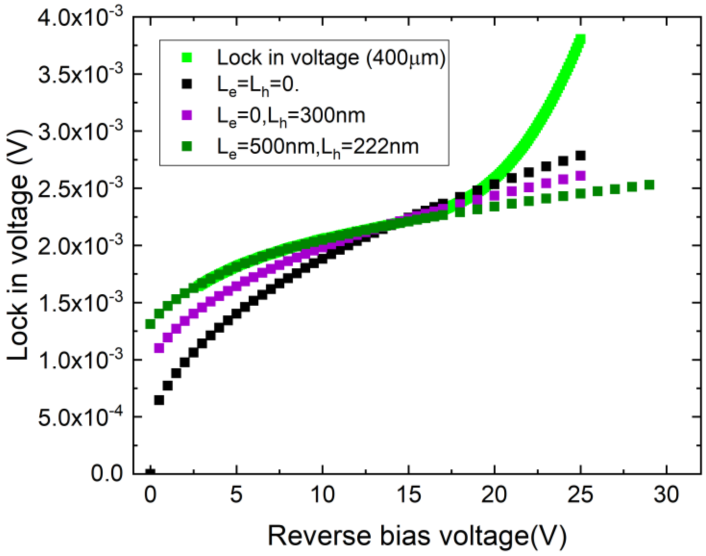

Figure 6.15: Lock-in amplifier voltage as a function of the reverse bias voltage for a 400 μm diameter *n-i-p* diode illuminated with a 1550 nm laser source. The primary photocurrent fitted with and without the electron and hole diffusion length L_e (L_h).

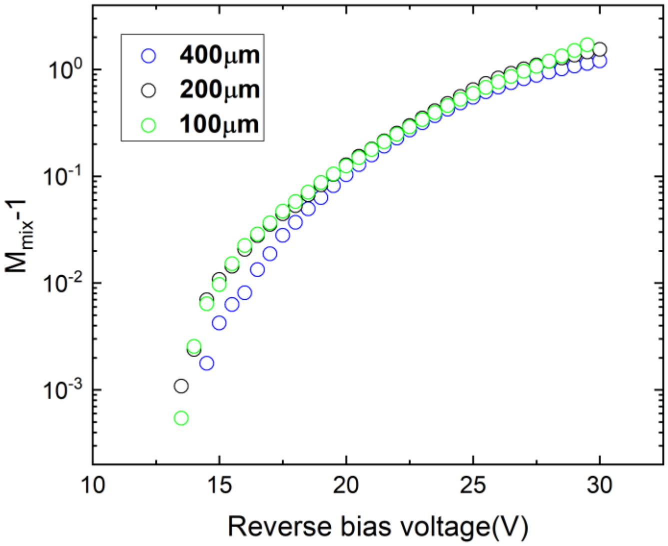

Figure 6.16: M_{mix}-1 as a function of reverse bias voltage for 100 μm, 200 μm, and 400 μm diameter *n- i-p* diodes illuminated with a 1550 nm laser source.

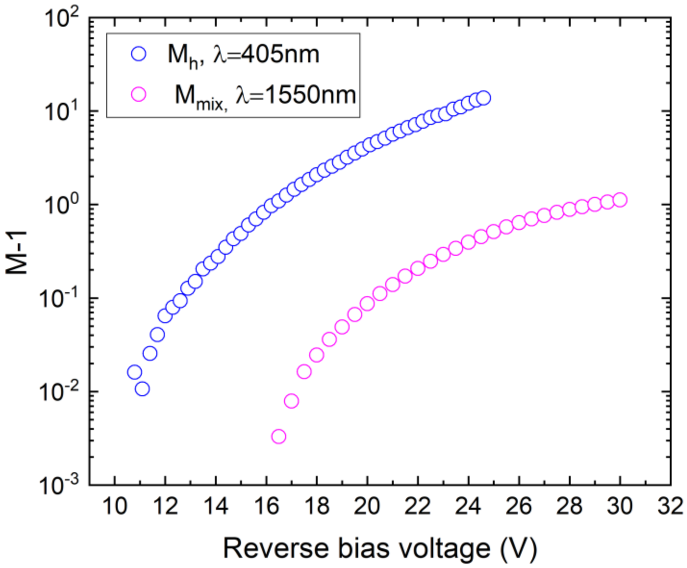

1

Figure 6.17: A comparison of pure hole-initiated multiplication using a 405 nm laser source and mixed injection multiplication using a 1550 nm laser source for a 400 μm diameter *n-i-p* diode.

In the mixed injection case, the electron contribution with the electron ionisation coefficient α reduces the multiplication compared to the pure M_h, which confirms that beta is higher than alpha. Figure 6.17 shows a significant difference between the pure and mixed injection multiplications, with the mixed multiplication being lower than reasonably expected. This can most probably be attributed to a very low hole contribution in the mixed injection case due to weak absorption in the n-cladding layer. Because of the high doping concentration in the n-cladding layer, the carriers fill up the lowest states in the conduction band. The corresponding energy of 1550 nm wavelength is 0.8 eV, which is almost the same band gap energy in dilute nitride. Hence absorption this close to the band edge in the n-cladding layer can be lower than expected. To study the possibilities of fitting with lower absorption coefficients in the n-cladding layer, the fitting process was repeated with absorption coefficients equal to 0 cm^{-1} and 1000 cm^{-1}. Figure 6.18 shows that in addition to the typical case with an absorption coefficient equal to 3000 cm^{-1}, the primary photocurrent can be well fitted in these two cases with suitable L_e and L_h. Then, the mixed injection multiplication for the three cases has been obtained as shown in Figure 6.19.

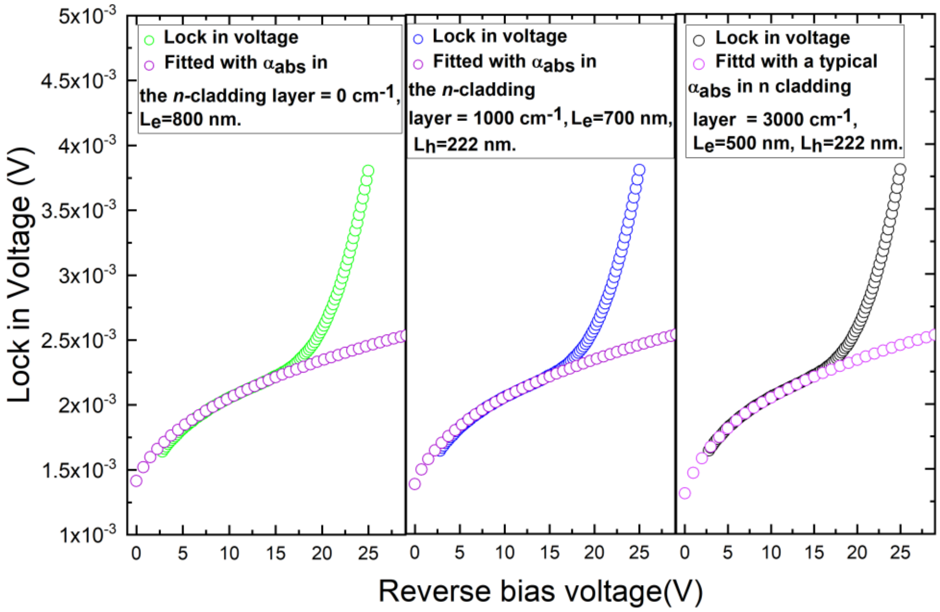

Figure 6.18: Lock-in amplifier voltage as a function of the reverse bias voltage for a 400 μm diameter *n-i-p* diode illuminated with a 1550 nm laser source. Primary photocurrent fitted with different absorption coefficients in the n-cladding layer and different L_e and L_h.

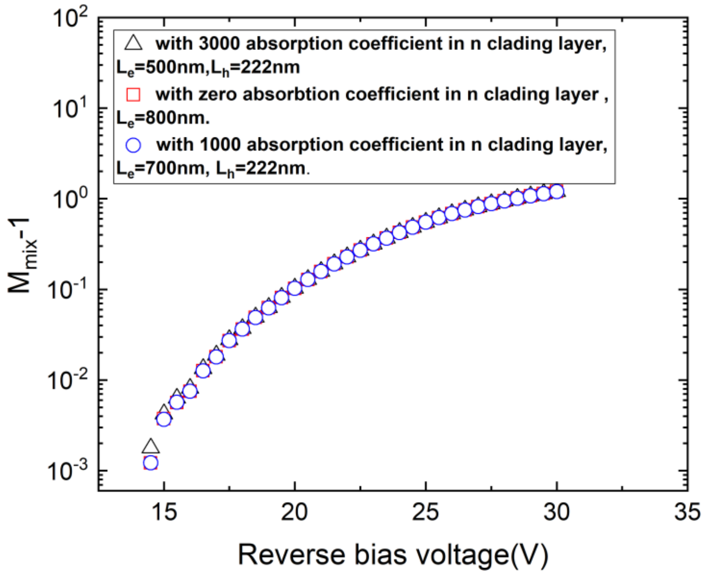

Figure 6.19: Mixed injection characteristics of a 400 μm diameter *n-i-p* diode illuminated with a 1550 nm laser source. Primary photocurrent fitted with different absorption coefficients in the n- cladding layer and different L_e and L_h.

From the analysis above, it is clear that to correctly simulate the mixed injection multiplication in the *n-i-p* diode, the absorption coefficient in each layer must be known precisely. Therefore, a slightly shorter wavelength with a photon energy higher than the band gap energy and immune to the effects of doping is required to generate photocurrent. As a result, the absorption process cannot be affected, and hence the pure hole contribution cannot be reduced due to the high doping concentration in the n-cladding layer. This can be achieved by using a 1310 nm laser source with an absorption coefficient expected to be 10000 cm^{-1} in all dilute nitride layers as shown in Figure 6.13 (c). For a 400 μm diameter *n-i-p* diode, the primary photocurrent fitted well with L_e equal to 500 nm and L_h equal to 200 nm as shown in Figure 6.20. The mixed injection multiplication for different areas was investigated as shown in Figure 6.21.

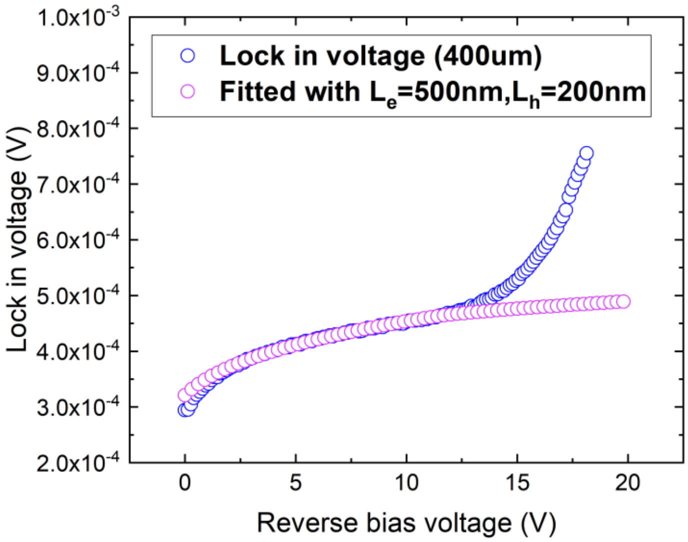

Figure 6.20: Lock-in amplifier voltage as a function of the reverse bias voltage for a 400 μm diameter *n*-*i*-*p* diode illuminated with a 1310 nm laser source. The primary photocurrent is fitted with a 500 nm electron diffusion length and 200 nm hole diffusion length.

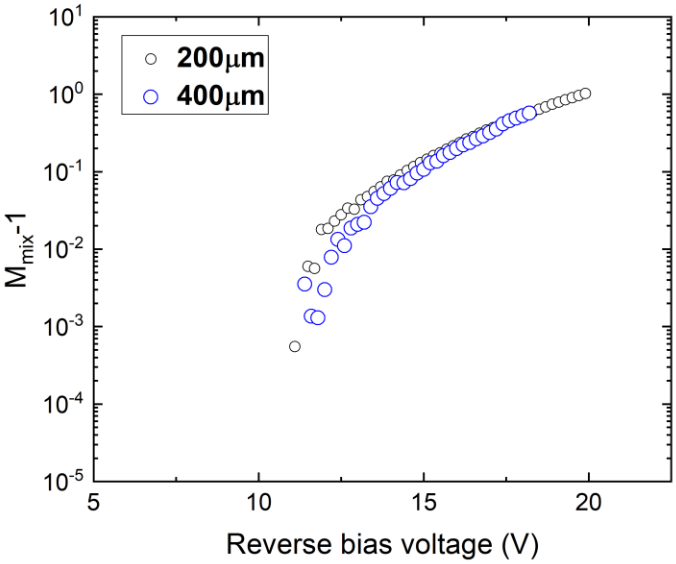

Figure 6.21: M_{mix}-1 as a function of reverse bias voltage for 200 μm, and 400 μm diameter *n*-*i*-*p* diodes illuminated with a 1310 nm laser source.

For a 400 µm diameter *n-i-p* diode, the pure hole-initiated multiplication and the mixed injection multiplication using 1550 nm ($M_{mix1550}$) and 1310 nm ($M_{mix1310}$) lasers have been shown in Figure 6.22. The 1550 nm laser, characterized by a longer wavelength and lower photon energy compared to the 1310 nm laser, exhibits stronger penetration into the epilayer structure. Considering the electric field profile, diffusion length and absorption coefficient, the percentage of incident light expected to give pure hole contribution to the mixed multiplication was calculated for both 1550 nm and 1310 nm illumination. Due to exponential light decay, the expected pure hole contribution with the 1310 nm laser is 18.7% of the light at 10 V in the ideal absorption situation, while it is only 6% with the 1550 nm laser. This helps explain why $M_{mix1310}$ is higher than $M_{mix1550}$ and closer to M_h. However, the figure illustrates a slight difference between $M_{mix1310}$ and M_h, in contrast to the significant difference observed between $M_{mix1550}$ and M_h. This difference is more significant than expected based on the calculated absorption profiles. This further supports the argument that the 1550 nm laser, with a photon energy very close to the dilute nitride band gap, is absorbed more-weakly than expected, due to the high doping concentration in the n- cladding layer filling the conduction band states.

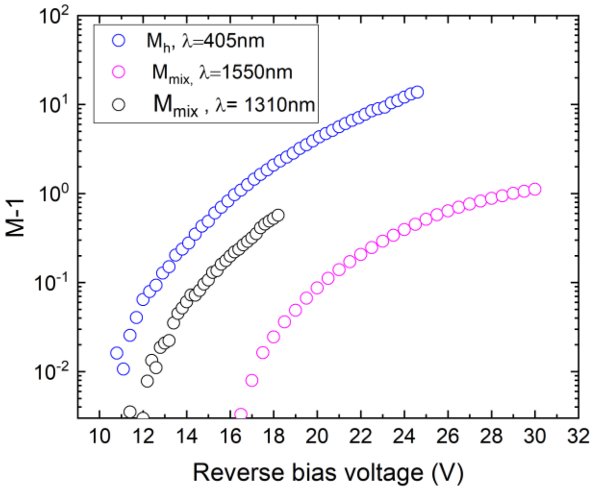

Figure 6.22: A comparison of pure hole-initiated multiplication using a 405 nm laser source and mixed injection multiplication using 1550 nm and 1310 nm laser sources for a 400 µm diameter *n-i-p* diode.

6.6.3 Mix injection multiplication on *p-i-n* diode

In the *p-i-n* diode, as the junction is far away from the top of the diode, the absorption in the high-doping concentration p-cladding layer is negligible. In addition, since the intensity of light decays exponentially, the absorption in the high-doping concentration n-cladding layer is relatively insignificant. As a result, it is considered that mixed injection multiplication can be obtained and accurately simulated with a 1550 nm laser source ($M_{mix1550}$) as shown in Figure 6.23 (b). As shown in Figure 6.24, the primary photocurrent for a 400 µm diameter *p-i-n* diode illuminated with a 1550 nm laser source fitted well with L_e equal to 500 nm and L_h equal to 233 nm. In addition, mixed injection multiplication has been investigated for different device areas, as shown in Figure 6.25. As the area decreases, the alignment of the fibre at the top of the diode becomes challenging. Consequently, some illumination of the side walls will lead to unintended primary carrier profiles. The reducing values of mixed- initiated multiplication indicate an increasing electron fraction in the primary photocurrent as the area reduces. This is somewhat counterintuitive, and the overall behaviour seen may also be affected by re-emission.

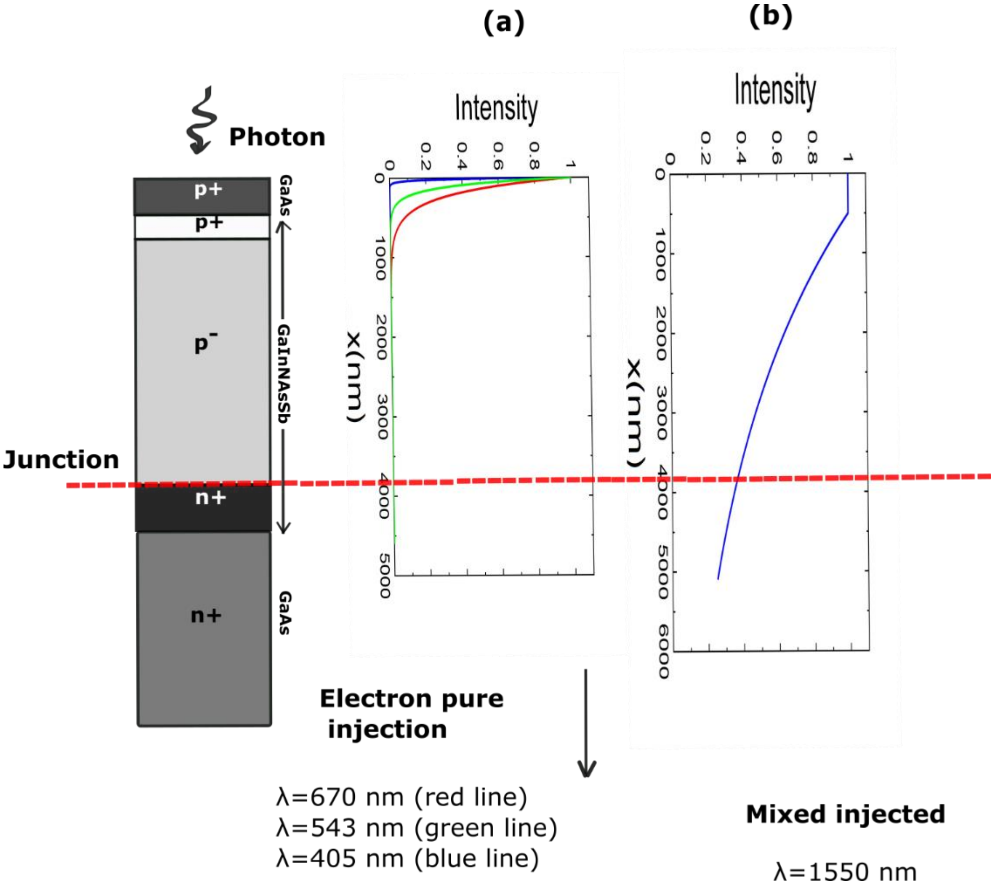

Figure 6.23: A schematic representation of how the pure electron injection and the mixed injection can be obtained in the *p*-*i*-*n* diode. (a) The intensity of light as a function of the position using red, green and blue laser source. (b) The mixed injection using 1550 nm laser source.

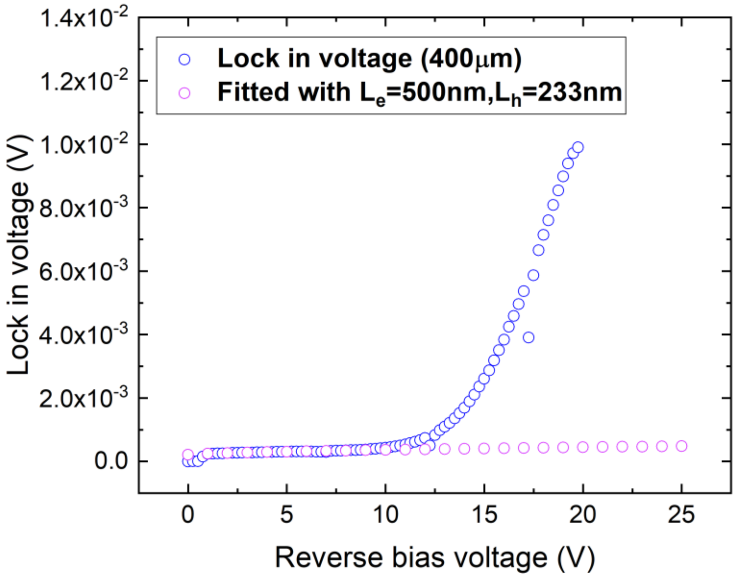

Figure 6.24: Lock-in amplifier voltage as a function of the reverse bias voltage for a 400 μm diameter *p-i-n* diode illuminated with a 1550 nm laser source. The primary photocurrent is fitted with a 500 nm electron diffusion length and a 233 nm hole diffusion length.

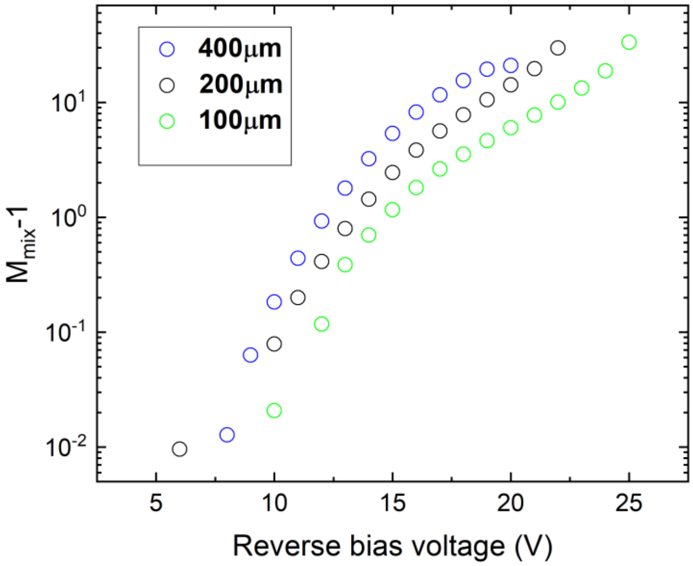

Figure 6.25: M$_{mix}$-1 as a function of reverse bias voltage for 100 μm, 200 μm, and 400 μm diameter *p- i-n* diodes illuminated with a 1550 nm laser source.

6.6.4 pure electron-initiated multiplication on *p-i-n* diode

Since *p-i-n* and *n-i-p* have been fabricated using GaInNAsSb with nominally identical composition, confirmed by near identical band gap energies 0.796 eV and 0.807 eV respectively, it is expected for β to be higher than α in the *p-i-n* diode as well. As described above, in the ideal case when beta is higher than alpha, starting with mixed multiplication ($M_{mix1550}$), with decreasing the wavelength the multiplication is expected to reduce and converge to the pure electron injection case. Since Dr Collin found it difficult to get pure electron injection using the green laser due to the risk of re-emission, this work tried to minimise this effect by using a longer wavelength red laser (670 nm). On the other hand, as shown in Figure 6.23 (a), the wavelength of the red laser is not long enough to allow the light to be absorbed deeper into the structure. Therefore, the collection efficiency of photogenerated carriers in the depletion region is low and the risk of re-emission is still high, which affects the purity. This results in more mixed injection multiplication rather than the aimed pure electron-initiated multiplication. As shown in Figure 6.26, this multiplication (M_{mix670}) which is aimed to be pure is higher than the intentionally mixed multiplication ($M_{mix1550}$).

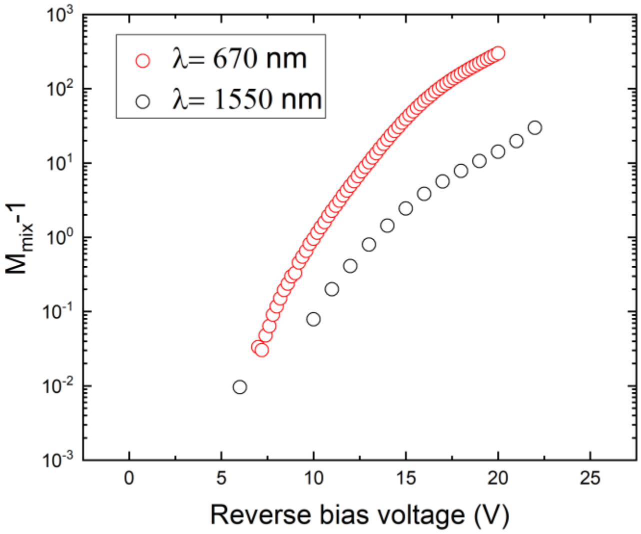

Figure 6.26: M_{mix}-1 as a function of reverse bias voltage for 200 µm diameter *p-i-n* diodes illuminated with a 670 nm (red) laser source, which is aimed to be pure electron-initiated multiplication, and a 1550 nm laser source to obtain mixed injection multiplication.

6.6.5 pure electron-initiated multiplication on cap-etched *p-i-n* diode

The above results confirm that the use of a red laser is not able to achieve pure electron injection. Consequentially, in order to eliminate the re-emission effect and to obtain pure electron injection and accurate mixed initiated multiplication, a certain width must be etched from the top of the diode. By using equation 6.1 with the absorption coefficient of the red laser in dilute nitride, the desirable etching width value was determined. 2000 nm was etched from the topside of the diode. Thereafter, the pure electron injection was achieved by illuminating the topside of variety numbers of 200 µm and 400 µm diameter *p-i-n* diodes with a 405 nm laser source. Then, the pure electron-initiated multiplication for the diodes was obtained. The data with baselines which best fit the expected bias dependence for the primary photocurrent were selected, as shown in Figure 6.27. There are three possible reasons contributing to the spatial variation from device to device across the sample observed in the impact ionization coefficients, which could result in variation in multiplication characteristics across different diodes on a single sample. Firstly, the most likely reason is experimental uncertainty, where the variation could be attributed to the alignment position of the fibre. For example, in the case of pure injection, a more mixed injection would be achieved if the fibre were shifted toward the side wall of the device.

Secondly, if the lattice defects are common enough to affect the overall material properties, for example, N interstitials, they could lead to spatially varying multiplication characteristics across the wafer. Alternatively, compositional variation in the alloy could also have the same effect. Both these growth-related factors are unlikely to be driven by spatial variation in temperature during growth, since this changes over a very long scale compared to the separation between devices. The size of the devices is only a few hundred micrometres, with a very small distance between them compared to the size of the wafer, which is 50 mm. So, if the temperature changes across the whole wafer by 10 degrees, it is changing relatively slowly from one device to another. On the other hand, they are more likely to be driven by small- scale variations due to growth dynamics.

Thirdly, the variation of the electric field profile across the sample due to the variation of the doping concentration and the layer width is on a very long scale, and not considered likely to be the cause of the variation in measured multiplication.

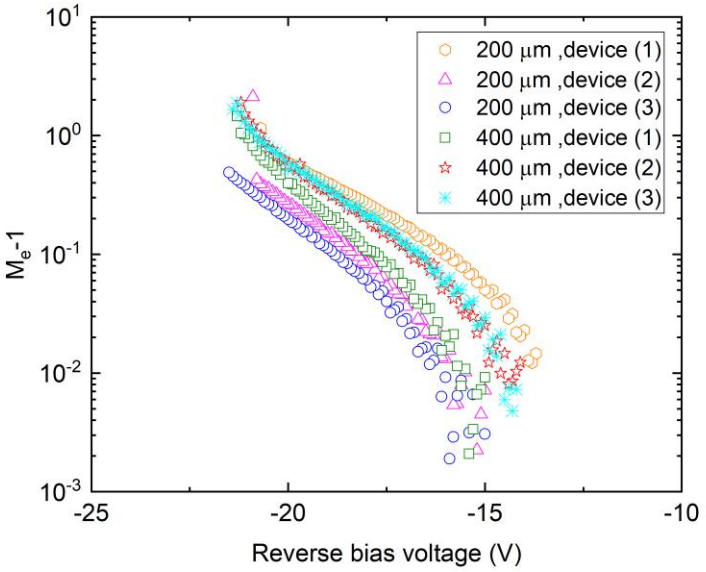

Figure 6.27: The multiplication characteristics of a variety of 200 µm and 400 µm-diameter cap-etched *p-i-n* diodes illuminated with a 405 nm laser source.

The lowest multiplication was selected to be included in the fitting as a pure electron-initiated multiplication for two reasons. The captured data has a high resolution and a good linear region for fitting a plausible baseline. Also, based on the knowledge that alpha is lower than beta, the lowest multiplication should represent the purest one.

6.6.6 Mixed-initiated multiplication on cap-etched *p-i-n* diode

In order to obtain mixed-initiated multiplication for the cap-etched *p-i-n* diode, a variety of 200 µm and 400 µm diameter *p-i-n* diodes were illuminated with a 1550 nm laser source. The observed variations in multiplication can be attributed to the same factors that were stated for the pure case mentioned earlier. Due to absorption within the bias-dependent depletion width, a simulated baseline technique was employed to fit the primary photocurrent. Subsequently, the average value of these multiplications was calculated, as depicted in Figure 6.28.

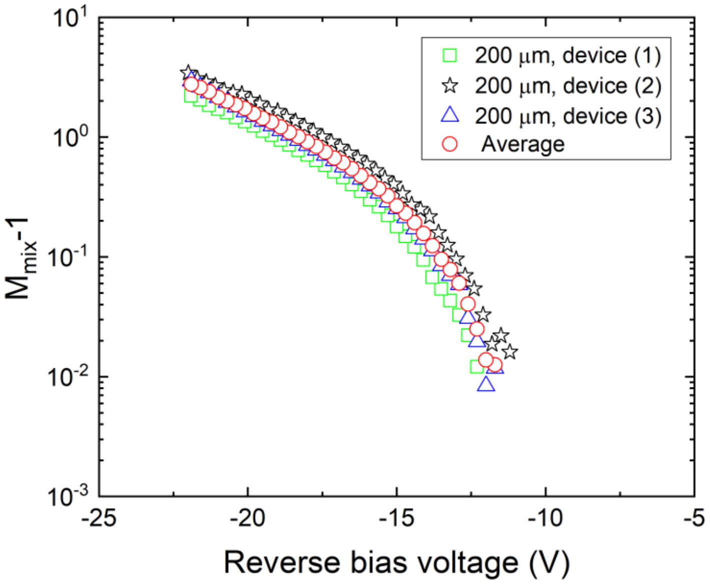

Figure 6.28: M_{mix}-1 as a function of reverse bias voltage for a variety of 200 μm diameter cap-etched *p*-*i*-*n* diodes illuminated with a 1550 nm laser source, as well as the average of these multiplications.

As shown in Figure 6.29, by comparing the pure electron-initiated multiplication to the mixed-initiated multiplication, it is obvious that alpha is less than beta. This result confirms the previous findings from *n*-*i*-*p* diode measurements.

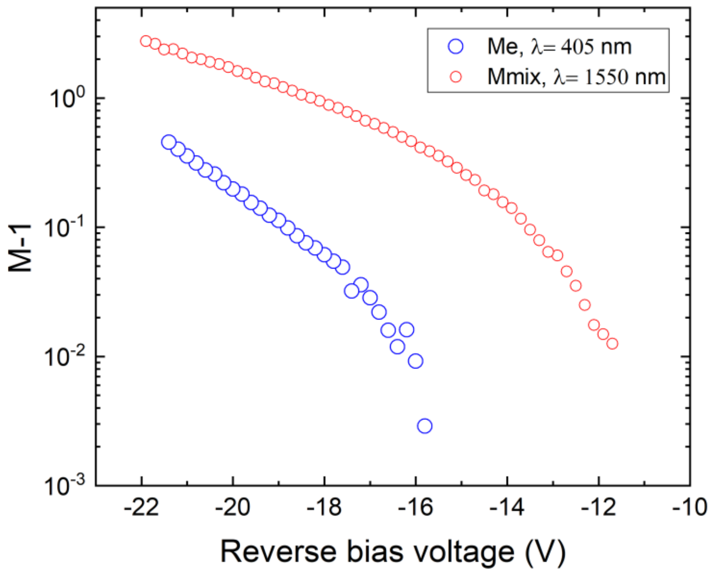

Figure 6.29: A comparison of a pure electron-initiated multiplication using a 405 nm laser source and a mixed injection multiplication using a 1550 nm laser source for a 200 µm diameter cap-etched *p-i-n* diode.

6.7 Electron and hole impact ionization coefficients

In order to extract the electron and hole impact ionisation coefficients of GaInNAsSb, an evolutionary fitting algorithm using the RPL model was utilised as described in Section 4.5. The fitting process employed four different types of multiplication data, including pure electron-initiated multiplication and mixed-initiated multiplication for the cap-etched *p-i-n* diodes, as well as pure hole-initiated multiplication and mixed- initiated multiplication for *n-i-p* diodes. The algorithm was initiated using the impact ionisation coefficients of comparable band gap materials, such as InGaAs [12] and GaInNAs [15]. The minimum electron and hole threshold energies have been set at the material band gap, which is about 0.8 eV. From the best of my knowledge, C has not been reported to be more than 3. Consequentially, the fitting was carried out with limited C <3 as well as with non-limited C over a field range of 250 kV cm^{-1} to 550 kV cm^{-1}. Hereafter, the electron and hole impact ionisation coefficients are reported for these two cases. As explained previously, since the electric field profile is triangular and the peak field will dominate the impact ionisation, the range of the electric field for which the coefficient is considered to fit, was taken to be the peak electric field across the voltage range where the multiplication was measured

Figure 6.30 illustrates how good the fitting is in the two cases for the four types of multiplication data by comparing the experimental and the simulated multiplication using obtained coefficients and threshold energies. It is obvious from the figure that, compared to limited C, non-limited C can improve the fitting, especially for M_h. Table 6.3 shows the extracted electron and hole impact ionisation coefficients and threshold energies for both cases.

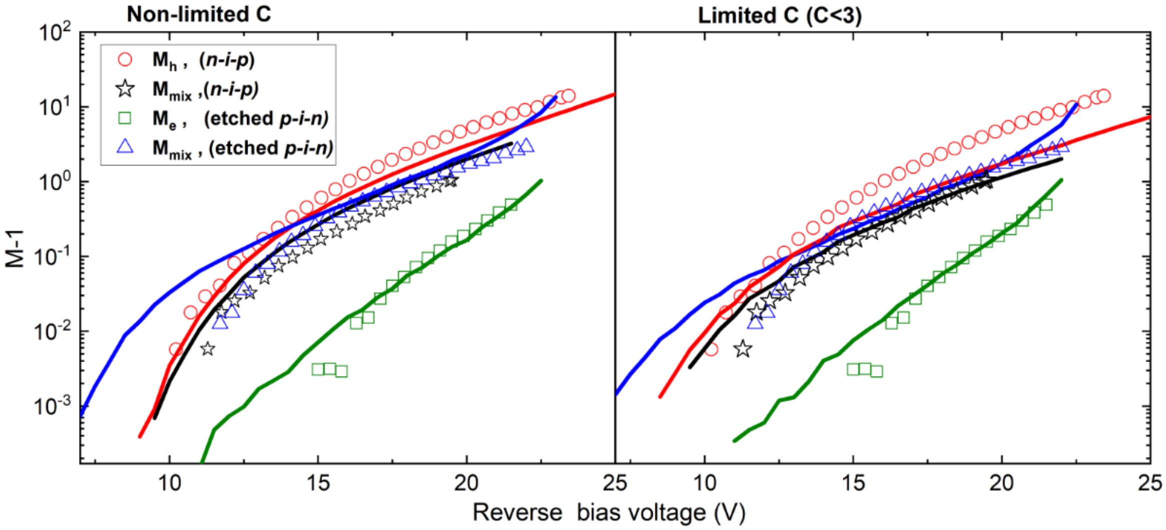

Figure 6.30: Multiplication characteristics of GaInNAsSb *n-i-p* and cap-etched *p-i-n* diodes. The symbols represent the experimental data, while the solid lines indicate results calculated using the RPL model and GaInNAsSb impact ionisation coefficients and threshold energies. Two fittings were carried out to parametrize the coefficients and threshold energies: using limited (C<3) and using non- limited C.

Electron $\boldsymbol{\alpha} = \boldsymbol{A}\,\mathbf{exp}\,[-\left(\frac{\boldsymbol{B}}{\boldsymbol{\xi}}\right)^{\boldsymbol{C}}]$	**Hole** $\boldsymbol{\alpha} = \boldsymbol{A}\,\mathbf{exp}\,[-\left(\frac{\boldsymbol{B}}{\boldsymbol{\xi}}\right)^{\boldsymbol{C}}]$
Non-limited C **A**= 2.905 x 10^4 cm^{-1} **B**= 7.34 x 10^2 kV cm^{-1} **C**= 2.637	**Non-limited C** **A**= 2.498 x10^5 cm^{-1} **B**= 3.34x 10^2 kV cm^{-1} **C**= 5.203
$\mathbf{E_{the}}$= 1.37 eV	$\mathbf{E_{thh}}$= 1.99 Ev
C<3 **A**= 2.243 x10^5 cm^{-1} **B**= 9.96x 10^2 kV cm^{-1} **C**= 2.114	**C<3** **A**= 4.375 x10^5 cm^{-1} **B**= 4.18 x10^2 kV cm^{-1} **C**= 3.0
$\mathbf{E_{the}}$= 2.021 eV	$\mathbf{E_{thh}}$= 1.96 eV

Table 6.3: Parametrized ionization coefficients in GaInNAsSb, where ξ is the electric field in kV cm^{-1}.

The coefficients are plotted and compared with the coefficients of different materials. Figure 6.31 illustrates the first comparison with GaAs [16] , InGaAs [12] that has a comparable band gap where alpha is higher than beta by approximately 1 - 2 orders of magnitude, and with another dilute nitride material (GaInNAs) which has a different nitrogen and In compositions (N=3% and In=10%) [15].

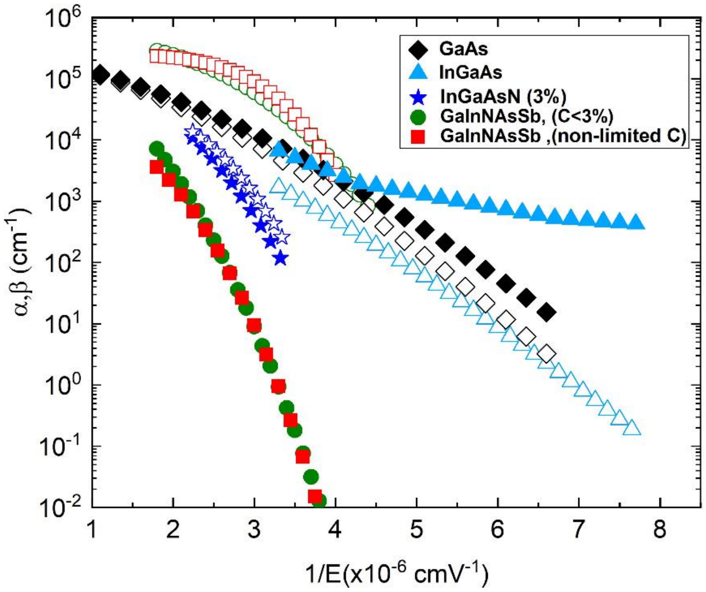

Figure 6.31: A comparison of the extracted coefficients for GaInNAsSb with those reported for GaAs [16] and InGaAs [12] , and InGaAsN (3%) [15]. Solid symbols indicate the electron ionisation coefficients, while open symbols indicate the hole ionisation coefficients.

The incorporation of In into GaAs can slowly increase alpha, especially at lower electric fields, as demonstrated by the trend seen in published coefficients for GaAs, InGaAs, and InAs. This can be attributed to reduction in the band gap. In addition, the gamma valley becomes deeper in energy which reduces electron scattering. As a result, electrons can gain energy and reach the ionisation threshold energy more easily at low electric fields. On the other hand, adding N to GaAs can also reduce the bandgap, but it increases electron scattering, which in turn reduces the rate of energy gain and hence reduces alpha. This is attributed to the interaction between the localized N states and the extended conduction-band (CB) states of GaAs through a process called band anti-crossing (BAC) as shown in Figure 6.32 [17]. As a result, CB splits into two sub bands known as E_+ and E_-. The downward shift of the lower subband, E_-, is not only responsible for the reduction of the fundamental band-gap energy, but also for an increase of the scattering and the electron effective mass, m_e*.

These effects arise from the strong non-parabolic nature of the lower subband and its associated effective mass. As a result, a reduction in the rate at which electrons can gain energy and hence the electron ionisation coefficient is to be expected. Since the N level sits in the conduction band, the valence band (VB) offset in GaInNAs is known to be negligible.

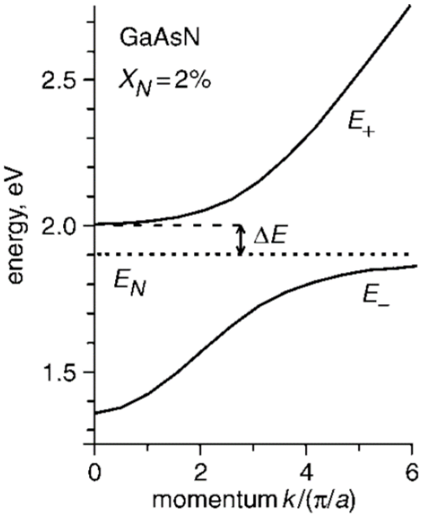

Figure 6.32: Conduction band structure of GaAsN with 2% nitrogen. Adopted from [17].

Starting from GaAs [16], adding 10 % of In to achieve GaInNAs [15] would increase alpha, while adding 3 % of N would decrease alpha. As Figure 6. 31 shows, the effect of N is dominant particularly at lower electric fields, reducing alpha to be lower than beta. Comparing InGaAs [12] to GaInNAs, both reducing In to 10% and adding 3% of N have the same effect, which is to significantly decrease alpha. GaInNAsSb has more N (5%) and In (20%) as well as 1% Sb, compared to GaInNAs. These changes appear to greatly increase beta and decrease alpha, making a significant difference between beta and alpha. Both sets of coefficients for dilute nitride materials, with 3% and 5% of N, have the same trend, which is uncommon among the III–V materials, with beta being higher than alpha. It is assumed that the coefficient for InGaAs in the upper field range has not been extracted due to the onset of excessive tunnelling, because the threshold electric field for tunnelling has been reported to be $1.8\text{x}10^5$ V/cm [18]. On the other hand, the background doping concentration in GaInNAsSb is not low enough to provide the coefficient in a low field range for that material.

Furthermore, another comparison with materials where beta is higher than alpha, such as InP [19] and lower Al composition of AlGaAsSb [10] and $Al_{0.9}Ga_{0.1}As_{0.08}Sb_{0.92}$ [4] is illustrated in Figure 6.33. The figure demonstrates that GaInNAsSb has the highest beta and the lowest alpha, with the most significant difference between alpha and beta in comparison to other materials. Given that hole ionisation dominates in GaInNAsSb and the significant difference between beta and alpha, there is potential for desirable APD properties. The noise associated with pure hole injection will be low, and the signal-to-noise ratio will be high. In addition, a high beta value leads to increased hole-initiated multiplication, resulting in reduced operating voltage and decreased breakdown voltage. As a result, the device can be thinner as the effect of tunnelling is low.

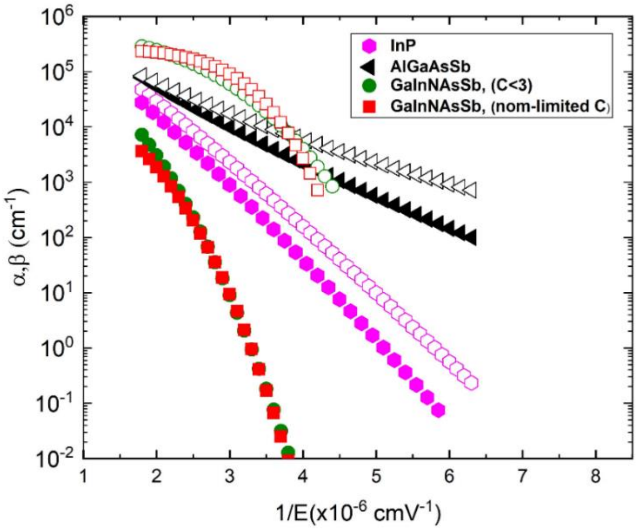

Figure 6.33: A comparison of the extracted coefficients for GaInNAsSb with those reported for InP [19] ,and AlGaAsSb [4]. Solid symbols indicate the electron ionisation coefficients, while open symbols indicate the hole ionisation coefficients

6.8 Conclusion

In this chapter, the multiplication characteristics of GaInNAsSb have been investigated. Therefore, the electron and hole impact ionization coefficients and threshold energies have been extracted. In order to assess these coefficients, they were graphically represented and compared with the coefficients of other materials.

Since the diodes have a non-uniform electric field the C-V characteristics of homojunction GaInNAsSb *p-i-n* and *n-i-p* diodes were initially investigated, to determine the fitting structure. Then, the electric field profiles of both diodes were identified. Thereafter, multiplication measurements were carried out on the two diodes at room temperature. Pure electron and pure hole-initiated multiplication factors, M_e and M_h measured on the same diode, are commonly employed for the easy and accurate calculation of the ionization coefficients. On the other hand, due to the impossibility of obtaining pure electron and pure hole injection from the same diode as described previously, pure initiated multiplication and mixed injection multiplication have been obtained for each diode. Subsequently, the relationship between pure initiated-multiplication and mixed injected multiplication was employed to explain the impact ionisation characteristics of GaInNAsSb in both diodes.

Starting with the *n-i-p* diode, pure hole-initiated multiplication has been achieved by utilising a range of wavelengths over various device areas. To perform mixed injection multiplication, the initial step was to use a laser source operating at a wavelength of 1550 nm. There is uncertainty about the mixed multiplication due to the possibility of the absorption coefficient in the n-cladding layer, with a high doping concentration, being lower than expected. Hence to get an accurate estimation of the mixed injection multiplication, a laser source operating at a wavelength of 1310 nm, which has photon energy slightly higher than the band gap of GaInNAsSb, has been employed. In the case of the *p-i-n* diode, due to the significant distance between the junction and the top diode, there is a considerable possibility of re-emission. Consequently, achieving precise mixed injection multiplication with a 1550 nm laser source is unlikely.

Furthermore, for the same reason, the achievement of pure electron-initiated multiplication utilising a red laser, which already has a longer wavelength compared to the green laser employed by Dr. Collins, is considered impossible. One potential solution for addressing this problem and reducing the re-emission effect is to apply a technique involving the removal of a certain width from the top diode by etching. Consequently, a variety of diameters of cap-etched *p-i-n* diodes have been used to successfully carry out pure electron initiated-multiplication with a 405 nm laser source and mixed injection multiplication with a 1550 nm laser source.

An evolutionary fitting algorithm using the RPL model was utilised to extract the electron and hole impact ionization coefficients and threshold energies of GaInNAsSb. As the fitting was based on a non-uniform electric field profile, as previously explained, and an approximate absorption profile, these coefficients are not the final and most accurate coefficients for GaInNAsSb. This can also be attributed to the impossibility of obtaining pure electron and pure hole from the same diode, as well as the difficulty of achieving pure injection and precise mixed injection due to the risk of re-emission. Despite some concerns about the accuracy of these coefficients, they provide a good start from which to build further research into this material, and motivation to do so. In addition, they can provide valuable information indicating that beta is very significantly higher than alpha, an exciting characteristic, as well as the approximated field where the multiplication starts and breaks down.

This study of the impact ionisation in GaInNAsSb which is lattice-matched to GaAs, can support SAM APDs with GaInNAsSb absorber layer. The use of this material as an absorption layer in SAM APDs can exploit its narrow energy band gap to effectively detect light with longer wavelengths. The determination of impact ionisation coefficients is critical for the design of SAM APDs, as they provide crucial information on the electric field required for adequate multiplication and the optimal charge sheet thickness to maintain a low field in the low bandgap absorber. Moreover, achieving precise control over the charge sheet doping density and thickness is expected to be a difficulty in order to tailor the electric field profile of (SAM APD) structure. The low field in the small band gap dilute nitride absorption layer is required for two reasons.

First to minimize the tunnelling and SRH and hence reduce the leakage current. When designing SAM APDs, it is important to take into account whether or not the absorber and avalanche materials have similar electron / hole ionisation coefficient ratios. The worst case for APD noise and response time occurs when the absorber and multiplication layer have opposing coefficient ratios. However, in all cases noise is minimised when the electric fields of the (dilute nitride) absorption layer is maintained lower than the electric field required to initiate multiplication in the absorption layer. Given that beta is much larger than alpha in GaInNAsSb, it is worth noting that ionisation in the absorber would be very detrimental, if it were combined with a multiplication region such as AlGaAs where alpha is bigger than beta. Feedback holes, generated by ionization in the high-field AlGaAs multiplication layer, are likely to ionize in the GaInNAsSb layer because of its high value of β, generating more electrons, which subsequently enter the high-field AlGaAs layer and may create more carriers, leading to extended multiplication chains. This results in a wider distribution of multiplication factors in the AlGaAs APD when ionization is allowed in the GaInNAsSb layer for a given mean value of multiplication, leading to increased excess noise. [20]

In the future, more improvements on the measurements and the fitting can be made to effectively extract accurate electron and hole impact ionisation coefficients. This can be done by designing and fabricating new ideal *p-i-n* and *n-i-p* diodes with a range of multiplication widths to cover a wide range of electric fields without the detrimental effect of re-emission. Also, designing these diodes with more uniform electric field profiles and the ability to obtain both pure electron and hole-initiated multiplication from the same diode, as well as accurate knowledge of the absorption profile, will be an effective way. This can improve the fitting by reducing uncertainty in the measured multiplication and the number of parameters it depends on, to provide a precise characterisation of the impact ionisation coefficient of GaInNAsSb.

6.9 References

[1] X. Collins, *Dilute Nitride GaInNAsSb for Next Generation Optical Communications*. Lancaster University (United Kingdom), 2021.

[2] S. L. Tan *et al.*, "GaInNAsSb/GaAs Photodiodes for Long-Wavelength Applications," *IEEE electron device letters,* vol. 32, no. 7, pp. 919-921, 2011.

[3] M. M. Hayat, B. E. Saleh, and M. C. Teich, "Effect of dead space on gain and noise of double-carrier-multiplication avalanche photodiodes," *IEEE transactions on electron devices,* vol. 39, no. 3, pp. 546-552, 1992.

[4] X. Collins, A. P. Craig, T. Roblin, and A. R. J. Marshall, "Impact ionisation in Al0. 9Ga0. 1As0. 08Sb0. 92 for Sb-based avalanche photodiodes," *Applied Physics Letters,* vol. 112, no. 2, p. 021103, 2018.

[5] J. Callaway, "Optical absorption in an electric field," *Physical Review,* vol. 134, no. 4A, p. A998, 1964.

[6] G. Bulman, L. Cook, and G. Stillman, "The effect of electroabsorption on the determination of ionization coefficients," *Applied Physics Letters,* vol. 39, no. 10, pp. 813-815, 1981.

[7] B. Ng *et al.*, "Nonlocal effects in thin 4H-SiC UV avalanche photodiodes," *IEEE Transactions on Electron Devices,* vol. 50, no. 8, pp. 1724-1732, 2003.

[8] T. Li *et al.*, "Low-noise back-illuminated Al/sub x/Ga/sub 1-x/N-based pin solar-blind ultraviolet photodetectors," *IEEE journal of quantum electronics,* vol. 37, no. 4, pp. 538-545, 2001.

[9] J. Brown *et al.*, "Visible-blind UV digital camera based on a 32× 32 array of GaN/AlGaN pin photodiodes," *MRS Internet Journal of Nitride Semiconductor Research,* vol. 4, pp. 1-10, 1999.

[10] M. Grzesik *et al.*, "Impact ionization in AlxGa1− xAsySb1− y avalanche photodiodes," *Applied Physics Letters,* vol. 104, no. 16, p. 162103, 2014.

[11] W. Loh *et al.*, "Impact ionization coefficients in 4H-SiC," *IEEE Transactions on electron devices,* vol. 55, no. 8, pp. 1984-1990, 2008.

[12] J. Ng, C. Tan, J. David, G. Hill, and G. Rees, "Field dependence of impact ionization coefficients in In/sub 0.53/Ga/sub 0.47/As," *IEEE Transactions on Electron Devices,* vol. 50, no. 4, pp. 901-905, 2003.

[13] M. Woods, W. Johnson, and M. Lampert, "Use of a Schottky barrier to measure impact ionization coefficients in semiconductors," *Solid-State Electronics,* vol. 16, no. 3, pp. 381-394, 1973.

[14] A. Marshall, A. Craig, C. J. Reyner, and D. L. Huffaker, "GaAs and AlGaAs APDs with GaSb absorption regions in a separate absorption and multiplication structure using a hetero-lattice interface," *Infrared Physics & Technology,* vol. 70, pp. 168-170, 2015.

[15] S. Tan *et al.*, "Experimental evaluation of impact ionization in dilute nitride GaInNAs diodes," *Applied Physics Letters,* vol. 103, no. 10, p. 102101, 2013.

[16] S. Plimmer, J. David, G. Rees, and P. Robson, "Ionization coefficients in AlxGa1-xAs (x= 0-0.60)," *Semiconductor science and technology,* vol. 15, no. 7, p. 692, 2000.

[17] A. Adams, "Band-structure engineering to control impact ionisation and related high-field processes," *Electronics Letters,* vol. 40, no. 17, pp. 1086-1088, 2004.

[18] S. Cao *et al.*, "Theoretical studies on InGaAs/InAlAs SAGCM avalanche photodiodes," *Nanoscale Research Letters,* vol. 13, pp. 1-15, 2018.

[19] L. Tan, J. Ng, C. Tan, and J. David, "Avalanche noise characteristics in submicron InP diodes," *IEEE Journal of Quantum Electronics,* vol. 44, no. 4, pp. 378-382, 2008.

[20] J. Ng, C. Tan, J. David, and G. Rees, "Effect of impact ionization in the InGaAs absorber on excess noise of avalanche photodiodes," *IEEE journal of quantum electronics,* vol. 41, no. 8, pp. 1092-1096, 2005.

Chapter 7

$Al_{0.8}Ga_{0.2}As$/GaAs SAM Avalanche Photo Diodes and SPADs

7.1 Introduction

One potential use of GaInNAsSb is as the absorber in a GaAs based SAM APD, allowing the important telecoms wavelength of 1550 nm to be reached on this most mature III-V substrate. Prior to this PhD project, attempts were made to grow an AlGaAs/GaInNAsSb SAM APD, however they were compromised by modelling inaccuracies related to the ionisation coefficient. The dilute nitride is a five-component material with complicated growth conditions. Therefore, the development structure was simplified and in order to prepare for $Al_{0.8}Ga_{0.2}As$ /GaInNAsSb SAM APDs, a GaAs layer was initially utilised as the absorber layer in the SAM structure instead of GaInNAsSb. This GaAs layer was intentionally doped to be p-type with a concentration comparable to that of the expected GaInNAsSb at 4.0×10^{16} cm^{-3}. This simplified SAM APD structure can be used to identify the optimum charge sheet conditions without the extra complications caused by dilute nitride absorber. It can also be used to study properties for the $Al_{0.8}Ga_{0.2}As$ multiplication layer, as reported in this chapter.

In terms of the $Al_{0.8}Ga_{0.2}As$ multiplication layer, the non-local impact ionisation coefficients extracted using the hard dead space model of $Al_{0.8}Ga_{0.2}As$ were reported in Chapter 5, allowing even thin $Al_{0.8}Ga_{0.2}As$ diodes to be simulated and investigated. In addition, Chapter 6 presents essential background on the impact ionisation characteristics of GaInNAsSb, which can be used later for further research. This chapter, in addition to the previous ones, can provide valuable information and lay the groundwork for future studies of $Al_{0.8}Ga_{0.2}As$ /GaInNAsSb SAM APDs.

7.2 Device design

In order to achieve the ideal charge sheet characteristics for GaAs/ $Al_{0.8}Ga_{0.2}As$ SAM APDs, the structure of APD (sample 3) was designed by a recent PhD student (X. Collins), as shown in Table 7.1. The electric field conditions in both the absorber layer and the multiplication layer were controlled by the width and the doping concentration of the charge sheet. In order to achieve sufficient electric field in the multiplication layer required for the avalanche process and to maintain the electric field in the absorber layer under a threshold field to collect photogenerated carriers without inducing tunnelling and excessive SRH currents, different devices with different charge densities in the charge sheet were designed based on RPL model using incorrect Ng's ionisation coefficients as shown in Table 7.2 [1]**.** Then, the doping concentration and the width of the layers were controlled by IQE. Samples 1 and 2 aimed to achieve punch-through at a lower voltage and samples 4 and 5 aimed to achieve punch-through at a higher voltage, to cover uncertainty in modelling and growth. Due to the preferences of IQE, who grew the samples, changing thickness and doping were both tried to give the variation in punch-through.

Layer	Material	Thickness (nm)	Doping (cm^{-3})	
Contact	$GaAs$	100	p	5.0×10^{18}
Cladding	$GaAs$	200	P	1.0×10^{18}
Absorber	$GaAs$	1000	P	4.0×10^{16}
Grading 1	$GaAs$	50	P	2.0×10^{17}
Grading 2	$Al_{0.4}Ga_{0.6}As$	40	P	2.0×10^{17}
Charge Sheet	$Al_{0.8}Ga_{0.2}As$	25	P	2.0×10^{18}
Multiplication	$Al_{0.8}Ga_{0.2}As$	50	UID	-
Cladding	$Al_{0.8}Ga_{0.2}As$	250	N	1.0×10^{18}
Contact	$GaAs$	1000	N	5.0×10^{18}
Semi-Insulating GaAs Substrate				

Table 7.1: The design of APD (sample 3) [1]

Doping increases →

Thickness increases ↓

	Sample 1 18 nm 2.0×10^{18}	
Sample 2 25 nm 1.5×10^{18}	Sample 3 25 nm 2.0×10^{18}	Sample 4 25 nm 2.4×10^{18}
	Sample 5 32 nm 2.0×10^{18}	

Table 7.2: The range of GaAs-based APDs [1].

X. Collins fabricated these devices a year before starting this study and subsequent extracting of the AlGaAs non-local impact ionisation coefficient that accurately models the multiplication and breakdown voltage for thin multiplication diodes. He modelled the multiplication for the five samples using the RPL model, which was developed from the model of ref [2] as described in Section 2.2.3, with local electron and hole impact ionisation coefficients reported by Ng *et al*. [3], together with the given threshold energies. These coefficients failed to correctly simulate the multiplication, resulting in an overestimation of the breakdown voltage. The electric field profile and the I-V characteristics of the samples show some error in the design of the structure, as described later. Indeed, the five samples reported here were the third attempt to successfully design and grow such thin AlGaAs SAM APDs, mostly due to inaccurate modelling.

In this work, the devices have been fabricated using the mixed area mask, a type of photomask with circular mesas whose diameters range from 25 µm to 800 µm, designed by A. R. J. Marshall, as shown in Figure 7.1. *p*-*i*-*n* (*n*-*i*-*p*) photodiodes made with two top contacts, a *p*-type contact (*n*-type contact) on top of each mesa, and an *n*- type (*p*-type) grid contact deposited onto the *n*-type (*p*-type) epilayer, after the mesa has been etched. Since series resistance is an essential parameter for many APD applications, high series resistance can be a serious problem for high-speed or low- bias APDs. Proper selection of metals, which vary based on the semiconductor and the type of doping concentration in the contact layer, is essential for achieving ohmic contacts, low contact series resistance, and a negligible rectifying Schottky barrier. For instance, for p-type GaAs, Au (10 nm)/Zn (20 nm)/Au (200 nm) contacts were usually utilised [4] whereas InGe (20 nm)/Au (200 nm) contacts were used in the case of n-type GaAs.

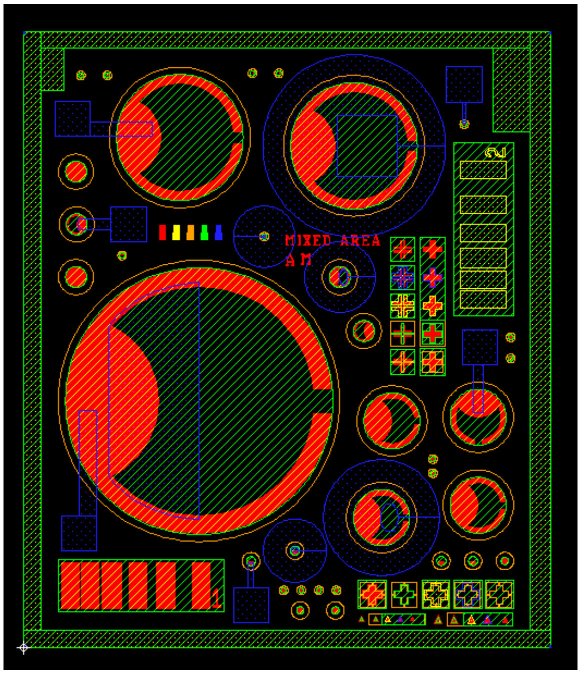

Figure 7.1: An image of "mixed area" mask used, with circular mesas of diameters ranging from 25 μm to 800 μm, a grid contact, and TLM patterns. Designed by A. R. J. Marshall.

7.3 Electrical characterization

The current-voltage measurements and capacitance-voltage measurements were carried out for the five samples.

7.3.1 Current-Voltage (I-V) Measurements

Current-voltage I-V measurement is one of the most fundamental APD characterization techniques. Forward and reverse IV measurements have been employed to assess and offer a great deal of information about an APD, including its contact, fabrication method, and the material that is used.

An example of the forward measurements for sample (1), as shown in Figure 7.2. The figure shows the contact resistance affecting the forward diode characteristic at currents above 10^{-5} A. The gradient at low voltage gave an ideality factor (n) of 1.9 while at high voltage, the ideality factor was 1.7. At the low voltage range, since there is a low number of injection carriers, the majority of them can be recombined with the assistance of the fixed number the defects, making SRH the dominant recombination mechanism and n close to 2. On the other hand, at the high voltage range, the number of carriers increases significantly, and the defects tend to be saturated which limits the SRH recombination and makes radiative recombination more significant, reducing n.

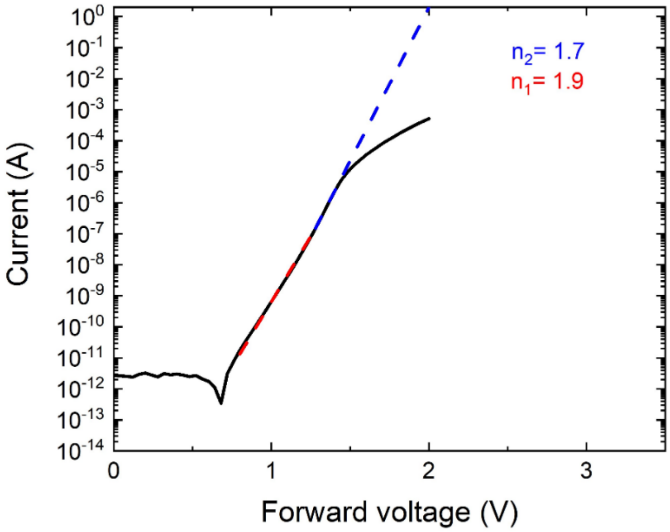

Figure 7.2: Forward I-V characteristic of a 200 μm diameter diode from sample 1. The two values of the ideality factor n_1 and n_2 were fitted at low and high voltage ranges respectively.

The I-V characteristics of all samples in the dark and with a white LED light source have been investigated to select the best device with a suitable charge sheet for APD applications.

Since the dependence of the dark current and photocurrent on device areas is similar for the five samples, sample 2 is illustrated in Figure 7.3 as an example. The figure shows that the photocurrent is always higher than the dark current, and both the photocurrent and the dark current are proportional to the device area. It also illustrates that breakdown voltage changes between devices and breakdowns occur suddenly and do not behave as expected for bulk breakdowns. This can be attributed to the edge breakdown, which limits the upper gain values achievable. This effect is more obvious in sample 2, where the electric field depletes the junction between GaAs and AlGaAs layers. These layers etch at different rates, changing the shape of the sidewall [5]. The electric field is affected by the shape of the sidewall, and it is known that non-vertical sidewalls lead to field hot spots and cause earlier edge breakdown. The figure also shows the resistance effect, which limits the total current flow after the breakdown.

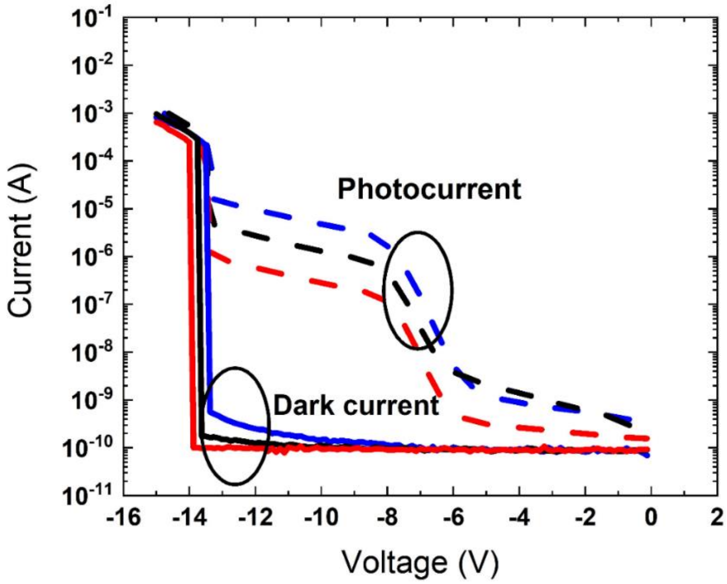

Figure 7.3: Current-Voltage characteristics of GaAs/AlGaAs APD (sample 2). Dark current (solid line) and photocurrent (dashed line) for detectors of diameter 800 µm (blue), 400 µm (black) and 200 µm (red).

These samples exhibit low dark current, which is measured to be less than 1 nA at 90 % of the breakdown voltage. This behaviour can be attributed to two dominant reasons. As GaAs and AlGaAs have similar lattice constants, the dark current due to the defects created through the growth is low. Moreover, the charge sheets of samples 2, 3, and 5 have a suitable charge density, which results in a high electric field in the wide band gap AlGaAs multiplication layer and a low electric field in the smaller band gap GaAs absorption region. This can limit the tunnelling and SRH currents in the absorber layer, which reduces the dark current.

One of the critical techniques to evaluate the diode behaviour and identify the dominant leakage current is through the reverse I-V characteristics. As all samples have the same characteristics in their current density and current per unit perimeter, for simplicity, the measurements have been illustrated just for sample 1, as shown in Figure 7.4. The figure shows that there is a good agreement in current per unit perimeter for different device areas, while there is a clear difference in current density. It can be concluded that the leakage current flowing is predominantly surface in nature.

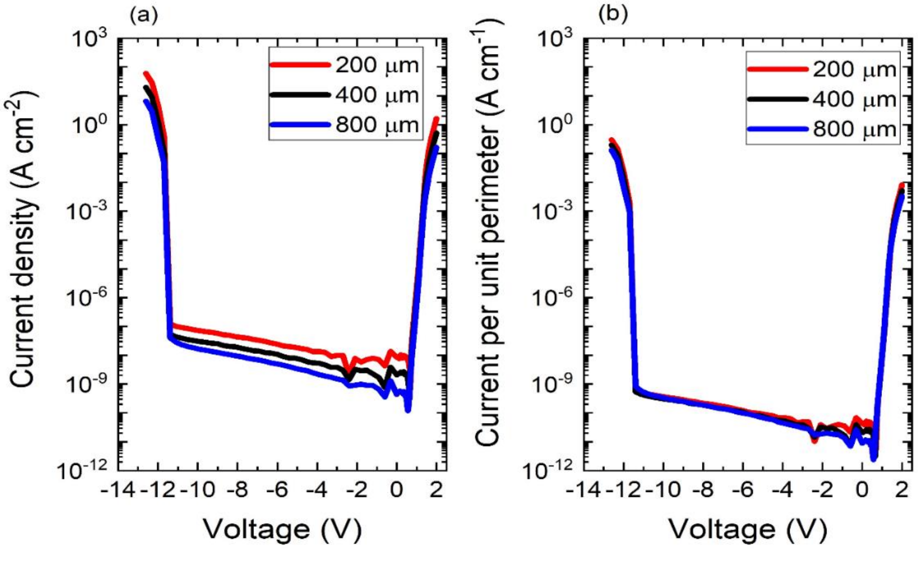

Figure 7.4: Current density (a) and current per unit perimeter (b) as a function of the voltage of the GaAs/AlGaAs APD of diameter 200 μm,400 μm, and 800 μm for sample (1).

Figure 7.5 shows the measured photocurrent as a function of voltage for the five samples using a simple white LED light source. Since samples 1 and 2 have similar behaviour and samples 4 and 5 also have similar characteristics, the I-V measurements for samples 2, 3, and 5 have been investigated. Punch-through voltage is a significant variable in SAM APDs, which is the voltage value where the electric field starts to deplete the absorber layer, resulting in the drift of the photogenerated carriers from the absorber layer to the multiplication region. As mentioned before in Section 5.1, since sample 2 has the lowest charge sheet doping concentration, its absorber layer starts to deplete at a punch-through voltage of ~ -9.4 V, and the useful APDs operation can be considered only up to ~14 V due to the earlier edge breakdown. Due to the significant difference between the punch-through voltage and the breakdown voltage, sample 2 can be used as an example of a device functioning as a SAM APD. However, samples 3 and 5 never fully punch through due to the high dopant level in their charge sheets, and the breakdown voltage occurs at ~-12V in both samples. Consequently, these samples are not appropriate for SAM APD applications. From this initial photocurrent characterization, it is clear that attempts to adjust the nominal design (sample 3) in response to the errors in modelling with old coefficients have not been fully successful. This can be demonstrated by the electric field profiles of samples 2, 3, and 5, as shown in Figure 7.6. In sample 2, 14 V is used as an estimated value of the breakdown voltage, while the true bulk breakdown is hidden by the edge breakdown. At breakdown voltage V_{bd}, the electric field partially depletes the absorber layer in sample 2, while it does not reach the absorber layer in samples 3 and 5. By using GaInNAsSb as an absorber, the electric field should be kept lower than the electric field required to initiate the multiplication which is about 250 kV/cm. This is achievable in sample 2, where the electric field in the absorber at the estimated breakdown voltage does not exceed 88 kV/cm.

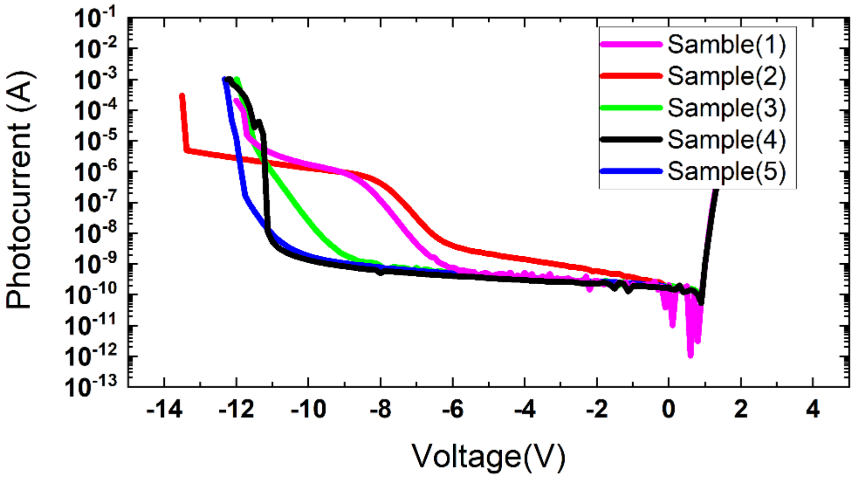

Figure 7.5: The photocurrent in each GaAs/AlGaAs APDs of diameter 400 µm when illuminated by a white light source. All samples exhibit light detection, although samples 1 and 2 only exhibit light in significant levels.

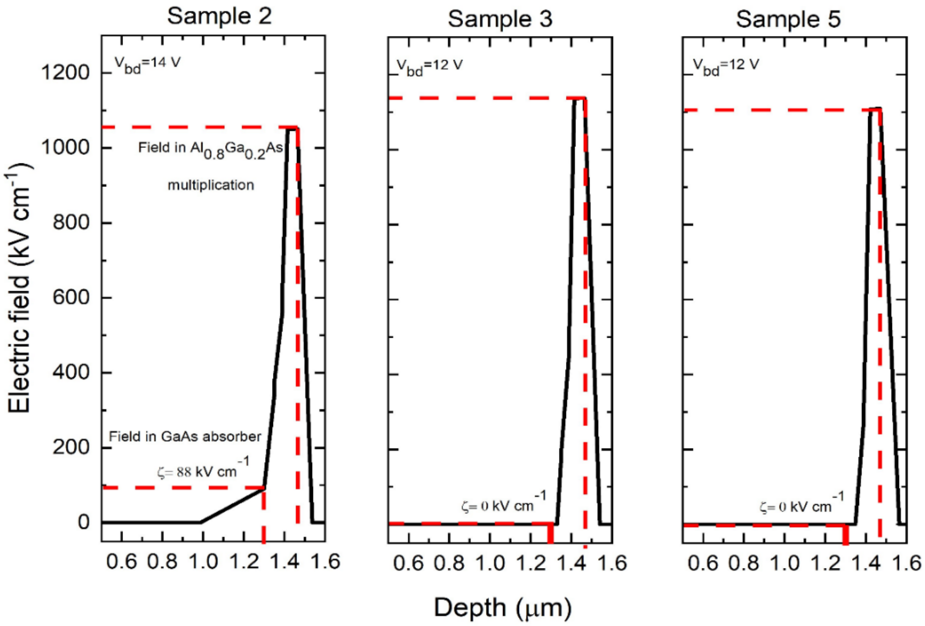

Figure7.6: A comparison of the electric field profile at breakdown voltage V_{bd} for samples 2,3 and 5 using the fitted input structure for the simulated capacitance.

7.3.2 TLM Measurements

Since significant contact resistance is demonstrated in Figure 7.2 for the forward measurement, TLM was used to check for ohmic contacts and to identify the contact resistance for the upper contact layers (p GaAs-metal contact) and lower contact layers (n GaAs-metal contact). The same method described in the experimental chapter was applied. The I-V measurement for one pair of upper and lower contacts has been shown in Figure 7.7 (a), (b) respectively. The figure illustrates that the contact resistance is ohmic for the p GaAs-metal contact but not for n GaAs-metal contact. This high non-ohmic resistance can be attributed to some possible reasons. The etching might be deeper than expected, and the metal might be deposited on the semi-insulating (SI) substrate rather than on the n-GaAs contact layer. The other reason might be due to a growth error where the n-GaAs layer was not properly doped. To check the etching uncertainty, one of the samples was etched again, and the same result was obtained. This can increase the possibility of the second reason, having lower doping than expected in n-GaAs. However, since the area of the n GaAs-metal contact (grid contact) was very large, the effects of the non-ohmic resistance should not prohibit further characterisation. In the case of the ohmic contact in the upper contact layer, the plot of R_t as a function of *L* must intercept the y-axis to obtain 2Rc, making R_c approximately 75 Ohms, as shown in Figure 7.8.

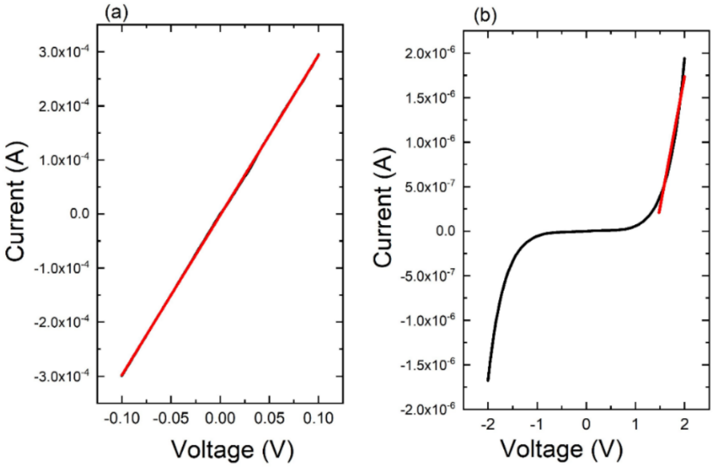

Figure7.7: I-V measurements for one pair of upper contact layers (p GaAs-metal contact) (a) and lower contact layers (n GaAs-metal contact) (b).

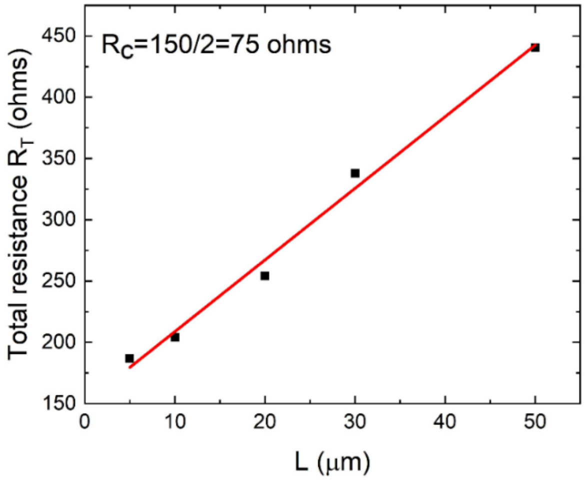

Figure7.8: Total resistance R_T as a function of the separation between pads L. The linear fit intercepts the y-axis at $2R_C$ which is equal to 150 ohms.

7.3.3 Capacitance-Voltage (C-V) Measurements

In order to identify the actual doping profile of samples 2, 3, and 5, the capacitance model was used to fit the modelled capacitance to the measured one. The layer thicknesses were fixed because the MBE growth used has excellent growth control, while their doping was changed. The comparison of the simulated and measured capacitance densities of the samples 2, 3, and 5 is shown in Figure 7.9. The intentional and fitted doping profiles of samples 2 and 5 are shown in Tables 7.3 and 7.4, respectively. The tables illustrate that the fitted doping concentration is close to the designed structure. Also, both fits show a reduction in the charge sheet's doping concentration and n-AlGaAs layer, while the fitted doping in the p-$Al_{0.4}Ga_{0.6}As$ layer is shown to be increased. As the figure shows, sample 5, which has the highest doping concentration in the charge sheet, does not punch through, and its charge sheet is fully depleted around 7 V just before the breakdown. The first heterojunction between the charge sheet and grading 2 starts to partially deplete, while the second one between grading 2 and grading 1 is not depleted. As a result, the I-V characteristic for sample 5 in Figure 7.5 does not show any significant photocurrent before the breakdown.

Since sample 3 has a lower doping concentration in its charge sheet compared to sample 5, the charge sheet is fully depleted and the first heterojunction starts to deplete at a lower voltage of -4 V, and its grading 2 is fully depleted and the second heterojunction starts to deplete around -8 V, and it does not exhibit punch-through. As a result, Figure 7.5 shows a small photocurrent in sample 3 before the breakdown due to the diffusion through the heterojunctions. On the other hand, the charge sheet and grading 2 of sample 2, which has the lowest doping concentration, are completely depleted at lower voltages of about -2 V and -4 V, respectively. Also, sample 2 punches through around -10 V, which is significantly lower compared to the breakdown voltage at -14 V. So, sample 2 in Figure 7.5 shows a significant photocurrent. As a result, samples 2 and 5 can be studied as examples of a device functioning as a SAM and a device functioning as an AlGaAs *p*-*i*-*n*, respectively. Figure 7.10 illustrates the modelled band structure of sample 2 at zero bias voltage.

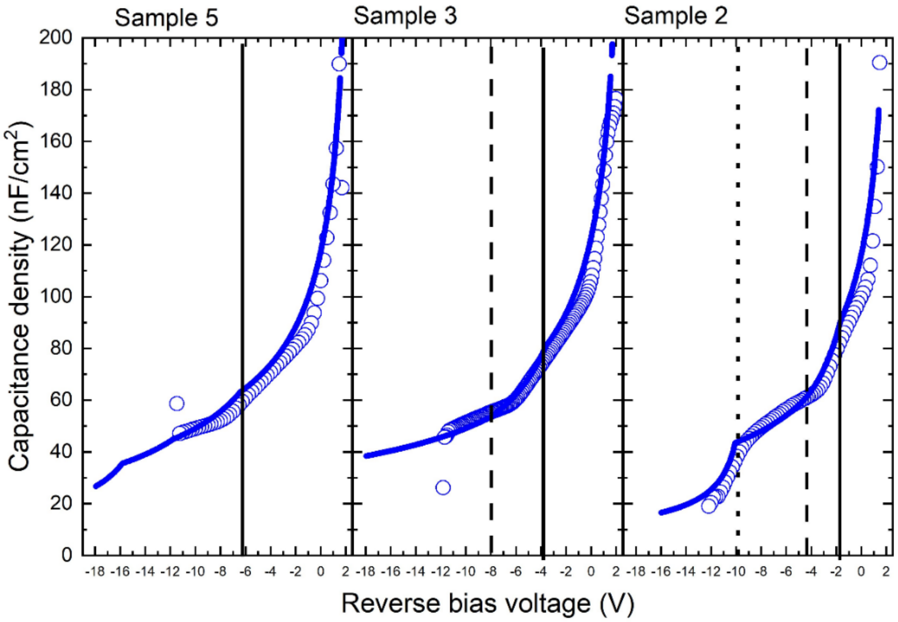

Figure7.9: The experimental (symbols) and modelled (solid line) capacitance density of samples 2, 3, and 5. The solid black line indicates the full depletion of the charge sheet, while the dashed line indicates the full depletion of grading 2. The dotted line represents the full depletion of the two grading layers and absorber punch-through.

Layer	**Material**	**Thickness (nm)**	**Doping** (cm^{-3})		**Fitted doping** (cm^{-3})
Contact	$GaAs$	100	5.0×10^{18}	P	5.0×10^{18}
Cladding	$GaAs$	200	1.0×10^{18}	P	1.0×10^{18}
Absorber	$GaAs$	1000	4.0×10^{16}	P	2.1×10^{16}
Grading 1	$GaAs$	50	2.0×10^{17}	P	3.6×10^{17}
Grading 2	$Al_{0.4}GaAs$	40	2.0×10^{17}	P	3.1×10^{17}
Charge Sheet	$Al_{0.8}GaAs$	25	1.5×10^{18}	P	1.0×10^{18}
Multiplication	$Al_{0.8}GaAs$	50	-	UID	1.0×10^{15}
Cladding	$Al_{0.8}GaAs$	250	1.0×10^{18}	N	0.85×10^{18}
Contact	$GaAs$	1000	5.0×10^{18}	N	5.0×10^{18}
Semi-Insulating GaAs Substrate					

Table 7.3: A comparison of the intentional doping levels and the fitted doping concentrations of sample 2.

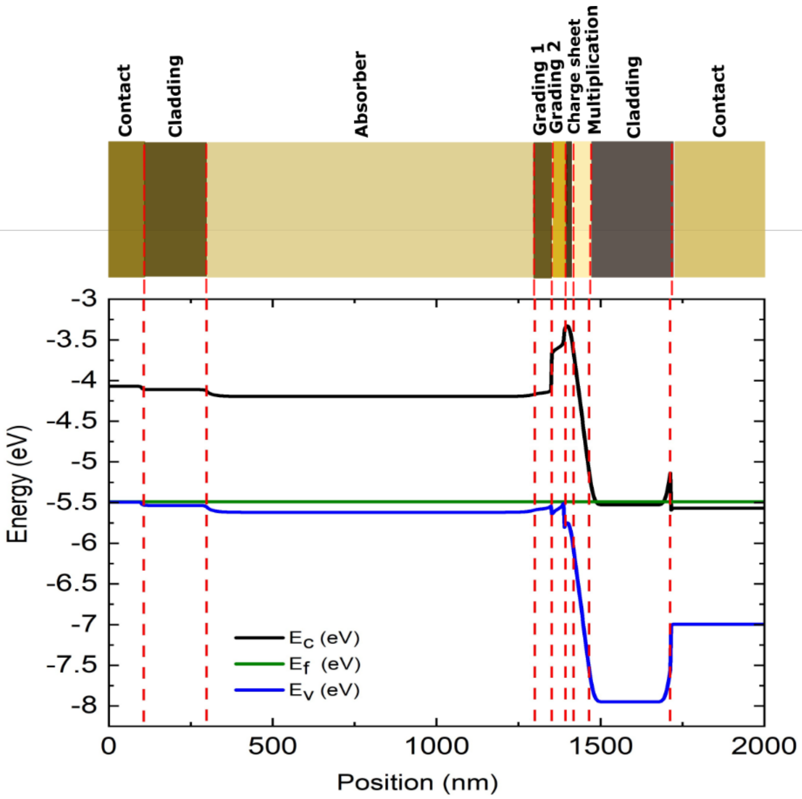

Figure 7.10: The band diagram for sample 2 at zero bias voltage.

Layer	Material	Thickness (nm)	Doping (cm^{-3})		Fitted doping (cm^{-3})
Contact	$GaAs$	100	5.0×10^{18}	P	5.0×10^{18}
Cladding	$GaAs$	200	1.0×10^{18}	P	1.0×10^{18}
Absorber	$GaAs$	1000	4.0×10^{16}	P	4.0×10^{16}
Grading 1	$GaAs$	50	2.0×10^{17}	P	2.0×10^{17}
Grading 2	$Al_{0.4}GaAs$	40	2.0×10^{17}	P	4.4×10^{17}
Charge Sheet	$Al_{0.8}GaAs$	32	2.0×10^{18}	P	1.48×10^{18}
Multiplication	$Al_{0.8}GaAs$	50	-	UID	1.0×10^{15}
Cladding	$Al_{0.8}GaAs$	250	1.0×10^{18}	N	0.7×10^{18}
Contact	$GaAs$	1000	5.0×10^{18}	N	5.0×10^{18}
Semi-Insulating GaAs Substrate					

Table 7.4: A comparison of the intentional doping levels and the fitted doping concentrations of sample 5.

The built-in voltage was calculated for the five samples over different areas as described in the experimental chapter. All samples exhibit a similar built-in voltage which ranges from 1.5 V to 2 V. An example of sample 2 is shown in Figure 7.11.

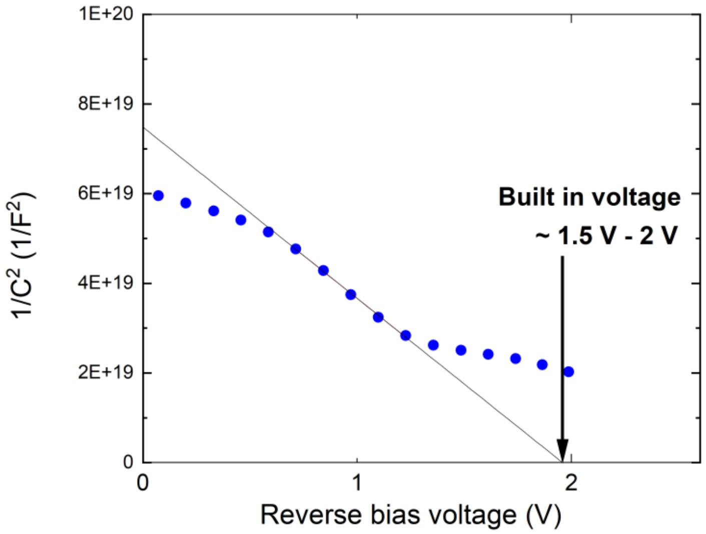

Figure 7.11: A plot of 1/C^2 calculated from measurements on sample 2.

7.4 Photomultiplication measurements

In Chapter 5, the nonlocal electron and hole impact ionization coefficient parameters, which are consistent with the RPL model, have been extracted. To validate these parameters with the RPL model, a comparison was made between the experimental multiplication of samples 2 and 5 and the modelled multiplication utilising the RPL model with these revised coefficients. This is a valuable comparison because the samples have very thin multiplication widths, in the range where the new coefficients should improve simulation accuracy. The samples are also grown entirely independently from those used to derive the coefficients, on a different continent two decades later. So, they are a good test of the universal applicability of the coefficients. The pure electron-initiated multiplication of sample 2 was measured by illuminating the top of the device using the blue (405 nm) laser. The absorption coefficient α_{abs} of GaAs at 405 nm is $\sim 6\times10^{5}\,cm^{-1}$ [6]. This coefficient can be used to calculate the intensity of light remaining $\varphi\,(x)$ as the light travels through the p-type GaAs contact, cladding and absorber layers, which have a combined thickness of x = 1300 nm. Using equation 2.2, it was found that $\varphi\,(1000\,nm)= 1.33\times10^{-34}$ which means that much greater than 99.9 % of the light which enters the diode will be absorbed by the p-type

GaAs absorber and overlying layers. As a result, the photogenerated carriers must be collected from the absorber layer into the multiplication region. Since there is a heterojunction and band offset between the charge sheet and grading 2 and another one between grading 2 and grading 1, it is necessary to apply electric field at these junctions, to allow the photocurrent to flow. As shown in Figure 7.12, at sufficiently high bias, the electric field will bend the barriers caused by the band offsets, allowing the photogenerated carriers which diffuse through the absorber, to drift into the multiplication region. In a simple *p*-*i*-*n*, the multiplication factor can be calculated accurately using the baseline technique, where the primary photocurrent varies with depletion width and can be fitted at low voltage before starting the gain. On the other hand, in this sample, due to the presence of the two junctions before the absorber layer, the primary photocurrent does not behave the same way as simple *p*-*i*-*n*, and the baseline technique is no longer applicable. Consequently, an approximate experimental gain was calculated by first determining the modelled gain value at punch-through voltage using the non-local coefficients with the RPL model, which is -10 V. This gain value was then used in the experimental data to calculate the primary photocurrent at punch-through voltage. Then, the primary photocurrent was utilized to calculate the gain at each voltage value.

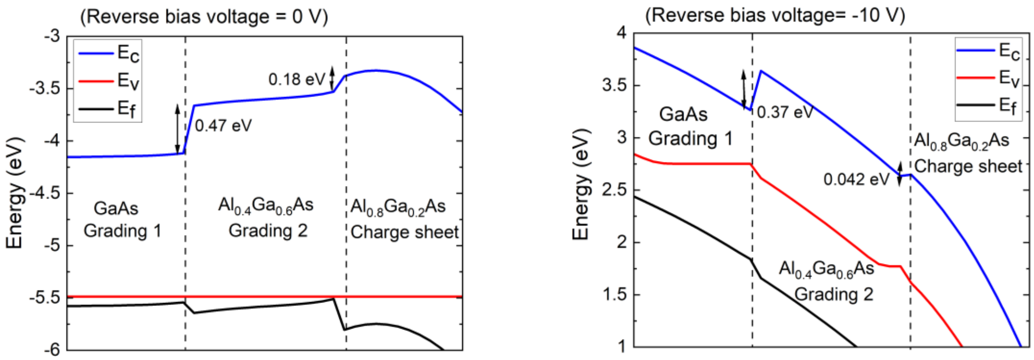

Figure 7.12: The band diagram of sample 2 at 0 V and -10 V reverse bias voltage.

It is known that the total applied voltage is divided between the diode and the series resistance. Then, as the laser power increases, the photocurrent increases too, leading to a drop in some voltage across the series resistance and subsequently reducing the voltage dropped across the diode, which reduces the multiplication. In order to investigate the effect of the resistance on the multiplication, the photocurrent measurements were carried out on sample 2 using a range of power values. In this case, as shown in Figure 7.13, at voltage values up to 12 V, for all the powers, the photocurrent through the diode is small and not enough to show the effect of resistance on the multiplication. On the other hand, above ~13 V, the lowest power (0.01 mw) can be considered the upper true limit with negligible effect of resistance. With an increase in power and associated photocurrent, the effect of resistance increases, increasing the total applied voltage required for a given multiplication and shifting the curve to a higher voltage. In our diodes, the dark current is very low, and the signal is clear; hence, there is no need to use high power and the correction can be avoided.

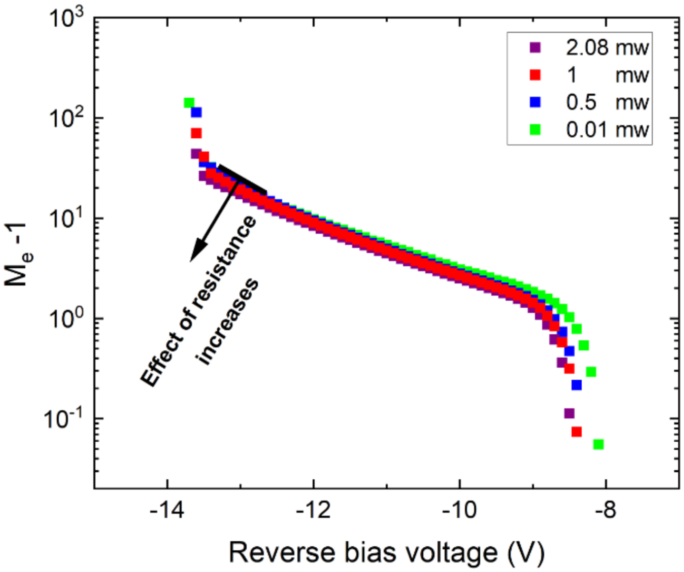

Figure 7.13: M_e-1 as a function of reverse bias voltage for sample 2 using a range of power values.

Sample 5, as described previously, acts as a simple *p-i-n* with an undepleted potential barrier between the multiplication layer and the absorber, making it impossible to achieve primary electron photocurrent and hence, calculate the pure electron- initiated multiplication by the top illumination. Therefore, the experimental multiplication was calculated in a different way and compared to the model. In order to achieve pure hole injection, the fibre was positioned to illuminate next to and as close as possible to the device to achieve a measurable primary photocurrent by diffusion. On the other hand, the fibre had to be sufficiently far away from the side wall to avoid any mixed injection from light falling on the sidewall. Then, the baseline technique was used to calculate pure hole-initiated multiplication, M_h.

Figure 7.14 illustrates a comparison between the experimental multiplication and the modelled multiplication using the RPL model with the new nonlocal coefficient for samples 2 and 5 and for a simple 25 nm intrinsic width *p-i-n* diode. For simplicity the simple *p-i-n* is included to demonstrate how the new non-local coefficients might enhance the fitting and return an accurate breakdown voltage.

The model simulates only the bulk and does not simulate multiplication at the hot spots, that cause the earlier edge breakdown. As a result, in the comparison for sample 2, the experimental multiplication breaks down at a lower voltage than the expected voltage in the model.

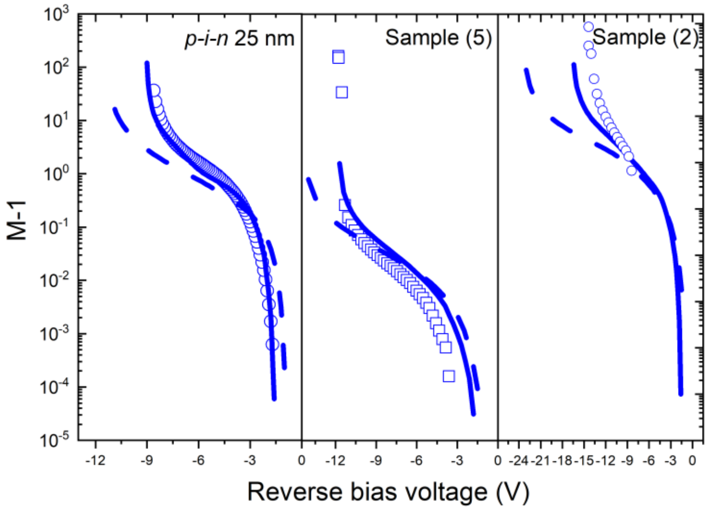

Figure 7.14: Multiplication characteristics of a 25 nm intrinsic width *p-i-n* diode, sample 5 and sample 2. Symbols represent experimental data while solid lines represent results calculated using RPL model with the non-local impact ionization coefficients extracted in Chapter 5. Dashed lines represent results calculated using RPL model with Ng's local coefficients.

7.5 Dark Count Rate DCR

DCR measures the number of dark counts per second, one of the core parameters for any SPAD. This has been measured with gated overbiasing and quenching. The DCR includes primary and secondary pulses. Primary dark pulses can be attributed to the thermal energy exciting electrons (SRH) during the overbias time, which then trigger avalanches. In addition, a high over-bias voltage also contributes to the primary dark pulses in two ways. It may increase the tunnelling or avalanche probability by increasing the electric field across the junction. The secondary dark pulses are generated due to the effect of afterpulsing. Afterpulsing takes place when trapped carriers in the avalanche region are released, as defined by a time constant, and trigger avalanche breakdown in a subsequent overbias cycle. It is obviously desirable to minimise the DCR for a practical SPAD.

7.5.1 Primary dark count rate

To achieve a primary DCR without significant influence from afterpulsing, DCR measurements were investigated at room temperature for sample 3 with diodes of 50 and 100 µm diameters, at a low frequency of 1 Hz and a 1% duty cycle over a variety of over-bias voltage. The DC bias voltage was 9 V, and the breakdown voltage was 11.6 V. Since the gate-off time is much longer than the gate-on time with these test conditions, trapped carriers have time for release before the subsequent bias pulses, eliminating the afterpulsing effect. Figure 7.15 illustrates DCR as a function of over- bias voltage. As the dark current increases with area, more DCR was observed in a larger area. However, the difference in DCR is not consistently a factor of 4 in line with the area factor between the devices. This suggests that surface contributions cannot be neglected in AlGaAs SPADs and will need consideration in further analysis.

Figure 7.15 also illustrates that the DCR increases with the over-bias bias voltage. This can be attributed to increasing both the breakdown probability and the dark carrier generation, such as tunnelling. As the tunnelling is exponentially increased with over- bias voltage, the exponential rise of DCR could be evidence that DCR is dominated by tunnelling. This would allow for an estimate of bias-dependent dark carrier generation beyond breakdown, where obviously, normal dark current measurements are not possible.

Since the breakdown probability code was written and successfully confirmed by comparing it with other people's work and the accurate electron and hole impact ionisation coefficients of AlGaAs were extracted, the breakdown probability can be simulated correctly and compared to the measured DCR. This comparison helps to identify how much of the rise in DCR is due to increased breakdown probability and how much is due to increased dark carrier generation. The breakdown probability increases with overbias and saturates at a given voltage, if the DCR still increases after this voltage, this increase is due to dark carrier generation, usually tunnelling. As a result, using any higher voltage is definitely undesirable since it will not improve the detection efficiency but just increase the DCR.

Recently, the most suitable and common devices used for SPAD operation at 1550 nm are InGaAs/InP devices. These devices offer the lowest DCR compared to other epitaxial growth SAM structures such as InGaAs/InAlAs SPADs and germanium- on- silicon SPADs. Karve *et al.* [7] found that InGaAs/InP devices, even at higher operating temperatures, exhibit an order of magnitude lower DCR probability than InGaAs/InAlAs. In addition, in germanium-on-silicon SPADs, despite the super quality and low DCR of the Si multiplication layer, the Ge/Si lattice mismatch decreases germanium quality and limits the SPADs performance by increasing the DCR probability [8].

The tunnelling in InGaAs/InP devices usually limits the minimum achievable multiplication thickness, which is often ~1 µm. Our SPADs using a much smaller multiplication thickness and less mature structure already exhibit slightly lower DCR at room temperature compared to the DCR reported for InGaAs/InP SPADs [9]. Using a thinner multiplication layer can improve SPAD performance by reducing the avalanche build-up time and jitter. In the future, our SPADs can be improved by using more sophisticated structures, such as the planar design commonly observed in InGaAs/InP, which reduces surface leakage current and hence DCR and edge breakdown.

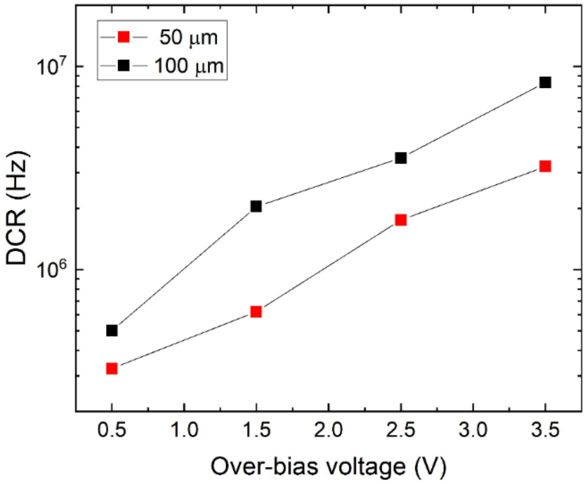

Figure 7.15: DCR as a function of over-bias voltage for sample (3) with 50 and 100 μm diameters at 1 Hz and 1% duty cycle.

7.5.2 Afterpulsing probability

In order to investigate the effect of the afterpulsing probability, DCR measurements were repeated on sample 3 with a 25 μm diameter for a frequency ranging from 1 to 100 kHz and at a constant over-bias voltage of 1.5 V and 50 μs gate-on time. The 25 μm diameter device was used to allow exploration of shorter gate off times with enough time resolution, because overall the DCR is smaller in the small device. When the gate off time decreases, the afterpulsing and hence DCR increases which requires a higher time resolution to accurately measured DCR. Figure 7.16 shows a DCR dependence on gate-off time. The figure illustrates that at low-frequency values with long gate-off times, the DCR remains constant. This indicates that the main contribution to the DCR is given by thermally generated initiating carriers rather than by carriers trapped during previous avalanche events. On the other hand, the afterpulsing effect starts to show at a long off time of ~ 400 ms which limits the maximum frequency at which this SPAD could be operated. This indicates the significant effect of afterpulsing in this AlGaAs SPAD. The afterpulsing observed in this AlGaAs SPAD is significantly higher than the negligible afterpulsing observed in InGaAs/InAlAs SPAD [10]. It is also significantly higher than the afterpulsing reported for both planar germanium-on-silicon SPAD [8] and InP/InGaAs SPAD, which shows afterpulsing only below off time equal to 10 μs [9].

One of the most important factors influencing the afterpulsing probability is gate-on time. The high afterpulsing probability observed in our case could in-part at least be attributed to the considerably longer gate-on time used compared to more advanced SPADs measurement set-ups, which only use a few tens of nanoseconds.

As shown in Figure 7.16, by fitting the DCR, the release time of trapped carriers or the time constant can be determined. Since a single value of the time constant would not be enough for the fitting, three values were determined using the following exponential equation:

$$y = y_\circ + A_1 * \exp(-(x - x_\circ)/t_1) + A_2 * \exp(-(x - x_\circ)/t_2) + A_3 * \exp(-(x - x_\circ)/t_3) \qquad 7.1$$

where $y_\circ$, A_1, A_2, A_3, and $x_\circ$ are fitting constants, and t_1, t_2, and t_3 are the first, second, and third time constants, respectively. This means that there are likely three main families of deep levels responsible for trapping avalanche carriers.

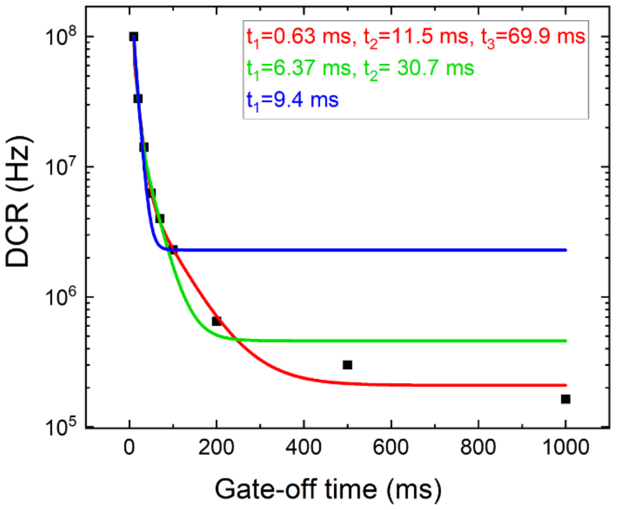

Figure 7.16: DCR of sample 3 with a 25 μm diameter versus gate-off time at room temperature at a constant over-bias voltage equal to 1.5 V. The blue solid line represents the fitting with one time constant while the green line indicates the fitting with two-time constants. The red line represents the fitting with three time constants.

The existence of deep traps in surface [11] or bulk [12], [13], [14], [15] AlGaAs devices at the same or similar structural and growth conditions has been confirmed. Ren *et al*. investigated how the dark count probability and afterpulsing probability changed after annealing arsine with hydrogen carrier gas [12]. He employed the double pulse separation set up with pulse width of only ~ 5 ns. As a result, the time scale used to look for afterpulsing is much smaller than in our case. As the release time of the deep defects is very long, their associated afterpulsing appears to be constant within this small-time window. These after-pulses can be considered a background, which increases the DCR probability. The deep defects were passivated during annealing, which greatly reduced the DCR probability. On the other hand, since only shallow defects and not deep ones can influence afterpulsing on this small-time scale, the annealing process had no effect on the observed afterpulsing probability. In the future, our SPADs can be improved by annealing, which would be expected to drastically decrease the DCR.

7.5.3 DCR per unit area and perimeter

The dominant bulk- and the dominant surface-related DCR should scale with diode area and perimeter, respectively. Hence, the origin of the DCR can be determined by normalizing the DCR to the diode area and perimeter. At two frequency values of 1 Hz and 15 Hz, the DCR measurements were carried out on 50, 100, and 200 μm diameter diodes from sample 1 with 50 μs gate-on time. In order to maintain the same time constant (R_1C_{SPAD}) across various areas, R_1 must be varied as the SPAD area varies. This ensures that the SPADs all charge to the overbias at the same time and there is no potential for the DCR fitted to be affected. This was achieved by using a switch- selected resistor (R_1) with a range of values as described in Section 4.4.

Since the DCR varied from one device to another, the measurements were repeated for many devices, and the most consistent DCR value was considered for each diameter. Then, to identify which DCR is dominant at each frequency, the DCR per unit area and perimeter was calculated as shown in Figure 7.17. The figure illustrates that the bulk mechanisms dominate the DCR at off time of ~1000 ms, whereas surface mechanisms dominate the DCR is dominant at off time of ~66.6 ms, when the gate off time is reduced.

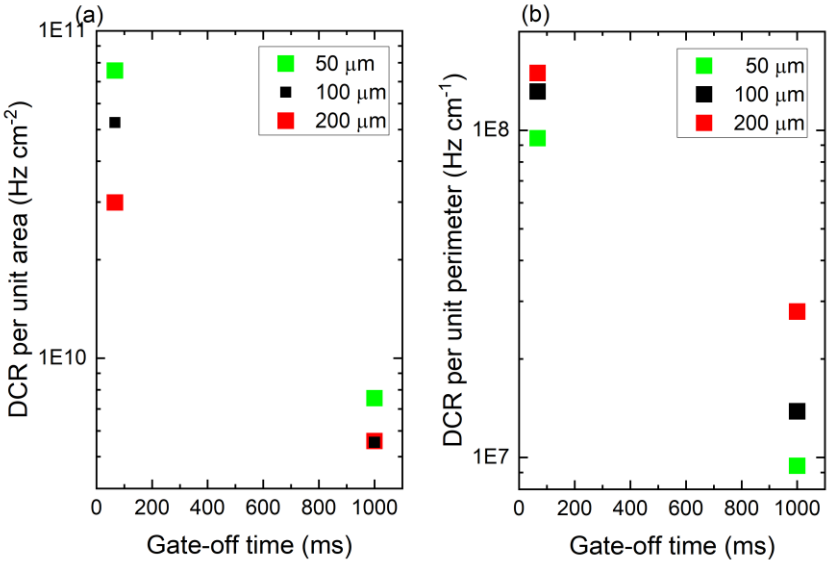

Figure 7.17: DCR per unit area (a) and per unit perimeter (b) vs. gate-off time for sample (1).

The off time of ~1000 ms was used to show the dominant DCR without any effect of afterpulsing. On the other hand, to demonstrate the dominant DCR including afterpulsing, an off-time equal to ~66.6 ms was selected where the afterpulsing is significant as shown in Figure 7.16. At this off-time, only the third released time constant which is slightly longer time than the off-time is effective while the effect of the others shorter release times is negligible. This value of off-time was selected to allow resolution of DCR in large as well as small SPADs, given the measurement time resolution available.

As shown in Figure 7.4, sample 1 has consistent bulk breakdown and there is no variation of the breakdown voltage due to edge breakdown. As a result, despite the significant number of carriers flowing on the surface, evidenced by the dominant surface leakage current, these carriers do not experience enough multiplication to breakdown. On the other hand, the lower number of carriers in the bulk experience the dominant bulk breakdown probability, meaning overall DCR is dominated by bulk at 1000 ms off-time. However, with shorter off time, the afterpulsing effect starts to be significant. Interestingly in this region, the DCR shows an approximate perimeter dependence suggesting that the surface is the source of the additional primary dark carriers. Presumably a fraction diffuses into the bulk to experience the high gain and trigger the breakdowns. This indicates that the origin of the defects, particularly deep defects, is more likely to be the surface. Consequently, to minimise the afterpulsing effect and increase the upper useful frequency, more efforts should be made to improve the surface or adopt a planar architecture.

7.6 Conclusions

Some previously unpublished work has attempted to grow an $Al_{0.8}Ga_{0.2}As$/GaInNAsSb SAM APD. However, they were compromised by errors associated with the ionisation coefficient for AlGaAs at high fields. Dilute nitride is a five-component material with complicated growth conditions, grown by IQE for this work, limiting scope for repeat attempts. Also, there was not sufficient information about its ionisation coefficients, adding to uncertainty. As a result, in order to prepare for AlGaAs/GaInNAsSb SAM APDs, the structure was simplified by initially utilising a GaAs layer as the absorber layer in the SAM structure instead of GaInNAsSb. This GaAs layer was intentionally doped to be p-type with a concentration similar to that of the expected GaInNAsSb at 4.0 x 10^{16} cm^{-3}. In order to determine the ideal charge sheet characteristics for AlGaAs/GaAs SAM APDs, the five APD structures with varying doping and width of the charge sheet was designed one year prior to this work, by a recent PhD student (X. Collins) based on the RPL model with Ng's coefficients. Based on the failure of earlier AlGaAs/GaInNAsSb SAM APDs, X. Collins also made a change to reduce the charge sheet doping compared to the indications of the model.

Sample 2 exhibits the most optimal doping and thickness conditions for the charge sheet. It punches through at ~ 9 V, and the significant difference between the punch- through voltage and the breakdown voltage allows it to be used as an example of a device functioning as a SAM APD. It is important to control the electric field in the absorber layer not only to minimise the dark current in this layer but also to limit any probability of impact ionisation that can take place outside of the multiplication region. In addition, sample 2 successfully controlled the electric field in the planned dilute nitride absorber layer to be lower than the electric field required to initiate the multiplication which is about 250 kV/cm, as determined in Chapter 6. Consequently, in the future, the structure for sample 2 should be utilised as the nominal design when reintroducing a GaInNAsSb absorber layer. Multiple growths are still recommended, allowing for some spread in charge sheet thickness/doping as a contingency. During this work, it was observed that sample 1 APDs did not consistently exhibit punch through, despite the design of sample 1 being nearly equivalent to sample 2, in terms of total charge sheet doping.

Due to the errors in modelling with old coefficients, samples 3, 4 and 5 failed to punch through, and hence, they are not appropriate for SAM APD applications. As sample 3 is expected to punch through very shortly after breakdown with a minimum field in the absorber, hence it may be suitable for SPAD applications that operate above breakdown voltage. Also, as the breakdown voltage is consistent without the effect of edge breakdown seen in sample 2, the over-bias voltage can be defined correctly. All the current work has been carried out at room temperature. In the future, different degrees of temperature can be considered. For example, by increasing the temperature, the scattering will increase, and the carriers will lose a larger fraction of their energy, which shifts the equilibrium between the loss of energy by scattering and the gain of energy from the electric field. Hence, in order to have a sufficient electric field for the avalanche process, the breakdown voltage becomes higher, which may allow an obvious punch-through voltage to be identified in sample 3.

Samples 2 and 5 can be studied as examples of a device functioning as a SAM and a device functioning as an AlGaAs simple *p-i-n*, respectively. Since the AlGaAs multiplication widths in both samples are extremely small, comparing the experimental and simulated multiplication of both samples confirmed the validity of the non-local coefficients of AlGaAs with the RPL model, which were obtained in Chapter 5. These coefficients successfully simulated multiplication and accurately predicted the break-down voltage.

In the future, the RPL model with the accurate non-local coefficients of AlGaAs, can be used to simulate and redesign the structure of AlGaAs/GaAs samples to accurately control the charge sheet and achieve successfully the aimed punch-through voltage. As a result, this useful knowledge of the SAM structure and a sufficient understanding of the ionisation characteristics of AlGaAs and GaInNAsSb materials can be used as a fundamental base to investigate AlGAs/ GaInNAsSb APDs and SPADs. This should significantly improve the chances of future researchers successfully fabricating this interesting SAM APD structure and hopefully realising its potential.

The primary DCR of GaAs/AlGaAs SPADs, which have an extremely small multiplication layer, is lower than that of other common SPADs with thicker multiplication layers, such as InGaAs/InP, InGaAs/InAlAs, and Ge/Si SPADs. Therefore, taking advantage of the small multiplication width can improve the performance of future SPADs. On the other hand, at the moment, these SPADs provide a higher afterpulsing probability than other SPADs. The main source of afterpulsing appears to be defects on the surface, especially deep defects. Consequently, optimizing the surface can decrease the afterpulsing probability and improve the SPAD's performance. Also, using a smaller gate-on time would reduce the probability of afterpulsing by limiting the flow of carriers through the avalanche.

Compared to other SPADs, an extremely thinner multiplication layer (50 nm) was used. This can take advantage of minimising the temperature-dependent current GR at room temperature by reducing the volume of material. So, it can be considered the start of optimising the high-temperature SPADs using a very thin multiplication region, which is different from optimising low-temperature SPAD with a thick multiplication region. In addition, temperature dependence should be studied in the future. Reduction in primary DCR is expected to fall with reduced thermal generation rate. However as discussed in the literature review, afterpulsing probability can have a complex dependence on temperature and frequency/gate-off time, especially at very short gate-off times. This is suggested as an interesting area for further study. Characterising temperature dependence will also help explore the origin of the relatively high afterpulsing in AlGaAs and the slow-release time constants.

In order to optimise SPAD's performance, its associated DCR and SPDE need to be measured and evaluated. All the earlier SPAD’s measurements were undertaken in dark conditions to study DCR and prepare for photon detection. In the future, further investigation can be carried out under illumination to assess more characteristics including SPDE and photon timing jitter.

7.7 Reference

[1] X. Collins, *Dilute Nitride GaInNAsSb for Next Generation Optical Communications*. Lancaster University (United Kingdom), 2021.

[2] D. Ong, K. Li, G. Rees, J. David, and P. Robson, "A simple model to determine multiplication and noise in avalanche photodiodes," *Journal of applied physics,* vol. 83, no. 6, pp. 3426-3428, 1998.

[3] B. Ng *et al.*, "Avalanche multiplication characteristics of Al/sub 0.8/Ga/sub 0.2/As diodes," *IEEE transactions on electron devices,* vol. 48, no. 10, pp. 2198-2204, 2001.

[4] Y. Lu, T. Kalkur, and C. P. de Araujo, "Rapid Thermal Alloyed Ohmic Contacts to p-Type GaAs," *Journal of The Electrochemical Society,* vol. 136, no. 10, p. 3123, 1989.

[5] K. Hikosaka, T. Mimura, and K. Joshin, "Selective dry etching of AlGaAs-GaAs heterojunction," *Japanese Journal of Applied Physics,* vol. 20, no. 11, p. L847, 1981.

[6] O. I. Dosunmu *et al.*, "Resonant cavity enhanced Ge photodetectors for 1550 nm operation on reflecting Si substrates," *IEEE Journal of selected topics in quantum electronics,* vol. 10, no. 4, pp. 694-701, 2004.

[7] G. Karve *et al.*, "Geiger mode operation of an In/sub 0.53/Ga/sub 0.47/As-In/sub 0.52/Al/sub 0.48/As avalanche photodiode," *IEEE journal of quantum electronics,* vol. 39, no. 10, pp. 1281-1286, 2003.

[8] P. Vines *et al.*, "High performance planar germanium-on-silicon single-photon avalanche diode detectors," *Nature communications,* vol. 10, no. 1, p. 1086, 2019.

[9] A. Tosi, A. Dalla Mora, F. Zappa, S. Cova, M. Itzler, and X. Jiang, "InGaAs/InP single-photon avalanche diodes show low dark counts and require moderate cooling," in *Quantum Sensing and Nanophotonic Devices VI*, 2009, vol. 7222: SPIE, pp. 426-434.

[10] X. Meng, "InGaAs/InAlAs single photon avalanche diodes at 1550 nm and X-ray detectors using III-V semiconductor materials," University of Sheffield, 2015.

[11] A. N. Kamel, M. Pu, and K. Yvind, "Surface defect effects in AlGaAs-on-Insulator photonic waveguides," *Optics Express,* vol. 31, no. 12, pp. 20424-20439, 2023.

[12] M. Ren *et al.*, "Al 0.8 Ga 0.2 As Avalanche Photodiodes for Single-Photon Detection," *IEEE Journal of Quantum Electronics,* vol. 51, no. 11, pp. 1-6, 2015.

[13] R. H. Mari, M. Shafi, M. Aziz, A. Khatab, D. Taylor, and M. Henini, "Electrical characterisation of deep level defects in Be-doped AlGaAs grown on (100) and (311) A GaAs substrates by MBE," *Nanoscale research letters,* vol. 6, pp. 1-5, 2011.

[14] J. Afalla, M. H. Balgos, A. Garcia, J. J. Ibanes, A. Salvador, and A. Somintac, "Observation of picosecond carrier lifetimes in GaAs/AlGaAs single quantum wells grown at 630° C," *Journal of luminescence,* vol. 143, pp. 538-541, 2013.

[15] Z. Cevher *et al.*, "Optimization of the defects and the nonradiative lifetime of GaAs/AlGaAs double heterostructures," *Journal of Applied Physics,* vol. 123, no. 16, 2018.

Chapter 8

Conclusions and future work

The work in this thesis attempts to form the basis for developing a SAM APD by using $Al_{0.8}Ga_{0.2}As$ as the multiplication layer and GaInNAsSb as an absorber layer. The wider indirect bandgap in $Al_{0.8}Ga_{0.2}As$ enables the use of very thin multiplication regions with negligible tunnelling effects and extremely low noise. As a result, the desirable advantages of employing thin-multiplication APDs can be exploited. In order to design and simulate the characteristics of thin $Al_{0.8}Ga_{0.2}As$ APDs, non-local ionization coefficients were extracted in Chapter 5. These coefficients were compared with the local coefficients reported by Ng *et al*. and the non-local coefficients of other materials. Although very high dead space to ionization path length ratios have previously been reported in GaAs, this new work shows that that they can also be achieved in AlGaAs. Importantly the required electric fields do not lead to excessive tunnelling in AlGaAs, unlike in GaAs, opening up the potential for practical APDs exploiting this near optimum condition.

The incorporation of nitrogen in the GaInNAsSb absorber layer provides an effective bandgap matching $In_{0.53}Ga_{0.47}As$ with an acceptable dark current, enabling operation at long wavelengths up to 1.5 μm. The lattice matching condition between GaInNAsSb and GaAs introduces the basis of cheap GaAs-based telecommunication APDs. When designing SAM APDs, it is crucial to determine the impact ionization coefficients of the material used for the absorber layer. These coefficients can offer important knowledge on the electric field at which multiplication would start in the absorber. Therefore, an optimal charge sheet condition that keeps a low field in the absorber can be determined. In addition, to design SAM APDs, it is essential to figure out if the electron/hole ionization coefficient ratios of the absorber and multiplication materials are comparable. When the coefficient ratios of the absorber and multiplication layer are opposite, the APDs will experience the worst case with high noise and a long response time.

In chapter 6, the multiplication measurements of GaInNAsSb have been carried out, and the ionization coefficients and threshold energies have been reported using an evolutionary fitting algorithm with the RPL model. These coefficients cannot be considered the final and most precise coefficients for GaInNAsSb. This is in part due to the difficulty of fitting unique parameter-sets when using a non-uniform electric field profile. Other potential reasons include the impossibility of getting pure electron and pure hole multiplication from the same diode, with existing samples, and the challenge of achieving pure injection and accurate mixed injection without the detrimental effect of re-emission. Moreover, the accuracy of the coefficients depends on the absorption profile, which is not known to a high degree of precision. However, these coefficients provide the estimated field where multiplication begins and breaks down and they also offer significant indications suggesting that beta is much larger than alpha. These are important pieces of information, determined for the first time in this work. Already it is clear that, when the dilute nitride absorber is combined with an AlGaAs multiplication region, where alpha is larger than beta, any ionization in the absorber will be extremely detrimental and must be avoided.

A significant proposed area for future work is determining the ionization coefficients and threshold energies of GaInNAsSb more precisely. To do this new *p-i-n* and *n-i-p* diodes with more uniform electric fields can be designed and fabricated. Including diodes with a range of multiplication widths will cover a wide range of electric fields without the detrimental effect of re-emission. Also, the accuracy of the coefficients can be improved by using a precise absorption profile, which would require optical characterisation of the specific alloy. Furthermore, it would be highly desirable to achieve pure electron and hole-initiated multiplication from the same diode by top and back illumination, would made be possible by designing etch stops into the epistructure.

In order to further prepare for AlGaAs/GaInNAsSb SAM APDs, Chapter 7 initially introduced a simple structure using GaAs as the absorber layer in the SAM structure instead of GaInNAsSb. In this way, the complications associated with the five- component dilute nitride material can be avoided. One year before this study, a recent PhD student (X. Collins) attempted to determine the optimum charge sheet conditions for AlGaAs/GaAs SAM APDs. He designed and fabricated multiple campaigns targeting this structure, the third of which comprised five samples studied in this work. It is now understood that Collins' use of the RPL model with Ng's coefficients lead to many of the designs not exhibiting punch through, something which can be avoided in the future by using the new coefficients.

Fortunately, one sample, sample 2, can be considered an example of a device functioning as a SAM APD that has acceptable doping and thickness conditions for the charge sheet. Importantly, in sample 2, the electric field in the planned dilute nitride absorber layer was controlled to be below 250 kV/cm, which is now known to be required to avoid multiplication in the absorber and increased noise. Therefore, in the future, it is recommended to use the structure from sample 2 as the nominal design for development, when reintroducing a GaInNAsSb absorber layer. Several growth variants should be planned, allowing for some variation in doping and thickness of the charge sheet to ensure punch through occurs at the desired field and as already emphasised, multiplication in the absorber is supressed.

Since Collins designed using old and incorrect coefficients, samples 3, 4, and 5 did not show punch-through. However, CV fitting predicts that sample 3 will punch through very shortly after breakdown with a low field in the absorber. This is an interesting case which is worthy of further investigation since it may be optimal for SPAD applications that function above the breakdown voltage. In the future, by operating at a higher temperature, the punch-through voltage of sample 3 could be determined experimentally to check this. Furthermore, unlike sample 2, sample 3 exhibits a consistent breakdown voltage that is unaffected by edge breakdown, allowing for the over-bias voltage to be identified accurately. It is hoped that some of the surface effects could be avoided in sample 3.

Samples 2 and 5 were investigated as examples of devices operating as SAM and a simple AlGaAs *p-i-n* diodes, respectively. Due to the extremely thin AlGaAs multiplication thickness of these samples, they were used to verify the new non-local coefficients of AlGaAs with the RPL model, which were obtained in Chapter 5. It was found that these coefficients adequately modelled multiplication and predicted the break-down voltage, further confirming that in the future they can be used for optimising the design of ultra-thin AlGaAs APDs.

The last section in Chapter 7 made a preliminary investigation into the DCR characteristics of GaAs/AlGaAs SPADS. These SPADs show a primary DCR lower than that of other common SPADs, despite having a much thinner multiplication layer which would usually be associated with higher tunnelling related DCRs. This supports the theory that AlGaAs SPADs could offer enhanced timing performance due to a thin multiplication width, without inherent detrimental effects to DCR. On the other hand, a higher afterpulsing probability was seen in these SPADs, compared to other more mature SPADs. It was found that the afterpulsing is mostly due to carriers originating from the surface, with time constants indicating a high level of deep traps. As a result, it is proposed that the afterpulsing probability can be minimised through surface optimization or the use of a planar architecture. Also, a smaller gate-on time, which limits the flow of carriers through the avalanche, can be expected to reduce the afterpulsing probability. These areas related to how the device is made and operated, have significant potential to reduce the DCR in future generations.

This thesis has set out some important foundational understanding regarding the materials and device structures required for AlGaAs/GaInNAsSb APDs and SPADs. In some areas further work is necessary to expand or improve on what is initial research into a challenging novel area. However, it is clear that AlGaAs/GaInNAsSb APDs and SPADs have significant potential for unique performance characteristics and further research and development is highly recommended.